

# Realizing dissipative time crystals in an atom-cavity system

Dissertation  
zur Erlangung des Doktorgrades  
an der Fakultät für Mathematik, Informatik und Naturwissenschaften  
Fachbereich Physik  
der Universität Hamburg

vorgelegt von  
Phatthamon Kongkhambut

Hamburg  
2024



Gutachter/innen der Dissertation:	Prof. Dr. Andreas Hemmerich Prof. Dr. Henning Moritz
Zusammensetzung der Prüfungskommission:	Prof. Dr. Andreas Hemmerich Prof. Dr. Henning Moritz Prof. Dr. Ludwig Mathey Prof. Dr. Roman Schnabel Dr. Juliette Simonet
Vorsitzende/r der Prüfungskommission:	Prof. Dr. Roman Schnabel
Datum der Disputation:	02.02.2024
Vorsitzender Fach-Promotionsausschuss PHYSIK:	Prof. Dr. Markus Drescher
Leiter des Fachbereichs PHYSIK:	Prof. Dr. Wolfgang J. Parak
Dekan der Fakultät MIN:	Prof. Dr.-Ing. Norbert Ritter





# Abstract

Spontaneous symmetry breaking of a system's ground state always results in a phase transition. Symmetry breaking can happen in both space and time domains, e.g., a spontaneous breaking of translation symmetry in space gives rise to a crystalline phase, while a spontaneous breaking of translation symmetry in time gives rise to a dynamical phase called *time crystal* (TC). The main characteristics of TCs include many-body interaction-sustained dynamics and robustness against temporal perturbations. TCs can be classified as discrete or continuous depending on whether they break discrete or continuous time translation symmetry. In this thesis, we experimentally realized both discrete [1–3] and continuous TCs [4] for the first time in an open system, so-called dissipative TCs. Moreover, it is the first time a continuous TC has been observed. Our experimental system comprises a Bose-Einstein condensate of  $^{87}\text{Rb}$  atoms coupled to a single mode of a high-finesse optical cavity. The system is transversely pumped by a standing wave light field. By driving the relevant pump parameter periodically, we realized discrete time crystalline phases using the pump frequency red-detuned to the atomic transition. The periodic modulation of the pump intensity gives rise to a commensurate discrete TC, such that its main feature is the switching between two symmetry-broken states with the sub-harmonic frequency of the driving frequency [1]. On the other hand, periodic modulation of the phase of the standing wave pump potential results in an incommensurate discrete TC, whose response frequency is an irrational fraction of the modulation frequency [2]. We showed that the incommensurate discrete TC dynamics can be captured by the non-standard parametrically driven three-level open Dicke model [3]. Further investigations concluded that the incommensurate TC has a transient behavior such that in a particular parameter regime, the atoms are transferred into the dark state of the atom-cavity system [5]. While discrete TC has been widely studied in the past years, continuous TC has remained elusive. By continuously pumping the system with the blue-detuned pump, we reported for the first time an observation of a continuous TC [4]. We observed the emergence of limit cycle dynamics characterized by an oscillation of the intra-cavity light intensity, which is stable in a large area of the relevant parameter space and robust against temporal perturbations. The time phase of the oscillation of different experimental realizations takes random values between 0 and  $2\pi$ . Therefore, it hints at the spontaneous breaking of the continuous time translation symmetry, resulting in a continuous TC.



# Zusammenfassung

Die spontane Symmetriebrechung des Grundzustands eines Systems führt immer zu einem Phasenübergang. Eine Symmetriebrechung kann sowohl im Raum als auch in der Zeit auftreten, z. B. führt die spontane Brechung der Translations-symmetrie im Raum zu einer kristallinen Phase, während eine spontane Brechung der Translations-symmetrie in der Zeit zu einer dynamischen Phase führt, die als "Zeitkristall" (TC) bezeichnet wird. Das Hauptmerkmal eines TCs ist seine periodische Dynamic, welche durch Vielteilcheneffekte stabilisiert ist und dadurch besonders stabil gegen Störungen ist. TCs können je nachdem, ob sie diskrete oder kontinuierliche zeitliche Translations-symmetrie brechen, als diskrete oder kontinuierliche TCs klassifiziert werden. In dieser Arbeit haben wir erstmals sowohl diskrete TCs [1–3] als auch kontinuierliche TCs [4] in einem offenen System, sogenannte dissipative TCs, experimentell realisiert. Darüber hinaus handelt es sich um das erste Mal, dass ein kontinuierlicher TC überhaupt beobachtet wurde. Unser experimentelles System besteht aus einem Bose-Einstein-Kondensat von  $^{87}\text{Rb}$ -Atomen, welches mit dem Lichtfeld in einem Resonator hoher Güte gekoppelt ist. Das System wird transversal mit einer Stehwelle aus Licht gepumpt. Mit Hilfe von Pumplicht, welches im Bezug auf die atomare Resonanz rot verstimmt ist, konnten wir durch geeignetes modulieren der relevanten Pump-Parameter diskrete zeitkristalline Phasen realisieren. Die periodische Modulation der Pumpintensität führt zu einem kommensurablen diskreten TC, bei dem das Hauptmerkmal eine Oszillation zwischen zwei symmetriegebrochenen Zuständen mit der halben Modulationsfrequenz ist [1]. Andererseits führt periodische Modulation der Phase des stehenden Wellenpotentials zu einem inkommensurablen diskreten TC, dessen Antwortfrequenz ein irrationaler Bruchteil der Modulationsfrequenz ist [2]. Wir haben gezeigt, dass die Dynamik des inkommensurablen diskreten TCs durch das parametrisch angetriebene offene dreiniveau-Dicke-Modell beschrieben werden kann [3]. Weitere Experimente ergaben, dass der inkommensurable TC ein transientes Verhalten aufweist und die Atome in einem bestimmten Parameterbereich in einen Dunkelzustand des Atom-Resonator Systems überführt werden [5]. Während diskrete TCs in den letzten Jahren weit verbreitet untersucht wurden, war die Realisierung eines kontinuierlichen Zeitkristalls bisher noch nicht gelungen. Durch kontinuierliches Pumpen des Systems mit blau vertstimmttem Licht, ist es uns erstmals gelungen einen kontinuierlichen TC zu erzeugen [4]. Er zeichnet sich durch stabile Oszillationen der Lichtintensität im Resonator aus, welche in einem großen Parameterbereich beobachtet werden konnten und besonders stabil gegen Störungen sind. Die Zeitphase der Oszillationen in verschiedenen experimentellen Realisierungen nimmt zufällige Werte zwischen 0 und  $2\pi$  an. Das deutet auf eine spontane Brechung der kontinuierlichen Zeit-Translations-symmetrie hin und diese Beobachtungen bestätigen die Realisierung eines kontinuierlichen Zeitkristalls.



# Acknowledgements

This thesis would not have been completed without contributions of the following people. As an international student from a developing country pursuing my passion for studying physics, the journey has not been easy. I would like to express my heartfelt gratitude to everyone who has supported me along this path.

I would like to express my deepest gratitude to my supervisor, Prof. Andreas Hemmerich, for always inspiring and motivating me during my doctoral research. He mentioned that taking the research journey would be like exploring an unknown path. Now, I take pride in the hope that my PhD projects have contributed to paving that unexplored territory. I genuinely appreciate your guidance over the years and for being a role model who has made me a better experimentalist.

I'm extremely grateful to Prof. Henning Moritz for dedicating his time to serve as my second supervisor and as a reviewer for this thesis. I greatly appreciate your advice, which has not only improved my scientific knowledge but also enhanced my personal soft skills as an individual.

I am deeply indebted to the Hamburg cavity team, with a special big thanks to Hans Keßler for his unwavering support and patience while training me in the lab. I greatly appreciate the countless hours we spent in the laboratory, as well as the motivational and fruitful discussions we had. I am especially thankful for your positive attitude towards research and your dedication, which have created a highly motivating atmosphere in the lab for me. Many thanks to our group's former members, Christoph Georges and Jens Klinder, for their help and support in the lab even after their graduation. A special thanks to Hans Keßler and Anton Bölian for proofreading my thesis. I would also like to thank our theory collaborators, Jayson G. Cosme, Jim Skulte, and Prof. Ludwig Mathey, for the many insightful discussions that have helped me better understand and appreciate our observations even more.

It has been my pleasure to be part of the Hemmerich group. I would like to thank David, Max, Yann, José, Sahana, Anton, Hans, and Christoph, for creating a welcoming atmosphere within the institute. I appreciate our discussions or small chats over the group meetings and lunch breaks, as well as the recreational activities we enjoyed together like Christmas parties, BBQ get-togethers, and Tuesday brunches. I would also like to thank the Collaborative Research Center SFB 925 and CUI: Advanced Imaging of Matter for their financial support, which enabled me to gain experience through participation in conferences and workshops.

I would also like to acknowledge my teachers and instructors since my childhood, for the valuable knowledge and wisdom they shared. I am also thankful to my classmates and friends, for their emotional and moral support. I am especially very grateful to have Delia and Ben with me in Hamburg. With your presence and kindness, our shared apartment feels like home to me.

Lastly, I could not have undertaken this journey without the unconditional love and support from my family. Thank you for raising me with love (and delicious food). Thank you Dad, for building all the 'experimental tools' for my young scientist self.

In loving memory of Ya Khao, my beloved grandmother, who would have been extremely proud to see me with my thesis today.



## **Eidesstattliche Versicherung / Declaration on oath**

Hiermit versichere ich an Eides statt, die vorliegende Dissertationsschrift selbst verfasst und keine anderen als die angegebenen Hilfsmittel und Quellen benutzt zu haben.

Hamburg, den 02.02.2024

---

Unterschrift der Doktorandin





# Contents

<b>Publications and Author's Contributions</b>	<b>xiii</b>
<b>1 Introduction</b>	<b>1</b>
<b>2 The experimental apparatus</b>	<b>7</b>
2.1 BEC preparation . . . . .	7
2.2 Self-organized superradiant phase transition . . . . .	9
2.3 Balanced heterodyne detector . . . . .	12
<b>3 The theoretical framework</b>	<b>17</b>
3.1 Atom-cavity Hamiltonian . . . . .	17
3.2 Dicke Model . . . . .	18
3.3 Periodically driven three-level Dicke Model . . . . .	19
<b>4 Red-detuned pump experiments</b>	<b>23</b>
4.1 Commensurate discrete time crystals . . . . .	23
4.1.1 Publication I . . . . .	23
4.2 Incommensurate discrete time crystal . . . . .	31
4.2.1 Publication II & III . . . . .	31
4.3 Publication IV: Condensate formation in a dark state . . . . .	54
<b>5 Blue-detuned pump experiments</b>	<b>61</b>
5.1 Publication V: Continuous time crystal . . . . .	61
<b>6 Conclusions and Outlook</b>	<b>69</b>
6.1 From a continuous to a discrete time crystal . . . . .	70
6.2 Observation of limit cycles for red-detuned pump light . . . . .	71
<b>A Supplement material of publication I</b>	<b>73</b>
<b>B Supplement material of publication II</b>	<b>79</b>
<b>C Supplement material of publication IV</b>	<b>89</b>
<b>D Supplement material of publication V</b>	<b>99</b>
<b>Bibliography</b>	<b>117</b>



# Publications

**This thesis is a cumulative dissertation based on the following publications:**

[1] H. Keßler, P. Kongkhambut, C. Georges, L. Mathey, J. G. Cosme, and A. Hemmerich. *Observation of a Dissipative Time Crystal*, [Phys. Rev. Lett.](#), **127**, 043602 (2021).

[2] P. Kongkhambut, H. Keßler, J. Skulte, L. Mathey, J. G. Cosme, and A. Hemmerich, *Realization of a Periodically Driven Open Three-Level Dicke model*, [Phys. Rev. Lett.](#), **127**, 253601 (2021).

[3] J. Skulte, P. Kongkhambut, H. Keßler, A. Hemmerich, L. Mathey, and J. G. Cosme, *Parametrically driven dissipative three-level Dicke model*, [Phys. Rev. A](#), **104**, 063705 (2021).

[4] P. Kongkhambut, J. Skulte, L. Mathey, J. G. Cosme, A. Hemmerich, and H. Keßler, *Observation of a continuous time crystal*, [Science](#), **37**, 670-673 (2022).

[5] P. Kongkhambut, J. Skulte, S. Rao, L. Mathey, H. Keßler, A. Hemmerich, and J. G. Cosme, *Condensate formation in a dark state of a driven atom-cavity system*, [Phys. Rev. Lett.](#) **130**, 163603 (2023).

## Author's contributions

In the beginning of my PhD research, I upgraded the experimental setup by building and integrating the heterodyne detection into our ultra cold atom-cavity apparatus. This allows us to be able to, for the first time in our setup, detect a phase difference between the intra-cavity and the pump field which heralds the two  $Z_2$  symmetry broken ground states of the self-organized superradiant phase. This heterodyne detector facilitates the observation of dynamical phases in [1–5], while the existing detection scheme is inadequate. I also performed experiments, carried out developments of data analysis scripts, designed the figures, and took part in the preparation of manuscripts.

## Publications in preparation

Preliminary results shown in section 6.1 and section 6.2 are in the manuscript preparation stage during the process of writing this thesis



# Abbreviations

<b>AMO</b>	atomic, molecular, and optical physics
<b>AOM</b>	acousto-optic modulator
<b>BEC</b>	Bose-Einstein condensate
<b>BS</b>	beam splitter
<b>CTC</b>	continuous time crystal
<b>DTC</b>	discrete time crystal
<b>HD</b>	heterodyne detector
<b>ITC</b>	incommensurate time crystal
<b>LC</b>	limit cycle
<b>lo</b>	local oscillator
<b>NP</b>	normal phase
<b>PID</b>	proportional–integral–derivative
<b>PBS</b>	polarizing beam splitter
<b>TWA</b>	truncated-Wigner Approximation
<b>TOF</b>	time-of-flight
<b>s</b>	signal
<b>SPCM</b>	single-photon-counting module
<b>SR</b>	superradiant self-organization phase
<b>cQED</b>	cavity quantum electrodynamics



# Chapter 1

## Introduction

A physical system possesses a certain symmetry if its properties are invariant under certain probing aspects. For example, water in its liquid state has a homogeneous macroscopic density distribution, and therefore, manifests a *continuous translation symmetry*. Another example is spherical objects equipped with a *rotational symmetry* because they appear the same after a rotation by *any angle*.

Spontaneous symmetry breaking of a physical system always leads to a phase transition, giving rise to a new phase of matter with new fundamental properties. In everyday life, this occurs when water solidifies into ice. When the temperature and pressure of water are suitable, the water molecules crystallize spontaneously. The first few water molecules from arbitrary positions are triggered by thermal fluctuations to crystallize, and the whole ice structure starts to grow from that point. In ice, the density of water molecules is *fixed discretely in space*, therefore, it exhibits a *discrete translation symmetry*, as its structure repeats itself only if we probe at every fixed distance. In physics, a spontaneous phase transition happens when the system's ground state possesses a different symmetry than that of the equations governing its properties. Many times, the ground state exhibits a lower symmetry class.

While the spontaneous breaking of translation symmetry in space and the crystallization process is well known, it remains elusive whether it is possible to observe an analogous phenomenon of spontaneous symmetry breaking in the time domain. The biologist Arthur T. Winfree pointed out in the 70s that the self-sustaining synchronization oscillatory behavior observed in many biological systems [6, 7] has a *temporal phenomenon analogous to crystallization* [8, 9]. This was the first time the idea of *time crystals* was introduced to the scientific community. In 2012, Nobel laureate in Physics Frank Wilczek posed an idea: if space and time are interchangeable, spontaneous symmetry breaking could also happen in the time domain, analogous to spatial crystals. If the system's ground state breaks the time translation spontaneously, the system thus crystallizes into a *time crystal* [10, 11]. Not long after this proposal, a series of no-go theorems ruled out the possibility of Wilczek's time crystal in nature [12–14]. Nonetheless, the excitement of searching for time crystals was not extinguished, as one could tweak from the original idea. For example, one can circumvent the no-go theorems by realizing time crystals in a non-equilibrium state, such as in a Floquet-driven system [15–17]. The Floquet drive imprints the discrete-time translation symmetry into the system. Thus, when the system responds to the drive with a different periodicity, it breaks the discrete-time translation symmetry, therefore forming a *discrete time crystal* (DTC). The essential signatures of

DTCs are persistent oscillations at a frequency lower than that of its external Floquet drive, and the robustness of the response oscillation against temporal perturbations supported by many-body interactions [18].

In 2017, the first realizations of DTCs were demonstrated in a periodically driven trapped ion chain [19] and dipolar spin impurities in diamond [20]. Many more followed in 2018, such as DTCs in nuclear spins system [21] and ultra-cold atoms [22]. In these realizations, the system responds with an oscillation frequency at half of the driven frequency, thus exhibiting a *sub-harmonic* response. However, time crystals in closed systems are sensitive to heating, such that their lifetime is limited, unless phenomena such as many-body localization breaks ergodicity [23]. Theoretical studies suggested that well-controlled dissipation and fluctuations in a driven open system can help stabilize the time crystalline dynamics [24–28]. Following these ideas, we employ an experimental system consisting of an ultra-cold quantum gas coupled to an optical cavity, providing a versatile quantum simulator platform to simulate many-body physics of strong light-matter coupling with a well-controlled dissipative channel.

Quantum simulators were proposed by Richard Feynman in the 80s. He stated that the physical world is quantum mechanical; therefore, we need quantum simulators to study nature efficiently [29]. When computing the quantum dynamics of many-body systems, the computational power required by classical computers is infeasible expensive. Feynman suggested that a quantum computer/simulator can achieve precisely what nature does in an appropriate timescale and number of constituents. The idea is to employ a well-controlled quantum system to engineer the Hamiltonian and simulate ground states or the system’s time evolution. Promising platforms for quantum simulations include quantum gas machines of neutral atoms [30–34], cold trapped ions [35–38], superconducting circuits [39–41], nitrogen-vacancy centers in diamond [42–44], and photonic qubits [45–47]. A commonality among these systems is that they have very low operating temperatures, such that quantum mechanical effects dominate.

One important ingredient of our quantum gas machine is the ultra-cold atomic ensemble. Advanced developments in the field of atomic, molecular, and optical physics (AMO) in the past decades enable us to cool [48–52], capture [53], and manipulate atomic, ionic, and molecular states of matter. In 1995, an ultra-cold ensemble of bosonic alkali atoms in a range of nanokelvin temperature was reached with an evaporative cooling technique [54, 55]. At such low temperatures, the particle’s de Broglie wavelength is on the same order as its particle spacing. This leads to a macroscopic population of the system’s ground state forming the so-called BEC, predicted by Einstein and Bose in 1924 [56]. Since then, a quantum gas machine with a BEC has been a leading platform for quantum simulators [32]. Advanced physics problems that a quantum gas machine can study range from many-body problems in condensed matter physics e.g. quantum phase transitions [57, 58] and quantum magnetism [59], to cosmological studies such as black holes [60] and dark matter [61]. For simulating a time crystal using an ultra-cold quantum gas machine, we need a many-body long-range type of interaction which we realized by coupling the BEC to a high-finesse optical cavity.

To increase the coupling between light and matter in free space, an effective measure is to place the atomic ensemble inside a high-finesse optical cavity, where light-matter interactions are strongly enhanced due to the long lifetime of the intra-



cavity light field. This regime has been studied extensively in the area of cavity quantum electrodynamics (cQED). It started with the study of coupling single mode radiation to single atoms, and later branched out to coupling a single mode radiation to macroscopic objects, e.g., sub-micron mechanical oscillators [62, 63], quantum dots [64], or an ultra-cold ensemble of atoms [65]. Optical cavities have a well-controlled dissipative channel and are ideal for studying quantum systems coupled to an environment [66]. Detecting the light field leaking out of the cavity also provides a non-destructive real-time observation channel [67–70], as well as a platform for studying quantum measurement back-action [71–75]. Atom-cavity systems also pave the way for the study of non-equilibrium phases, such as the second-order phase transition to a superradiant self-organized phase, which can be achieved by pumping the atoms transversely to the cavity axis, as was proposed by Domokos and Ritsch in 2002 [76]. The system can be mapped onto the Dicke model, which describes  $N$  two-level atoms coupled to a single light mode. In the 1970s, Hepp and Lieb discovered the superradiant phase transition predicted by the Dicke model [77, 78]. Later, this superradiant self-organized phase has been realized in many experiments, comprising either a cold ensemble of atoms [79] or quantum gases like a BEC [80, 81] coupled to a single mode of an optical cavity. This phase also manifests a cavity-mediated infinite range all-to-all interaction between atoms. Furthermore, A BEC-cavity platform serves as a very versatile platform to study non-linear dynamics such as optical bistability [82–84], cavity cooling in a recoil resolved regime [85], geometrical pumping [86], and most recently during my PhD projects, time crystalline phases [1–5].

**In this thesis:**

For the first time, we demonstrated various dissipative time crystalline phases, which are accessible uniquely with our recoil-resolved cavity; see fig. 1.1. First, in 2021, we demonstrated discrete time translation symmetry breaking in an open system by periodically driving the intensity of a pump field [1]. This gives rise to a DTC that has a commensurate response with respect to the driving frequency  $\omega_{\text{dr}}$ ; specifically, in this observation, it reveals a sub-harmonic response. Later in the same year, we explored the system in a different aspect. Inspired by a theoretical prediction by the group of Ludwig Mathey [87], we realized another type of DTCs characterized by an incommensurate sub-harmonic response [2], which can be qualitatively mapped to a parametrically driven three-level Dicke model [3]. Furthermore, we observed a peculiarly long-lived condensate fraction in a checkerboard pattern without detecting an intra-cavity light field. We later interpreted the results in 2022 as condensate formation in a dark state [5]. At that time, while DTCs were widely studied and realized, a CTC remained elusive. By changing the pump detuning to the blue side of the atomic resonance, we observed a region in the phase diagram where the intra-cavity photon  $N_p$  exhibits limit cycle behavior with an oscillation frequency of  $\omega_{\text{lc}}$ , while the pump parameters remained constant [4]. Investigations showed that the time phase of the oscillation from many experimental realizations takes random values between 0 and  $2\pi$ , as expected for the spontaneous breaking of the continuous time translation symmetry. The observation brought us closer to the original idea of time crystals that Wilczek proposed in 2012, while circumventing the no-go theorems by employing an open system. Note that this was the first time a CTC has been

observed.

We categorized the results into two main chapters based on the detuning of the pump light with respect to the atomic resonance. Chapter 4 and chapter 5 discuss the cases of red and blue detunings, respectively.

**Overview:** See as well fig. 1.1 for an illustration of an overview of this thesis.

- **Chapter 2** introduces our experimental apparatus and detection techniques.
- **Chapter 3** discusses the theoretical framework. This includes Hamiltonian of a strongly coupled atom-cavity system, standard two-level Dicke model, and a parametrically driven three-level Dicke model.
- **Chapter 4** includes publications conducted with a red pump-atom detuning. They are grouped into two main sections based on an experimental point of view and ordered chronologically. Publication I [1], in section 4.1.1, presented the first observation of a dissipative DTC, which results from modulating the intensity of the pump. Section 4.2.1 consists of publication II-IV [2, 3, 5], which are conducted by phase modulation of the pump potential. Publications II and III reported on an observation of incommensurate time crystals (ITC). Publication IV showed that, for a certain parameter space exhibiting the ITC, the system relaxes into a dark state of the atom-cavity system.
- **Chapter 5** discusses the experiments using blue pump-atom detuning, publication V: an observation of continuous time crystals [4].
- **Chapter 6** gives a conclusion, final remarks, and an outlook.

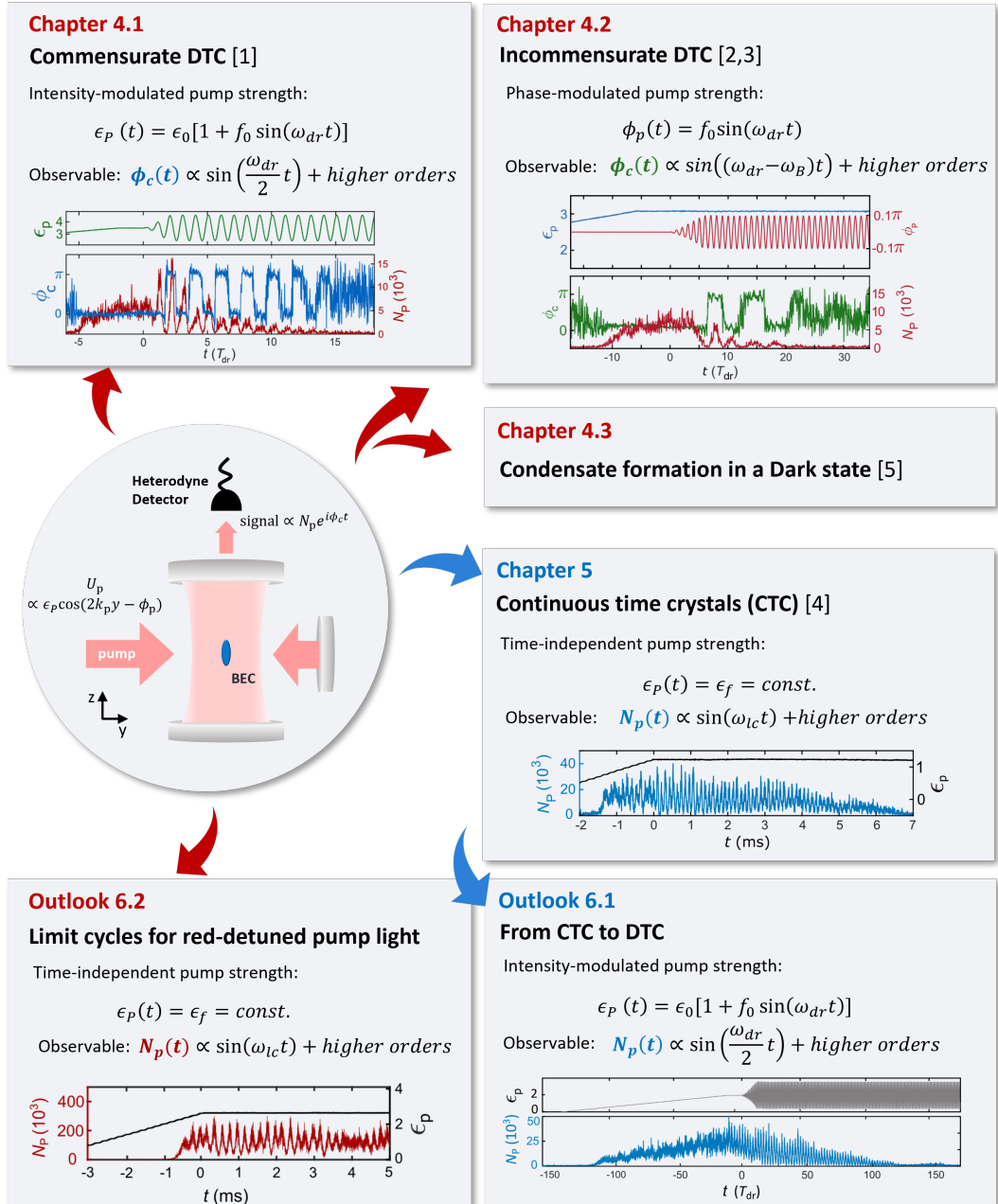


**Figure 1.1:** Illustration of an overview of this thesis. The center shows a schematic of the experimental setup. The BEC of  $^{87}\text{Rb}$  atoms is overlapped with a single fundamental mode of the cavity. The BEC-cavity system is transversely pumped by laser light operated in the dispersive regime. The pump is retro-reflected, creating a standing wave potential  $U_p$ . The potential is spatially dependent along the  $y$ -axis and is proportional to the pump intensity  $\epsilon_p$ , the pump wave number  $k_p$ , and its phase  $\phi_p$ . We detect the intra-cavity light field that is transmitted through one of the cavity mirrors using a heterodyne detector, see section 2.3, which measures the phase  $\phi_c$  and the intensity  $N_p$  of the light field. Each experiment is indicated by an arrow, the color of which indicates whether a red or blue pump-atom detuning was used for the given experiment. In each experiment, the initial variable, the observable showing the signature of the phase transition, and the exemplary protocol and results are presented.



# Chapter 2

## The experimental apparatus

As this thesis is focused on the scientific outcomes described in the following chapters, this chapter only gives a short overview of the experimental platform and the new heterodyne detector that I designed and implemented into the setup. The new detector improved the detection efficiency and gave, for the first time, access to the phase of the intra-cavity field.

### 2.1 BEC preparation

The BEC preparation consists of three main operations, the magneto-optical trap (MOT) [53, 88], magnetic transport, and the evaporative cooling in the magnetic trap. The MOT stage takes around 29 s and consists of two simultaneously-running MOT configurations, the adapted two dimensional MOT (2D<sup>+</sup>-MOT)<sup>1</sup> and the three-dimensional MOT (3D-MOT) [88]. The vacuum chamber is separated by a differential pumping tube into two parts, the source chamber and the science chamber, where the 2D<sup>+</sup>-MOT and the 3D-MOT are implemented, respectively. More details about the design and set up of the vacuum chambers can be found in PhD theses of M. Wolke [90] and J. Klinner [91]. After the atom number in the 3D-MOT has saturated, we compress the confinement of the atomic ensemble by increasing the magnetic field gradient and gain a higher atomic density. Then, the atomic ensemble is cooled down further by the optical molasses technique [49, 51, 92]. After that, we optically pump the atoms into the hyperfine Zeeman state  $|5^2S_{1/2}, F = 2, m_F = 2\rangle$  to be able to efficiently load the ensemble into the magnetic trap in the next step. More details about the optical pumping can be found in the PhD thesis of J. Klinner [91]. Finally, the ensemble is loaded into a magnetic trapping potential, which is created by rapidly ramping the current of the 3D-MOT coils to a high value. More details about laser systems used to cool, repump, optically pump, and image the atoms can be found in the PhD thesis of C. Georges [93] and details about cooling protocols can be found in the PhD thesis of M. Wolke [90] and J. Klinner [91]. In the second stage, the cold ensemble gets magnetically transported to close to the experimental cavity and trapped in a quadrupole Ioffe configuration (QUIC) trap. For more details on this, see the PhD thesis of M. Wolke [90].

---

<sup>1</sup>Consists of a conventional 2D-MOT [89] creating a cooling effect in the  $xy$  plane and one additional beam in  $z$  axis, the push beam, which cools and also transports atoms to the science chamber at the same time.

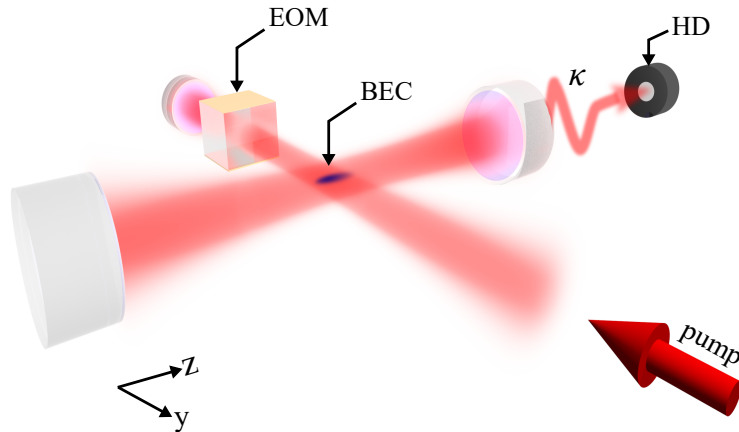


*Figure 2.1:* Schematic drawing of the experimental setup adapted from fig. 1 of publication IV [5]. The BEC of  $^{87}\text{Rb}$  atoms is coupled to a single mode cavity with decay rate  $\kappa$ . The transverse pump light along the  $y$ -axis is retro-reflected by a mirror forming an optical standing wave potential to the BEC. An electro-optic modulator (EOM) can be placed between the BEC and the retro-reflected mirror to modulate the phase of the optical standing wave potential, see results in section 4.2 and section 4.3. The light, leaking from one of the cavity mirrors is measured by the heterodyne detector (HD).

In the third stage, the cold atomic ensemble in the QUIC trap [94] is cooled to reach quantum degeneracy using evaporative cooling [54, 95]. The center of the QUIC trap locates close to, but still outside of, the cavity mode to avoid heating of the ultra cold ensemble due to the light used to stabilize the laser to the cavity's resonance. Therefore, the BEC is micro-transported to be overlapped with the  $TEM_{00}$  mode of an optical cavity by using magnetic offset fields in  $xy$  direction. See more about cavity stabilization schemes in PhD theses of J. Klinder [96], H. Keßler [97], and C. Georges [93]. After the micro transport, we decrease the trapping potential to reduce the BEC density, and thus reduce the three-body collision loss and prolong the lifetime of the BEC. At this stage we are finished with the BEC production and we can start the main part of the experiments by applying pump protocols to study dynamical phases emerging in the atom-cavity system [1–5].

In the following, I will give the main parameters of the setup to provide an overview. The BEC in the optical cavity has approximately  $N_a \approx 5 \times 10^4$  atoms held in space by a magnetic trap, creating a harmonic potential with trapping frequencies  $\omega = 2\pi \times (102.7, 119.0, 24.7) \text{ Hz}^2$ . The ultra-high finesse optical cavity operates in the recoil-resolved regime [84], i.e. the field decay rate of the cavity,  $\kappa \approx 2\pi \times 3.4 \text{ kHz}$ , is comparable to a recoil frequency of the atoms,  $\omega_{\text{rec}} \approx 2\pi \times 3.7 \text{ kHz}^3$ . More details about the cavity parameters can be found in the PhD thesis of M. Wolke [90]. Note that  $\kappa$  and  $\omega_{\text{rec}}$  depend on a pump wavelength  $\lambda_P$ . We measured  $\kappa$  and calculated  $\omega_{\text{rec}}$  at a pump wavelength in a range of 792–803 nm

<sup>2</sup>For an experiment in chapter 5. The trapping frequencies used in the experiments in chapter 4 are slightly higher. We have been gradually reducing the trapping frequencies from experiments in chapter 4 to chapter 5 to prolong the lifetime of the BEC sample by reducing the three-body particle loss which highly dependent with the density of the BEC.

<sup>3</sup>Measured at a pump wavelength of 792.55 nm.

and obtained  $\kappa \in 3-4$  kHz and  $\omega_{\text{rec}} \in 3.5-3.7$  kHz. The cavity free spectral range is  $\Delta_{\text{FSR}} = \frac{c}{2L} \approx 3063$  MHz, where  $c$  is the speed of light and  $L = 48.93$  mm is the cavity length [90]. The finesse  $F$  is derived from the free spectral range and field decay rate as  $F = \Delta_{\text{FSR}}/2\kappa$  and we measured it to be in a range of  $4.5 - 4.8 \times 10^5$ .

During the experiments presented in this thesis, the atom-cavity system is transversely pumped with a retro-reflected laser beam with wavelength  $\lambda_{\text{p}}$ , see fig. 2.1 for a schematic drawing. With the current laser system,  $\lambda_{\text{p}}$  can be tuned between 790 nm and 805 nm. The pump light is operated in the dispersive regime as it is far-off resonance with respect to the atomic transition, such that only coherent Rayleigh scattering arises. The retro-reflected pump beam creates a standing wave potential  $U_{\text{p}}$  for the atoms. This pump potential can be written as  $U_{\text{p}} \propto \epsilon_{\text{p}} \cos(2k_{\text{p}}y + \phi_{\text{p}})$ , where  $\epsilon_{\text{p}}$  is the pump intensity,  $k_{\text{p}}$  is the pump wave number, and  $\phi_{\text{p}}$  is the phase of the standing wave potential. Section 4.2 shows that one can modulate the phase of this standing wave potential using an electro-optical modulator (EOM) placed between the BEC and the retro-reflecting mirror, see fig. 2.1. The pump wavelength used in the experiments presented in chapter 4 is 803 nm. It is red-detuned with respect to the  $D_1$  transition line of  $^{87}\text{Rb}$ , at 794.98 nm. In chapter 5, we set the pump wavelength to 792.55 nm, which is in the blue detuned regime. The light force of the pump can be repulsive or attractive to the atoms, if the pump is blue- or red-detuned, respectively. As a results, with the red detuned pump, the atoms localize at the pump intensity maxima. On the other hand, if the bump is blue-detuned, the atoms localize at the pump intensity minima.

In total, the BEC preparation process takes around 39 s. The pumping protocol takes around 30 ms. After the experiments with the pump protocols, we add 18 s of holding time where we switch off all the in-vacuum coils to prevent overheating and damage. Note that this is crucial for us, since the coils responsible for the magnetic fields of the 3D-MOT, the transport, the QUIC trap, and the micro-transport locate inside of the science chamber.

## 2.2 Self-organized superradiant phase transition

To study the dynamical phases presented in this thesis, we initialize our atom-cavity system in the self-organized superradiant (SR) phase and then either periodically drive [1–3, 5] or time-independently drive [4] the relevant pump parameters. This section gives an introduction to the SR phase and the accessible observables in our setup.

The BEC in the cavity shifts the cavity resonance  $\omega_{\text{c}}$  by an amount of  $\delta_{-} = N_{\text{a}}U_0/2$ , where  $U_0$  is the maximal light shift per intra-cavity photon and  $N_{\text{a}}$  is a number of atoms in the BEC. A blue-detuned pump with respect to the atomic resonance leads to positive  $U_0$ , while in the case of a red-detuned pump,  $U_0$  is negative. We define the effective detuning  $\delta_{\text{eff}} \equiv \delta_{\text{c}} - \delta_{-}$  where  $\delta_{\text{c}} \equiv \omega_{\text{p}} - \omega_{\text{c}}$  is the detuning between the pump frequency  $\omega_{\text{p}}$  and the resonance frequency of the empty cavity  $\omega_{\text{c}}$ . At negative  $\delta_{\text{eff}}$ , ramping up  $\epsilon_{\text{p}}$  across a critical pump strength  $\epsilon_{\text{c}}$  causes the system to undergo a second order phase transition from a homogeneous normal phase to a SR phase [81]. In the SR phase, the scattering of pump photons by atoms into the cavity, and vice versa, is favorable, leading to an all-to-all cavity-mediated interaction between atoms. This is an infinitely long-range interaction, since all atoms within the cavity mode interact with each other.



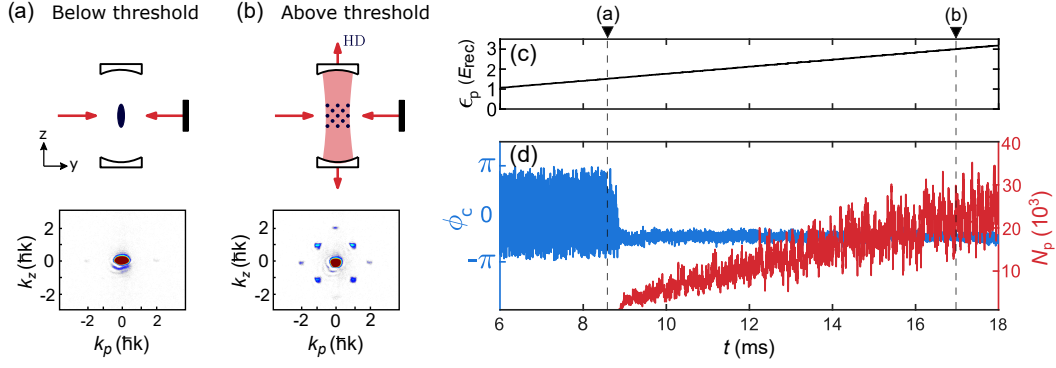


**Figure 2.2:** Illustrations and experimental data showing a phase transition from the normal phase to the superradiant self-organized phase at the critical pump strength  $\epsilon_c$ . (a,b) Top panel: schematic drawing of the atom-cavity system (a) below and (b) above  $\epsilon_c$ . The cavity is oriented along the  $z$  axis, while the transverse pump beam, represented by red arrows, is aligned perpendicular to it. The BEC is represented by a dark blue ellipse. Note that the drawings are not-to-scale. Bottom panel: corresponding momentum spectra taken at times marked with dashed lines in (c,d). The protocol of the pump strength  $\epsilon_p$  in units of  $E_{\text{rec}}$  is shown in (c). For this data,  $\epsilon_c$  is at  $1.6 E_{\text{rec}}$ . (d) The intensity of an intra-cavity photon field  $N_p$ , and its phase difference from the pump field  $\phi_c$  as a function of time detected by a heterodyne detector (HD).

The bottom plot of fig. 2.2(a) shows momentum spectra of the system in the normal phase (NP), taken below the critical pump strength  $\epsilon_c$ . Momentum spectra are obtained by taking an absorption time-of-flight (TOF) image [98] after switching off all trapping potential followed by a free expansion of 25 ms. This TOF technique maps the sample's initial momentum distribution onto a real space distribution. The emerging density pattern in the SR phase fulfills the Bragg condition for  $\pm 90^\circ$  forward or backscattering of photons between the pump and the cavity. This makes the discrete momentum modes along the  $y - z$  plane a good basis for describing the dynamics of the atomic section of our coupled atom-cavity system. The momentum spectra of an atomic condensate in presence of the one-dimensional standing wave pump potential show a momentum distribution with population in mainly the lowest mode  $\{p_y, p_z\} = \{0, 0\}\hbar k$  and two peaks of  $\{\pm 2, 0\}\hbar k$  due to the localization of the BEC on a standing wave potential with periodicity of  $\lambda_p/2$ . Above  $\epsilon_c$ , the system self-organizes in a 2D checkerboard density pattern with periodicity  $\lambda_p/\sqrt{2}$ , see fig. 2.2 (b) and fig. 2.3. This SR phase is characterized by a finite intra-cavity photon number  $N_p$ , see fig. 2.2 (d) and a momentum spectra with  $\{0, 0\}\hbar k$  and four peaks at  $\{\pm 1, \pm 1\}\hbar k$ , corresponding to a real space distribution of the checkerboard pattern.

The NP has only one ground state – the homogeneous BEC – while the SR phase has two degenerate ground states, namely even and odd configurations/sublattices, see fig. 2.3. During the phase transition from NP to SR, the system spontaneously localizes in one of the configurations, meaning that the final state is random and triggered by quantum fluctuations. Consequently, the system spontaneously breaks a  $Z_2$  symmetry in space by transitioning from the NP to the SR phase. In appendix A section I, we showed that this symmetry in our experiments is well established.

The two sublattices fulfill the Bragg condition for constructive interference of



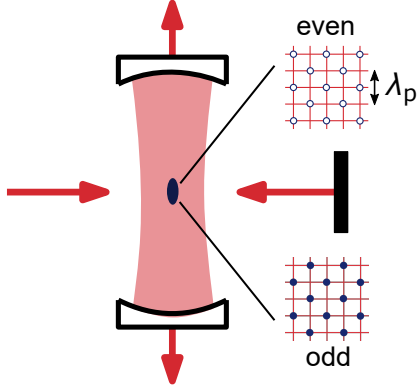
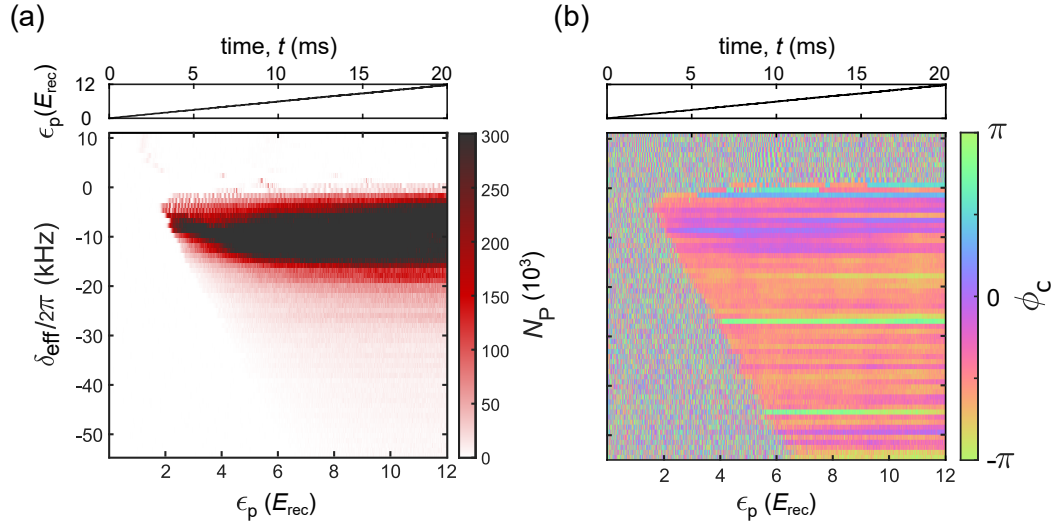


Figure 2.3: Two energetically degenerated sublattice configurations that both fulfill the Bragg condition for constructive interference between the pump and cavity field, scattered by the localized atoms.

photons scattering from the pump to the cavity and vice versa. Therefore, one characteristic of the SR is the finite intra-cavity field intensity. While the momentum spectra we measured only reveals the magnitude squared of the the atomic density distribution in  $k$ -space, any information about its complex amplitude used to distinguish its real space distribution is not captured. The cavity fields corresponding to the even and odd sublattices can be distinguished by a phase difference of  $\pi$ , as their real space configurations differ, see fig. 2.3. To be able to measure this phase difference, I implemented a heterodyne detector (HD) which gives access to both quadratures of the detected intra-cavity light field, see details in section 2.3. Exemplary results of the HD can be found in fig. 2.2 (d).

Figure 2.4 (a) shows an example of a phase diagram spanned by  $\delta_{\text{eff}}$  and  $\epsilon_p$  recorded at the pump wavelength of 803.34 nm and  $N_a = 5.5 \times 10^4$  atoms. The color scales in fig. 2.4 (a) and (b) represent  $N_p$  and  $\phi_c$  detected from the HD, respectively. The experimental protocol is as follows: we record the intra-cavity light field detected by the HD while linearly increasing the pump strength  $\epsilon_p$  from 0 to  $12 E_{\text{rec}}$  within 20 ms, keeping  $\delta_{\text{eff}}$  constant. By repeating the same protocol with difference  $\delta_{\text{eff}}$ , one can construct the phase diagram shown in fig. 2.4. For this pump wavelength, the light-shift per photon is  $U_0 = -0.4$  Hz. For a fixed negative  $\delta_{\text{eff}}$ , a finite detected  $N_p$  and constant phase difference proves that the system self-organizes into one of the sublattices and remains. At positive  $\delta_{\text{eff}}$ , i.e. a pump that is blue-detuned with respect to the effective cavity resonance, an inelastic scattering which excite the atoms into high lying momentum states is observed and indicated by superradiant pulses [84].



*Figure 2.4:* Phase diagram spanned by the pump parameters, the effective detuning  $\delta_{\text{eff}}$  and the pump strength  $\epsilon_p$ . To construct this phase diagram, we linearly increase the pump strength from 0-12  $E_{\text{rec}}$  within 20 ms for a fixed  $\delta_{\text{eff}}$  and repeat it for different  $\delta_{\text{eff}}$ . (a) Top: pump protocol. Bottom: measured photon number  $N_p$  as color code using the HD detector. (b) Corresponding phase difference  $\phi_c$  between the intra-cavity field and the pump field, see section 2.3 for methods. The region having a single stable color along the horizontal axis indicates a fixed  $\phi_c$ , hence, the system being localized in one of the sublattices.

## 2.3 Balanced heterodyne detector

In our system, the light field in the cavity is strongly coupled to the atomic ensemble. Information on the dynamics of the light-matter system is obtained by analyzing momentum spectra of the atoms and the intra-cavity light field leaking out through one of the cavity mirrors.

Before I started with my PhD project, the intra-cavity light field leaking out of the cavity was only detected using a single-photon-counting module (SPCM) which gives only the information of the intensity of the field. Besides the intensity, the SPCM has the ability to measure the arrival information of an individual intra-cavity photon which gives access to the time correlation function [69]. The main characteristic of the DTC phase proposed in ref. [24, 25] is a periodic switching between the two sublattices, corresponding to periodic switching between two values of  $\phi_c$  which differ by  $\pi$ . Therefore, the SPCM is an inappropriate detector to observe the DTC phase, since it cannot detect the phase difference  $\phi_c(t)$  between the intra-cavity light field and the pump field. For this reason, in the beginning of my PhD, I designed and implemented a heterodyne detector (HD) into the experimental setup, see fig. 2.5. This new detection significantly changed our data evaluation structure because it required a new set of evaluation software to extract the amplitude and phase information from the data. Therefore, I structured and wrote a new generation of evaluation software that has been used in our experiments since 2020. All of the work that has been explored and published during the years 2020 to 2022 [1–4] are conducted with the HD I built. In 2022, together with our Master’s student Sahana Rao, we set up another improved version of the HD with increased phase stability

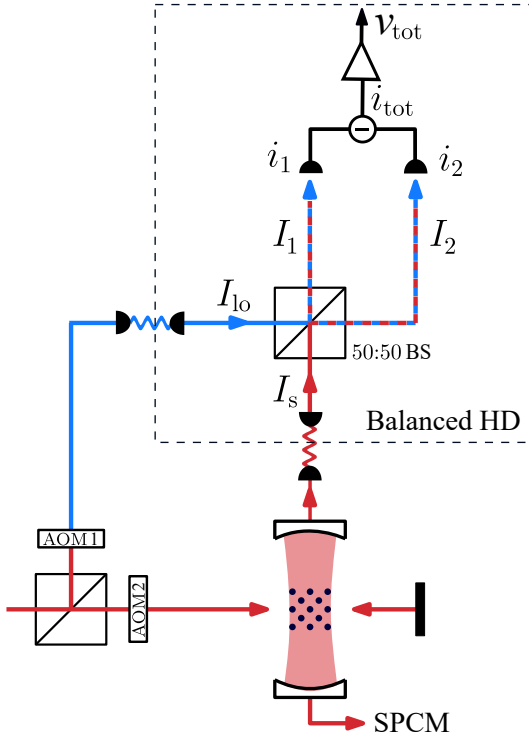


Figure 2.5: Schematic drawing of the balanced heterodyne detector (HD). The local oscillator and the transverse pump are frequency-shifted by AOM1 and AOM2, respectively. The local oscillator (lo) and the intra-cavity light leaking through one of the cavity mirror (s), indicated by blue and red lines respectively, are fiber-coupled to the balanced HD system. The two beams are overlapped on a 50:50 beam splitter (BS), resulting in two paths with intensities  $I_{1,2}$ . The balanced photodetector contains a matching pair of photoreceivers that detect photocurrents of  $i_{1,2}$  and internally subtract them from each other. Finally, the resulting photocurrent  $i_{\text{tot}} = i_1 - i_2$  is converted into a voltage  $v_{\text{tot}}$  by a transimpedance amplifier. The implementation of this setup can be seen in fig. 2.6.

and detection efficiency. The second version of the HD such as the design, the electronic components, the implemented optics, and its characterizations can be found in the Master's thesis of S. Rao [99]. In this section, I will summarize the main principle of the HD and describe briefly how to extract the light field information from the detected signal.

The main working principle of a balanced heterodyne detector is to amplify a weak signal (s) with a stronger local oscillator (lo) by overlapping them together and analyzing the beating signal. In our case, the weak signal is the intra-cavity field, transmitted through one of the cavity mirrors, and guided by several optics to the HD. Its power is on the order of pW, while the lo beam power has a power of 10 mW. The lo signal is split from the same beam as the transverse pump, but is frequency shifted by 60 MHz with respect to the transverse pump light by an acousto-optic modulator (AOM), see blue beam path in fig. 2.5. The complex electric field of the lo can be written as

$$\bar{E}_{\text{lo}} = E_{\text{lo}} e^{i(\omega_{\text{lo}} t + \phi_{\text{lo}})}, \quad (2.1)$$

where  $E_{\text{lo}}$  is the real amplitude of the lo,  $\omega_{\text{lo}}$  is the frequency of the lo beam, and  $\phi_{\text{lo}}(t)$  a constant arbitrary phase of the lo field, which we will set to zero and omit in the following, because we are only interested in the relative phase between the lo and the intra-cavity field. The same applies to the signal, the intra-cavity field leaking through one of the cavity mirrors. Its expression can be written as

$$\bar{E}_{\text{s}} = E_{\text{s}} e^{i(\omega_{\text{s}} t + \phi_{\text{c}}(t))}, \quad (2.2)$$

where  $E_{\text{s}}$  is the real amplitude of the s,  $\omega_{\text{s}}$  is the frequency of the intra-cavity light field, and  $\phi_{\text{c}}(t)$  is its time dependent phase. Intensity of both beams can be expressed as  $I_{\text{lo,s}} = |\bar{E}_{\text{lo,s}}|^2$ . The well mode-matched lo and signal beam are over-

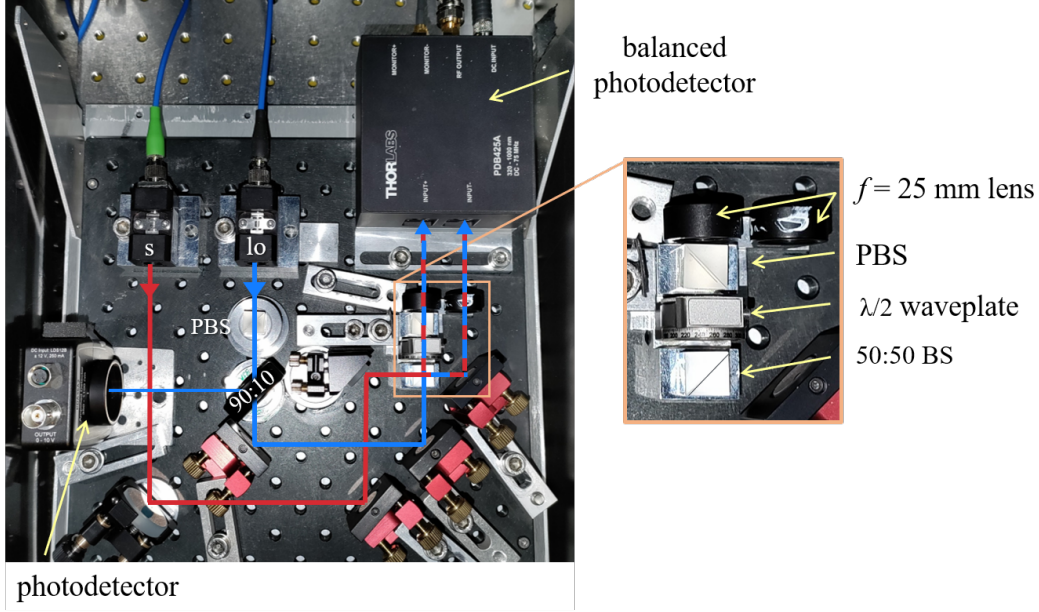


Figure 2.6: Top view of the implementation of the balanced HD in 2020, see also the schematic drawing in fig. 2.5. The blue and red arrows represent the beam path of the local oscillator (lo) and the signal (s) beam respectively. A small part of the lo is split by a 90:10 BS and detected by a photodetector for the purpose of the intensity stabilization. The lo and s beams are overlapped on the 50:50 BS. Due to the imperfection of the splitting ratio, we add an attenuation stage after the 50:50 BS to adjust the balance of the lo intensity perfectly, see the inset. The attenuation stage consists of a  $\lambda/2$  waveplate on a micrometer rotation mount and a polarizing beam splitter (PBS). Finally, the two overlapped beam paths are focused on the balanced photodetector by an achromatic lens with a focal length of 25 mm.

lapped by a 50:50 beam splitter (BS), resulting in two beam paths with intensities  $I_{1,2} = |\vec{E}_s + \vec{E}_{lo}|^2$  detected by a balanced photodetector which consists of two matching photoreceivers, see fig. 2.5. The detected photocurrents  $i_{1,2}$  generated at the photoreceivers are proportional to the light intensity  $I_{1,2}$  and can be written as

$$i_{1,2} \approx i_s + i_{lo} \pm 2\sqrt{i_s i_{lo}} \cos(\omega t + \phi_c(t)), \quad (2.3)$$

where  $\omega = |\omega_{lo} - \omega_s|$ , is chosen to be 60 MHz to ensure that it is well below the cut-off frequency of the balanced photodetector. The total photocurrent of the balanced HD follows

$$\begin{aligned} i_{\text{tot}} &= i_1 - i_2 \\ &= 4\sqrt{i_s i_{lo}} \cos(\omega t + \phi_c(t)), \end{aligned} \quad (2.4)$$

and is converted into the total output voltage  $v_{\text{tot}}$  by a transimpedance amplifier integrated in the balanced photodetector.

The implementation of the balanced HD in fig. 2.6 contains more optical components than the schematic in fig. 2.5 for a few technical reasons. For the best mode matching of the lo and s, the polarization of both beams need to be matched. For that reason, we filter the polarization of the lo beam by adding a polarizing beam splitter (PBS) after the fiber. Furthermore, we intensity stabilize the lo by splitting off

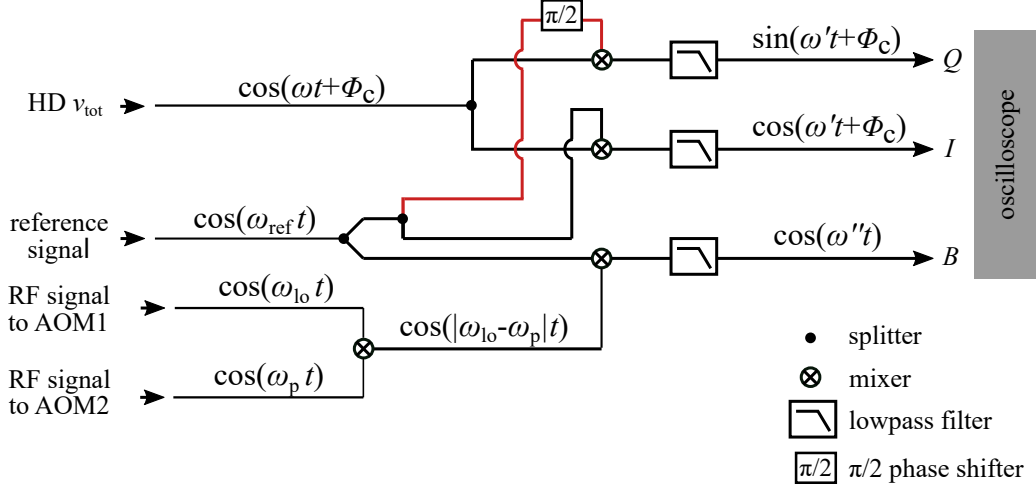


Figure 2.7: Electronic demodulation scheme of the total voltage  $v_{\text{tot}}$  from the balanced HD with the reference signal at a frequency of  $\omega_{\text{ref}} = 59.8$  MHz, generated by a frequency generator. For simplicity, amplitudes of the sine and cosine terms for all signals are omitted. One of the reference signal paths, indicated in red, gets an additional path length corresponding to a  $\pi/2$  phase shift compared to the other reference signal paths. For the purpose of the final digital demodulation, we record a beating signal  $B \propto \cos(\omega''t)$  where  $\omega'' = |\omega_{\text{ref}} - |\omega_{\text{lo}} - \omega_{\text{p}}||$ . The demodulated signals  $Q$ ,  $I$ , and  $B$  are sent through a lowpass filter, resulting in a frequency of  $\omega' = |\omega - \omega_{\text{ref}}| = 200$  kHz and recorded in the oscilloscope.

10% of the beam and measuring its intensity, which serves as an input signal of the proportional–integral–derivative (PID) regulator. Another challenge is to perfectly balance the lo power on both paths to the photoreceivers of the balanced photodetector to avoid saturation due to the remaining DC part of  $i_{\text{tot}}$ . The balancing of lo powers also help to obtain the best common mode noise suppression. Since the dominant power in the two beam paths is from the lo, the balancing lo power has to be very well set. In practice, the 50:50 BS transmits more light power than reflects, therefore, an attenuation stage is added after the 50:50 BS. The attenuation stage, as can be seen on the inset of fig. 2.6, consists of a  $\lambda/2$  waveplate on a micrometer rotation mount and a PBS. We can precisely adjust the waveplate orientation to get a balanced lo intensity on both photoreceivers. Finally, each overlapped beam with intensity  $I_{1,2}$  is focused using an achromatic lens with a focal length of 25 mm to ensure that the beam size is well within the active area of the photodetector.

The next step is to electronically demodulate the output voltage  $v_{\text{tot}}$  with a frequency 60 MHz down to a few hundred kHz to be well below the sampling rate of the oscilloscope, where the signals are finally recorded. The electronic demodulation scheme is presented in fig. 2.7. The demodulation electronics are the same as used for the setup described in the master thesis of S. Rao [99].

The total voltage  $v_{\text{tot}}$  is split into two paths. Each path gets demodulated by the reference frequency  $\omega_{\text{ref}} = 59.8$  MHz generated by a stable frequency generator. The two final demodulated signals will be called  $Q$  and  $I$ , where one signal is phase shifted with respect to the other before demodulation by  $\pi/2$ . The demodulation frequency is chosen to be  $\omega' = |\omega - \omega_{\text{ref}}| = 200$  kHz, resulting from the optimization between the limitation of the oscilloscope's sampling rate and the signal-to-noise

ratio, where the major source of the noise is found to be the electronic  $1/f$  noise. On one of the reference paths, indicated in a red line in fig. 2.7, we add an additional path length of 1.25 m, corresponding to  $\pi/2$  phase shift of the electromagnetic wave with a frequency of 59.8 MHz. This introduces the phase difference between path  $Q$  and  $I$  such that,

$$Q \propto \sin(\omega't + \phi_c)$$

and

$$I \propto \cos(\omega't + \phi_c).$$

The two demodulated signals are recorded by an oscilloscope together with a pump strength, SPCM signal, and reference beating  $B \propto \cos(\omega''t)$ , which is the frequency difference between the lo and the transverse pump, see in fig. 2.7.

The final step is to digitally demodulate the two components  $Q$  and  $I$  down to DC and obtain the two quadratures of the intra-cavity light field, see also in the PhD thesis of R. Landig [100]. This process is done using Matlab based software developed by myself. The idea is as follows. First, the frequency  $\omega''$  of  $B$  is extracted using a cosine fit function. In the case of elastic scattering in the self-organized phase, the intra-cavity field frequency  $\omega_s$  is the same as the transverse pump frequency  $\omega_p$ . Therefore, the frequency of signal  $B$  is the same as  $I$  and  $Q$  since  $\omega'' = \omega'$  and we can use this information to demodulate  $I$  and  $Q$  to DC as follows. First, the DC offset obtained from its mean value is subtracted from  $I$  and  $Q$  as

$$\hat{I} = I - \langle I \rangle \quad \text{and} \quad (2.5)$$

$$\hat{Q} = Q - \langle Q \rangle. \quad (2.6)$$

Next, we demodulate to DC with the known  $\omega'$ . This results in a complex quadrature  $A = X + iY$ , where  $X$  is the amplitude quadrature and  $Y$  is the phase quadrature as

$$X = \cos(\omega't)\hat{I} + \sin(\omega't)\hat{Q} \quad (2.7)$$

$$Y = -\sin(\omega't)\hat{I} + \cos(\omega't)\hat{Q}. \quad (2.8)$$

The intensity of the intra-cavity light field  $N_p$  is proportional to the amplitude of  $A$  as

$$N_p = C\sqrt{X^2 + Y^2}, \quad (2.9)$$

where  $C$  is the calibration factor taking into account the detection efficiency of the silicon detectors at the pump wavelength, the free spectral range of the cavity, and the transmission ratio of the two cavity mirrors and all the optics in the signal beam path. The relative phase between the intra-cavity light field and the transverse pump field is

$$\phi_c = \arctan(Y/X). \quad (2.10)$$

An example of a final result is shown in fig. 2.2(b).

In summary, the balanced HD is a very sensitive detector with an output signal that is proportional to  $\sqrt{i_s i_o}$ . Note that the power of the intra-cavity light signal leaking through the cavity mirror, is in the order of pW, and the local oscillator's power is 10 mW, together resulting in an amplitude amplification factor of over  $10^5$ . In addition, the balanced HD offers both information of the amplitude  $N_p$  and the phase of the intra-cavity light field  $\phi_c(t)$  which are both essential to observe and characterize the time crystalline phases reported in this thesis.



# Chapter 3

## Theoretical framework

During my PhD work, I have been part of a collaboration between my experimental team and a team of theoretical physicists. This collaboration has been a key prerequisite for achieving a solid understanding of my experimental findings. This chapter summarizes the theoretical models used to simulate our atom-cavity system. I will start by introducing a Hamiltonian of the system that allows to carry out numerical calculations using the truncated Wigner approximation method. Later, I demonstrate that when the system is close to the pump threshold for entering the self-organized superradiant phase, it can be mapped into a conventional 2-level open Dicke model. In section 3.3, I will then introduce a three-level Dicke model [3], which predicts the emergence of an ITC upon phase modulation of the pump wave. A focus of my description will be to point out which parameters arise in the theoretical treatment that can be directly accessed in the experiments by dynamical driving. More details of the models and methods can be found in ref. [3, 87].

### 3.1 Atom-cavity Hamiltonian

The dynamics of any system is dictated by the Hamiltonian and evolves according to corresponding equations of motion. Since our system comprises a BEC coupled to a single mode optical cavity, the full Hamiltonian  $\hat{H}$  consists of a Hamiltonian of a cavity part  $\hat{H}_c$ , an atomic part  $\hat{H}_a$ , an interaction term between the atoms  $\hat{H}_{aa}$ , and the coupling term between the atoms and the cavity  $\hat{H}_{ac}$ . The atom-cavity Hamiltonian can be written as

$$\hat{H} = \hat{H}_c + \hat{H}_a + \hat{H}_{aa} + \hat{H}_{ac}. \quad (3.1)$$

$\hat{H}_c$  for a single mode cavity with detuning between the pump and cavity frequencies  $\delta_c$  is,

$$\hat{H}_c = -\hbar\delta_c\hat{a}^\dagger\hat{a}, \quad (3.2)$$

where  $\hat{a}$  ( $\hat{a}^\dagger$ ) is the cavity mode annihilation (creation) operator. Since the pump and the cavity are aligned in  $y$  and  $z$  direction, see fig. 2.2, the dynamics of the system is well-captured in a  $2D$  model. The atomic part is governed by

$$\hat{H}_a = \int dydz \hat{\Psi}^\dagger(y, z) \left[ -\frac{\hbar^2}{2m} \nabla^2 + \epsilon_p \cos^2(k_p y + \phi_p) \right] \hat{\Psi}(y, z), \quad (3.3)$$

where  $\hat{\Psi}(y, z)$  is the atomic field operator and  $m$  is a mass of an atom,  $\epsilon_p$  is the standing wave pump potential depth,  $k_p$  is the wave number, and  $\phi_p$  is the phase of

the standing wave potential. The atom-atom interaction is captured by

$$\hat{H}_{aa} = U_a \int dydz \hat{\Psi}^\dagger(y, z) \hat{\Psi}^\dagger(y, z) \hat{\Psi}(y, z) \hat{\Psi}(y, z), \quad (3.4)$$

where  $U_a = \sqrt{2\pi} a_s \hbar^2 / m \ell_x$  is the effective 2D interaction strength,  $a_s$  is the  $s$ -wave scattering length, and  $\ell_x$  is the harmonic oscillator length in the  $x$  direction. The Hamiltonian for the light-matter interaction is

$$\begin{aligned} \hat{H}_{ac} = \int dydz \hat{\Psi}^\dagger(y, z) & \left[ U_0 \cos^2(k_p z) a^\dagger a \right. \\ & \left. + \sqrt{|U_0| \epsilon_p / \hbar} \cos(k_p y + \phi_p) \cos(kz) (a + a^\dagger) \right] \hat{\Psi}(y, z), \end{aligned} \quad (3.5)$$

where  $U_0$  is a light shift per atom,  $\omega_{\text{rec}}$  is a recoil frequency. To take into account the decay in the cavity mode, the dynamics of the system follow the following Heisenberg-Langevin equations,

$$\frac{\partial}{\partial t} \hat{\Psi} = \frac{i}{\hbar} [\hat{H}, \hat{\Psi}], \quad (3.6)$$

$$\frac{\partial}{\partial t} \hat{a} = \frac{i}{\hbar} [\hat{H}, \hat{a}] - \kappa \hat{a} + \xi, \quad (3.7)$$

where  $\kappa$  is a field decay rate of the cavity, and  $\xi$  is the stochastic noise term satisfying  $\langle \xi^*(t) \xi(t') \rangle = \kappa \delta(t - t')$ . We then numerically simulate field propagation in a semi-classical limit by transforming  $\hat{\Psi}$  and  $\hat{a}$  into classical fields. In addition, we can also use the truncated Wigner approximation (TWA), which includes the leading order quantum corrections in addition to the mean-field model. TWA samples an initial state within a Wigner distribution [101]. Next, we propagate the initial state with the Langevin equation, then average the results over many trajectories to get observables with the leading order corrections.

By controlling and modulating the pump strength  $\epsilon_p$  and the phase of the standing wave potential  $\phi_p$ , we engineer the light-matter interaction. We experimentally modulate  $\epsilon_p$  and  $\phi_p$  by a waveform generator. Specifically we parametrically drive the pump intensity in section 4.1.1 as  $\epsilon_p = \epsilon_p(t) = \epsilon_f (1 + f_0 \sin(\omega_{\text{dr}} t))$  and modulate the phase of the standing wave potential in section 4.2.1 as  $\phi_p = \phi_p(t) = f_0 \sin(\omega_{\text{dr}} t)$ , where  $\omega_{\text{dr}}$  is the modulation frequency and  $f_0$  is the modulation strength.

## 3.2 Dicke Model

The Dicke model describes  $N$  two-level systems coupled to a quantized light mode. Above a critical light-matter coupling strength, Hepp and Lieb showed in the 1970s that the Dicke model predicts a superradiant phase transition [77, 78]. In our case, the two-level states are the two lowest momentum states of the atomic ensemble. The ground state  $|1\rangle = |p_z, p_y\rangle = |0, 0\rangle \hbar k$ . The excited state is a superposition of four components  $|2\rangle = \sum_{i=\pm 1} |i, i\rangle \hbar k$ . The two energy levels are separated by an energy spacing proportional to a frequency of  $\omega_{12} = 2\omega_{\text{rec}}$ . The Dicke model can be written as

$$H/\hbar = \omega \hat{a}^\dagger \hat{a} + \omega_{12} \hat{J}_z^{12} + \frac{\lambda_{12}}{\sqrt{N}} (\hat{a}^\dagger + \hat{a}) (\hat{J}_+^{12} + \hat{J}_-^{12}), \quad (3.8)$$



where  $\omega$  is a photon frequency related to the detuning of the pump as  $-\delta_c + \frac{NU_0}{2} = -\delta_{\text{eff}}$  and  $\lambda_{12}$  is a light-matter coupling strength  $\frac{\lambda_{12}}{\sqrt{N}} = \frac{\sqrt{\omega_{\text{rec}}|U_0|\epsilon}}{2}$  [96].

### 3.3 Periodically driven three-level Dicke Model

For the experiments presented in section 4.2 and section 4.3, we modulate the phase of the standing wave pump potential by using an EOM placed between the BEC and the retro-reflecting mirror, see fig. 2.1. The periodic time-dependent phase of the pump potential is written as  $\phi_p = \phi_p(t) = f_0 \sin(\omega_{\text{dr}}t)$ , where  $f_0$  is the driving amplitude and  $\omega_{\text{dr}}$  is a driving frequency. It is shown in ref. [2, 3] that it is necessary for this driving scheme to extend the standard two-level Dicke model [102–104] to a three-level Dicke model [3], where  $N$  three-level systems are coupled to one light mode. Here, each atom has three states  $|1\rangle$ ,  $|2\rangle$ , and  $|3\rangle$ . The three-level Dicke model Hamiltonian is defined as,

$$H/\hbar = \omega \hat{a}^\dagger \hat{a} + \omega_{12} \hat{J}_z^{12} + \omega_{13} \hat{J}_z^{13} + \frac{2}{\sqrt{N}} (\hat{a}^\dagger + \hat{a}) \left( \lambda_{12} \hat{J}_x^{12} + \lambda_{13} \hat{J}_x^{13} \right), \quad (3.9)$$

where  $\hbar\omega_{nm}$  is the energy difference between states  $|m\rangle$  and  $|n\rangle$  and  $\lambda_{nm}$  is the light-matter interaction strength associated with the photon-mediated coupling between states  $|n\rangle$  and  $|m\rangle$ .  $\hat{J}_\mu^{12}$ ,  $\hat{J}_\mu^{13}$ , and  $\hat{J}_\nu^{23}$  with  $\mu \in \{z, \pm\}$  and  $\nu \in \{\pm\}$ , are three classes of pseudospin operators corresponding to the transitions between  $|1\rangle \leftrightarrow |2\rangle$ ,  $|1\rangle \leftrightarrow |3\rangle$ , and  $|2\rangle \leftrightarrow |3\rangle$ , respectively. These pseudospin operators follow the SU(3) algebra [3]. The  $x$ - and  $y$ -components of the pseudospins are defined as  $\hat{J}_x^\ell = (\hat{J}_+^\ell + \hat{J}_-^\ell)/2$  and  $\hat{J}_y^\ell = (\hat{J}_+^\ell - \hat{J}_-^\ell)/2i$ , respectively with  $\ell \in \{12, 13, 23\}$ .

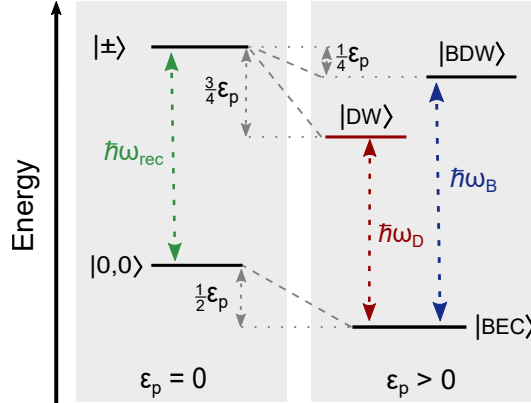


*Figure 3.1:* Schematic drawing showing momentum states without ( $\epsilon_p = 0$ ) and with ( $\epsilon_p > 0$ ) the light shift due to the presence of the pump potential. This figure is adapted from fig. 1 of appendix B. The bare momentum ground state is  $|0, 0\rangle \hbar k$  and the two degenerate excited states are labeled as  $|\pm\rangle$ . The presence of the pump potential lifts the degeneracy of the two excited states. States acquiring a light shift are labeled as  $|BEC\rangle$ ,  $|DW\rangle$ , and  $|BDW\rangle$ . The corresponding excitation energy to excite  $|BEC\rangle$  to  $|DW\rangle$  and  $|BDW\rangle$  are  $\hbar\omega_D$  and  $\hbar\omega_B$ , respectively.

In the context of our atom-cavity system, the three levels comprise of three momentum states in a presence of the pump potential labeled as BEC  $|BEC\rangle$ , density

wave  $|DW\rangle$ , and bond density wave  $|BDW\rangle$ , see fig. 3.1. The three states are derived from bare momentum modes that acquire light shifts as  $|0, 0\rangle\hbar k \rightarrow |BEC\rangle$ ,  $|+\rangle \equiv \sum_{\nu, \mu \in \{-1, 1\}} |\nu, \mu\rangle\hbar k \rightarrow |DW\rangle$  and  $|-\rangle \equiv \sum_{\nu, \mu \in \{-1, 1\}} \nu |\nu, \mu\rangle\hbar k \rightarrow |BDW\rangle$ . The excited state  $|+\rangle$  and  $|-\rangle$  are energetically degenerate without the pump potential. In the presence of the standing wave pump potential, all states acquire light shifts differently depending on their spatial overlap with the pump potential. Here we consider the case of the red-detuned pump where atoms are high field seeking. The homogeneous  $|BEC\rangle$  overlaps with the pump potential and obtains a light shift of  $-\epsilon_p/2$ . The spatial density of the  $|DW\rangle$  state varies as  $\propto |\cos(k_p y) \cos(k_p z)|^2$ , localizing at the pump potential minima and therefore obtaining the highest light shift of  $-3\epsilon_p/4$ . On the other hand, the density distribution of  $|BDW\rangle$  state varies as  $\propto |\sin(k_p y) \cos(k_p z)|^2$  and coincides with the bonds between the two potential minima hence obtaining the lowest light shift of  $-\epsilon_p/4$ . Thus, the degeneracy of the two excited states is lifted. Note that the two states,  $|BEC\rangle$  and  $|DW\rangle$ , are sufficient to span the conventional two-level Dicke model and predict the SR phase.

Above the critical pump strength  $\epsilon_p > \epsilon_c$ , there is an admixture of the  $|DW\rangle$  state in the  $|BEC\rangle$  state, creating a checkerboard pattern, where its density maxima locate at the pump potential minima, see fig. 3.2. The same pattern appears in the admixture between the  $|BEC\rangle$  and the  $|BDW\rangle$  states. However, unlike the checkerboard pattern from a mixture between the  $|DW\rangle$  and  $|BEC\rangle$  states, its density maxima localize at the pump potential maxima, see fig. 3.2.

Ref. [3] shows that we can get a parametrically driven three-level Dicke model Hamiltonian according to our three-level system as

$$H/\hbar = \omega \hat{a}^\dagger \hat{a} + \omega_D \hat{J}_z^D + \omega_B \hat{J}_z^B + 2\phi_p(t)(\omega_B - \omega_D) \hat{J}_x^{DB} + \frac{2\lambda}{\sqrt{N}} (\hat{a}^\dagger + \hat{a}) \left( \hat{J}_x^D - \phi_p(t) \hat{J}_x^B \right), \quad (3.10)$$

where the effective cavity field frequency is  $\omega = (3U_0N)/4 - \delta_C = U_0N/4 - \delta_{\text{eff}}$ , the light-matter coupling strength is  $\lambda/\sqrt{N} = -\sqrt{\omega_{\text{rec}}\epsilon_p}|U_0|/2$ , and  $\omega_{D/B}$  are the corresponding resonance frequencies between  $|BEC\rangle$  state and  $|DW/BDW\rangle$  state. We want to emphasize eq. (3.10) that the time-dependent phase modulation  $\phi_p(t)$  enables the coupling between  $|DW\rangle$  and  $|BDW\rangle$  states through pseudospin operators  $\hat{J}_z^{DB}$ . This is the key ingredient to realize the ITC in section 4.2. On the other hand, for a modulation amplitude  $f_0 = 0$ , we recover the standard two-level Dicke model.

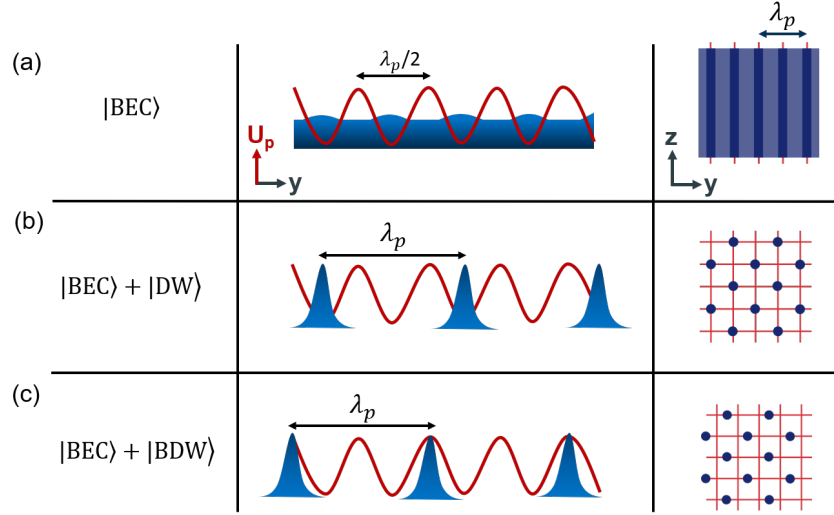


*Figure 3.2:* Density distribution illustrations of three different states of the atom-cavity system in the presence of the red-detuned pump potential. The middle column shows the atomic distribution (blue) together with the light shift potential  $U_p$  (red lines). The right column shows a view of the density distribution in the  $y - z$  plane. Crosses of red lines indicate the positions, where the light-shift potentials of the pump light and the intra-cavity light are both minimal. (a) shows the case of the homogeneous density  $|BEC\rangle$  state overlaps with the pump potential when  $\epsilon_p > 0$ , thus the  $|BEC\rangle$  state acquires small density modulations at the potential minima. (b) shows the case of  $\epsilon_p > \epsilon_c$ , when the coupling to  $|BDW\rangle$  state is zero. The  $|BEC\rangle$  acquires an admixture of  $|DW\rangle$  state, forming a checkerboard pattern in the  $y - z$  plane, such that its density maxima localize at the potential minima, hence obtaining the largest light shift. (c) shows the case of  $\epsilon_p > \epsilon_c$ , when the coupling to  $|DW\rangle$  state is zero. The  $|BEC\rangle$  acquires an admixture of  $|BDW\rangle$  state, forming a checkerboard pattern in  $y - z$  plane with density maxima localized at the maxima of the pump potential, hence only a small light shift arises.



# Chapter 4

## Red-detuned pump experiments

In this chapter, I present publications conducted with a pump light at a wavelength  $\lambda_p = 803$  nm, which is red-detuned with respect to the atomic resonance. For each experiment, some pump parameter is periodically modulated and the corresponding time-dependent Hamiltonian follows  $H(t) = H(t + T_{\text{dr}})$ , where  $T_{\text{dr}}$  is the driving period. An observable arises that it exhibits an oscillatory response with a period larger than  $T_{\text{dr}}$ . Publications I-VI show different versions of DTCs. We further discriminate them in terms of their response frequencies, which can either be commensurate or incommensurate with respect to their driving frequencies. Note that the observations in this chapter are not restricted to the red-detuned pump light. The commensurate DTC and incommensurate DTC presented in section 4.1 and section 4.2 can be realized with blue-detuned pump light as well.

### 4.1 Commensurate discrete time crystals

#### 4.1.1 Publication I: Observation of a dissipative time crystal

Observations of discrete time crystals in closed systems were first reported in 2017 [19, 20]. They were the first time crystals that are experimentally realized after many theoretical proposals. While dissipation is unfavorable and usually limiting the lifetime of time crystalline dynamics, recent proposals showed systems where dissipation takes a positive role and stabilize the dynamics of the system [24–28]. It was shown that a well controlled dissipation channel in a periodically driven open Dicke model can stabilize time crystal dynamics [24, 25]. Motivated by these proposals, we periodically modulate the intensity of the transverse pump, leading to a time-dependent pump strength of the form  $\epsilon_p(t) = \epsilon_f(1 + f_0 \sin(\omega_{\text{dr}}t))$ , where  $\epsilon_f$  is a constant pump strength,  $f_0$  is the modulation strength, and  $\omega_{\text{dr}}$  is the driving frequency. The main observable exhibiting the dynamics that is used to characterize a time crystalline phase in publication I is the phase difference between the pump field and the intra-cavity light field  $\phi_c(t)$ , which is detected using a HD.  $\phi_c(t)$  shows an oscillatory behavior at half of the driving frequency, referred to as sub-harmonic response. Furthermore, we showed experimentally that the sub-harmonic response of  $\phi_c(t)$  corresponds to a switching between the energetically degenerate even-odd superradiant sublattices. The time phase distribution of many realizations showed two distinct time phases, 0 and  $\pi$ , and thus, hinting us at the  $Z_2$  symmetry breaking of discrete time translation symmetry. We also showed that the DTC is robust

against temporal perturbations of the driving parameter  $f_0$ .

**Status of the publication:**

This article was published in July 2021 in Physical Review Letters as an editor’s suggestion [1] and was featured in a Physics viewpoint article [105]. The corresponding supplemental material can be found in appendix A.

**Note:**

Due to a mismatch between notation used in different publications and this thesis, I would like to improve the readability of the publication by listing the notation changes in table 4.1.

parameters	this thesis	publication I
pump strength	$\epsilon_p$	$\epsilon$
driving period	$T_{\text{dr}}$	$T_D$
driving frequency	$\omega_{\text{dr}}$	$\omega_D$
phase difference between the intra-cavity and the pump fields	$\phi_c$	$\varphi$

*Table 4.1:* Notation differences between this thesis and publication I.

## Observation of a Dissipative Time Crystal

Hans Keßler<sup>1,\*</sup>, Phatthamon Kongkhambut,<sup>1</sup> Christoph Georges,<sup>1</sup> Ludwig Mathey,<sup>1,2</sup>  
Jayson G. Cosme<sup>3</sup>, and Andreas Hemmerich<sup>1,2</sup>

<sup>1</sup>Zentrum für Optische Quantentechnologien and Institut für Laser-Physik, Universität Hamburg, 22761 Hamburg, Germany

<sup>2</sup>The Hamburg Center for Ultrafast Imaging, Luruper Chaussee 149, 22761 Hamburg, Germany

<sup>3</sup>National Institute of Physics, University of the Philippines, Diliman, Quezon City 1101, Philippines

 (Received 21 January 2021; revised 12 April 2021; accepted 28 May 2021; published 19 July 2021)

We present the first experimental realization of a time crystal stabilized by dissipation. The central signature in our implementation in a driven open atom-cavity system is a period doubled switching between distinct checkerboard density wave patterns, induced by the interplay between controlled cavity dissipation, cavity-mediated interactions, and external driving. We demonstrate the robustness of this dynamical phase against system parameter changes and temporal perturbations of the driving.

DOI: [10.1103/PhysRevLett.127.043602](https://doi.org/10.1103/PhysRevLett.127.043602)

Phase transitions of matter can be associated with the spontaneous breaking of a symmetry. For crystallization, this broken symmetry is the spatial translation symmetry, as the atoms spontaneously localize in a periodic arrangement. In analogy to spatial crystals, the spontaneous breaking of temporal translation symmetry can result in the formation of time crystals. Following its initial proposal [1,2], the possibility of time crystals in the ground state of equilibrium many-body systems was ruled out for fundamental reasons [3,4]. This development led to a paradigm shift, directing the search for time crystals towards genuine nonequilibrium scenarios [5–11]. In particular, the no-go theorem [3,4] can be circumvented by periodic driving, which imposes a discrete time translation symmetry on the system. Floquet or discrete time crystals emerge, when discrete time translation symmetry is spontaneously broken, which manifests as a subharmonic response of an observable [12–15]. Previous experimental studies have focused on driven closed quantum systems with long-lived time crystalline response enabled by many-body mechanisms, which impede excessive heating [5–7,16,17]. However, as proposed by theoretical work [18–22], dissipation and fluctuations, induced via controlled coupling to a suitable environment can also serve as a source for stabilization of time-crystal dynamics.

Here, we report the experimental realization of a dissipative time crystal (DTC) phase in an atom-cavity platform [23]. This is inspired by a recent theoretical proposal for a time crystal stabilized through an interplay between interaction and dissipation in the open Dicke model, arising when the light-matter coupling is periodically modulated [18–20]. The defining feature of this paradigmatic DTC is a subharmonic response, where the system periodically switches between pairs of  $\mathbb{Z}_2$  symmetry broken superradiant states.

A Bose-Einstein condensate (BEC) of  $^{87}\text{Rb}$  atoms is prepared inside a high-finesse optical cavity pumped by a retroreflected laser beam at wavelength  $\lambda_p = 803$  nm, aligned perpendicular to the cavity axis, as depicted in Fig. 1(a). The atom-cavity system operates in the recoil-resolved regime, where the cavity field and the atomic distribution evolve at a similar timescale leading to a retarded infinite-range cavity-mediated interaction between the atoms [24]. Above a critical value of the pump strength  $\epsilon$ , the system undergoes a self-organization transition from a BEC phase to a density wave (DW) phase, which emulates the superradiant phase transition in the open Dicke model [25,26]. In a spontaneous  $\mathbb{Z}_2$  symmetry breaking process, an intracavity optical lattice arises, which traps the atoms either in the black or the white squares of a checkerboard pattern, denoted as odd and even DW.

An effective driving of the light-matter coupling can be realized by modulating the pump strength. Off-resonant driving of the pump strength at a frequency  $\omega_D$  notably exceeding the recoil frequency  $\omega_{\text{rec}} \equiv \hbar k^2 / (2m) = 2\pi \times 3.55$  kHz, with  $k \equiv 2\pi / \lambda_p$  and the atomic mass  $m$ , leads to a dynamical renormalization of the phase boundary between the BEC and DW phases [27,28]. On the other hand, a period doubling response characterized by periodic switching between the odd and even DWs has been predicted for modulating only slightly above the recoil frequency [18,29,30]. This phase, originally addressed as dynamical normal phase [18], shows subharmonic oscillations between the two  $\mathbb{Z}_2$  symmetry broken even and odd DW states and is closely related to the DTC phase proposed in the open Dicke model [19]. In the thermodynamic limit,  $N \rightarrow \infty$ , the Dicke model can be transformed into a parametrically driven coupled oscillator system with two polaritonic states. Driving at twice the lower polariton frequency leads to an instability, which gives rise to a period-doubling response in the full atom-cavity model



(cf. Ref. [31]). In the following, we describe the experimental realization of a DTC in our atom-cavity system and analyze its properties as a time crystal.

Each experimental sequence begins with preparing the atom-cavity system in the self-organized DW phase (see Ref. [31]). An example of a time sequence for the pump is shown in Fig. 1(b). For  $t < -5T_D$  the system is in the BEC phase. The intracavity photon number  $N_P$  is zero and the observed momentum spectrum in the upper panel of Fig. 1(d) shows the BEC mode at zero momentum and two Bragg resonances at  $\pm 2\hbar k$  along the  $y$  direction, associated with the matter grating induced by the pump wave. This grating is illustrated in the lower panel of Fig. 1(d) by showing the single-particle density distribution obtained from a mean-field model (see Ref. [31]). The self-organization transition into the DW phase is observed in

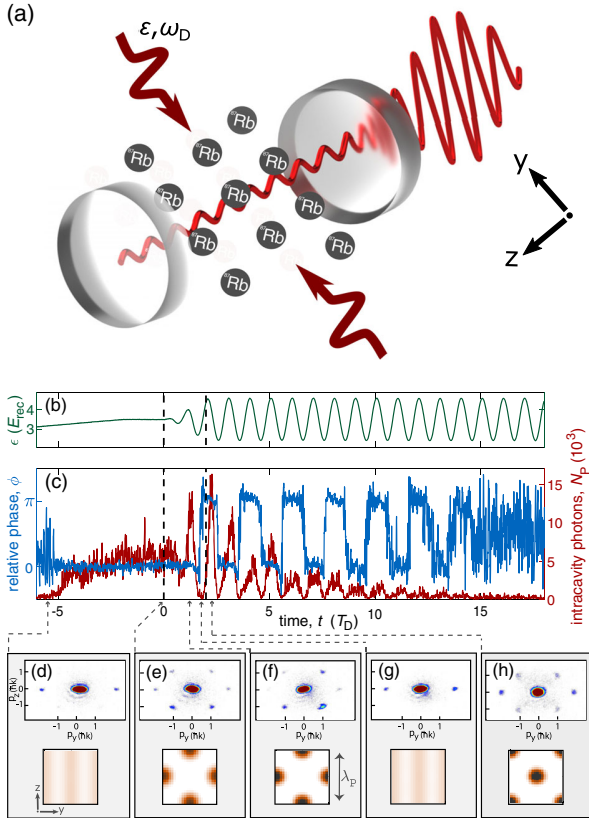


FIG. 1. Dissipative time crystal. (a) Schematic diagram of the transversely pumped atom-cavity system. (b) Time sequence for the pump with modulation strength  $f_0 = 0.3$  and modulation period  $T_D = 0.25$  ms. In the time interval delimited by dashed lines,  $f_0$  is linearly ramped from zero to its desired value. (c) The corresponding response of the intracavity photon number  $N_P$  (red) and the relative phase  $\phi$  between the pump and the cavity light field (blue). (d)–(h) Top panels: momentum distributions measured at instances of time marked by dashed arrows in (c). Bottom panels: corresponding mean-field results for the single-particle density distribution, which shows periodic switching between even and odd DWs at twice the driving period.

Fig. 1(c) around  $t \approx -5T_D$ , as evidenced from a significant increase in the intracavity photon number  $N_P$  and the locking of the relative phase  $\phi$  between the pump and cavity fields at a constant value  $\phi \approx 0$ . A momentum spectrum, characteristic for the DW phase, is shown in the upper panel of Fig. 1(e) for  $t = 0$ . The occupation of the momentum modes  $\{p_y, p_z\} = \{\pm\hbar k, \pm\hbar k\}$  signals the formation of an intracavity checkerboard matter grating, as illustrated by the calculated single-particle density distribution, shown in the lower panel. The two possible energetically degenerate DW states can be distinguished by their associated values of the phase  $\phi = 0$  or  $\phi = \pi$  for odd and even realizations, respectively [37]. We measure  $N_P$  and  $\phi$  using a balanced heterodyne detection scheme [38]. The probability for the occurrence of the odd and even DW configurations is found to be close to 50% (see Ref. [31]), which confirms that the discrete symmetry breaking in the checkerboard DW phase is well established in our system.

Upon preparation of the DW phase, in the time interval delimited by the vertical dashed lines, we linearly increase the modulation strength  $f_0$  in 500  $\mu\text{s}$  from zero to its final value [see Fig. 1(b)]. Subsequently,  $f_0$  is kept constant for 5 ms, such that the pump strength evolves according to  $\epsilon = \epsilon_0[1 + f_0 \sin(\omega_D t)]$ . The dynamical response seen in Fig. 1(c) for positive  $t$  presents the key observation of this work: the emergence of a DTC phase characterized by pulsating behavior of the intracavity photon number  $N_P$  (red trace) and a period-doubling response of the relative phase  $\phi$  (blue trace). The presence of intracavity photons highlights the many-body aspect of the DTC phase since they induce a retarded infinite-range interaction or all-to-all coupling between the atoms. The period-doubling dynamics arises in the relative phase  $\phi$ . As  $\phi$  switches from zero to  $\pi$  or vice versa after one modulation cycle, the atomic ensemble self-organizes from one type of checkerboard lattice [see Fig. 1(f)] to its symmetry-broken partner [see Fig. 1(h)]. That is, the system requires two modulation cycles to return to its initial configuration. After half of a modulation period, the system crosses from the DW phase with significant occupation of the cavity mode, to the BEC phase, where the cavity is almost empty. This behavior, corroborated by the momentum distribution in Fig. 1(g), is responsible for the pulsating intracavity photon number in Fig. 1(c) (red trace).

In Figs. 2(a)–(f), we present the various dynamical regimes accessed by tuning the modulation strength. For weak modulation [see Figs. 2(a) and 2(d)], the system stays in the DW phase and the relative phase remains locked to its value before the pump modulation. For intermediate modulation strength, the relative phase exhibits period-doubling dynamics [see Fig. 2(b)], resulting in a subharmonic peak at  $\omega = \omega_D/2$  in the Fourier spectrum in Fig. 2(e). Increasing the modulation strength even further leads to chaotic dynamics dominated by heating and loss of spatiotemporal coherence [see Figs. 2(c) and 2(f)]. In



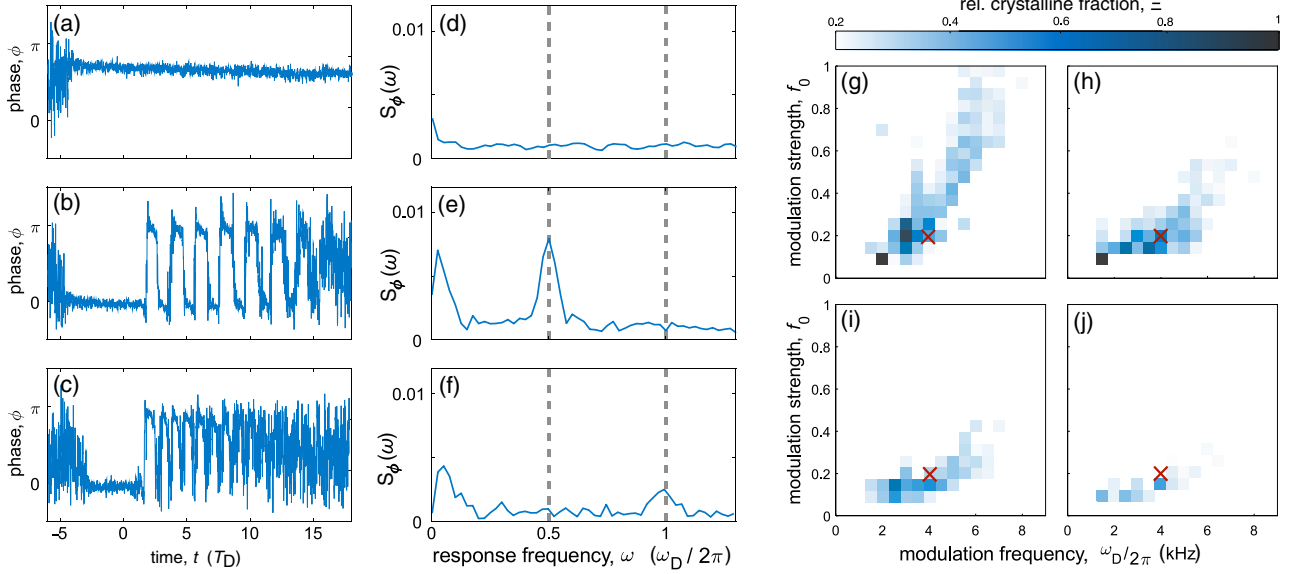


FIG. 2. Dynamical regimes. Dynamics of the relative phase  $\phi$  for (a)  $f_0 = 0.05$ , (b)  $f_0 = 0.25$ , and (c)  $f_0 = 0.95$  with fixed  $\omega_D = 2\pi \times 4$  kHz. (d)–(f) Corresponding Fourier spectra of the dynamics in (a)–(c). As the modulation strength is increased, the system transforms from a DW to a DTC phase. Strong modulation leads to heating and chaotic behavior. (g)–(j) Dynamical phase diagram showing the relative crystalline fraction  $\Xi$  as a function of the modulation frequency  $\omega_D$  and strength  $f_0$  for (g) clean modulation, (h) weak noise strength  $n = 9.6$ , (i) intermediate noise strength  $n = 15.9$ , and (j) large noise strength  $n = 22.3$ . The diagram is constructed by dividing the parameter space into  $18 \times 18$  plaquettes and within each averaging over multiple experimental runs (at least four realizations). Red crosses in (g)–(j) mark the modulation parameters used in Figs. 3(a)–(d). Increasingly large noise strengths shrink the area in the phase diagram where a stable DTC phase prevails.

contrast to the coherent switching observed in the DTC phase, the chaotic phase is characterized by intermittent dynamics of the relative phase, whereby the system appears to get stuck in one type of checkerboard pattern for two or more consecutive driving cycles [see Fig. 2(c)].

Next, we test the robustness of the DTC against variations of the system parameters and temporal perturbations. To this end, we calculate the relative crystalline fraction  $\Xi$  [6,7], defined by means of the amplitude of the subharmonic peak in the normalized Fourier spectrum  $S_\phi(\omega)$  of the relative phase  $\phi$  rescaled by its maximum, i.e.,  $\Xi = S_\phi(\omega_D/2)/S_{\max,\phi}$ , where  $S_{\max,\phi}$  is the maximum crystalline fraction measured in the parameter space spanned by  $f_0 \in [0, 1]$  and  $\omega_D \in 2\pi \times [0, 9]$  kHz. Figure 2(g) displays the relative crystalline fraction for varying modulation parameters  $\omega_D$  and  $f_0$ . We observe large relative crystalline fractions  $\Xi > 0.2$  for modulation frequencies  $\omega_D \in 2\pi \times [2, 8]$  kHz signaling a robust DTC order for a wide range of modulation parameters. Note that the overall shape of the relative crystalline fraction in Fig. 2(g) resembles the stability island of the DTC obtained from numerical simulations using a simple mean-field model (see Ref. [31], Fig. 3).

To explore the robustness of the DTC against temporal perturbations, we introduce a disorder in time by superimposing Gaussian white noise onto the signal of the pump strength. The noise strength is measured by

$n \equiv \sum_{\omega=0}^{2\pi \times 50 \text{ kHz}} |\mathcal{E}_{\text{noisy}}(\omega)| / \sum_{\omega=0}^{2\pi \times 50 \text{ kHz}} |\mathcal{E}_{\text{clean}}(\omega)|$ , where  $\mathcal{E}_{\text{noisy}}$  ( $\mathcal{E}_{\text{clean}}$ ) is the Fourier spectrum of the pump in the presence (absence) of white noise. Figures 2(h)–(j) show how the relative crystalline fraction changes with increasing noise strength. The area with clear DTC response, i.e., a large relative crystalline fraction, shrinks as the noise strength increases. Nevertheless, we still find a sizable region, where a DTC phase exists, for relatively large noise strength [Fig. 2(j)]. For a fixed set of modulation parameters marked by the red crosses in Figs. 2(g)–(j), typical single-shot results for varying noise strengths are depicted in Figs. 3(a)–(d). Note that even for a strongly distorted pump signal, as in Figs. 3(c) and 3(d), the system still switches multiple times between the two sublattices before the intracavity photons disappear. The relative crystalline fraction at fixed modulation parameters decreases with increasing noise strength, as shown in Fig. 3(e). The small offset for large noise strength  $n > 25$  is due to the background noise in the Fourier spectrum [see Fig. 2(f)]. Our experimental findings suggest that the DTC in the modulated atom-cavity system is robust against fluctuations not only from the nonunitary dynamics of the dissipative cavity but also from temporal disorder added via driving.

Finally, we address the decay of the time-translation symmetry breaking response in the DTC phase, for example, seen in Fig. 3(a). The experimental lifetimes of time crystal implementations are generally finite due to a

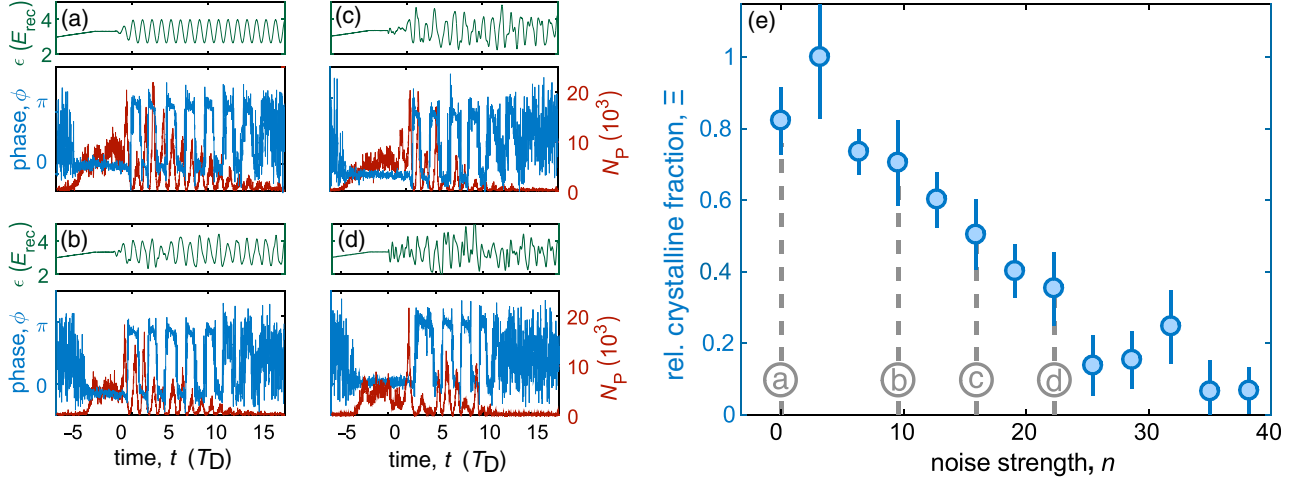


FIG. 3. Robustness of subharmonic response. (a)–(d) Single-shot experimental runs for the noise strengths applied in Figs. 2(g)–(j) and for values of  $\omega_D$  and  $f_0$  according to the red crosses in these figures. Top panels: single-shot protocols for the pump strength. Bottom panel: corresponding time evolution of the relative phase  $\phi$  (blue trace) and intracavity photon number  $N_P$  (red trace). (e) Dependence of the relative crystalline fraction  $\Xi$  on the noise strength averaged over 7 experimental runs with  $f_0 = 0.2$  and  $\omega_D = 2\pi \times 4$  kHz. The gray dashed lines mark the noise strengths used in (a)–(d).

combination of technical limitations and undesired relaxation dynamics [5–7,16,17]. In our experiment, the main cause for the decay of time-crystal dynamics can be attributed to two factors: (i) short-range collisional interaction and (ii) atom losses. In the case of the open Dicke model, the all-to-all coupling between the atoms makes it amenable to a mean-field description. In this theoretical limit, the mean-field solvability of the Dicke model provides the Dicke DTC with the necessary long-range spatiotemporal order and robustness such that it can persist to infinitely long times [19,20]. However, when mean-field breaking terms are present, the DTC may become unstable, leading to a decay of the symmetry breaking response [20]. In the atom-cavity system, the short-range interaction between the atoms competes with the collective coupling, induced by the cavity photons, and breaks the mean-field solvability of the model. To investigate the damping effects of short-range interaction and atom loss, we employ the truncated Wigner approximation (TWA). The transversely pumped atom-cavity system is thereby modeled by considering only the degrees of freedom along the pump ( $y$  direction) and the cavity ( $z$  direction) axes (see Ref. [31]). The short-range interaction is quantified in terms of the mean-field collisional interaction energy  $E_a = (U_a/N_a) \times \int dydz |\psi_0(y,z)|^4$ , where  $U_a$  denotes the effective two-dimensional interaction strength (see Ref. [31]),  $N_a$  is the number of atoms and  $\psi_0(y,z)$  is the wave function of the homogeneous BEC. We also include in our model a phenomenological atom loss channel described by  $dN_a/dt = -2\gamma N_a$ . We simulate the dynamics of the intracavity photon number  $N_P = \langle \hat{a}^\dagger \hat{a} \rangle$ , where  $\hat{a}$  ( $\hat{a}^\dagger$ ) is the bosonic operator that annihilates (creates) a photon in the single-mode cavity. To characterize temporal long-range

order, we calculate the two-point temporal correlation function  $C(t) = \text{Re}[\langle a^\dagger(t)a(t_0) \rangle] / \langle a^\dagger(t_0)a(t_0) \rangle$  at  $t_0 = 0$ , the time before the modulation is switched on.

The resulting evolution of  $N_P(t)$  and  $C(t)$  is studied in Fig. 4 for different values of  $E_a$ . First, we consider the dynamics in the absence of atom loss. For weak interaction strength  $E_a = 0.08E_{\text{rec}}$ ,  $N_P(t)$  and  $C(t)$  in the green traces of Fig. 4 are practically indistinguishable from the findings for  $E_a = 0$  in the blue traces. However, stronger short-range interactions with  $E_a = 0.30E_{\text{rec}}$  lead to a metastable DTC, where the period-doubling oscillations in  $C(t)$  decay after a few cycles, as seen in the red trace in Fig. 4(b). This translates to irregular dynamics of the corresponding intracavity photon number  $N_P(t)$  [red trace in Fig. 4(a)] in the long-time regime. Introducing an atom loss channel with  $\gamma = 40 \text{ s}^{-1}$ , which models the observed atom decay rate in the experiment, yields exponentially decaying behavior as shown in the black traces in Fig. 4. This behavior closely resembles the characteristic exponential decay of  $N_P$  in our experiment, such that the cavity is almost empty for  $t/T_D > 15$  [see Figs. 3(a)–(d)]. Atom loss leads to a trivial suppression of the atom-cavity coupling and hence of intracavity photons. When the number of intracavity photons falls below the detection level, the relative phase  $\phi$  becomes ill-defined leading to the fast and irregular oscillations of  $\phi$  seen in Figs. 3(a)–(d) for late times. Since we are operating close to the phase boundary between the DW and the normal phase the system is very sensitive to atom loss, which primarily limits the DTC lifetime in the experiment.

Our observations confirm the realization of a dissipative time crystal in an atom-cavity system with the defining feature of period-doubling dynamics. This quintessential

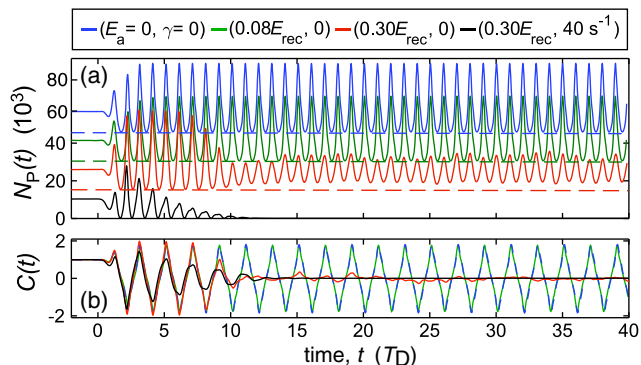


FIG. 4. Short-range interaction and atom loss. Numerical results from TWA for the dynamics of (a) the intracavity photon number  $N_p$  and (b) the nonequal time correlation  $C$  of the photons for different values of the collisional interaction energy  $E_a$  and the atom loss rate  $\gamma$ . To increase the quality of the presentation, the black, red, green, and blue traces in a are plotted with different offsets  $0, 15, 30, 45 \times 10^3$ , respectively. The modulation parameters are  $\omega_D = 2\pi \times 4$  kHz and  $f_0 = 0.2$ .

DTC is robust against changes of the system parameters and temporal perturbations added to the drive, thereby fulfilling the robustness property of time crystals. Numerical results based on a simplified semiclassical model imply that short-range interaction and atom loss limits the lifetime of the DTC phase.

This work is funded by the Deutsche Forschungsgemeinschaft (DFG, German Research Foundation) SFB-925 Project No. 170620586 and the Cluster of Excellence Advanced Imaging of Matter (EXC 2056), Project No. 390715994.

*Note added in the proof.*—During submission of this work, a subsequent example of dissipative time crystal was reported in an all-optical system [39].

\*Corresponding author.

hkessler@physnet.uni-hamburg.de

- [1] F. Wilczek, Quantum Time Crystals, *Phys. Rev. Lett.* **109**, 160401 (2012).
- [2] A. Shapere and F. Wilczek, Classical Time Crystals, *Phys. Rev. Lett.* **109**, 160402 (2012).
- [3] P. Bruno, Impossibility of Spontaneously Rotating Time Crystals: A No-Go Theorem, *Phys. Rev. Lett.* **111**, 070402 (2013).
- [4] H. Watanabe and M. Oshikawa, Absence of Quantum Time Crystals, *Phys. Rev. Lett.* **114**, 251603 (2015).
- [5] J. Zhang, P. W. Hess, A. Kyprianidis, P. Becker, A. Lee, J. Smith, G. Pagano, I. D. Potirniche, A. C. Potter, A. Vishwanath, N. Y. Yao, and C. Monroe, Observation of a discrete time crystal, *Nature (London)* **543**, 217 (2017).
- [6] S. Choi, J. Choi, R. Landig, G. Kucsko, H. Zhou, J. Isoya, F. Jelezko, S. Onoda, H. Sumiya, V. Khemani, C. Von Keyserlingk, N. Y. Yao, E. Demler, and M. D. Lukin, Observation of discrete time-crystalline order in a disordered dipolar many-body system, *Nature (London)* **543**, 221 (2017).
- [7] J. Rovny, R. L. Blum, and S. E. Barrett, Observation of Discrete-Time-Crystal Signatures in an Ordered Dipolar Many-Body System, *Phys. Rev. Lett.* **120**, 180603 (2018).
- [8] K. Sacha and J. Zakrzewski, Time crystals: A review, *Rep. Prog. Phys.* **81**, 016401 (2018).
- [9] D. V. Else, C. Monroe, C. Nayak, and N. Y. Yao, Discrete time crystals, *Annu. Rev. Condens. Matter Phys.* **11**, 467 (2020).
- [10] J. O'Sullivan, O. Lunt, Ch. W. Zollitsch, M. L. W. T., J. J. L. Morton, and A. Pal, Signatures of discrete time crystalline order in dissipative spin ensembles, *New J. Phys.* **22**, 085001 (2020).
- [11] A. Lazarides, S. Roy, F. Piazza, and R. Moessner, Time crystallinity in dissipative Floquet systems, *Phys. Rev. Research* **2**, 022002 (2020).
- [12] K. Sacha, Modeling spontaneous breaking of time-translation symmetry, *Phys. Rev. A* **91**, 033617 (2015).
- [13] D. V. Else, B. Bauer, and C. Nayak, Floquet Time Crystals, *Phys. Rev. Lett.* **117**, 090402 (2016).
- [14] N. Y. Yao, A. C. Potter, I.-D. Potirniche, and A. Vishwanath, Discrete Time Crystals: Rigidity, Criticality, and Realizations, *Phys. Rev. Lett.* **118**, 030401 (2017).
- [15] V. Khemani, A. Lazarides, R. Moessner, and S. L. Sondhi, Phase Structure of Driven Quantum Systems, *Phys. Rev. Lett.* **116**, 250401 (2016).
- [16] S. Autti, V. B. Eltsov, and G. E. Volovik, Observation of a Time Quasicrystal and Its Transition to a Superfluid Time Crystal, *Phys. Rev. Lett.* **120**, 215301 (2018).
- [17] J. Smits, L. Liao, H. T. C. Stoof, and P. van der Straten, Observation of a Space-Time Crystal in a Superfluid Quantum Gas, *Phys. Rev. Lett.* **121**, 185301 (2018).
- [18] R. Chitra and O. Zeitler, Dynamical many-body phases of the parametrically driven, dissipative Dicke model, *Phys. Rev. A* **92**, 023815 (2015).
- [19] Z. Gong, R. Hamazaki, and M. Ueda, Discrete Time-Crystalline Order in Cavity and Circuit QED Systems, *Phys. Rev. Lett.* **120**, 040404 (2018).
- [20] B. Zhu, J. Marino, N. Y. Yao, M. D. Lukin, and E. A. Demler, Dicke time crystals in driven-dissipative quantum many-body systems, *New J. Phys.* **21**, 073028 (2019).
- [21] B. Buča, J. Tindall, and D. Jaksch, Non-stationary coherent quantum many-body dynamics through dissipation, *Nat. Commun.* **10**, 1730 (2019).
- [22] N. Y. Yao, C. Nayak, L. Balents, and M. P. Zaletel, Classical discrete time crystals, *Nat. Phys.* **16**, 438 (2020).
- [23] H. Ritsch, P. Domokos, F. Brennecke, and T. Esslinger, Cold atoms in cavity-generated dynamical optical potentials, *Rev. Mod. Phys.* **85**, 553 (2013).
- [24] J. Klinder, H. Keßler, C. Georges, J. Vargas, and A. Hemmerich, Bose-Einstein condensates in an optical cavity with sub-recoil bandwidth, *Appl. Phys. B* **122**, 299 (2016).
- [25] K. Baumann, C. Guerlin, F. Brennecke, and T. Esslinger, Dicke quantum phase transition with a superfluid gas in an optical cavity, *Nature (London)* **464**, 1301 (2010).
- [26] J. Klinder, H. Keßler, M. Wolke, L. Mathey, and A. Hemmerich, Dynamical phase transition in the open

- Dicke model, *Proc. Natl. Acad. Sci. U.S.A.* **112**, 3290 (2015).
- [27] J. G. Cosme, C. Georges, A. Hemmerich, and L. Mathey, Dynamical Control of Order in a Cavity-BEC System, *Phys. Rev. Lett.* **121**, 153001 (2018).
- [28] C. Georges, J. G. Cosme, L. Mathey, and A. Hemmerich, Light-Induced Coherence in an Atom-Cavity System, *Phys. Rev. Lett.* **121**, 220405 (2018).
- [29] P. Mognini, L. Papariello, A. U. J. Lode, and R. Chitra, Superlattice switching from parametric instabilities in a driven-dissipative Bose-Einstein condensate in a cavity, *Phys. Rev. A* **98**, 053620 (2018).
- [30] J. G. Cosme, J. Skulte, and L. Mathey, Time crystals in a shaken atom-cavity system, *Phys. Rev. A* **100**, 053615 (2019).
- [31] See Supplemental Material at <http://link.aps.org/supplemental/10.1103/PhysRevLett.127.043602> for details on the experimental setup, the  $\mathbb{Z}_2$  symmetry breaking of the DW phase, and the theoretical model, which includes Refs. [32–36].
- [32] D. Nagy, G. Szirmai, and P. Domokos, Self-organization of a Bose-Einstein condensate in an optical cavity, *Eur. Phys. J. D* **48**, 127 (2008).
- [33] A. Polkovnikov, Phase space representation of quantum dynamics, *Ann. Phys. (Amsterdam)* **325**, 1790 (2010).
- [34] P. B. Blakie, A. S. Bradley, M. J. Davis, R. J. Ballagh, and C. W. Gardiner, Dynamics and statistical mechanics of ultracold Bose gases using c-field techniques, *Adv. Phys.* **57**, 363 (2008).
- [35] I. Carusotto and C. Ciuti, Quantum fluids of light, *Rev. Mod. Phys.* **85**, 299 (2013).
- [36] H. Keßler, J. G. Cosme, C. Georges, L. Mathey, and A. Hemmerich, From a continuous to a discrete time crystal in a dissipative atom-cavity system, *New J. Phys.* **22**, 085002 (2020).
- [37] K. Baumann, R. Mottl, F. Brennecke, and T. Esslinger, Exploring Symmetry Breaking at the Dicke Quantum Phase Transition, *Phys. Rev. Lett.* **107**, 140402 (2011).
- [38] J. M. Pino, R. J. Wild, P. Makotyn, D. S. Jin, and E. A. Cornell, Photon counting for Bragg spectroscopy of quantum gases, *Phys. Rev. A* **83**, 033615 (2011).
- [39] H. Taheri, A. B. Matsko, L. Maleki, and K. Sacha, All-optical dissipative discrete time crystals, [arXiv:2012.07927](https://arxiv.org/abs/2012.07927).

## 4.2 Incommensurate discrete time crystal

After realizing the first DTC by modulating the pump's intensity, in this section, motivated by a theoretical investigation by J. Cosme et. al. in 2019 [87], we modulate the phase of the pump potential instead. The proposal predicts the observation of an ITC in the shaken atom-cavity system. The phase modulation of the standing wave potential is realized by an EOM placed between the BEC and the retro-reflected mirror, see fig. 2.1. The time-dependent phase can be written as  $\phi_p(t) = f_0 \sin(\omega_{\text{dr}}t)$ , where  $f_0$  is a modulation strength and  $\omega_{\text{dr}}$  is a modulation frequency. We also developed a model to describe the dynamic of the shaken atom-cavity system, presented in publication III: Parametrically driven dissipative three-level Dicke model [3].

### 4.2.1 Publication II & III: Realization of periodically driven open three-level Dicke model

Publications II and III show that the three states involved in the incommensurate time crystalline dynamics are  $|BEC\rangle$ ,  $|DW\rangle$ , and  $|BDW\rangle$  states, see the theoretical model in section 3.3, while the standard two-level Dicke model spanned by only  $|BEC\rangle$  and  $|DW\rangle$ . The shaking of the standing wave pump potential enables the coupling to the third state,  $|BDW\rangle$  state, see eq. (3.10), resulting in a dynamical phase called a dynamical bond density wave (DBDW) phase.

The main feature of the DBDW phase is an oscillation between the two symmetry-broken states which is reflected in the oscillation of the phase difference between the pump field and the intra-cavity light field  $\phi_c$ <sup>1</sup>, the main frequency contribution of which follows the relation:  $\omega_{\text{DW}} = \omega_{\text{dr}} - \omega_{\text{BDW}}$ , where  $\omega_{\text{BDW}}$  is the  $|BDW\rangle$  state resonance frequency. Note that the ratio between the response frequency and the driving frequency,  $\omega_{\text{dr}}/\omega_{\text{DW}}$ , can take irrational values, unlike the sub-harmonic response of the observable in publication I. Therefore, together with evidence of robustness against temporal perturbations and the observation of persistent oscillations in a finite area in the relevant parameter space, the DBDW phase can be classified as an incommensurate time crystal (ITC). The observed ITC can be simulate well by the parametrically driven three-level open Dicke model, presented in publication III.

#### Status of the publication:

The results were published as joint publication II and III in December 2021 in Physical Review Letters [2] and Physical Review A [3], respectively. The corresponding supplemental material for publication II can be found in appendix B.

#### Note:

Due to a mismatch between notation used in different publications and this thesis, I would like to improve the readability of the publication by listing the notation changes in table 4.2.

---

<sup>1</sup>Note that it is the same observable as in publication I but with an incommensurate response.

parameters	this thesis	publication II & III
pump strength	$\epsilon_p$	$\epsilon$
phase of the standing wave pump potential	$\phi_p$	$\phi$
phase difference between the intra-cavity and the pump fields	$\phi_c$	$\varphi$

*Table 4.2:* Notation differences between this thesis and publication II and III.



## Realization of a Periodically Driven Open Three-Level Dicke Model

Phatthamon Kongkhambut,<sup>1</sup> Hans Keßler<sup>1,\*</sup>, Jim Skulte<sup>1,2</sup>, Ludwig Mathey,<sup>1,2</sup>

Jayson G. Cosme<sup>3</sup>, and Andreas Hemmerich<sup>1,2</sup>

<sup>1</sup>Zentrum für Optische Quantentechnologien and Institut für Laser-Physik, Universität Hamburg, 22761 Hamburg, Germany

<sup>2</sup>The Hamburg Center for Ultrafast Imaging, Luruper Chaussee 149, 22761 Hamburg, Germany

<sup>3</sup>National Institute of Physics, University of the Philippines, Diliman, Quezon City 1101, Philippines



(Received 26 August 2021; accepted 2 November 2021; published 13 December 2021)

A periodically driven open three-level Dicke model is realized by resonantly shaking the pump field in an atom-cavity system. As an unambiguous signature, we demonstrate the emergence of a dynamical phase, in which the atoms periodically localize between the antinodes of the pump lattice, associated with an oscillating net momentum along the pump axis. We observe this dynamical phase through the periodic switching of the relative phase between the pump and cavity fields at a small fraction of the driving frequency, suggesting that it exhibits a time crystalline character.

DOI: [10.1103/PhysRevLett.127.253601](https://doi.org/10.1103/PhysRevLett.127.253601)

Rapid technological advances have elevated cold-atom systems to preeminent platforms for realizing model systems of quantum-many body dynamics [1–6]. An intriguing subclass is hybrid light-matter systems, which are composed of cold atoms coupled to an optical cavity, and display a strongly enhanced light-matter interaction, giving access to the physics of strong light-matter coupling and long-range correlations [7,8]. A specific feature of these platforms is the well controlled dissipation, which allows for fast nondestructive *in situ* monitoring of the system dynamics [8–15]. One of the fundamental models for light-matter interaction is the Dicke model [16,17]. It describes a collection of  $N$  two-level systems coupled to a single light mode and displays a phase transition between a normal and a superradiant phase [16]. An open version of the Dicke model with a weak dissipation channel is approximately realized by a Bose-Einstein condensate (BEC) placed in a linear standing wave optical cavity and pumped by an optical standing wave oriented perpendicularly with respect to the cavity axis [10,11,15,18–26]. The normal phase is characterized by a BEC, light shifted by the pump potential, with a homogeneous density distribution along the cavity axis and a small number of photons in the cavity that do not display coherence. The superradiant phase shows a density grating enabling pronounced scattering of photons from the pump into the cavity and vice versa. Various extensions of the standard two-level Dicke model have been proposed and realized using atom-cavity systems, such as the spin-1 Dicke model [27,28] and the two-component Dicke model [29–31], all sharing the coupling of two-level systems to the same monochromatic light mode.

The extension of the Dicke model to the case of three-level systems has been theoretically considered in Refs. [32–34]. A specific example in a ring cavity has been used to experimentally demonstrate subradiance [35].

In the present work, we experimentally realize the periodically driven open three-level Dicke model by shaking the standing wave pump potential in an atom-cavity system as depicted in Fig. 1(a). It has been predicted in Ref. [36] that this enables a dynamical phase, characterized by atoms periodically localizing between the antinodes of the pump lattice, i.e., on the intersite bonds, which has been called dynamical bond density wave (DBDW) phase. This DBDW phase exhibits time crystalline character and is a characteristic signature of the periodically driven open three-level Dicke model. Its experimental observation is the central topic of this work.

We define the three-level Dicke model to describe the interaction between a single quantized light mode and  $N$  three-level atoms comprising energy eigenstates  $|1\rangle$ ,  $|2\rangle$ , and  $|3\rangle$  in a V configuration. Its Hamiltonian is

$$H/\hbar = \omega \hat{a}^\dagger \hat{a} + \omega_{12} \hat{J}_z^{12} + \omega_{13} \hat{J}_z^{13} + \frac{2}{\sqrt{N}} (\hat{a}^\dagger + \hat{a}) (\lambda_{12} \hat{J}_x^{12} + \lambda_{13} \hat{J}_x^{13}). \quad (1)$$

The bosonic operator  $\hat{a}$  ( $\hat{a}^\dagger$ ) annihilates (creates) a photon with frequency  $\omega$ . The frequency detuning between the lowest energy state  $|1\rangle$  and the other two states  $|2\rangle$  and  $|3\rangle$  are  $\omega_{12}$  and  $\omega_{13}$ , respectively. For small detuning  $\omega_{23}$  between the states  $|2\rangle$  and  $|3\rangle$ , i.e., when  $\omega_{23} \ll \omega_{12}, \omega_{13}$ , the only relevant light-matter interactions are those that couple state  $|1\rangle$  with states  $|2\rangle$  and  $|3\rangle$ , the strengths of which are given by  $\lambda_{12}$  and  $\lambda_{13}$ , respectively. We introduce the pseudospin operators  $\hat{J}_\mu^\ell$  with  $\ell \in \{12, 13, 23\}$ , which are related to the eight generators of the SU(3) group [37]. Note that the Gell-Mann matrices, the standard representation of the SU(3) group, can be obtained by an appropriate superposition of  $\hat{J}_\mu^\ell$  [37]. Equation (1) is an extended

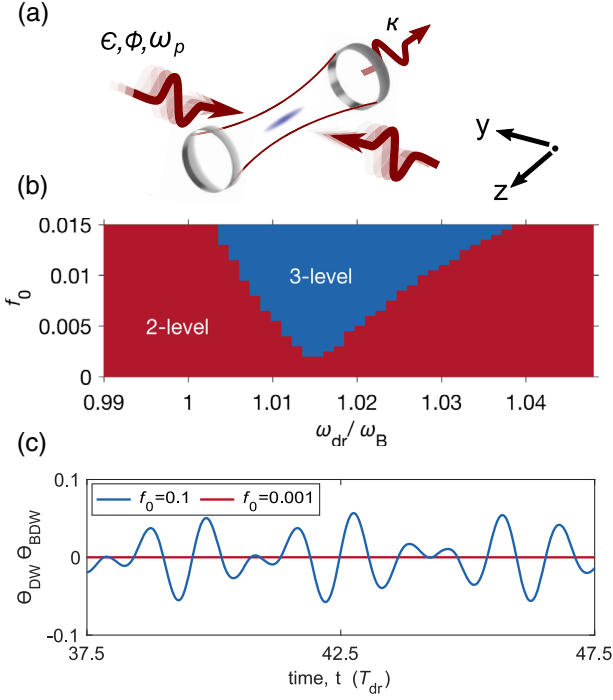


FIG. 1. (a) Schematic of the transversely pumped and shaken atom-cavity system. A sample of cold atoms is placed in a cavity oriented along the  $z$  axis. A standing wave potential is periodically shifted along the  $y$  axis using phase modulation techniques. (b) Dynamical phase diagram with two distinct regions: In the red area, the dynamics of the system is captured by a two-level Dicke model. In the blue area, a three-level Dicke model is required. (c) Dynamics of the product of the relevant order parameters for strong driving in the three-level Dicke regime (blue) and for weak driving in the two-level Dicke regime (red). The modulation frequency is  $\omega_{dr}/2\pi = 9.4$  kHz and  $\omega_B/2\pi = 8$  kHz.

form of the two-component Dicke model [29–31]. However, the latter obeys the SU(2) algebra, while the pseudospin operators in Eq. (1) fulfill the SU(3) algebra, instead.

To implement the three-level Dicke model, we consider atoms in their electronic ground state occupying the following three momentum states forming a V-shaped level structure (see Fig. 1 in Supplemental Material [38]). The ground state is the so called BEC state  $|\text{BEC}\rangle$  given by the zero momentum state  $|0, 0\rangle$  with respect to the  $yz$  plane, light shifted by the pump field by an amount  $-\epsilon/2$ , where  $\epsilon$  denotes the potential depth of the pump wave [37]. The first excited state is the superposition  $\sum_{\nu, \mu \in \{-1, 1\}} |\nu \hbar k, \mu \hbar k\rangle$  of the four momentum modes  $|\pm \hbar k, \pm \hbar k\rangle$  associated with the  $yz$  plane, light shifted by the pump field by an amount  $-3\epsilon/4$  (here,  $k$  denotes the wave number of the pump field) [37]. In view of its spatially varying density  $\propto |\cos(ky) \cos(kz)|^2$ , it is denoted as the density wave state  $|\text{DW}\rangle$ . The light shift for  $|\text{DW}\rangle$  is larger compared to that of  $|\text{BEC}\rangle$ , since the density distribution of  $|\text{DW}\rangle$  is localized in the antinodes of the

pump field [37]. The two states  $|\text{BEC}\rangle$  and  $|\text{DW}\rangle$  span the matter sector of the regular two-level Dicke model. If  $\epsilon$  exceeds a critical value  $\epsilon_{\text{crit}}$ ,  $|\text{BEC}\rangle$  acquires an admixture of  $|\text{DW}\rangle$ . A Bragg grating is thus imprinted upon the density of the  $|\text{BEC}\rangle$  state, which via efficient scattering of pump light builds up a coherent intracavity light field. The  $|\text{BEC}\rangle$  state, thus dressed by the cavity field, is denoted super-radiant phase. In this work, we operate either with  $\epsilon < \epsilon_{\text{crit}}$  or with  $\epsilon$  only very slightly above  $\epsilon_{\text{crit}}$ , such that the additional dressing by the cavity field is zero or negligibly small. The second excited state is associated with the momentum state superposition  $\sum_{\nu, \mu \in \{-1, 1\}} \nu |\nu \hbar k, \mu \hbar k\rangle$ . This state exhibits the smallest light shift  $-\epsilon/4$ , because its density distribution  $\propto |\sin(ky) \cos(kz)|^2$  matches with the nodes of the pump wave [37]. This state is called bond density wave (abbreviated  $|\text{BDW}\rangle$ ) as its density maxima coincide with the bonds between two potential minima of the pump wave. We denote the energy separation between  $|\text{DW}\rangle$  and  $|\text{BEC}\rangle$  as  $\hbar\omega_D$ , and that between  $|\text{BDW}\rangle$  and  $|\text{BEC}\rangle$  as  $\hbar\omega_B$ , respectively. See Supplemental Material for a more detailed description [38].

In the atom-cavity implementation of the standard Dicke model,  $|\text{BDW}\rangle$  is not coupled to  $|\text{BEC}\rangle$  and hence can be dropped. To implement a coupling between  $|\text{BDW}\rangle$  and  $|\text{BEC}\rangle$ , the transverse pump lattice is periodically shaken in space [36]. In Ref. [37], we show that the Hamiltonian for the shaken atom-cavity system can be mapped onto a parametrically driven version of the three-level Dicke model.

$$H/\hbar = \omega \hat{a}^\dagger \hat{a} + \hat{J}_z^D \omega_D + \hat{J}_z^B \omega_B + 2\phi(t)(\omega_B - \omega_D) \hat{J}_x^{DB} + \frac{2\lambda}{\sqrt{N}} (\hat{a}^\dagger + \hat{a}) [\hat{J}_x^D - \phi(t) \hat{J}_x^B], \quad (2)$$

where  $\phi(t) = f_0 \sin(\omega_{dr} t)$  is the time-dependent spatial phase of the pump lattice introduced by the shaking protocol, and  $\lambda$  is the overall coupling strength parameter. The pseudospin operators  $\hat{J}_\mu^D$  and  $\hat{J}_\mu^B$  with  $\mu \in \{x, y, z\}$  are directly associated with the  $|\text{DW}\rangle$  and the  $|\text{BDW}\rangle$  states via the relations to their order parameters  $\Theta_{\text{DW}} \equiv \langle \cos(ky) \cos(kz) \rangle = \langle \hat{J}_x^D \rangle$  and  $\Theta_{\text{BDW}} \equiv \langle \sin(ky) \cos(kz) \rangle = \langle \hat{J}_x^B \rangle$ , respectively. Comparing Eqs. (1) and (2), we identify  $\hat{J}_\mu^{12} = \hat{J}_\mu^D$ ,  $\hat{J}_\mu^{13} = \hat{J}_\mu^B$ ,  $\hat{J}_\mu^{23} = \hat{J}_\mu^{DB}$ ,  $\omega_{12} = \omega_D$ ,  $\omega_{13} = \omega_B$ ,  $\lambda_{12} = \lambda$ , and a time-dependent light-matter coupling  $\lambda_{13} = -\phi(t)\lambda$ . Moreover, in Eq. (2), the standing wave potential of the pump introduces an additional albeit negligible term proportional to  $\hat{J}_x^{DB}$ , which couples  $|\text{DW}\rangle$  and  $|\text{BDW}\rangle$  [37].

For driving frequencies  $\omega_{dr}$  slightly above  $\omega_B$ , the DBDW phase shows periodic oscillations of  $\Theta_{\text{BDW}}$  and  $\Theta_{\text{DW}}$  around zero with frequencies  $\omega_{\text{BDW}}$  and  $\omega_{\text{DW}}$ , respectively. Theory predicts the relation  $\omega_{\text{DW}} = \omega_{dr} - \omega_{\text{BDW}}$  such that  $\omega_{\text{DW}}$  is not an integer fraction of the driving frequency  $\omega_{dr}$  [36]. This is a hallmark of an incommensurate time crystal [36].



Thus, the long-time average of  $\Theta_{\text{DW}}$  is zero in the three-level Dicke region of the dynamical phase diagram, while it is nonzero in the two-level Dicke region for an initial superradiant phase. This behavior is captured in Fig. 1(b), which shows the time-averaged value of  $\langle \hat{J}_x^D \rangle / N \equiv j_x^D$  obtained by solving the equations of motion corresponding to Eq. (2) in the semiclassical limit of a large atom number [37].

The DBDW dynamics may be experimentally studied via the product of the order parameters  $\Theta_{\text{DW}} \times \Theta_{\text{BDW}}$ , which can be approximately measured by the normalized occupation imbalance  $\Delta \bar{F} \equiv (F_{+1,\pm 1} - F_{-1,\pm 1}) / (F_{+1,\pm 1} + F_{-1,\pm 1})_{\text{max}}$ , where  $F_{\pm 1,\pm 1}$  denotes the population of the momentum state  $|\pm \hbar k, \pm \hbar k\rangle$  (see Supplemental Material for details [38]). In the standard Dicke model realized for off-resonant driving,  $\Theta_{\text{BDW}} \approx 0$  and  $\Delta \bar{F}$  is negligible. On the other hand, for driving frequencies  $\omega_{\text{dr}}$  slightly above  $\omega_B$ , a beating signal is expected in  $\Theta_{\text{DW}} \times \Theta_{\text{BDW}}$  [see Fig. 1(c)], which can be observed via  $\Delta \bar{F}$ . Furthermore, the periodic switching of  $\Theta_{\text{DW}}$  in the three-level model amounts to a periodic switching of the experimentally observable relative phase of the pump and the cavity fields  $\varphi \equiv \arg(\langle \hat{a} \rangle)$  between 0 and  $\pi$ .

In our experiment, a BEC of  $^{87}\text{Rb}$  atoms is superimposed with the fundamental mode of a high-finesse optical cavity pumped by a retroreflected laser beam at wavelength  $\lambda_p = 803$  nm. The resulting optical pump lattice has a depth  $\epsilon$  and is aligned perpendicular to the cavity axis, as depicted in Fig. 1(a). The cavity has a field decay rate  $\kappa = 2\pi \times 3.6$  kHz comparable to the recoil frequency  $\omega_{\text{rec}} \equiv \hbar k^2 / 2m$  ( $m =$  atomic mass), such that the cavity field and the atomic density distribution evolve on similar timescales. This leads to a retarded infinite-range cavity-mediated interaction between the atoms [13]. The system realizes the Dicke phase transition from a homogeneous BEC to a superradiant phase if  $\epsilon$  exceeds a critical strength. The  $\mathbb{Z}_2$  symmetry is spontaneously broken, when the atoms localize at either the even or odd sites of a two dimensional checkerboard optical lattice formed by the interference between the pump and intracavity fields. The two symmetry broken states can be distinguished by the relative phase difference  $\varphi$  between the pump and intracavity light fields using a balanced heterodyne detection of the cavity field. The appearance of the superradiant phase can be detected *in situ* by the observation of a nonzero cavity mode occupation  $N_p$  [see red line in Fig. 2(b)], the locking of the relative  $\varphi$  to zero or  $\pi$  [see green line Fig. 2(b)], or in a destructive way through a nonzero occupation of the  $\{p_y, p_z\} = \{\pm \hbar k, \pm \hbar k\}$  modes in a momentum spectrum [see Fig. 2(g)].

The experimental sequence proceeds as follows. We prepare the system in the BEC phase or in the superradiant phase close to the phase boundary towards the BEC phase, followed by a 500  $\mu\text{s}$  long waiting period to let the system reach its steady state. Then, we shake the pump potential by modulating the phase of the pump field using an

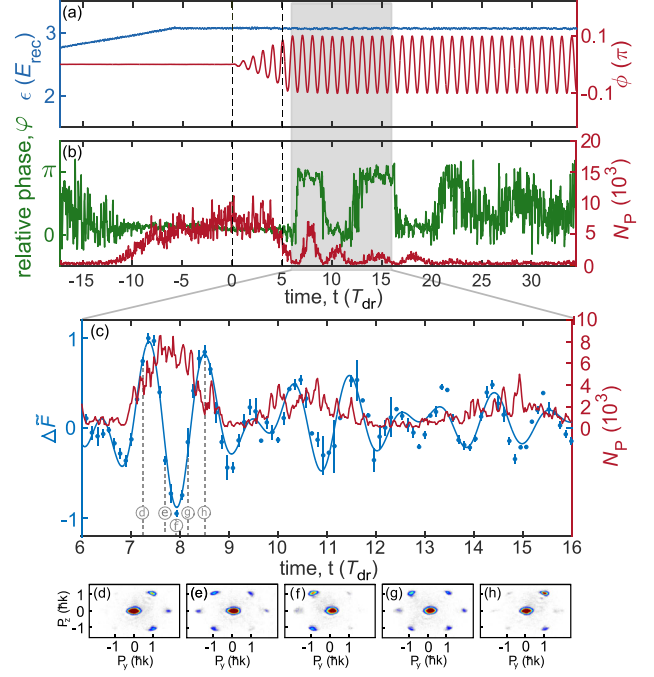


FIG. 2. Single-shot realization of DBDW order. (a) Time sequence for the pump lattice depth (blue) and the phase  $\varphi$  of the pump field (red) with modulation strength  $f_0 = 0.1\pi$  and a modulation frequency  $\omega_{\text{dr}} = 11.5$  kHz. (b) Phase difference  $\varphi$  between the pump and intracavity field (green trace) and photon number  $N_p$  in the cavity (red trace). The dashed vertical lines mark the time interval during which the modulation strength is increased. The gray shaded area shows the time window for the close-up presented in (c). (c) The red trace repeats the intracavity photon number  $N_p$  from (b). The blue data points plot the product  $\Theta_{\text{DW}} \times \Theta_{\text{BDW}}$ , approximately given by  $\Delta \bar{F}$  [see also Fig. 1(c)]. Each data point is averaged over five realizations. The solid line shows a fit with a product of two harmonic oscillations. (d)–(h) Single-shot momentum distributions recorded at the times marked in (c).

electro-optical modulator. The modulation strength  $f_0$  is linearly increased to its desired value within 500  $\mu\text{s}$  and kept constant for 6.5 ms. A typical sequence of the pump protocol is presented in Fig. 2(a). Resonant driving induces a switching of the system between the two possible sublattices of the superradiant phase at a frequency  $\omega_{\text{DW}}$  and the intracavity photon number pulsates at a rate of  $2\omega_{\text{DW}}$ . This behavior is exemplified in the green and red curves in Fig. 2(b).

In Fig. 3(a), we plot  $\omega_{\text{DW}}$  as a function of  $\omega_{\text{dr}}$  and average each data point over 100 experimental runs including different modulation strength  $f_0$ . The solid gray trace shows a linear fit. We find good agreement with the theoretical prediction  $\omega_{\text{DW}} = \omega_{\text{dr}} - \omega_{\text{BDW}}$  of Ref. [36]. In Supplemental Material, we present a similar plot for fixed  $\omega_{\text{dr}}$  and varying  $f_0$  to show that the dependence of  $\omega_{\text{DW}}$  on  $f_0$  is very weak and negligible within the experimental precision [38]. From the linear fit in Fig. 3(a),

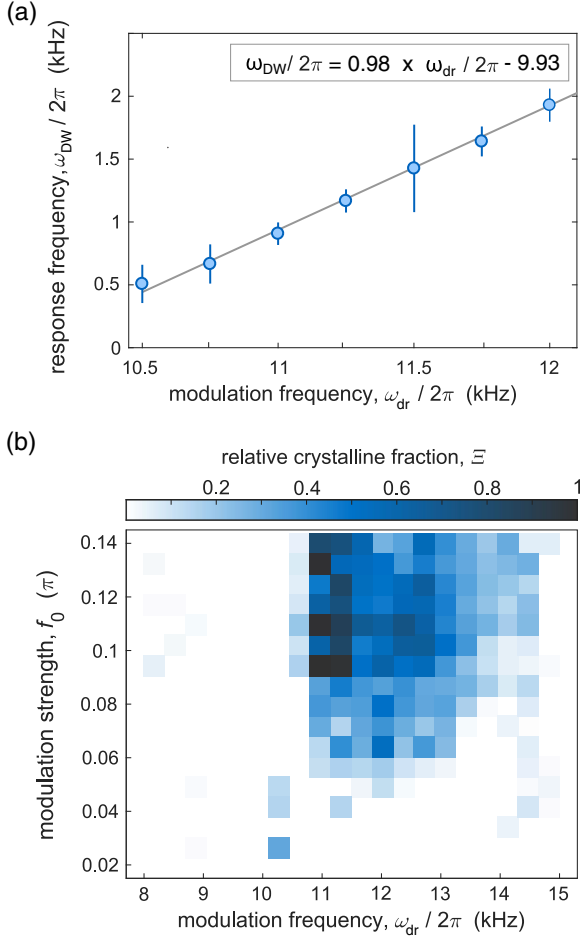


FIG. 3. (a)  $\omega_{\text{DW}}$  is plotted against  $\omega_{\text{dr}}$ .  $\omega_{\text{DW}}$  is extracted by the position of a Gaussian fit of the amplitude spectrum calculated from the measured time evolution of the phase difference between the pump and cavity fields  $\varphi$ . Each data point is averaged over hundreds of realizations with different modulation strength  $f_0$  and fixed  $\omega_{\text{dr}}$ . The gray line is a linear fit yielding the result shown in the plot legend. (b) The relative crystalline fraction  $\Xi$  is plotted as a function of the modulation frequency  $\omega_{\text{dr}}$  and strength  $f_0$ . The diagram is constructed by dividing the parameter space into  $20 \times 16$  plaquettes and averaging over multiple experimental runs within each.

we extract the value of the parametric resonance as  $\omega_{\text{BDW}} = 9.93 \pm 0.30$  kHz. In Supplemental Material, we also present an alternative protocol for measuring  $\omega_{\text{BDW}}$  from the depletion of the cavity field for resonant modulation [38]. In Fig. 3(b), we present the dynamical phase diagram, highlighting the DBDW order obtained from measuring the relative crystalline fraction  $\Xi$  quantified by the color scale. The relative crystalline fraction is a quantity commonly used in studies of time crystals. Here, we define it as the amplitude of the Fourier spectrum, calculated from the relative phase  $\varphi$ , at the expected DW frequency  $\omega_{\text{DW}}$ , rescaled by its maximum value across the parameter space spanned in the phase diagram [15].

The observed DW frequency follows the linear equation  $\omega_{\text{DW}} = \xi \times \omega_{\text{dr}} - \omega_{\text{BDW}}$  with  $\xi$  determined according to the linear fit in Fig. 3(a) as 0.98, i.e., very close to the expected value of unity. This incommensurate subharmonic response of the system with respect to the modulation frequency  $\omega_{\text{dr}}$  is observed within a broad area of the dynamical phase diagram in Fig. 3(b). In Supplemental Material, we present the robustness of the subharmonic response against temporal noise, which corroborates the classification of this dynamical phase as an incommensurate time crystal.

Finally, we discuss the observed dynamics of the momentum imbalance parameter  $\Delta\tilde{F}$  related to the calculations in Fig. 1(c). The oscillation frequencies  $\omega_{\text{DW}}$  and  $\omega_{\text{BDW}}$  are extracted from the data in Fig. 2(c) using  $f(t) = \exp(-\tau t)A \sin(\omega_{\text{BDW}}t + \alpha) \sin(\omega_{\text{DW}}t)$  as a fit function. Here,  $\tau$  is the decay rate of  $N_P$  and  $A$  is an overall amplitude parameter. This measurement demonstrates a third option for measuring  $\omega_{\text{BDW}}$ . However, since recording the momentum spectra is a destructive measurement, this method is much more time consuming than simply detecting the light leaking out of the cavity, which makes it extremely difficult to explore large areas in the parameter space. Nevertheless, we repeated this measurement for a second set of modulation parameters shown in Supplemental Material [38]. The frequency  $\omega_{\text{BDW}}$  is independent of  $\omega_{\text{dr}}$  and we measure  $\omega_{\text{BDW}} = 2\pi \times 9.8 \pm 0.1$  kHz. For a driving frequency of  $\omega_{\text{dr}} = 11.5$  kHz, we measure a slow oscillation frequency of  $\omega_{\text{DW}} = 2\pi \times 1.8 \pm 0.1$  kHz [see Fig. 2(c)], which agrees well with the theoretical prediction of  $\omega_{\text{DW}} = \omega_{\text{dr}} - \omega_{\text{BDW}} = 2\pi \times (11.5 - 9.8)$  kHz =  $2\pi \times 1.7$  kHz.

While we have mostly focused on the case when initially the superradiant state is prepared, we have also confirmed that it is possible to enter the three-level regime heralded by the emergence of the DBDW phase by initializing with the homogeneous BEC or normal phase as exemplified in Fig. 4.

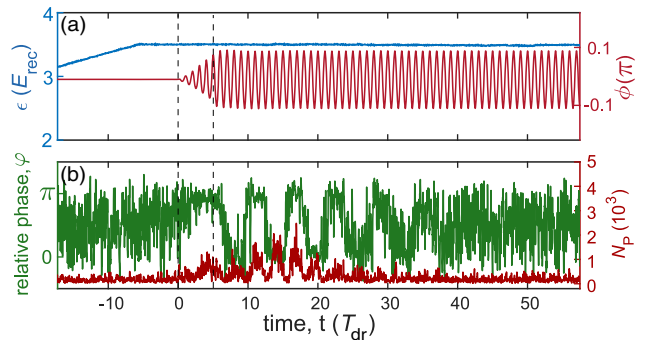


FIG. 4. Dynamics in the three-level Dicke regime using an initial homogeneous BEC state. (a) Time sequence for the pump lattice depth (blue) and the phase  $\phi$  of the pump field (red) with modulation strength  $f_0 = 0.1\pi$  and a modulation frequency  $\omega_{\text{dr}} = 11.5$  kHz. (b) The phase difference  $\varphi$  between the pump and intracavity field is plotted in green and the photon number  $N_P$  in the cavity in red.

The finite lifetime of the emergent DBDW phase in our experiment can be mainly attributed to atom losses. Furthermore, we note that our numerical simulations indicate that contact interactions [36] and larger detunings  $\omega_{\text{dr}} - \omega_B$  [38] decrease the lifetime of the time crystalline response. In the experiment, however, it is difficult to quantitatively separate the effects of atom losses, contact interaction, and detuning from the resonance.

In conclusion, we have realized a periodically driven open three-level Dicke model using a resonantly shaken atom-cavity system. As the main signature of the three-level Dicke model, we have demonstrated the emergence of a dynamical bond density wave phase. When prepared in the three-level Dicke regime, our system realizes an incommensurate time crystal, whereby the atoms periodically self-organize along the bonds of the pump lattice. This advances the understanding of cavity-BEC systems beyond the standard two-level Dicke model, and broadens the scope of dynamically induced many-body states in this and related hybrid light-matter systems.

We thank G. Homann and L. Broers for useful discussions. This work is funded by the Deutsche Forschungsgemeinschaft (DFG, German Research Foundation) SFB-925 Project No. 170620586 and the Cluster of Excellence Advanced Imaging of Matter (EXC 2056), Project No. 390715994. J.S. acknowledges support from the German Academic Scholarship Foundation.

\*Corresponding author.





hkessler@physnet.uni-hamburg.de

- [1] I. Bloch, J. Dalibard, and W. Zwerger, Many-body physics with ultracold gases, *Rev. Mod. Phys.* **80**, 885 (2008).
- [2] I. Bloch, Quantum gases, *Science* **319**, 1202 (2008).
- [3] W. S. Bakr, J. I. Gillen, A. Peng, S. Fölling, and M. Greiner, A quantum gas microscope for detecting single atoms in a Hubbard-regime optical lattice, *Nature (London)* **462**, 74 (2009).
- [4] I. Bloch, J. Dalibard, and S. Nascimbène, Quantum simulations with ultracold quantum gases, *Nat. Phys.* **8**, 267 (2012).
- [5] C. Gross and I. Bloch, Quantum simulations with ultracold atoms in optical lattices, *Science* **357**, 995 (2017).
- [6] L. Bayha, M. Holten, R. Klemt, K. Subramanian, J. Bjerlin, S. M. Reimann, G. M. Bruun, P. M. Preiss, and S. Jochim, Observing the emergence of a quantum phase transition shell by shell, *Nature (London)* **587**, 583 (2020).
- [7] H. Ritsch, P. Domokos, F. Brennecke, and T. Esslinger, Cold atoms in cavity-generated dynamical optical potentials, *Rev. Mod. Phys.* **85**, 553 (2013).
- [8] F. Mivehvar, F. Piazza, T. Donner, and H. Ritsch, Cavity QED with quantum gases: New paradigms in many-body physics, *Adv. Phys.* **70**, 1 (2021).
- [9] A. T. Black, H. W. Chan, and V. V. Vuletic, Observation of Collective Friction Forces due to Spatial Self-Organization of Atoms: From Rayleigh to Bragg Scattering, *Phys. Rev. Lett.* **91**, 203001 (2003).
- [10] K. Baumann, R. Mottl, F. Brennecke, and T. Esslinger, Exploring Symmetry Breaking at the Dicke Quantum Phase Transition, *Phys. Rev. Lett.* **107**, 140402 (2011).
- [11] J. Klinder, H. Keßler, M. Wolke, L. Mathey, and A. Hemmerich, Dynamical phase transition in the open Dicke model, *Proc. Natl. Acad. Sci. U.S.A.* **112**, 3290 (2015).
- [12] H. Keßler, J. Klinder, B. P. Venkatesh, C. Georges, and A. Hemmerich, In situ observation of optomechanical Bloch oscillations in an optical cavity, *New J. Phys.* **18**, 102001 (2016).
- [13] J. Klinder, H. Keßler, C. Georges, J. Vargas, and A. Hemmerich, Bose-Einstein condensates in an optical cavity with sub-recoil bandwidth, *Appl. Phys. B* **122**, 299 (2016).
- [14] C. Georges, J. Vargas, H. Keßler, J. Klinder, and A. Hemmerich, Bloch oscillations of a Bose-Einstein condensate in a cavity-induced optical lattice, *Phys. Rev. A* **96**, 063615 (2017).
- [15] H. Keßler, P. Kongkhambut, C. Georges, L. Mathey, J. G. Cosme, and A. Hemmerich, Observation of a Dissipative Time Crystal, *Phys. Rev. Lett.* **127**, 043602 (2021).
- [16] K. Hepp and E. H. Lieb, On the superradiant phase transition for molecules in a quantized radiation field: The Dicke maser model, *Ann. Phys. (N.Y.)* **76**, 360 (1973).
- [17] P. Kirton, M. M. Roses, J. Keeling, and E. G. Dalla Torre, Introduction to the Dicke model: From equilibrium to nonequilibrium, and *vice versa*, *Adv. Quantum Technol.* **2**, 1800043 (2019).
- [18] D. Nagy, G. Szirmai, and P. Domokos, Self-organization of a Bose-Einstein condensate in an optical cavity, *Eur. Phys. J. D* **48**, 127 (2008).
- [19] K. Baumann, C. Guerlin, F. Brennecke, and T. Esslinger, Dicke quantum phase transition with a superfluid gas in an optical cavity, *Nature (London)* **464**, 1301 (2010).
- [20] M. P. Baden, K. J. Arnold, A. L. Grimsmo, S. Parkins, and M. D. Barrett, Realization of the Dicke Model Using Cavity-Assisted Raman Transitions, *Phys. Rev. Lett.* **113**, 020408 (2014).
- [21] F. Piazza and H. Ritsch, Self-Ordered Limit Cycles, Chaos, and Phase Slippage with a Superfluid inside an Optical Resonator, *Phys. Rev. Lett.* **115**, 163601 (2015).
- [22] A. U. J. Lode and C. Bruder, Fragmented Superradiance of a Bose-Einstein Condensate in an Optical Cavity, *Phys. Rev. Lett.* **118**, 013603 (2017).
- [23] H. Keßler, J. G. Cosme, M. Hemmerling, L. Mathey, and A. Hemmerich, Emergent limit cycles and time crystal dynamics in an atom-cavity system, *Phys. Rev. A* **99**, 053605 (2019).
- [24] P. Molognini, L. Papariello, A. U. J. Lode, and R. Chitra, Superlattice switching from parametric instabilities in a driven-dissipative Bose-Einstein condensate in a cavity, *Phys. Rev. A* **98**, 053620 (2018).
- [25] H. Keßler, J. G. Cosme, C. Georges, L. Mathey, and A. Hemmerich, From a continuous to a discrete time crystal in a dissipative atom-cavity system, *New J. Phys.* **22**, 085002 (2020).
- [26] C. Georges, J. G. Cosme, H. Keßler, L. Mathey, and A. Hemmerich, Dynamical density wave order in an atom-cavity system, *New J. Phys.* **23**, 023003 (2021).
- [27] Z. Zhiqiang, C. H. Lee, R. Kumar, K. J. Arnold, S. J. Masson, A. S. Parkins, and M. D. Barrett, Nonequilibrium

- phase transition in a spin-1 Dicke model, *Optica* **4**, 424 (2017).
- [28] S. J. Masson, M. D. Barrett, and S. Parkins, Cavity QED Engineering of Spin Dynamics and Squeezing in a Spinor Gas, *Phys. Rev. Lett.* **119**, 213601 (2017).
- [29] E. I. Rodríguez Chiacchio and A. Nunnenkamp, Dissipation-Induced Instabilities of a Spinor Bose-Einstein Condensate inside an Optical Cavity, *Phys. Rev. Lett.* **122**, 193605 (2019).
- [30] B. Buča and D. Jaksch, Dissipation Induced Nonstationarity in a Quantum Gas, *Phys. Rev. Lett.* **123**, 260401 (2019).
- [31] N. Dogra, M. Landini, K. Kroeger, L. Hruby, T. Donner, and T. Esslinger, Dissipation-induced structural instability and chiral dynamics in a quantum gas, *Science* **366**, 1496 (2019).
- [32] C. C. Sung and C. M. Bowden, Phase transition in the multimode two- and three-level Dicke model (Green's function method), *J. Phys. A* **12**, 2273 (1979).
- [33] A. Crubellier, S. Liberman, D. Pavolini, and P. Pillet, Superradiance and subradiance: I. Interatomic interference and symmetry properties in three-level systems, *J. Phys. B* **18**, 3811 (1985).
- [34] A. Crubellier and D. Pavolini, Superradiance and subradiance: II. Atomic systems with degenerate transitions, *J. Phys. B* **19**, 2109 (1986).
- [35] P. Wolf, S. C. Schuster, D. Schmidt, S. Slama, and C. Zimmermann, Observation of Subradiant Atomic Momentum States with Bose-Einstein Condensates in a Recoil Resolving Optical Ring Resonator, *Phys. Rev. Lett.* **121**, 173602 (2018).
- [36] J. G. Cosme, J. Skulte, and L. Mathey, Time crystals in a shaken atom-cavity system, *Phys. Rev. A* **100**, 053615 (2019).
- [37] J. Skulte, P. Kongkhambut, H. Keßler, A. Hemmerich, L. Mathey, and J. G. Cosme, companion paper, Parametrically driven dissipative three-level Dicke model, *Phys. Rev. A* **104**, 063705 (2021).
- [38] See Supplemental Material at <http://link.aps.org/supplemental/10.1103/PhysRevLett.127.253601> for details on the experimental setup, the three-level scheme, dependence of the density wave frequency on modulation strength, measurement of parametric resonance using the depletion of intracavity field, and robustness against temporal noise of the dynamical BDW phase.



## Parametrically driven dissipative three-level Dicke model

Jim Skulte <sup>1,2</sup>, Phatthamon Kongkhambut,<sup>1</sup> Hans Keßler <sup>1</sup>, Andreas Hemmerich <sup>1,2</sup>,  
Ludwig Mathey,<sup>1,2</sup> and Jayson G. Cosme <sup>3</sup>

<sup>1</sup>Zentrum für Optische Quantentechnologien and Institut für Laser-Physik, Universität Hamburg, 22761 Hamburg, Germany

<sup>2</sup>The Hamburg Center for Ultrafast Imaging, Luruper Chaussee 149, 22761 Hamburg, Germany

<sup>3</sup>National Institute of Physics, University of the Philippines, Diliman, Quezon City 1101, Philippines



(Received 26 August 2021; accepted 22 November 2021; published 13 December 2021)

We investigate the three-level Dicke model, which describes a fundamental class of light-matter systems. We determine the phase diagram in the presence of dissipation, which we assume to derive from photon loss. Utilizing both analytical and numerical methods we characterize the incommensurate time crystalline, light-induced, and light-enhanced superradiant states in the phase diagram for the parametrically driven system. As a primary application, we demonstrate that a shaken atom-cavity system is naturally approximated via a parametrically driven dissipative three-level Dicke model.

DOI: [10.1103/PhysRevA.104.063705](https://doi.org/10.1103/PhysRevA.104.063705)

### I. INTRODUCTION

The Dicke model is a paradigmatic model capturing the physics of a fundamental class of light-matter systems [1]. The standard two-level Dicke model describes the interaction between  $N$  two-level systems and a quantized single-mode light field. The dissipative or open standard Dicke model was first realized by using an atom-cavity setup allowing for an approximate description, in which the intracavity light field is adiabatically eliminated [2]. Later, it was also implemented in the recoil-resolved regime, which requires independent dynamical descriptions of the cavity and the matter field [3]. Meanwhile, extensions of the two-level Dicke models [4–11] and variations of the transversely pumped atom-cavity systems [12–19] have been studied.

An important class of quantum optical phenomena derive from three-level systems interacting with light. These phenomena include electromagnetically induced transparency (EIT) [20,21] and lasing without inversion (LWI) [22,23], as well as methods such as stimulated Raman adiabatic passage (StiRAP) [24,25]. They are based primarily on three-level systems in a  $\lambda$  or a  $V$  configuration. These three-level system configurations occur naturally in numerous physical systems, which is the origin of the universality of the phenomena that derive from them. In the context of the Dicke model, its generalization to three-level atoms interacting with a multi-mode photonic field has been proposed in Ref. [26]. A similar three-level model has been used to demonstrate subradiance [27–30].

In this work, we study a system of three-level atoms coupled to a photonic mode modeled by a three-level Dicke mode, in which the three-level system forms a  $V$  configuration, as depicted in Fig. 1(a). The three-level system can be described by using pseudospin operators following the algebra of the  $SU(3)$  group. Our representation maps onto the standard  $SU(3)$  basis, the Gell-Mann matrices [31], spanning the Lie

algebra in the defining representation of the  $SU(3)$  group. The Gell-Mann matrices are commonly used in particle physics to explain color charges [32,33]. We obtain the equilibrium phase diagram of the three-level Dicke model in the presence of dissipation due to photon loss. Moreover, we show that periodic driving of the light-matter interaction strength may lead to the emergence of new nonequilibrium phases, such as an incommensurate time crystal (ITC), light-induced superradiance (LISR), and light-enhanced superradiance (LESR).

Here, we present a comprehensive discussion of a parametrically driven three-level Dicke model. We discuss its dynamical phase diagram including the incommensurate crystalline phase, predicted by us in Ref. [34] and experimentally implemented in Ref. [35]. We show that this phase is a characteristic signature of the driven three-level Dicke model. We give a detailed account of how this model can be approximately implemented by a light-driven atom-cavity system.

This work is organized as follows: In Sec. II, we introduce the three-level Dicke model and discuss its phase diagram. We explore the dynamical phase diagram of the driven three-level Dicke model in Sec. III. The mapping of a shaken atom cavity system onto the periodically driven three-level Dicke model is presented in Sec. IV. In Sec. V, we conclude this paper.

### II. THREE-LEVEL DICKE MODEL

We are interested in the properties of the three-level Dicke model for a system of  $N$  three-level atoms interacting with a quantized light mode, as schematically shown in Fig. 1(a). Each atom has three energy states  $|1\rangle$ ,  $|2\rangle$ , and  $|3\rangle$ . We define the three-level Dicke model by the Hamiltonian

$$H/\hbar = \omega \hat{a}^\dagger \hat{a} + \omega_{12} \hat{J}_z^{12} + \omega_{13} \hat{J}_z^{13} + \frac{2}{\sqrt{N}} (\hat{a}^\dagger + \hat{a}) (\lambda_{12} \hat{J}_x^{12} + \lambda_{13} \hat{J}_x^{13}), \quad (1)$$

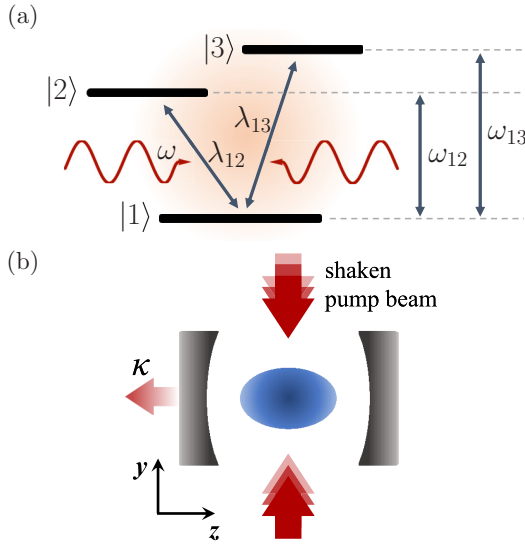


FIG. 1. (a) Three-level system coupled to a single light mode. (b) Schematic diagram of the shaken atom-cavity system. The cavity photon loss rate is  $\kappa$ . This atom-cavity configuration can emulate the driven dissipative three-level Dicke model.

where  $\omega$  is the photon frequency,  $\omega_{nm}$  is the detuning between states  $|n\rangle$  and  $|m\rangle$ , and  $\lambda_{nm}$  is the light-matter interaction strength associated with the photon-mediated coupling between states  $|n\rangle$  and  $|m\rangle$ . The bosonic operators  $\hat{a}$  and  $\hat{a}^\dagger$  annihilate and create a photon in the quantized light mode, respectively. There are three classes of pseudospin operators  $\hat{J}_\mu^{12}$ ,  $\hat{J}_\mu^{13}$ , and  $\hat{J}_\mu^{23}$  with  $\mu \in \{z, \pm\}$  and  $\nu \in \{\pm\}$ , corresponding to the transitions  $|1\rangle \leftrightarrow |2\rangle$ ,  $|1\rangle \leftrightarrow |3\rangle$ , and  $|2\rangle \leftrightarrow |3\rangle$ , respectively. These operators obey the commutation relation of the SU(3) algebra (see Appendix A). The  $x$  and  $y$  components of the pseudospins are defined as  $\hat{J}_x^\ell = (\hat{J}_+^\ell + \hat{J}_-^\ell)/2$  and  $\hat{J}_y^\ell = (\hat{J}_+^\ell - \hat{J}_-^\ell)/2i$ , respectively, with  $\ell \in \{12, 13, 23\}$ .

Note that, in principle, there is a light-matter coupling term proportional to  $\hat{J}_x^{23}$  in Eq. (1) [26]. However, this term is neglected here since we are only interested in the case when  $\omega_{12} \approx \omega_{13}$ . This leads to a negligibly small  $\lambda_{23}$  since the light-matter coupling strength is proportional to the energy difference between the relevant states [36,37]. Moreover, we could also use the Gell-Mann matrices as the representation of the SU(3) group in our system. To retain a form of the Hamiltonian reminiscent of the standard two-level Dicke model, which is often written using a representation of the SU(2) group, we instead use the pseudospin operators as described above. Nevertheless, the Gell-Mann matrices can be obtained from appropriate superpositions of the pseudospin operators (see Appendix A).

The Hamiltonian in Eq. (1) is superficially similar to the two-component Dicke model [9,10,16,17] (see also Appendix B for a brief discussion). However, we emphasize that, unlike in the two-component Dicke model, which describes two types of two-level systems coupled through the light field, the pseudospin operators introduced in Eq. (1) obey the SU(3) algebra resulting from the use of three-level systems. This fundamentally changes the dynamics of the parametrically driven system out of equilibrium since new

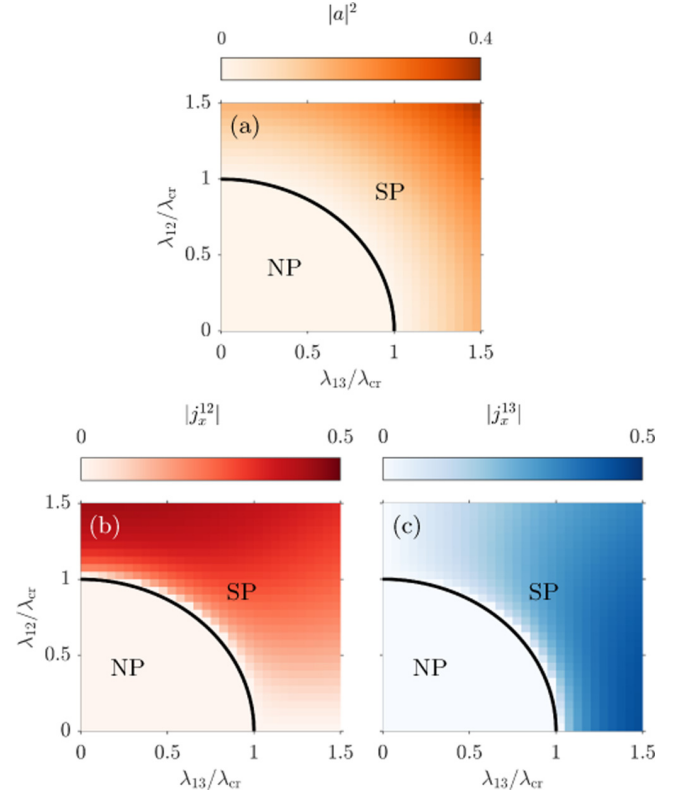


FIG. 2. Long-time average of the mean-field dynamics of the (a) cavity mode occupation  $|a|^2$ , (b)  $|j_x^{12}|^2$ , and (c)  $|j_x^{13}|^2$  for  $\omega = \omega_{12} = \omega_{13} = \kappa$ . The black curve denotes the critical line separating the normal and superradiant phases in the thermodynamic limit.

terms corresponding to additional spin operators are now present in the equations of motion.

### A. Holstein-Primakoff transformation

To obtain analytical predictions of the phase boundaries, we employ a Holstein-Primakoff (HP) approximation in the thermodynamic limit, i.e.,  $N \rightarrow \infty$ . This leads to the following Hamiltonian:

$$H/\hbar = \omega \hat{a}^\dagger \hat{a} + \omega_{12} \hat{a}_{12}^\dagger \hat{a}_{12} + \omega_{13} \hat{a}_{13}^\dagger \hat{a}_{13} + (\hat{a}^\dagger + \hat{a})[\lambda_{12}(\hat{a}_{12}^\dagger + \hat{a}_{12}) + \lambda_{13}(\hat{a}_{13}^\dagger + \hat{a}_{13})]. \quad (2)$$

We obtain an elliptic equation for the critical light-matter coupling from the stability matrix (see Appendix C for details):

$$\frac{(\kappa^2 + \omega^2)}{4\omega} = \left( \frac{\lambda_{12}^2}{\omega_{12}} + \frac{\lambda_{13}^2}{\omega_{13}} \right). \quad (3)$$

In the standard open Dicke model,  $\lambda_{13} = 0$ , the critical light-matter coupling,  $\lambda_{cr} = [(\kappa^2 + \omega^2)(\omega_{12}/\omega)]^{1/2}/2$ , is recovered [38]. To illustrate the resulting phases, we consider the case  $\omega = \omega_{12} = \omega_{13}$ . Then, the critical line in Eq. (5) defines a circle in the parameter space spanned by  $\lambda_{12}$  and  $\lambda_{13}$ , as seen in Fig. 2. For combinations of light-matter coupling strengths  $\{\lambda_{12}, \lambda_{13}\}$  within the area enclosed by Eq. (5), the stable phase corresponds to a normal phase (NP), while those outside the area will lead to an instability towards the formation of a superradiant phase (SP).

### B. Phase diagram

Next, we employ a mean-field approximation  $\langle \hat{a} \hat{J}_\mu^\ell \rangle \approx \langle \hat{a} \rangle \langle \hat{J}_\mu^\ell \rangle$  starting from Eq. (1) to obtain the dynamics of the system in a semiclassical approximation (see Appendix D for details). This approximation becomes exact in the thermodynamic limit  $N \rightarrow \infty$  in or near the steady state. Furthermore, we introduce the rescaled  $c$  numbers  $a \equiv \langle \hat{a} \rangle / \sqrt{N}$  and  $j_\mu^\ell \equiv \langle \hat{J}_\mu^\ell \rangle / N$ . The resulting mean-field equations of motion that we simulate are shown in Appendix E. We further note that the SU(3) group inherits two Casimir charges, a quadratic  $C_1$  and a cubic  $C_2$ . In contrast with this, the group SU(2) has only one quadratic Casimir charge, namely, the total spin  $J^2 = (J_x)^2 + (J_y)^2 + (J_z)^2$ . The expressions for the charges are shown in Appendix A. We track these quantities when solving the equations of motion to ensure convergence of our numerical results. In our simulations, we initialize in the normal phase  $j_\mu^\ell = 0$ , except for  $j_z^{12} = j_z^{13} = -1/2$ . This amounts to all the atoms initially occupying the lowest energy state  $|1\rangle$ . We initialize the cavity field as  $a = 10^{-2}$ .

An observable of interest is the occupation of the photonic mode  $|a|^2$  because this differentiates the normal ( $|a|^2 \rightarrow 0$  for  $N \rightarrow \infty$ ) and superradiant ( $|a|^2 > 0$ ) phases. Moreover, we are interested in the magnitude of the  $x$  component of the collective spin operators corresponding to the transition  $|1\rangle \leftrightarrow |2\rangle$  and  $|1\rangle \leftrightarrow |3\rangle$ , which are  $|j_x^{12}|$  and  $|j_x^{13}|$ , respectively. In Fig. 2, we present the long-time average of  $|a|^2$ ,  $|j_x^{12}|$ , and  $|j_x^{13}|$ , calculated by numerically solving the equations of motion. Similar to the standard two-level Dicke model [39], the photonic mode occupation or the  $x$  component of the pseudospin operators can be regarded as order parameters because they are zero in the NP and are nonzero in the SP. Furthermore, we demonstrate in Fig. 2 that the onset of superradiance according to our mean-field dynamics agrees with the analytical critical line defined by Eq. (5). In the superradiant phase,  $|j_x^{12}| > |j_x^{13}|$  for  $\lambda_{12} > \lambda_{13}$  and  $|j_x^{12}| < |j_x^{13}|$  for  $\lambda_{12} < \lambda_{13}$ , as inferred from Figs. 2(b) and 2(c).

### III. PARAMETRICALLY DRIVEN OPEN THREE-LEVEL DICKE MODEL

We now explore the parametrically driven three-level Dicke model by the Hamiltonian

$$H/\hbar = \omega \hat{a}^\dagger \hat{a} + \omega_D \hat{J}_z^D + \omega_B \hat{J}_z^B + 2\phi(t)(\omega_B - \omega_D) \hat{J}_x^{DB} + \frac{2\lambda}{\sqrt{N}} (\hat{a}^\dagger + \hat{a})(\hat{J}_x^D - \phi(t)\hat{J}_x^B). \quad (4)$$

This particular choice of the Hamiltonian is motivated by its connection to the shaken atom-cavity system, which we demonstrate and explore in more detail later. Comparing with the undriven case in Eq. (1), it can be seen that  $\omega_{12} = \omega_D$ ,  $\omega_{13} = \omega_B$ ,  $\hat{J}_\mu^{12} = \hat{J}_\mu^D$ ,  $\hat{J}_\mu^{13} = \hat{J}_\mu^B$ ,  $\lambda_{12} = \lambda$ . We define  $\phi(t) = f_0 \sin(\omega_{dr} t)$ , which then means that  $\lambda_{13} = -f_0 \sin(\omega_{dr} t) \lambda$ . This labeling is motivated by the association of the pseudospins with the density wave states in the atom-cavity setup discussed later in Sec. IV. For now, we simply note that the photonic mode corresponds to a single cavity mode while the operators  $\hat{J}_\mu^D$  and  $\hat{J}_\mu^B$  are associated with the density wave (DW) and bond-density wave (BDW) states in the shaken atom-cavity system, respectively [34]. A small term

proportional to  $\hat{J}_x^{23} \equiv \hat{J}_x^{DB}$  is included in Eq. (6) since this will appear later when we show how the atom-cavity system can be mapped onto the specific form of the parametrically driven three-level Dicke model Eq. (6).

### A. Holstein-Primakoff transformation

In Sec. II A, we have applied the HP transformation to the undriven system described by Eq. (3). We now extend this analysis to include the driving term. Applying the transformation and identifying  $\hat{d} \equiv \hat{a}_{12}$  and  $\hat{b} \equiv \hat{a}_{13}$ , we obtain a HP Hamiltonian shown in Eq. (F3) of Appendix F. In particular, we are interested in  $d \equiv \langle \hat{d} \rangle$  and  $b \equiv \langle \hat{b} \rangle$ .

We recall that, for a quantum harmonic oscillator,  $\hat{f}^\dagger = \sqrt{\omega_F/\hbar}[x_F - (i/\omega_F)p_F]$  and  $\hat{f} = \sqrt{\omega_F/\hbar}[x_F + (i/\omega_F)p_F]$ . Then, we can express the corresponding HP Hamiltonian in momentum-position representation as

$$H = \frac{\omega^2}{2} \hat{x}^2 + \frac{\hat{p}^2}{2} + \frac{\omega_D^2}{2} \hat{x}_D^2 + \frac{\hat{p}_D^2}{2} + \frac{\omega_B^2}{2} \hat{x}_B^2 + \frac{\hat{p}_B^2}{2} + 2\lambda \sqrt{\omega\omega_D} \hat{x} \hat{x}_D - 2\phi(t)\lambda \sqrt{\omega\omega_B} \hat{x} \hat{x}_B + \phi(t)(\omega_B - \omega_D) \sqrt{\omega_D\omega_B} \left( \hat{x}_D \hat{x}_B + \frac{\hat{p}_D \hat{p}_B}{\omega_D \omega_B} \right). \quad (5)$$

This has the form of a Hamiltonian for three coupled oscillators: (i) the *cavity oscillator*, (ii) the *DW oscillator*, and (iii) the *BDW oscillator* with frequencies  $\omega$ ,  $\omega_D$ , and  $\omega_B$ , respectively. Here, the two coupling constants connecting the BDW oscillator to the cavity and DW oscillators are periodically switched on and off or parametrically driven. Interestingly, due to the shaking of the pump, the momenta of the DW and BDW oscillators are also periodically coupled, as seen from the last term in Eq. (8). However, we find that this does not alter the qualitative features of the dynamics, as shown in Fig. 8 in Appendix E.

We initialize the system in the normal state corresponding to having  $d = 0$  and  $b = 0$ , which amounts to the absence of bosons in the excited states  $|2\rangle$  and  $|3\rangle$ , respectively. Note that a small nonzero occupation of the photonic mode ( $\hat{a} \equiv a = 10^{-2}$ ) is necessary to push the system out of the normal phase when it becomes an unstable state [9]. The dynamics is obtained according to Eq. (F4) for varying driving strength  $f_0$  and driving frequency  $\omega_{dr}$ . A parametric resonance in a linear system corresponding to a bilinear Hamiltonian, such as the simplified toy model (F3), manifests itself as an oscillatory solution with exponentially diverging amplitude. The dotted curves in Figs. 3(a)–3(d) denote the points in the  $(\omega_{dr}, f_0)$  space, where  $(b + b^*)$  exceeds unity within the first 100 driving cycles, signaling a diverging solution (see also Fig. 5). They indicate the regions where the normal phase is unstable towards a different collective phase.

We identify two resonances responsible for the driving-induced destabilization of the normal phase: (i) resonance at the BDW oscillator frequency  $\omega_B$  and (ii) a sum resonance involving  $\omega_B$  and the lower polariton frequency  $\omega_{LP}$  of the atomic modes dressed by the cavity mode forming the lower polariton state [40]. Note that we derive the expression for  $\omega_{LP}$  within the HP approach and we describe our method for obtaining the lower polariton frequency by exploiting a parametric resonance in Appendix G. The resonance

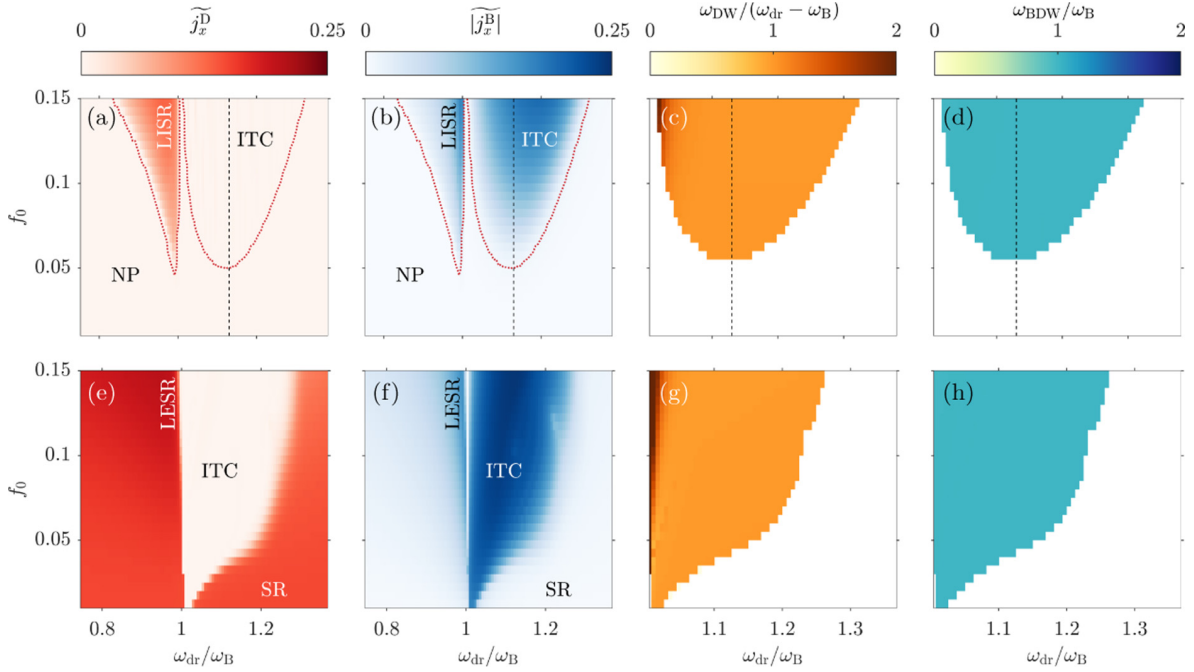


FIG. 3. Dynamical phase diagram for (a)–(d)  $\lambda = 0.98\lambda_{\text{cr}}$  and (e), (f)  $\lambda = 1.02\lambda_{\text{cr}}$ . Time-averaged (a), (e)  $\widetilde{j}_x^{\text{D}}$  and (b), (f)  $|\widetilde{j}_x^{\text{B}}|$  taken over 100 driving cycles,  $\tau = 100T$ , for varying modulation parameters. The dominant or peak frequency in the power spectrum of (c), (g)  $j_x^{\text{D}}$  and (d), (h)  $j_x^{\text{B}}$  for  $\omega_{\text{dr}} > \omega_{\text{B}}$ . The dotted lines in panels (a) and (b) denote the instability boundary according to the oscillator model. In panels (c), (d), (g), and (h), we are only showing the response frequencies  $\omega_{\text{DW}}$  and  $\omega_{\text{BDW}}$  for parameter sets, which yield  $|\widetilde{j}_x^{\text{B}}| > 0.01$  and  $\widetilde{j}_x^{\text{D}} < 0$ . Note that we are rescaling the response frequencies in panels (c) and (g) to  $\omega_{\text{DW}}/(\omega_{\text{dr}} - \omega_{\text{B}})$  and it is rescaled in panels (d) and (h) to  $\omega_{\text{BDW}}/\omega_{\text{B}}$ . The vertical dashed lines in panels (a)–(d) correspond to the sum frequency  $\omega_{\text{sum}} = \omega_{\text{LP}} + \omega_{\text{B}}$ .

frequencies are identified as the driving frequencies with the lowest modulation strength needed to induce an exponential instability. For  $\omega_{\text{dr}} < \omega_{\text{B}}$ , the resonance frequency is close to

$\omega_{\text{B}}$ . For  $\omega_{\text{dr}} > \omega_{\text{B}}$ , the sum resonance at  $\omega_{\text{sum}} = \omega_{\text{B}} + \omega_{\text{LP}}$  is the main mechanism, as highlighted by the vertical dashed line in Figs. 3(a)–3(d) (see also Fig. 5).

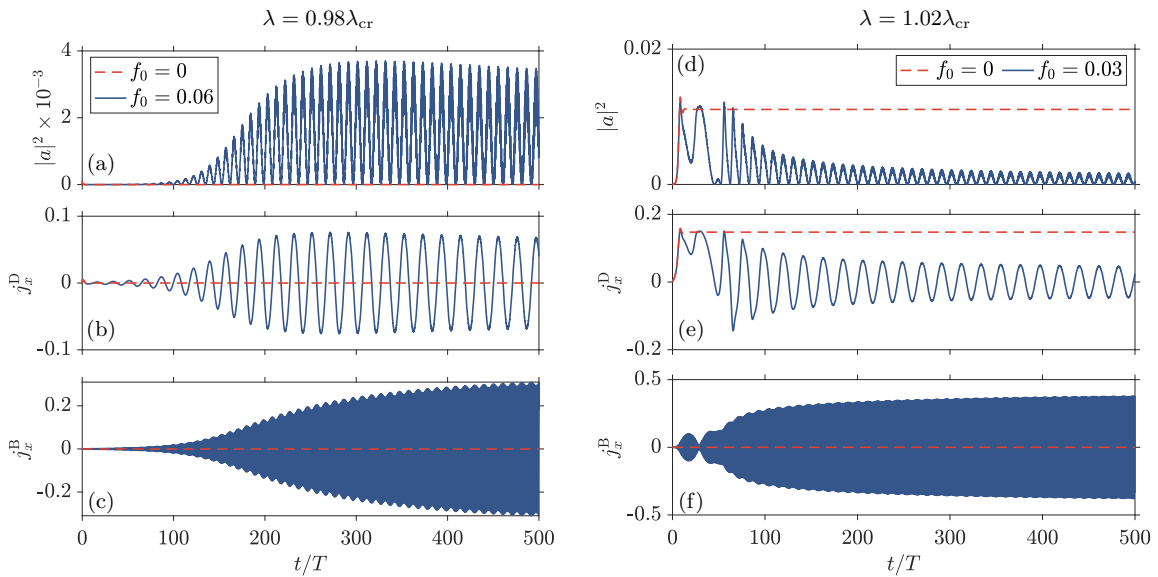


FIG. 4. Comparison between unmodulated and resonantly modulated dynamics for light-matter coupling strengths close to the NP-SR phase of the unmodulated system, (a)–(c)  $\lambda = 0.98\lambda_{\text{cr}}$  and (d)–(f)  $\lambda = 1.02\lambda_{\text{cr}}$ . The relevant observables are the (a), (d) cavity mode occupation  $|a|^2$ , and the order parameters (b), (e)  $j_x^{\text{D}}$  and (c), (f)  $j_x^{\text{B}}$ . The modulation frequency is fixed at  $\omega_{\text{dr}} = 1.05\omega_{\text{B}}$ .



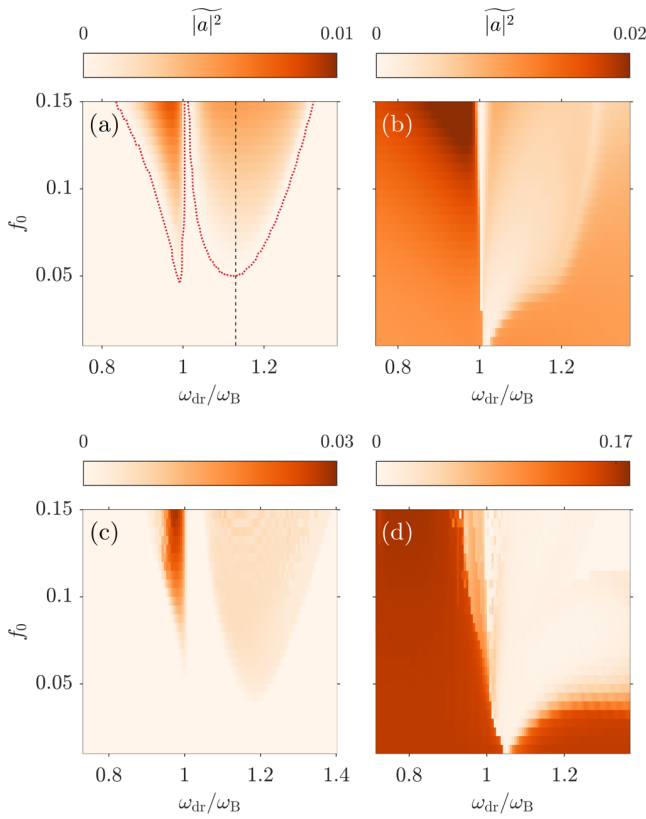


FIG. 5. Time-averaged cavity mode occupation  $|a|^2$  taken over 100 driving cycles,  $\tau = 100T$ , according to (a), (b) the three-level Dicke model and (c), (d) the full atom-cavity model. For the three-level model, the light-matter coupling strengths are (a)  $\lambda = 0.98\lambda_{\text{cr}}$  and (b)  $\lambda = 1.02\lambda_{\text{cr}}$ . The broken lines denote the instability boundary from the oscillator model. The vertical dashed line in panel (a) corresponds to the sum frequency  $\omega_{\text{sum}} = \omega_{\text{LP}} + \omega_{\text{B}}$  involving the lower polariton frequency  $\omega_{\text{LP}}$ .  $\omega_{\text{LP}}$  has the value  $\omega_{\text{LP}}/2\pi \approx 1.06$  kHz for this example. For the full atom-cavity model, the pump strengths are (c)  $\epsilon_{\text{p}} = 0.96\epsilon_{\text{cr}}$  and (d)  $\epsilon_{\text{p}} = 1.04\epsilon_{\text{cr}}$ , which corresponds to  $\lambda = 0.98\lambda_{\text{cr}}$  and  $\lambda = 1.02\lambda_{\text{cr}}$ , respectively.

## B. Dynamical phase diagrams

To further understand the resonant collective phases, we obtain the dynamics of the system. Within the mean-field approximation, we simulate the semiclassical equations of motion shown in Appendix E. Similar to the HP theory in the previous section, we initialize the system in the normal phase with small nonzero occupation of the photonic mode  $a = 10^{-2}$ . We further choose  $j_{\mu}^{\ell} = 0$ , except for  $j_z^{\text{D}} = j_z^{\text{B}} = -1/2$ . In addition to the photonic mode occupation  $|a|^2$ , we are also interested in the  $x$  component of the pseudospins  $j_x^{\text{D}}$  and  $j_x^{\text{B}}$ . Time is in units of the modulation period  $T = 2\pi/\omega_{\text{dr}}$ . The parameters for the simulation are shown in Appendix H.

In Fig. 4, we present exemplary dynamics for resonant modulation, specifically for  $\omega_{\text{dr}} = 1.05\omega_{\text{B}}$ . We choose light-matter coupling strengths close to the phase boundary between the normal and superradiant phases, specifically  $\lambda = 0.98\lambda_{\text{cr}}$  and  $\lambda = 1.02\lambda_{\text{cr}}$ , respectively. In the absence of driving,  $f_0 = 0$ , we reproduce the prediction of a normal phase NP and superradiant phase SP from the standard two-level Dicke

model. Periodic driving closed to but blue-detuned from  $\omega_{\text{B}}$  leads to similar long-time behavior for  $\lambda < \lambda_{\text{cr}}$  and  $\lambda > \lambda_{\text{cr}}$ . That is, the spin components related to the order parameters in the atom-cavity system,  $j_x^{\text{D}}$  and  $j_x^{\text{B}}$ , periodically changes their sign concomitant to pulses of light being emitted. The slow subharmonic oscillations in  $j_x^{\text{D}}$ , as exemplified in Fig. 4(b), reflects the temporal periodicity of the entire light-matter system. Note that  $j_x^{\text{B}}$  rapidly switches sign, as shown in Figs. 4(c) and 4(f). We quantify the dynamical regimes in the system using the response frequencies  $\omega_{\text{DW}}$  and  $\omega_{\text{BDW}}$ , which we define as the frequency at which  $j_x^{\text{D}}$  and  $j_x^{\text{B}}$  has a maximum in the power spectrum. Considering blue-detuned driving with respect to the BDW oscillator frequency  $\omega_{\text{dr}} > \omega_{\text{B}}$ , we find that the DBDW phase is characterized by fast oscillations of  $j_x^{\text{B}}$  at  $\omega_{\text{BDW}} = \omega_{\text{B}}$  and slow oscillations of  $j_x^{\text{D}}$  at  $\omega_{\text{DW}} = \omega_{\text{dr}} - \omega_{\text{B}}$ . These observations are valid for both  $\lambda < \lambda_{\text{cr}}$  and  $\lambda > \lambda_{\text{cr}}$ , as demonstrated in Figs. 3(c), 3(d), 3(g), and 3(h), where the relations  $\omega_{\text{DW}}/(\omega_{\text{dr}} - \omega_{\text{B}}) = 1$  and  $\omega_{\text{BDW}}/\omega_{\text{B}} = 1$  are satisfied over a wide range modulation parameters. In general, the system's response frequency  $\omega_{\text{DW}}$  is subharmonic and incommensurate with respect to the driving frequency  $\omega_{\text{dr}}$ , underpinning the classification of the DBDW phase as an ITC. Thus, we show that the emergence of the ITC phase is one of the signatures of the parametrically driven three-level Dicke model. In contrast, the system has a harmonic response, meaning that  $|a|^2$  and  $j_x^{\text{D}}$  have the same response frequency  $\omega_{\text{DW}} = 2\omega_{\text{dr}}$  [34], for combinations of driving parameters outside the dark areas in Figs. 3(c), 3(d), 3(g), and 3(h), including red-detuned driving  $\omega_{\text{dr}} < \omega_{\text{B}}$ .

In the ITC phase for  $\omega_{\text{dr}} > \omega_{\text{B}}$ , the oscillations of  $j_x^{\text{D}}$  and  $j_x^{\text{B}}$  around zero translate to vanishing time-averaged values,

$$\tilde{j}_x^{\ell} = \frac{1}{\tau} \int_0^{\tau} j_x^{\ell} dt. \quad (6)$$

This property is visible in the light area in Fig. 3(e). Note, however, that even though  $\tilde{j}_x^{\text{D}} = 0$ , the time-averaged cavity mode occupation  $|a|^2$  does not necessarily vanish, especially when  $j_x^{\text{D}}$  has nonzero oscillation amplitude, as shown in Figs. 3(a) and 5(a). The normal phase has  $j_x^{\text{D}} = 0$  for all times and as such,  $|\tilde{j}_x^{\text{D}}|$  also vanishes, albeit trivially, similar to the ITC phase. Therefore, to distinguish between the normal phase and the ITC phase, we calculate  $|\tilde{j}_x^{\text{B}}|$ , a quantity that vanishes for the normal phase and is nonzero for the ITC phase. In Figs. 3(b) and 3(f), it can be seen that the BDW states are resonantly excited not only for the ITC phase in  $\omega_{\text{dr}} > \omega_{\text{B}}$  but also for red-detuned driving  $\omega_{\text{dr}} < \omega_{\text{B}}$ . We emphasize that the dynamical response for  $\omega_{\text{dr}} < \omega_{\text{B}}$  remains harmonic, making this phase distinct from the ITC, normal, and superradiant phases.

We now focus on red-detuned driving  $\omega_{\text{dr}} < \omega_{\text{B}}$  to illustrate the effects of resonantly exciting the BDW states in this case. For  $\lambda < \lambda_{\text{cr}}$ , the normal phase, expected to be dominant in the absence of driving, is suppressed, which then gives rise to a superradiant phase enabled by the excitation of the BDW states. We call this resonant phase for  $\lambda < \lambda_{\text{cr}}$  and  $\omega_{\text{dr}} < \omega_{\text{B}}$  the *light-induced superradiant* (LISR) phase. In this phase, the long-time average of the cavity mode occupation  $|a|^2$  and  $j_x^{\text{D}}$  are both nonzero, similar to the superradiant phase, as seen from the resonance lobe in Figs. 3(a) and 5(a) for  $\omega_{\text{dr}} < \omega_{\text{B}}$ .

However, the occupation of BDW states, demonstrated in Fig. 3(b), distinguishes the LISR phase from the usual SR phase in the undriven case. An analogous effect for  $\lambda > \lambda_{cr}$  is the enhancement of the superradiant phase, the stationary phase in the absence of driving. This *light-enhanced superradiant* (LESR) phase is identified by an increase in  $|a|^2$  and  $j_x^D$ , accompanied by large amplitude oscillations of  $j_x^B$ , as shown in Figs. 5(b), 3(e), and 3(f). In addition to the ITC phase, the presence of LISR and LESR phases, depending on  $\lambda$ , is another signature of the driven dissipative three-level Dicke model.

#### IV. EMULATION USING A SHAKEN ATOM-CAVITY SYSTEM

We now show that the parametrically driven open three-level Dicke model can be emulated by a shaken atom-cavity system. To this end, we first describe the many-body Hamiltonian of the shaken atom-cavity. Then, we present the approximation needed to obtain Eq. (6) from the atom-cavity Hamiltonian.

##### A. Shaken atom-cavity Hamiltonian

We consider a minimal model for describing the dynamics along the pump and cavity directions of an atom-cavity system schematically depicted in Fig. 1(b). The corresponding many-body Hamiltonian is given by [34]

$$\begin{aligned} \hat{H}/\hbar = & -\delta_C \hat{a}^\dagger \hat{a} + \int dydz \hat{\Psi}^\dagger(y, z) \left[ -\frac{\hbar}{2m} \nabla^2 \right. \\ & - \omega_{\text{rec}} \epsilon_p \cos^2[ky + \phi(t)] + U_0 \hat{a}^\dagger \hat{a} \cos^2(kz) \\ & \left. - \sqrt{\omega_{\text{rec}} |U_0| \epsilon_p} \cos[ky + \phi(t)] \cos(kz) (\hat{a}^\dagger + \hat{a}) \right] \hat{\Psi}(y, z), \end{aligned} \quad (7)$$

where  $\hat{a}$  ( $\hat{a}^\dagger$ ) annihilates (creates) a photon in the single-mode cavity and  $\hat{\Psi}(y, z)$  is the bosonic field operator for the atoms with mass  $m$ . The pump-cavity detuning is  $\delta_C$ . The frequency shift per atom is taken to be redshifted,  $U_0 < 0$ . The pump intensity  $\epsilon_p$  is measured in units of the recoil energy  $E_{\text{rec}} = \hbar^2 k^2 / 2m$ , where the wave vector is  $k = 2\pi / \lambda_p$ . Note that, in Eq. (11), we neglect the effects of short-range collisional interaction. The pump lattice is periodically shaken by introducing a time-dependent phase in the pump mode

$$\phi(t) = f_0 \sin(\omega_{\text{dr}} t), \quad (8)$$

where  $f_0$  is the unitless modulation strength and  $\omega_{\text{dr}}$  is the modulation frequency. The characteristic timescale is thus set by the driving period  $T = 2\pi / \omega_{\text{dr}}$ .

The dynamics of the atom-cavity system follows from the Heisenberg-Langevin equations [40,41],

$$\frac{\partial}{\partial t} \hat{\Psi} = \frac{i}{\hbar} [\hat{H}, \hat{\Psi}], \quad (9)$$

$$\frac{\partial}{\partial t} \hat{a} = \frac{i}{\hbar} [\hat{H}, \hat{a}] - \kappa \hat{a} + \xi, \quad (10)$$

where  $\kappa$  is the cavity dissipation rate and the associated fluctuations are captured by the noise term  $\xi$  satisfying

$\langle \xi^*(t) \xi(t') \rangle = \kappa \delta(t - t')$ . In the mean-field limit of large particle number  $N$ , quantum fluctuations are neglected and the bosonic operators can be approximated as  $c$  numbers. The dynamics can then be obtained by numerically solving the resulting coupled differential equations corresponding to the equations of motion of the system. This approach and its extension beyond a mean-field approximation have been successfully used to predict and observe various dynamical phases in the transversely pumped atom-cavity system from a driving-induced renormalization of the phase boundary to time crystals [34,42–47].

##### B. Low-momentum approximation

The atom-cavity system can be mapped onto the Dicke model using a low-momentum approximation. To this end, we assume that the majority of the atoms only occupy the five-lowest momentum modes, namely the zero-momentum mode,  $|k_y, k_z\rangle = |0, 0\rangle$ , and the states associated with the self-organized checkerboard phase,  $|\pm k, \pm k\rangle$ . These momentum modes are coupled by the scattering of photons between the pump and cavity fields. This low-momentum approximation is valid close to the phase boundary between the homogeneous BEC phase and the self-organized DW phase.

Resonant shaking has been shown to lead to the emergence of an incommensurate time crystal, where atoms localize at positions between the antinodes of the pump lattice [34,35]. That is, in addition to the spatial mode  $\cos(ky) \cos(kz)$  in the DW phase, the atoms are driven into additional states, namely the BDW states, as the atomic distribution acquires an overlap with the spatial mode  $\sin(ky) \cos(kz)$ . Note that this mode is made available by the periodic shaking of the pump lattice since it explicitly breaks the spatial symmetry along the pump axis. Owing to how the system periodically switches between superpositions of DW and BDW states, we call this dynamical phase as the dynamical BDW (DBDW) phase. Since the DBDW phase has been previously identified as an incommensurate time crystal (ITC), we will use the term DBDW and ITC phase interchangeably.

The atomic field operator is expanded to include the relevant spatial modes

$$\hat{\Psi}(y, z) = \hat{c}_1 + 2\hat{c}_2 \cos(ky) \cos(kz) + 2\hat{c}_3 \sin(ky) \cos(kz), \quad (11)$$

where the  $c_i$  are bosonic annihilation and creation operator. We use this expansion in the many-body Hamiltonian (11). Evaluating the integrals within one unit cell and for weak driving  $f_0 \ll 1$ , we obtain a Hamiltonian in a reduced subspace,

$$\begin{aligned} H/\hbar = & -\delta_C \hat{a}^\dagger \hat{a} + 2\omega_{\text{rec}} (\hat{c}_2^\dagger \hat{c}_2 + \hat{c}_3^\dagger \hat{c}_3) + \frac{U_0}{2} \hat{a}^\dagger \hat{a} [\hat{c}_1^\dagger \hat{c}_1 \\ & + \frac{3}{2} (\hat{c}_2^\dagger \hat{c}_2 + \hat{c}_3^\dagger \hat{c}_3)] - \frac{\omega_{\text{rec}} \epsilon_p}{4} [2(\hat{c}_1^\dagger \hat{c}_1 + \hat{c}_2^\dagger \hat{c}_2 + \hat{c}_3^\dagger \hat{c}_3) \\ & + (\hat{c}_2^\dagger \hat{c}_2 - \hat{c}_3^\dagger \hat{c}_3) - 2\phi(t) (\hat{c}_2^\dagger \hat{c}_3 + \hat{c}_3^\dagger \hat{c}_2)] - \frac{\sqrt{\omega_{\text{rec}} |U_0| \epsilon_p}}{2} \\ & \times (\hat{a}^\dagger + \hat{a}) [(\hat{c}_1^\dagger \hat{c}_2 + \hat{c}_2^\dagger \hat{c}_1) - \phi(t) (\hat{c}_1^\dagger \hat{c}_3 + \hat{c}_3^\dagger \hat{c}_1)]. \end{aligned} \quad (12)$$

### C. Schwinger boson representation

We transform the bosonic operators in Eq. (12) into collective pseudospin operators through the Schwinger boson representation. The additional spatial mode  $\sin(ky)\cos(kz)$  is described by the operator  $c_3$ , so the atomic motion is represented as a three-level system. We introduce the pseudospin operators obeying SU(3) algebra via

$$\begin{aligned} N &= \hat{c}_1^\dagger \hat{c}_1 + \hat{c}_2^\dagger \hat{c}_2 + \hat{c}_3^\dagger \hat{c}_3, \\ \hat{J}_+^D &= \hat{c}_2^\dagger \hat{c}_1, & \hat{J}_-^D &= \hat{c}_1^\dagger \hat{c}_2, & \hat{J}_z^D &= \frac{1}{2}(\hat{c}_2^\dagger \hat{c}_2 - \hat{c}_3^\dagger \hat{c}_3 - \hat{c}_1^\dagger \hat{c}_1), \\ \hat{J}_+^B &= \hat{c}_3^\dagger \hat{c}_1, & \hat{J}_-^B &= \hat{c}_1^\dagger \hat{c}_3, & \hat{J}_z^B &= \frac{1}{2}(\hat{c}_3^\dagger \hat{c}_3 - \hat{c}_2^\dagger \hat{c}_2 - \hat{c}_1^\dagger \hat{c}_1), \\ \hat{J}_+^{DB} &= \hat{c}_2^\dagger \hat{c}_3, & \hat{J}_-^{DB} &= \hat{c}_3^\dagger \hat{c}_2. \end{aligned} \quad (13)$$

This representation suggests that the operators  $\hat{J}_\mu^D$  are associated with the DW state while  $\hat{J}_\mu^B$  are related to the BDW state. Applying the commutation relations for the bosonic operators  $[\hat{c}_m, \hat{c}_n^\dagger] = \delta_{mn}$ , we recover the same commutation relations for the pseudospin operators presented in Eq. (A1). That is, we identify  $\hat{J}_\mu^D \equiv \hat{J}_\mu^{12}$ ,  $\hat{J}_\mu^B \equiv \hat{J}_\mu^{13}$ , and  $\hat{J}_\mu^{DB} \equiv \hat{J}_\mu^{23}$ .

Substituting the Schwinger boson representation in Eq. (14) into Eq. (12) yields the driven dissipative three-level Dicke model (6). Within the shaken-atom cavity platform, the effective cavity field frequency is  $\omega = (3U_0N)/4 - \delta_C = U_0N/4 - \delta_{\text{eff}}$ , the effective pump-cavity detuning is  $\delta_{\text{eff}}$ , and the light-matter coupling strength is  $\lambda/\sqrt{N} = -\sqrt{\omega_{\text{rec}}\epsilon_p}|U_0|/2$ . The pump intensity  $\epsilon_p$  shifts the frequencies of the pair of two-level transitions,  $\omega_D = 2\omega_{\text{rec}}(1 - \epsilon_p/8)$  and  $\omega_B = 2\omega_{\text{rec}}(1 + \epsilon_p/8)$ . We can infer from Eq. (6) that weak periodic shaking effectively leads to a parametric driving of the light-matter coupling between the cavity and the spin associated with the BDW state. With these correspondences, we find that indeed the shaken atom-cavity system can be approximated by the driven three-level Dicke model presented in Eq. (6) and discussed in Sec. III. Moreover, we can identify the order parameters of the self-organized density wave states, namely the DW order parameter  $\Theta_{\text{DW}} = \langle \cos(ky)\cos(kz) \rangle = j_x^D$  and the BDW order parameter  $\Theta_{\text{BDW}} = \langle \sin(ky)\cos(kz) \rangle = j_x^B$ .

### D. Comparison with the full atom-cavity model

We compare the dynamics of the cavity mode occupation and the DW order parameter for the full atom-cavity model (11) and the effective three-level model according to Eq. (E2). The parameters for the simulation are shown in Appendix H. For results based on the full atom-cavity model Eq. (11), we numerically determine  $\epsilon_{\text{cr}}$  from the onset of intracavity photon number [34]. Moreover, the BDW oscillator frequency  $\omega_B$  for the full atom-cavity model is extracted from the oscillation frequency of the BDW order parameter  $\Theta_{\text{BDW}}$  [34]. We show in Fig. 5 the time-averaged occupation of the cavity mode  $|a|^2$ ,

$$|\widetilde{a}|^2 = \frac{1}{\tau} \int_0^\tau |a|^2 dt, \quad (14)$$

for  $\tau = 100T$ , as a function of modulation strength  $f_0$  and modulation frequency  $\omega_{\text{dr}}$ . For  $\lambda < \lambda_{\text{cr}}$ , we obtain a qualitatively similar dynamical phase diagrams for the three-level Dicke model and the full atom-cavity model, as depicted in

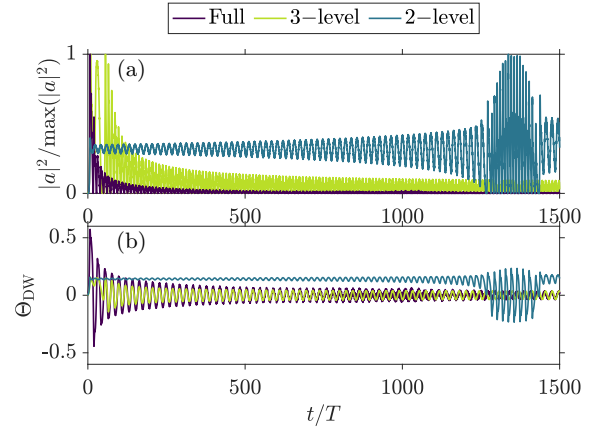


FIG. 6. Comparison of the dynamics between the full atom-cavity model [in purple (black)], three-level [in green (light gray)], and coupled two-level Dicke model [in blue (dark gray)] for the (a) cavity mode occupation and (b) DW order parameter. For the Dicke models, the light-matter coupling strength is  $\lambda = 1.02\lambda_{\text{cr}}$ . This corresponds to a pump strength of  $\epsilon_p/\epsilon_{\text{cr}} = 1.04$  in the full-atom cavity model. The driving parameters are fixed to  $f_0 = 0.03$  and  $\omega_{\text{dr}} = 1.05\omega_B$ .

Figs. 5(a) and 5(c). Therefore, in this regime, the approximation of Eq. (11) via Eq. (6) is applicable. That is, the parametrically driven open three-level Dicke Hamiltonian is realized approximately by the shaken atom-cavity system. Moreover, the instability region from the oscillator model in the thermodynamic limit Eq. (F3) matches the onset of the cavity mode occupation in Fig. 5(a).

For  $\lambda > \lambda_{\text{cr}}$ , the dark areas in Figs. 5(b) and 5(d) signify that the system has entered the DW or SR phase indicated by a nonvanishing cavity mode occupation, as expected for weak and off-resonant driving. However, the DW phase is suppressed for driving frequencies blue-detuned from  $\omega_B$  as indicated by the relative decrease in the cavity photon number in the light areas in Figs. 5(b) and 5(d). Crucially, the correspondence between Eqs. (11) and (6) breaks down for driving frequencies far-detuned from  $\omega_B$  as inferred from the parameter region  $\omega_{\text{dr}} > \omega_B$  in Figs. 5(b) and 5(d). This can be attributed to the occupation of higher momentum modes, specifically  $|\pm 2k, 0\rangle$ , in the full atom-cavity system [34], which is not captured in the low-momentum expansion (11) utilized in the mapping. Nevertheless, we still find good agreement on the qualitative features for driving frequencies near  $\omega_B$ .

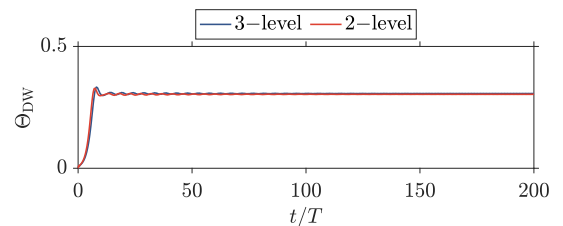


FIG. 7. Dynamics of the density wave order parameter for  $\omega_{\text{dr}} = 0.8\omega_B$  and  $f_0 = 0.05$ . The remaining parameters are the same as in Fig. 6.

We also consider the dynamics according to a coupled two-level Dicke model for the same set of parameters (see Appendix B for details). In Fig. 6, we present the dynamics for  $\lambda > \lambda_{\text{cr}}$  with a driving frequency blue-detuned with respect to  $\omega_B$ . The results of the coupled two-level systems clearly do not capture the dynamics of the full atom-cavity system. On the other hand, the three-level Dicke model and the full atom-cavity model predict the same dynamical response, which is a subharmonic motion exhibited as a pulsating photon number [see Fig. 6(a)] and a periodic switching of the sign of the DW order parameter [see Fig. 6(b)]. This further supports our claim that the mapping between the three-level Dicke model and the full-atom cavity system is applicable to  $\lambda > \lambda_{\text{cr}}$  for as long as the driving frequency is close to  $\omega_B$ . Note, however, that the coupled two-level systems model and the three-level model agree with each other for off-resonant driving when  $j_x^B \approx 0$ , as demonstrated in Appendix B.

## V. CONCLUSIONS

In this work, we have investigated a three-level Dicke model, and derived its equilibrium phase diagram, which features a normal phase and a superradiant phase. We advanced the model to a driven dissipative system by including a dissipation mechanism via photon loss and a periodic driving process. For this system, we developed the dynamical phase diagram, which shows the phases for varying driving parameters, utilizing analytical and numerical methods. As a central result we characterized the regime of an incommensurate time crystalline state in the phase diagram. Furthermore, we obtained light-enhanced and light-induced superradiant states, in which the equilibrium superradiant state is dynamically stabilized. As a physical system that can be naturally approximated

via the three-level Dicke model, we identified a periodically shaken atom-cavity system. While the nonshaken atom-cavity system can be approximated via the standard two-level Dicke model, the shaking induces the atoms to populate additional states that are modeled via a third state in the three-level Dicke model. We note that the LISR and LESR phases display similarities with light-induced [48] and light-enhanced superconductivity [49], for which mechanisms have been proposed that involve the excitation of auxiliary modes, such as phonons [50–52] and Higgs bosons [53], by means of optical pumping. Photoexcitation of the Higgs mode in cuprate superconductors has also been predicted to lead to an incommensurate time crystal [54]. In this work, the BDW state plays the role of such an auxiliary mode, as its excitation [or equivalently, the  $|1\rangle \rightarrow |3\rangle$  in Fig. 1(a)] can be used to dynamically control the system to induce or enhance superradiance, or to enter a genuine dynamical order, namely, the incommensurate time crystalline phase. We therefore expand the dynamical control of phases in atom-cavity systems to include light-induced and light-enhanced superradiance, in addition to the previously observed light-enhanced BEC or normal phase [42,43].

*Note added.* Recently, an example of the driven three-level Dicke model was presented in Ref. [55].

## ACKNOWLEDGMENTS

We thank G. Homann and L. Broers for useful discussions. This work is funded by the Deutsche Forschungsgemeinschaft (DFG, German Research Foundation) - SFB-925 - project 170620586 and the Cluster of Excellence ‘‘Advanced Imaging of Matter’’ (EXC 2056), Project No. 390715994. J.S. acknowledges support from the German Academic Scholarship Foundation.

## APPENDIX A: THE SU(3) ALGEBRA, GELL-MANN MATRICES, AND CASIMIR CHARGES

$$\begin{aligned}
[\hat{J}_z^{12}, \hat{J}_\pm^{12}] &= \pm \hat{J}_\pm^{12}, & [\hat{J}_-^{12}, \hat{J}_+^{12}] &= 2\hat{J}_z^{12} + \hat{J}_z^{13} + \frac{N}{2}, \\
[\hat{J}_z^{13}, \hat{J}_\pm^{13}] &= \pm \hat{J}_\pm^{13}, & [\hat{J}_-^{13}, \hat{J}_+^{13}] &= 2\hat{J}_z^{13} + \hat{J}_z^{12} + \frac{N}{2}, \\
[\hat{J}_\pm^{12}, \hat{J}_\mp^{13}] &= \pm \hat{J}_\pm^{23}, & [\hat{J}_+^{23}, \hat{J}_-^{23}] &= \hat{J}_z^{12} - \hat{J}_z^{13}, \\
[\hat{J}_z^{12}, \hat{J}_\pm^{23}] &= \pm \hat{J}_\pm^{23}, & [\hat{J}_z^{13}, \hat{J}_\pm^{23}] &= \mp \hat{J}_\pm^{23}, \\
[\hat{J}_\pm^{12}, \hat{J}_\mp^{23}] &= \mp \hat{J}_\pm^{13}, & [\hat{J}_\pm^{13}, \hat{J}_\mp^{23}] &= \mp \hat{J}_\pm^{12}.
\end{aligned} \tag{A1}$$

The remaining commutators not listed above vanish. Our choice of pseudospin operators for the SU(3) algebra can be mapped onto the Gell-Mann matrices [31] via

$$\begin{aligned}
F_1 &\equiv J_x^{12} = \frac{1}{2}\lambda_1, \\
F_2 &\equiv J_y^{12} = \frac{1}{2}\lambda_2, \\
F_3 &\equiv J_z^{12} + \frac{1}{2}J_z^{13} + N/4 = \frac{1}{2}\lambda_3, \\
F_4 &\equiv J_x^{23} = \frac{1}{2}\lambda_4, \\
F_5 &\equiv J_y^{23} = \frac{1}{2}\lambda_5,
\end{aligned}$$

$$\begin{aligned}
F_6 &\equiv J_x^{13} = \frac{1}{2}\lambda_6, \\
F_7 &\equiv -J_y^{13} = \frac{1}{2}\lambda_7, \\
F_8 &\equiv -\frac{\sqrt{3}}{2}(J_z^{13} + N/6) = \frac{1}{2}\lambda_8.
\end{aligned} \tag{A2}$$

### Casimir charges

The group SU(3) enjoys two Casimirs, which can be written in matrix form using the Gell-Mann basis as

$$C_1 = \sum_{i=1}^8 F_i F_i, \tag{A3}$$

$$C_2 = \sum_{j,k,l=1}^8 d_{jkl} F_j F_k F_l, \tag{A4}$$

with

$$d_{jkl} = \frac{1}{4} \text{Tr}(\{\lambda_j, \lambda_k\} \lambda_l). \tag{A5}$$

In our chosen basis, they take the form of

$$\langle C_1 \rangle / N = \frac{1}{12} + (j_x^{12})^2 + (j_y^{12})^2 + (j_z^{12})^2 + (j_x^{13})^2 + (j_y^{13})^2 + (j_z^{13})^2 + (j_x^{23})^2 + (j_y^{23})^2 + \frac{1}{2}(j_z^{12} + j_z^{13} + 2j_z^{12} j_z^{13}), \tag{A6}$$

$$\begin{aligned}
\langle C_2 \rangle / N^{3/2} &= \frac{1}{72} \{ -18(j_y^{12})^2 + 216j_y^{23}(j_y^{12} j_x^{13} - j_x^{12} j_y^{13}) + 216j_x^{23}(j_x^{12} j_x^{13} + j_y^{12} j_y^{13}) \\
&\quad - (1 + 6j_z^{12})[1 + 3j_z^{12} + 18(j_x^{13})^2 + 18(j_y^{13})^2] - 9j_z^{13} + 36(j_x^{23})^2(1 + 3j_z^{12} + 3j_z^{13}) \\
&\quad + 36(j_y^{23})^2(1 + 3j_z^{12} + 3j_z^{13}) \\
&\quad - 18\{(j_x^{12})^2(1 + 6j_z^{13}) + j_z^{13}[6(j_y^{12})^2 + j_z^{13} + 2j_z^{12}(2 + 3j_z^{12} + 3j_z^{13})]\} \}.
\end{aligned} \tag{A7}$$

### APPENDIX B: TWO-COMPONENT DICKE MODEL

A modified version of the two-component Dicke model [9,10], which can be realized in a spinor BEC coupled to an optical cavity [16,17], is given by

$$H/\hbar = \omega \hat{a}^\dagger \hat{a} + \omega_1 \hat{J}_z^1 + \omega_2 \hat{J}_z^2 + \frac{2}{\sqrt{N}} (\hat{a}^\dagger + \hat{a})(\lambda_1 \hat{J}_x^1 + \lambda_2 \hat{J}_x^2). \tag{B1}$$

Note that this has the same form as the three-level Hamiltonian in Eq. (1) except that here, the pseudospin operators fulfill to the SU(2) group algebra with the commutation relations,

$$[\hat{J}_\pm^\ell, \hat{J}_\pm^\ell] = \pm \hat{J}_\pm^\ell, \quad [\hat{J}_-^\ell, \hat{J}_+^\ell] = 2\hat{J}_z^\ell, \tag{B2}$$

where  $\ell \in \{1, 2\}$ . Applying the same mean-field approximation as in Sec. II B, we obtain the following equations of motion consistent with those in Refs. [9,10,16,17],

$$\begin{aligned}
\frac{da}{dt} &= -(i\omega + \kappa)a - i2 \sum_{\ell=1}^2 \lambda_\ell j_x^\ell, \\
\frac{dj_x^\ell}{dt} &= -\omega_\ell j_y^\ell, \\
\frac{dj_y^\ell}{dt} &= \omega_\ell j_x^\ell - 2\lambda_\ell (a + a^*) j_z^\ell, \\
\frac{dj_z^\ell}{dt} &= 2\lambda_\ell (a + a^*) j_y^\ell.
\end{aligned} \tag{B3}$$

To obtain the relevant curves in Fig. 6, we propagate the above set of coupled equations with  $\omega_1 = \omega_D$ ,  $\omega_2 = \omega_B$ ,  $\lambda_1 = \lambda$ , and  $\lambda_2 = -\lambda f_0 \sin(\omega_{dt} t)$ . The exact values of these parameters are the same as those described in the main text. We present in Fig. 7 a comparison of the dynamics according to the two-component Dicke model and the three-level Dicke model for off-resonant driving.



### APPENDIX C: CRITICAL LIGHT-MATTER COUPLING

Using the Hamiltonian in Eq. (3) and the Heisenberg equation in Eq. (D1), we obtain the equations of motion as

$$\begin{aligned}\frac{da}{dt} &= -(i\omega - \kappa)a - i\lambda_{12}(a_{12}^\dagger + a_{12}) - i\lambda_{13}(a_{13}^\dagger + a_{13}), \\ \frac{da_{12}}{dt} &= -i\omega_{12}a_{12} - i\lambda_{12}(a^* + a), \\ \frac{da_{13}}{dt} &= -i\omega_{13}a_{13} - i\lambda_{13}(a^* + a).\end{aligned}\quad (\text{C1})$$

We can then construct the matrix  $M$  as  $\partial_t \vec{v} = M\vec{v}$  to obtain

$$M = \begin{pmatrix} \kappa - i\omega & 0 & -i\lambda_{12} & -i\lambda_{12} & -i\lambda_{13} & -i\lambda_{13} \\ 0 & \kappa + i\omega & i\lambda_{12} & i\lambda_{12} & i\lambda_{13} & i\lambda_{13} \\ -i\lambda_{12} & -i\lambda_{12} & -i\omega_{12} & 0 & 0 & 0 \\ i\lambda_{12} & i\lambda_{12} & 0 & i\omega_{12} & 0 & 0 \\ -i\lambda_{13} & -i\lambda_{13} & 0 & 0 & -i\omega_{13} & 0 \\ i\lambda_{13} & i\lambda_{13} & 0 & 0 & 0 & i\omega_{13} \end{pmatrix}.\quad (\text{C2})$$

A phase transition occurs if  $M$  inherits a zero energy eigenstate [39]. This means, to find the critical light-matter coupling  $\lambda$ , we need to calculate  $\det(M) = 0$ , giving us

$$\frac{(\kappa^2 + \omega^2)}{4\omega} = \left( \frac{\lambda_{12}^2}{\omega_{12}} + \frac{\lambda_{13}^2}{\omega_{13}} \right).\quad (\text{C3})$$

### APPENDIX D: HEISENBERG EQUATIONS OF MOTION

The dynamics of an observable  $\hat{O}$  in the dissipative system considered here is governed by the Heisenberg equation

$$\frac{d\langle \hat{O} \rangle}{dt} = \left\langle \frac{i}{\hbar} [\hat{H}, \hat{O}] + \kappa (2\hat{a}^\dagger \hat{O} \hat{a} - \{\hat{a}^\dagger \hat{a}, \hat{O}\}) \right\rangle.\quad (\text{D1})$$

Using the commutation relations Eq. (A1), we get the following equations for the expectation values of relevant operators in the open three-level Dicke model (1):

$$\begin{aligned}\frac{d\langle a \rangle}{dt} &= -(i\omega + \kappa)\langle a \rangle - i\frac{2}{\sqrt{N}}(\lambda_{12}\langle \hat{J}_x^{12} \rangle + \lambda_{13}\langle \hat{J}_x^{13} \rangle), \\ \frac{d\langle \hat{J}_x^{12} \rangle}{dt} &= -\omega_{12}\langle \hat{J}_y^{12} \rangle + \frac{\lambda_{13}}{\sqrt{N}}\langle (a^\dagger + a)\hat{J}_{23}^y \rangle, \\ \frac{d\langle \hat{J}_y^{12} \rangle}{dt} &= \omega_{12}\langle \hat{J}_x^{12} \rangle - \frac{\lambda_{12}}{\sqrt{N}}[2\langle (a^\dagger + a)\hat{J}_z^{12} \rangle + \langle (a^\dagger + a)\hat{J}_z^{13} \rangle + \langle (a^\dagger + a)N/2 \rangle] - \frac{\lambda_{13}}{\sqrt{N}}\langle (a^\dagger + a)\hat{J}_x^{23} \rangle, \\ \frac{d\langle \hat{J}_z^{12} \rangle}{dt} &= \frac{2\lambda_{12}}{\sqrt{N}}\langle (a + a^\dagger)\hat{J}_y^{12} \rangle, \\ \frac{d\langle \hat{J}_x^{13} \rangle}{dt} &= -\omega_{13}\langle \hat{J}_y^{13} \rangle - \frac{\lambda_{12}}{\sqrt{N}}\langle (a^\dagger + a)\hat{J}_y^{23} \rangle, \\ \frac{d\langle \hat{J}_y^{13} \rangle}{dt} &= \omega_{13}\langle \hat{J}_x^{13} \rangle - \frac{\lambda_{13}}{\sqrt{N}}[2\langle (a^\dagger + a)\hat{J}_z^{13} \rangle + \langle (a^\dagger + a)\hat{J}_z^{12} \rangle + \langle (a^\dagger + a)N/2 \rangle] - \frac{\lambda_{12}}{\sqrt{N}}\langle (a^\dagger + a)\hat{J}_x^{23} \rangle, \\ \frac{d\langle \hat{J}_z^{13} \rangle}{dt} &= \frac{2\lambda_{13}}{\sqrt{N}}\langle (a + a^\dagger)\hat{J}_y^{13} \rangle, \\ \frac{d\langle \hat{J}_x^{23} \rangle}{dt} &= (\omega_{13} - \omega_{12})\langle \hat{J}_y^{23} \rangle + \frac{\lambda_{12}}{\sqrt{N}}\langle (a^\dagger + a)\hat{J}_y^{13} \rangle + \frac{\lambda_{13}}{\sqrt{N}}\langle (a^\dagger + a)\hat{J}_y^{12} \rangle, \\ \frac{d\langle \hat{J}_y^{23} \rangle}{dt} &= (\omega_{12} - \omega_{13})\langle \hat{J}_x^{23} \rangle + \frac{\lambda_{12}}{\sqrt{N}}\langle (a^\dagger + a)\hat{J}_x^{13} \rangle - \frac{\lambda_{13}}{\sqrt{N}}\langle (a^\dagger + a)\hat{J}_x^{12} \rangle.\end{aligned}\quad (\text{D2})$$

On the other hand, the equations of motion for the parametrically driven open three-level Dicke model are

$$\begin{aligned}
\frac{d\langle\hat{a}\rangle}{dt} &= -(i\omega + \kappa)\langle\hat{a}\rangle - i\frac{2\lambda}{\sqrt{N}}\langle\hat{J}_x^D\rangle + i\phi(t)\frac{2\lambda}{\sqrt{N}}\langle\hat{J}_x^B\rangle, \\
\frac{d\langle\hat{J}_x^D\rangle}{dt} &= -\omega_D\langle\hat{J}_y^D\rangle - \phi(t)(\omega_B - \omega_D)\langle\hat{J}_y^B\rangle - \phi(t)\frac{\lambda}{\sqrt{N}}\langle(a^\dagger + a)\hat{J}_y^{DB}\rangle, \\
\frac{d\langle\hat{J}_y^D\rangle}{dt} &= \omega_D\langle\hat{J}_x^D\rangle - \frac{\lambda}{\sqrt{N}}\left[2\langle(a^\dagger + a)\hat{J}_z^D\rangle + \langle(a^\dagger + a)\hat{J}_z^B\rangle + \langle a^\dagger + a \rangle\frac{N}{2}\right] \\
&\quad + \phi(t)(\omega_B - \omega_D)\langle\hat{J}_x^B\rangle + \phi(t)\frac{\lambda}{\sqrt{N}}\langle(a^\dagger + a)\hat{J}_x^{DB}\rangle, \\
\frac{d\langle\hat{J}_z^D\rangle}{dt} &= \frac{2\lambda}{\sqrt{N}}\langle(a + a^\dagger)\hat{J}_y^D\rangle + 2(\omega_B - \omega_D)\phi(t)\langle\hat{J}_y^{DB}\rangle, \\
\frac{d\langle\hat{J}_x^B\rangle}{dt} &= -\omega_B\langle\hat{J}_y^B\rangle - \phi(t)(\omega_B - \omega_D)\langle\hat{J}_y^D\rangle - \frac{\lambda}{\sqrt{N}}\langle(a^\dagger + a)\hat{J}_y^{DB}\rangle, \\
\frac{d\langle\hat{J}_y^B\rangle}{dt} &= \omega_B\langle\hat{J}_x^B\rangle + \phi(t)\frac{\lambda}{\sqrt{N}}\left[2\langle(a^\dagger + a)\hat{J}_z^B\rangle + \langle(a^\dagger + a)\hat{J}_z^D\rangle + \langle a^\dagger + a \rangle\frac{N}{2}\right] \\
&\quad + \phi(t)(\omega_B - \omega_D)\langle\hat{J}_x^D\rangle - \frac{\lambda}{\sqrt{N}}\langle(a^\dagger + a)\hat{J}_x^{DB}\rangle, \\
\frac{d\langle\hat{J}_z^B\rangle}{dt} &= -\phi(t)(\omega_B - \omega_D)\langle(a + a^\dagger)\hat{J}_y^B\rangle - \frac{4\lambda^2}{U_0N}\phi(t)\langle\hat{J}_y^{DB}\rangle, \\
\frac{d\langle\hat{J}_x^{DB}\rangle}{dt} &= (\omega_B - \omega_D)\langle\hat{J}_y^{DB}\rangle + \frac{\lambda}{\sqrt{N}}\langle(a^\dagger + a)\hat{J}_y^B\rangle - \phi(t)\frac{\lambda}{\sqrt{N}}\langle(a^\dagger + a)\hat{J}_y^D\rangle, \\
\frac{d\langle\hat{J}_y^{DB}\rangle}{dt} &= (\omega_D - \omega_B)\langle\hat{J}_x^{DB}\rangle + \frac{\lambda}{\sqrt{N}}\langle(a^\dagger + a)\hat{J}_x^B\rangle + \phi(t)\frac{\lambda}{\sqrt{N}}\langle(a^\dagger + a)\hat{J}_x^D\rangle + 2(\omega_B - \omega_D)\phi(t)\langle\hat{J}_z^B - \hat{J}_z^D\rangle. \tag{D3}
\end{aligned}$$

#### APPENDIX E: MEAN-FIELD EQUATIONS OF MOTION

The mean-field equations for the dissipative three-level Dicke model are given by

$$\begin{aligned}
\frac{da}{dt} &= -(i\omega + \kappa)a - i2\lambda_{12}j_x^{12} - i2\lambda_{13}j_x^{13}, \\
\frac{dj_x^{12}}{dt} &= -\omega_{12}j_y^{12} + \lambda_{13}(a + a^*)j_{23}^y, \\
\frac{dj_y^{12}}{dt} &= \omega_{12}j_x^{12} - \lambda_{12}(a + a^*)(2j_z^{12} + j_z^{13} + 1/2) - \lambda_{13}(a + a^*)j_x^{23}, \\
\frac{dj_z^{12}}{dt} &= 2\lambda_{12}(a + a^*)j_y^{12}, \\
\frac{dj_x^{13}}{dt} &= -\omega_{13}j_y^{13} - \lambda_{12}(a + a^*)j_y^{23}, \\
\frac{dj_y^{13}}{dt} &= \omega_{13}j_x^{13} - \lambda_{13}(a + a^*)(2j_z^{13} + j_z^{12} + 1/2) - \lambda_{12}(a + a^*)j_x^{23}, \\
\frac{dj_z^{13}}{dt} &= 2\lambda_{13}(a + a^*)j_y^{13}, \\
\frac{dj_x^{23}}{dt} &= (\omega_{13} - \omega_{12})j_y^{23} + \lambda_{12}(a + a^*)j_y^{13} + \lambda_{13}(a + a^*)j_y^{12}, \\
\frac{dj_y^{23}}{dt} &= (\omega_{12} - \omega_{13})j_x^{23} + \lambda_{12}(a + a^*)j_x^{13} - \lambda_{13}(a + a^*)j_x^{12}. \tag{E1}
\end{aligned}$$

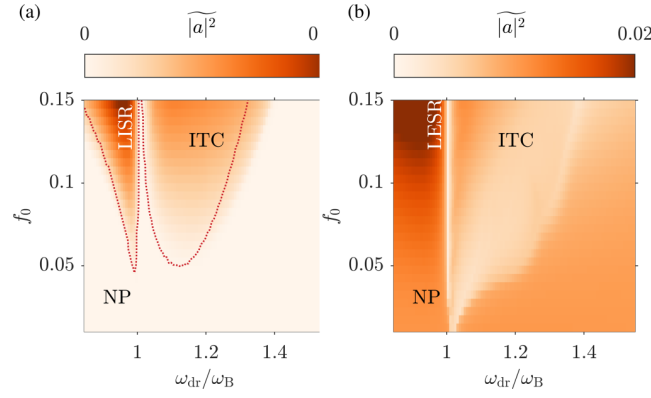


FIG. 8. Time-averaged cavity mode occupation  $|a|^2$  taken over 100 driving cycles,  $\tau = 100T$ . We choose  $\omega_D = \omega_B = \omega_{\text{rec}}$  while the remaining parameters are the same as those in Figs. 5(a) and 5(b).

For the parametrically driven open three-level Dicke model, the equations of motion are given by

$$\begin{aligned}
 \frac{da}{dt} &= -(i\omega + \kappa)a - i2\lambda j_x^D + i\phi(t)2\lambda j_x^B, \\
 \frac{dj_x^D}{dt} &= -\omega_D j_y^D - \phi(t)(\omega_B - \omega_D)j_y^B - \phi(t)\lambda(a + a^*)j_y^{DB}, \\
 \frac{dj_y^D}{dt} &= \omega_D j_x^D - \lambda(a + a^*)(2j_z^D + j_z^B + 1/2) + \phi(t)(\omega_B - \omega_D)j_x^B + \phi(t)\lambda(a + a^*)j_x^{DB}, \\
 \frac{dj_z^D}{dt} &= 2\lambda(a + a^*)j_y^D + 2(\omega_B - \omega_D)\phi(t)j_y^{DB}, \\
 \frac{dj_x^B}{dt} &= -\omega_B j_y^B - (\omega_B - \omega_D)\phi(t)j_y^D - \lambda(a + a^*)j_y^{DB}, \\
 \frac{dj_y^B}{dt} &= \omega_B j_x^B + \phi(t)\lambda(a + a^*)(2j_z^B + j_z^D + 1/2) + \phi(t)(\omega_B - \omega_D)j_x^D - \lambda(a + a^*)j_x^{DB}, \\
 \frac{dj_z^B}{dt} &= -\phi(t)2\lambda(a + a^*)j_y^B - 2(\omega_B - \omega_D)\phi(t)j_y^{DB}, \\
 \frac{dj_x^{DB}}{dt} &= (\omega_B - \omega_D)j_y^{DB} + \lambda(a + a^*)j_y^B - \phi(t)\lambda(a + a^*)j_y^D, \\
 \frac{dj_y^{DB}}{dt} &= (\omega_D - \omega_B)j_x^{DB} + \lambda(a + a^*)j_x^B + \phi(t)\lambda(a + a^*)j_x^D + 2(\omega_B - \omega_D)\phi(t)(j_z^B - j_z^D). \tag{E2}
 \end{aligned}$$

In Fig. 8, we demonstrate that the existence of the dynamical phases is independent of the term in the Hamiltonian with  $j_x^{DB}$ . That is, the momenta coupling inferred from Eq. (8) does not play a crucial role in the formation of the ITC, LESR, and LISR phases. This suggests that the emergence of these dynamical phases originates from the last term in Eq. (6). To confirm this, we set  $\omega_D = \omega_B$  in Fig. 8. For comparison, we show in dotted lines the phase boundary obtained for  $\omega_D \neq \omega_B$ .

#### APPENDIX F: HOLSTEIN-PRIMAKOFF TRANSFORMATION

We present a Holstein-Primakoff approximation in the thermodynamic limit, i.e.,  $N \rightarrow \infty$  [5,56]. To capture the correct SU(3) algebra, we use an extended version of the Holstein-Primakoff representation given by [57]

$$\begin{aligned}
 \hat{j}_z^{12} &= \hat{a}_{12}^\dagger \hat{a}_{12} - N/2, & \hat{J}_+^{12} &= \hat{a}_{12}^\dagger \sqrt{N - (\hat{a}_{12}^\dagger \hat{a}_{12} + \hat{a}_{13}^\dagger \hat{a}_{13})}, \\
 \hat{j}_-^{12} &= \sqrt{N - (\hat{a}_{12}^\dagger \hat{a}_{12} + \hat{a}_{13}^\dagger \hat{a}_{13})} \hat{a}_{12}, \\
 \hat{j}_z^{13} &= \hat{a}_{13}^\dagger \hat{a}_{13} - N/2, & \hat{J}_+^{13} &= \hat{a}_{13}^\dagger \sqrt{N - (\hat{a}_{12}^\dagger \hat{a}_{12} + \hat{a}_{13}^\dagger \hat{a}_{13})},
 \end{aligned}$$

$$\begin{aligned}
 \hat{j}_-^{13} &= \sqrt{N - (\hat{a}_{12}^\dagger \hat{a}_{12} + \hat{a}_{13}^\dagger \hat{a}_{13})} \hat{a}_{13}, \\
 \hat{J}_+^{23} &= \hat{a}_{12}^\dagger \hat{a}_{13}, & \hat{J}_-^{23} &= \hat{a}_{13}^\dagger \hat{a}_{12}. \tag{F1}
 \end{aligned}$$

In the  $N \rightarrow \infty$  limit, we can further approximate the pseudospin operators as

$$\begin{aligned}
 \hat{j}_z^D &= \hat{a}_{12}^\dagger \hat{a}_{12} - N/2, & \hat{J}_+^D &= \hat{a}_{12}^\dagger \sqrt{N}, & \hat{J}_-^D &= \sqrt{N} \hat{a}_{12}, \\
 \hat{j}_z^B &= \hat{a}_{13}^\dagger \hat{a}_{13} - N/2, & \hat{J}_+^B &= \hat{a}_{13}^\dagger \sqrt{N}, & \hat{J}_-^B &= \sqrt{N} \hat{a}_{13}, \\
 \hat{j}_+^{DB} &= \hat{a}_{12}^\dagger \hat{a}_{13}, & \hat{j}_-^{DB} &= \hat{a}_{13}^\dagger \hat{a}_{12}. \tag{F2}
 \end{aligned}$$



In an analog fashion for the driven three-level Dicke model we obtain the Hamiltonian with  $a_{12} \rightarrow d$  and  $a_{13} \rightarrow b$

$$\begin{aligned} H/\hbar = & \omega \hat{a}^\dagger \hat{a} + \omega_D \hat{d}^\dagger \hat{d} + \omega_B \hat{b}^\dagger \hat{b} + \lambda(\hat{a}^\dagger + \hat{a}) \\ & \times [(\hat{d}^\dagger + \hat{d}) - \phi(t)(\hat{b}^\dagger + \hat{b})] \\ & + \phi(t)(\omega_B - \omega_D)(\hat{d}^\dagger \hat{b} + \hat{b}^\dagger \hat{d}). \end{aligned} \quad (\text{F3})$$

The mean-field equations of motion for Eq. (F3) are

$$\begin{aligned} \frac{\partial a}{\partial t} &= -(i\omega - \kappa)a - i\lambda(d^* + d) + i\phi(t)\lambda(b^* + b), \\ \frac{\partial d}{\partial t} &= -i\omega_D d - i\lambda(a^* + a) - i(\omega_B - \omega_D)\phi(t)b, \\ \frac{\partial b}{\partial t} &= -i\omega_B b + i\phi(t)\lambda(a^* + a) - i(\omega_B - \omega_D)\phi(t)d. \end{aligned} \quad (\text{F4})$$

### APPENDIX G: LOWER POLARITON

Consider the standard closed Dicke model

$$\hat{H}/\hbar = \omega \hat{a}^\dagger \hat{a} + \omega_0 \hat{J}_z + \frac{2\lambda}{\sqrt{N}}(\hat{a}^\dagger + \hat{a})(\hat{J}_x). \quad (\text{G1})$$

In the thermodynamic limit, this can be diagonalized using the Holstein-Primakoff transformation, which leads to two polariton frequencies

$$\omega_{\text{LP},\kappa=0} = \left( \frac{\omega_0^2 + \omega^2}{2} - \frac{1}{2} \sqrt{(\omega_0^2 - \omega^2)^2 + 16\lambda^2 \omega \omega_0} \right)^{1/2}, \quad (\text{G2})$$

$$\omega_{\text{UP},\kappa=0} = \left( \frac{\omega_0^2 + \omega^2}{2} + \frac{1}{2} \sqrt{(\omega_0^2 - \omega^2)^2 + 16\lambda^2 \omega \omega_0} \right)^{1/2}. \quad (\text{G3})$$

The lower polariton frequency, Eq. (G2), is the upper bound in the presence of dissipation. When  $\kappa \neq 0$ , the lower polariton frequency can be numerically determined by exploiting the parametric resonance when the light-matter coupling is periodically driven [5,6]:

$$\lambda(t) = \lambda_0 [1 + f_0 \sin(\omega_{\text{dr}} t)]. \quad (\text{G4})$$

In the limit  $N \rightarrow \infty$ , the Hamiltonian can be reduced to a coupled oscillator, whereby the coupling strength is periodic in time. This possesses a parametric resonance manifesting as a resonance lobe centered at the primary resonance,  $\omega_{\text{dr}} = 2\omega_{\text{LP}}$ . Thus, we can determine  $\omega_{\text{LP}}$  by mapping the instability region for varying modulation parameters  $f_0$  and  $\omega_{\text{dr}}$ . To this

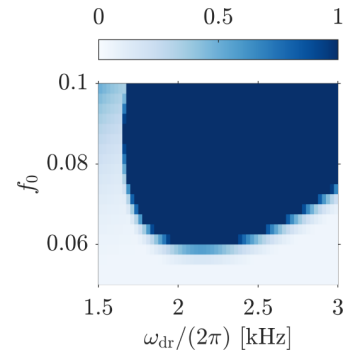


FIG. 9. Maximum value of  $(b + b^*)$ . The parameters are the same as those in Figs. 3(a)–3(d).

end, we solve the corresponding equations of motion given by

$$\begin{aligned} i \frac{\partial a}{\partial t} &= (\omega - i\kappa)a + \lambda(t)(b^* + b), \\ i \frac{\partial b}{\partial t} &= \omega_0 b + \lambda(t)(a^* + a). \end{aligned} \quad (\text{G5})$$

The unstable region indicating the parametric resonance is signalled by a diverging  $(b + b^*)$ , as depicted in Fig. 9. We obtain a lower polariton frequency  $\omega_{\text{LP}}/2\pi \approx 1.06$  kHz, which is the value used in the sum frequency condition denoted by the vertical line in Figs. 3(a)–(d).

### APPENDIX H: PARAMETERS

We consider realistic parameters based on the experimental setup in Ref. [35]. A BEC of  $N = 65 \times 10^3$   $^{87}\text{Rb}$  atoms is coupled to a high-finesse optical cavity with a photon loss rate of  $\kappa = 2\pi \times 3.6$  kHz. This is very close to the recoil frequency,  $\omega_{\text{rec}} = 2\pi \times 3.55$  kHz, associated with the standing-wave potential of the pump. The cavity light shift per atom is  $U_0 = -2\pi \times 0.36$  Hz. The effective pump-cavity detuning is fixed to  $\delta_{\text{eff}} = -2\pi \times 18.5$  kHz. We are interested in the two regimes  $\lambda < \lambda_{\text{cr}}$  and  $\lambda > \lambda_{\text{cr}}$ , where  $\lambda_{\text{cr}}$  is the critical light-matter coupling strength needed to enter the DW phase in the absence of modulation, where  $\lambda_{\text{cr}} = [(\kappa^2 + \omega^2)(\omega_D/\omega)]^{1/2}/2$ . By equating the expression for  $\lambda_{\text{cr}}$  and  $\lambda$  in terms of the atom-cavity parameters for the two-level Dicke model, we find that the critical pump strength is given by  $\epsilon_{\text{cr}} = 8(\omega^2 + \kappa^2)/[4N\omega|\Delta_0| + (\omega^2 + \kappa^2)]$ .

- [1] R. H. Dicke, Coherence in spontaneous radiation processes, *Phys. Rev.* **93**, 99 (1954).  
 [2] K. Baumann, C. Guerlin, F. Brennecke, and T. Esslinger, Dicke quantum phase transition with a superfluid gas in an optical cavity, *Nature (London)* **464**, 1301 (2010).  
 [3] J. Klinder, H. Keßler, M. Wolke, L. Mathey, and A. Hemmerich, Dynamical phase transition in the open Dicke model, *Proc. Natl. Acad. Sci. USA* **112**, 3290 (2015).

- [4] M. Hayn, C. Emary, and T. Brandes, Phase transitions and dark-state physics in two-color superradiance, *Phys. Rev. A* **84**, 053856 (2011).  
 [5] V. M. Bastidas, C. Emary, B. Regler, and T. Brandes, Nonequilibrium Quantum Phase Transitions in the Dicke Model, *Phys. Rev. Lett.* **108**, 043003 (2012).  
 [6] R. Chitra and O. Zilberberg, Dynamical many-body phases of the parametrically driven, dissipative Dicke model, *Phys. Rev. A* **92**, 023815 (2015).

- [7] Z. Zhiqiang, C. H. Lee, R. Kumar, K. J. Arnold, S. J. Masson, A. S. Parkins, and M. D. Barrett, Nonequilibrium phase transition in a spin-1 Dicke model, *Optica* **4**, 424 (2017).
- [8] M. Soriente, T. Donner, R. Chitra, and O. Zilberberg, Dissipation-Induced Anomalous Multicritical Phenomena, *Phys. Rev. Lett.* **120**, 183603 (2018).
- [9] E. I. Rodríguez Chiacchio and A. Nunnenkamp, Dissipation-Induced Instabilities of a Spinor Bose-Einstein Condensate Inside an Optical Cavity, *Phys. Rev. Lett.* **122**, 193605 (2019).
- [10] B. Buča and D. Jaksch, Dissipation Induced Nonstationarity in a Quantum Gas, *Phys. Rev. Lett.* **123**, 260401 (2019).
- [11] K. C. Stitely, S. J. Masson, A. Giraldo, B. Krauskopf, and S. Parkins, Superradiant switching, quantum hysteresis, and oscillations in a generalized Dicke model, *Phys. Rev. A* **102**, 063702 (2020).
- [12] H. Habibian, A. Winter, S. Paganelli, H. Rieger, and G. Morigi, Bose-Glass Phases of Ultracold Atoms Due to Cavity Backaction, *Phys. Rev. Lett.* **110**, 075304 (2013).
- [13] C. Kollath, A. Sheikhan, S. Wolff, and F. Brennecke, Ultracold Fermions in a Cavity-Induced Artificial Magnetic Field, *Phys. Rev. Lett.* **116**, 060401 (2016).
- [14] F. Mivehvar, F. Piazza, and H. Ritsch, Disorder-Driven Density and Spin Self-Ordering of a Bose-Einstein Condensate in a Cavity, *Phys. Rev. Lett.* **119**, 063602 (2017).
- [15] V. D. Vaidya, Y. Guo, R. M. Kroeze, K. E. Ballantine, A. J. Kollár, J. Keeling, and B. L. Lev, Tunable-Range, Photon-Mediated Atomic Interactions in Multimode Cavity QED, *Phys. Rev. X* **8**, 011002 (2018).
- [16] M. Landini, N. Dogra, K. Kroeger, L. Hruby, T. Donner, and T. Esslinger, Formation of a Spin Texture in a Quantum Gas Coupled to a Cavity, *Phys. Rev. Lett.* **120**, 223602 (2018).
- [17] N. Dogra, M. Landini, K. Kroeger, L. Hruby, T. Donner, and T. Esslinger, Dissipation-induced structural instability and chiral dynamics in a quantum gas, *Science* **366**, 1496 (2019).
- [18] G. Bentsen, I.-D. Potirniche, V. B. Bulchandani, T. Scaffidi, X. Cao, X.-L. Qi, M. Schleier-Smith, and E. Altman, Integrable and Chaotic Dynamics of Spins Coupled to an Optical Cavity, *Phys. Rev. X* **9**, 041011 (2019).
- [19] S. B. Jäger, M. J. Holland, and G. Morigi, Superradiant optomechanical phases of cold atomic gases in optical resonators, *Phys. Rev. A* **101**, 023616 (2020).
- [20] K.-J. Boller, A. Imamoglu, and S. E. Harris, Observation of Electromagnetically Induced Transparency, *Phys. Rev. Lett.* **66**, 2593 (1991).
- [21] M. Fleischhauer, A. Imamoglu, and J. P. Marangos, Electromagnetically induced transparency: Optics in coherent media, *Rev. Mod. Phys.* **77**, 633 (2005).
- [22] M. O. Scully, S.-Y. Zhu, and A. Gavrielides, Degenerate Quantum-Beat Laser: Lasing without Inversion and Inversion without Lasing, *Phys. Rev. Lett.* **62**, 2813 (1989).
- [23] J. Mompert and R. Corbalán, Lasing without inversion, *J. Opt. B: Quantum Semiclassical Opt.* **2**, R7 (2000).
- [24] U. Gaubatz, P. Rudecki, S. Schieman, and K. Bergmann, Population transfer between molecular vibrational levels by stimulated Raman scattering with partially overlapping laser fields. A new concept and experimental results, *J. Chem. Phys.* **92**, 5363 (1990).
- [25] N. V. Vitanov, A. A. Rangelov, B. W. Shore, and K. Bergmann, Stimulated Raman adiabatic passage in physics, chemistry, and beyond, *Rev. Mod. Phys.* **89**, 015006 (2017).
- [26] C. C. Sung and C. M. Bowden, Phase transition in the multimode two- and three-level Dicke model (Green's function method), *J. Phys. A: Math. Gen.* **12**, 2273 (1979).
- [27] A. Crubellier, S. Liberman, D. Pavolini, and P. Pillet, Superradiance and subradiance. I. Interatomic interference and symmetry properties in three-level systems, *J. Phys. B: At. Mol. Phys.* **18**, 3811 (1985).
- [28] A. Crubellier and D. Pavolini, Superradiance and subradiance. II. Atomic systems with degenerate transitions, *J. Phys. B: At. Mol. Phys.* **19**, 2109 (1986).
- [29] M. M. Cola, D. Bigerni, and N. Piovella, Recoil-induced subradiance in an ultracold atomic gas, *Phys. Rev. A* **79**, 053622 (2009).
- [30] P. Wolf, S. C. Schuster, D. Schmidt, S. Slama, and C. Zimmermann, Observation of Subradiant Atomic Momentum States with Bose-Einstein Condensates in a Recoil Resolving Optical Ring Resonator, *Phys. Rev. Lett.* **121**, 173602 (2018).
- [31] H. Georgi, *Lie Algebras In Particle Physics from Isospin To Unified Theories* (Taylor & Francis, Boca Raton, 2000).
- [32] W. Marciano and H. Pagels, Quantum chromodynamics, *Phys. Rep.* **36**, 137 (1978).
- [33] D. J. Griffiths, *Introduction to Elementary Particles* (Wiley, New York, 2008).
- [34] J. G. Cosme, J. Skulte, and L. Mathey, Time crystals in a shaken atom-cavity system, *Phys. Rev. A* **100**, 053615 (2019).
- [35] P. Kongkhambut, H. Keßler, J. Skulte, L. Mathey, J. G. Cosme, and A. Hemmerich, Realization of a periodically driven open Three-Level Dicke model, *Phys. Rev. Lett.* **127**, 253601 (2021).
- [36] J. J. Sakurai and J. Napolitano, *Modern Quantum Mechanics*, 2nd ed. (Cambridge University Press, Cambridge, 2017).
- [37] A. Baksic, P. Nataf, and C. Ciuti, Superradiant phase transitions with three-level systems, *Phys. Rev. A* **87**, 023813 (2013).
- [38] F. Dimer, B. Estienne, A. S. Parkins, and H. J. Carmichael, Proposed realization of the Dicke-model quantum phase transition in an optical cavity QED system, *Phys. Rev. A* **75**, 013804 (2007).
- [39] P. Kirton, M. M. Roses, J. Keeling, and E. G. Dalla Torre, Introduction to the Dicke model: From equilibrium to nonequilibrium, and vice versa, *Adv. Quantum Technol.* **2**, 1800043 (2019).
- [40] F. Mivehvar, F. Piazza, T. Donner, and H. Ritsch, Cavity QED with quantum gases: New paradigms in many-body physics, *Adv. Phys.* **70**, 1 (2021).
- [41] H. Ritsch, P. Domokos, F. Brennecke, and T. Esslinger, Cold atoms in cavity-generated dynamical optical potentials, *Rev. Mod. Phys.* **85**, 553 (2013).
- [42] J. G. Cosme, C. Georges, A. Hemmerich, and L. Mathey, Dynamical Control of Order in a Cavity-BEC System, *Phys. Rev. Lett.* **121**, 153001 (2018).
- [43] C. Georges, J. G. Cosme, L. Mathey, and A. Hemmerich, Light-Induced Coherence in an Atom-Cavity System, *Phys. Rev. Lett.* **121**, 220405 (2018).
- [44] H. Keßler, J. G. Cosme, M. Hemmerling, L. Mathey, and A. Hemmerich, Emergent limit cycles and time crystal dynamics in an atom-cavity system, *Phys. Rev. A* **99**, 053605 (2019).

- [45] H. Keßler, J. G. Cosme, C. Georges, L. Mathey, and A. Hemmerich, From a continuous to a discrete time crystal in a dissipative atom-cavity system, *New J. Phys.* **22**, 085002 (2020).
- [46] H. Keßler, P. Kongkhambut, C. Georges, L. Mathey, J. G. Cosme, and A. Hemmerich, Observation of a Dissipative Time Crystal, *Phys. Rev. Lett.* **127**, 043602 (2021).
- [47] C. Georges, J. G. Cosme, H. Keßler, L. Mathey, and A. Hemmerich, Dynamical density wave order in an atom-cavity system, *New J. Phys.* **23**, 023003 (2021).
- [48] D. Fausti, R. I. Tobey, N. Dean, S. Kaiser, A. Dienst, M. C. Hoffmann, S. Pyon, T. Takayama, H. Takagi, and A. Cavalleri, Light-induced superconductivity in a stripe-ordered cuprate, *Science* **331**, 189 (2011).
- [49] W. Hu, S. Kaiser, D. Nicoletti, C. R. Hunt, I. Gierz, M. C. Hoffmann, M. Le Tacon, T. Loew, B. Keimer, and A. Cavalleri, Optically enhanced coherent transport in  $\text{YBa}_2\text{Cu}_3\text{O}_{6.5}$  by ultrafast redistribution of interlayer coupling, *Nat. Mater.* **13**, 705 (2014).
- [50] R. Mankowsky, A. Subedi, M. Först, S. O. Mariager, M. Chollet, H. T. Lemke, J. S. Robinson, J. M. Glowia, M. P. Minitti, A. Frano, M. Fechner, N. A. Spaldin, T. Loew, B. Keimer, A. Georges, and A. Cavalleri, Nonlinear lattice dynamics as a basis for enhanced superconductivity in  $\text{YBa}_2\text{Cu}_3\text{O}_{6.5}$ , *Nature (London)* **516**, 71 (2014).
- [51] S. J. Denny, S. R. Clark, Y. Laplace, A. Cavalleri, and D. Jaksch, Proposed Parametric Cooling of Bilayer Cuprate Superconductors by Terahertz Excitation, *Phys. Rev. Lett.* **114**, 137001 (2015).
- [52] J.-i. Okamoto, A. Cavalleri, and L. Mathey, Theory of Enhanced Interlayer Tunneling in Optically Driven High- $T_c$  Superconductors, *Phys. Rev. Lett.* **117**, 227001 (2016).
- [53] G. Homann, J. G. Cosme, J. Okamoto, and L. Mathey, Higgs mode mediated enhancement of interlayer transport in high- $T_c$  cuprate superconductors, *Phys. Rev. B* **103**, 224503 (2021).
- [54] G. Homann, J. G. Cosme, and L. Mathey, Higgs time crystal in a high- $T_c$  superconductor, *Phys. Rev. Research* **2**, 043214 (2020).
- [55] R. Lin, R. Rosa-Medina, F. Ferri, F. Finger, K. Kroeger, T. Donner, T. Esslinger, and R. Chitra, Dissipation-engineered family of nearly dark states in many-body cavity-atom systems, [arXiv:2109.00422](https://arxiv.org/abs/2109.00422).
- [56] C. Emary and T. Brandes, Chaos and the quantum phase transition in the Dicke model, *Phys. Rev. E* **67**, 066203 (2003).
- [57] M. Wagner, A nonlinear transformation of  $\text{SU}(3)$ -spin-operators to bosonic operators, *Phys. Lett. A* **53**, 1 (1975).

### 4.3 Publication IV: Condensate formation in a dark state of a driven atom-cavity system

Publication IV considers experimental work using a shaken optical standing wave pump potential to drive the atom-cavity system, similarly as publications II and III. While focusing on the incommensurate time crystalline dynamics in publication II, we observed here a peculiar phenomenon that for some range of modulation parameters, the atomic density remains localized in the checkerboard pattern while there is no intra-cavity light field detected. This unexpected observation drew our attention to further investigate this parameter regime. We concluded that this phenomenon occurs as the atomic ensemble localizes at light shift potential maxima, and thus, decouples from the pump and cavity field. The atoms form a condensate in a dark state of the atom-cavity system. The dark state is a state which suppresses scattering from the pump into the cavity and vice versa, i.e., the state formed by an admixture of  $|BEC\rangle$  and  $|BDW\rangle$  states cannot scatter light because its density maxima are localized at the pump field's nodes, see section 3.3 and fig. 3.2. Publication IV concludes that there is a parameter regime, where the ITC described in publication III has a transient behavior, as eventually atoms are transferred to a dark state of the atom-cavity system.

To obtain an improved terminology that fits the observation of the dark state, the three levels introduced in publication II are renamed. The ground state  $|BEC\rangle$  is called the normal state  $|N\rangle$ , the density wave state  $|DW\rangle$  is called the bright state  $|B\rangle$ . The bond density wave state  $|BDW\rangle$  is called the dark state  $|D\rangle$ .

#### Status of the publication:

This article was published in April 2023 in Physical Review Letters [5]. The corresponding supplemental material can be found in appendix C. Moreover, fig. 1(a) of publication IV is selected by the editor team to be on the cover of the journal Physical Review Letters volume 130 issue 16.

#### Note:

Due to a mismatch between notation used in different publications and this thesis, I would like to improve the readability of the publication by listing the notation changes in table 4.3.

parameters	this thesis	publication IV
pump strength	$\epsilon_p$	$\epsilon$
phase of the standing wave pump potential	$\phi_p$	$\phi$
phase difference of the intra-cavity and the pump fields	$\phi_c$	$\varphi$
ground state of three-level Dicke model	$ BEC\rangle$	normal state $ N\rangle$
density wave state	$ DW\rangle$	bright state $ B\rangle$
bond density wave state	$ BDW\rangle$	dark state $ D\rangle$

Table 4.3: Notation differences between this thesis and publication IV.

## Condensate Formation in a Dark State of a Driven Atom-Cavity System

Jim Skulte<sup>1,2,\*</sup>, Phatthamon Kongkhambut<sup>1,\*</sup>, Sahana Rao<sup>1</sup>, Ludwig Mathey<sup>1,2</sup>, Hans Keßler<sup>1</sup>,  
Andreas Hemmerich<sup>1,2</sup> and Jayson G. Cosme<sup>3</sup>

<sup>1</sup>Zentrum für Optische Quantentechnologien and Institut für Laser-Physik, Universität Hamburg, 22761 Hamburg, Germany

<sup>2</sup>The Hamburg Center for Ultrafast Imaging, Luruper Chaussee 149, 22761 Hamburg, Germany

<sup>3</sup>National Institute of Physics, University of the Philippines, Diliman, Quezon City 1101, Philippines



(Received 6 September 2022; accepted 14 March 2023; published 21 April 2023)

We demonstrate the formation of a condensate in a dark state of momentum states, in a pumped and shaken cavity-BEC system. The system consists of an ultracold quantum gas in a high-finesse cavity, which is pumped transversely by a phase-modulated laser. This phase-modulated pumping couples the atomic ground state to a superposition of excited momentum states, which decouples from the cavity field. We demonstrate how to achieve condensation in this state, supported by time-of-flight and photon emission measurements. With this, we show that the dark state concept provides a general approach to efficiently prepare complex many-body states in an open quantum system.

DOI: [10.1103/PhysRevLett.130.163603](https://doi.org/10.1103/PhysRevLett.130.163603)

While dissipation is in general perceived as a destructive feature of a quantum system, it can also be utilized to engineer nontrivial states, often in conjunction with driving a system out of equilibrium. A prominent experimental platform for this purpose is ultracold quantum gases coupled to high-finesse optical cavities [1–4], due to the well-controlled dissipative channel resulting from the photon emission out of the cavity. Paradigmatic models of light-matter interaction can be explored, such as the celebrated Dicke model that describes the interaction between  $N$  two-level atoms with a single quantized light mode [5]. The driven-dissipative Dicke model, an extension of the standard Dicke model, captures the scenario, when both external driving and dissipation are present [6,7]. A wealth of phases, unique to driven light-matter systems, have been proposed and realized using variations of driven Dicke models, such as the three-level Dicke model [8–20]. In particular, the dissipation channel of the cavity has been utilized to demonstrate the emergence of nonequilibrium or dynamical phases [19,21–35].

An intriguing class of quantum states in light-matter systems, well known in quantum optics, are the so-called dark states [36]. These are superpositions of matter states with relative phases such that the quantum mechanical amplitudes, coupling the different sectors to an irradiated light field, interfere destructively. As a consequence, dark states decouple from the light field. Dark states play a crucial role in physical phenomena, such as stimulated Raman adiabatic passage [37,38], electromagnetically induced transparency [39,40], lasing without inversion [41,42], and combinations of these topics [9,20,43,44]. In conventional quantum optics scenarios, dark states typically arise on a single-particle level. In this Letter, we use the dark state concept in a many-body context,

specifically condensation. Our study suggests how the concept of dark state formation can be utilized in the context of quantum state engineering via dissipation.

In this Letter, we demonstrate in theory and experiment a robust condensate formation in a dark state of a driven atom-cavity system, approximately described by a parametrically driven three-level open Dicke model introduced in Refs. [17,19]. We consider a Bose-Einstein condensate (BEC) prepared in a high-finesse cavity, which is transversely pumped with a shaken one-dimensional optical lattice, as sketched in Fig. 1(a). Previously, we explored the weakly resonantly driven scenario leading to an incommensurate time crystal (ITC) [17,19,26]. Here, technical improvements in our setup allowed us to study theoretically and experimentally the so far unexplored regime of strong driving and a wider range of driving frequencies, which reveals that the ITC has transient character in certain parameter regimes, such that the atoms relax into a dark state of the atom-cavity system eventually.

To understand the dark state and to identify the relevant driving parameters, we employ the time-dependent atom-cavity Hamiltonian in Refs. [17,45] and an approximative parametrically driven three-level Dicke model [17,19], which includes only three atomic modes denoted as  $|N\rangle$ ,  $|B\rangle$ , and  $|D\rangle$ , in a plane-wave expansion of the atomic field operator. These modes are illustrated in terms of their momentum components in Fig. 1(b) and form the V-shaped three-level system sketched in Fig. 1(c). The normal state  $|N\rangle \equiv |(0, 0)\hbar k\rangle$  corresponds to a homogeneous density in real space, wherein all atoms occupy the lowest momentum mode  $\{p_y, p_z\} = \{0, 0\}\hbar k$  ( $k$  is the wave number of the pump field). The pump leads to a light shift of  $-\epsilon_p \omega_{\text{rec}}/2$ , where  $\epsilon_p$  is the unitless pump intensity and  $\omega_{\text{rec}}$  is the atomic



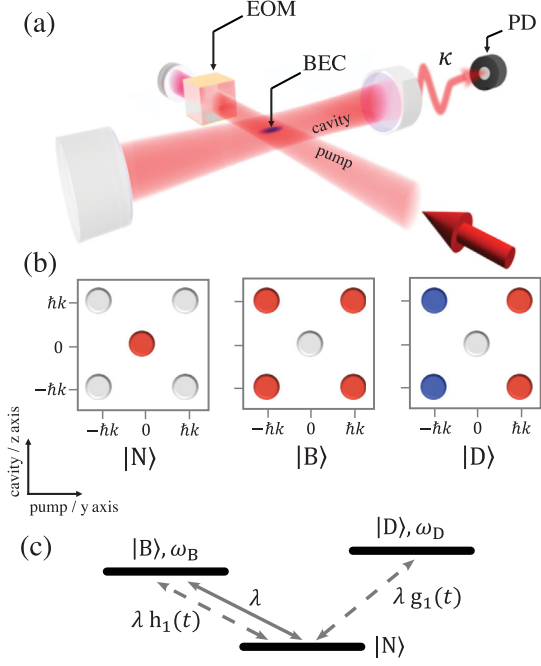


FIG. 1. (a) Sketch of the experimental setup. An electro-optical modulator (EOM) is used to modulate the phase of the pump field, which results in shaking the pump potential. The light leaking out the cavity is detected using a photo diode (PD). (b) Sketch of the momentum distribution of the three relevant superpositions of momentum modes, the normal state  $|N\rangle$ , the bright state  $|B\rangle$ , and the dark state  $|D\rangle$ , which form a three-level Dicke model shown in (c) with the atom-cavity coupling  $\lambda$  and the shaking-induced functions  $h_1(t)$  and  $g_1(t)$ . The colors in (b) represent the phase of the momentum states, where blue indicates a phase shift of  $\pi$  relative to red.

recoil frequency. The bright state  $|B\rangle \equiv \sum_{\nu, \mu \in \{-1, 1\}} |\nu \hbar k, \mu \hbar k\rangle$  is defined as the in-phase superposition of the  $\{\pm 1, \pm 1\} \hbar k$  momentum modes as depicted in Fig. 1(b). The real-space wave function of this state is  $\propto \cos(ky) \cos(kz)$ , which has even parity with respect to the inversion  $(y, z) \rightarrow (-y, -z)$ . It exhibits a kinetic energy of  $2E_{\text{rec}}$  and is light shifted by the pump wave by  $-3\epsilon_p \omega_{\text{rec}}/4$  such that its frequency separation relative to  $|N\rangle$  is  $\omega_B = (2 - \epsilon_p/4)\omega_{\text{rec}}$ . The dark state  $|D\rangle \equiv \sum_{\nu, \mu \in \{-1, 1\}} \nu |\nu \hbar k, \mu \hbar k\rangle$  is defined as the out-of-phase superposition of the  $\{+1, \pm 1\} \hbar k$  and  $\{-1, \pm 1\} \hbar k$  momentum modes. In real space, its order parameter is  $\propto \sin(ky) \cos(kz)$ , which has odd parity under the inversion  $(y, z) \rightarrow (-y, -z)$ .

The density distributions of the dark state  $|D\rangle$  and the bright state  $|B\rangle$  both prohibit collective scattering of photons into the cavity. Nonetheless, any admixture of the normal state  $|N\rangle$  to the bright state  $|B\rangle$  leads to a checkerboard pattern of the atomic density that allows pump photons to scatter into the cavity, which is the reason we refer to  $|B\rangle$  as a bright state. Above a critical pump strength, the system forms a superradiant (SR) phase as its stationary state, in which a superposition of  $|B\rangle$  and  $|N\rangle$

produces a density grating trapped by the intracavity optical lattice composed of the pump and cavity fields. In contrast to  $|B\rangle$ , the density grating of the dark state  $|D\rangle$ , due to its odd parity is shifted along the pump direction by a quarter of the pump wavelength, such that the atomic positions coincide with the nodes of the pump lattice, motivating our terminology of bond-density waves in Refs. [17,19]. Hence, even if  $|N\rangle$  is admixed to the dark state  $|D\rangle$ , scattering of pump photons remains suppressed, meaning that for any superposition of the normal and the dark state collective scattering of photons into the cavity cannot occur. The dark state  $|D\rangle$  exhibits the same kinetic energy  $2E_{\text{rec}}$  as  $|B\rangle$ , while its light shift due to the pump lattice is only  $-\epsilon_p \omega_{\text{rec}}/4$ . Thus, its frequency relative to that of  $|N\rangle$  is  $\omega_D = (2 + \epsilon_p/4)\omega_{\text{rec}}$ .

To excite the dark state, we shake the pump lattice by introducing a time-dependent phase in the pump field,  $\cos(ky + \phi(t))$ , where  $\phi(t) = f_0 \sin(\omega_{\text{dr}} t)$ ,  $f_0$  is the driving strength, and  $\omega_{\text{dr}}$  is the driving frequency. The excitation mechanism is readily understood by means of the three-level Dicke model  $\hat{H} = \hat{H}_{\text{stat}} + \hat{H}_{\text{dyn}}$  with a static part,

$$\hat{H}_{\text{stat}}/\hbar = \omega \hat{a}^\dagger \hat{a} + [\omega_B - \Omega(f_0)] \hat{J}_z^B + [\omega_D + \Omega(f_0)] \hat{J}_z^D + \frac{2\lambda}{\sqrt{N_a}} (\hat{a}^\dagger + \hat{a}) J_0(f_0) \hat{J}_x^B, \quad (1)$$

and a dynamical part,

$$\hat{H}_{\text{dyn}}/\hbar = h_2(t) \Delta\omega_{BD} (\hat{J}_z^D - \hat{J}_z^B) + 2g_2(t) \Delta\omega_{BD} \hat{J}_x^{BD} + \frac{4\lambda}{\sqrt{N_a}} (\hat{a}^\dagger + \hat{a}) [h_1(t) \hat{J}_x^B - g_1(t) \hat{J}_x^D], \quad (2)$$

where  $\Omega(f_0) = (\epsilon_p \omega_{\text{rec}}/4)[1 - J_0(2f_0)]$ ,  $\Delta\omega_{BD} = (\omega_B - \omega_D)$ ,  $h_m(t) = \sum_{n=1}^{\infty} J_{2n}(mf_0) \cos(2n\omega_{\text{dr}} t)$ ,  $g_m(t) = \sum_{n=1}^{\infty} J_{2n-1}(mf_0) \sin[(2n-1)\omega_{\text{dr}} t]$ , and  $J_n(r)$  is the  $n$ th Bessel function of the first kind. The time-dependent terms introduced by the pump lattice shaking are  $h_m(t)$  and  $g_m(t)$ . Details on the derivation of this Hamiltonian are given in the Supplemental Material [45]. The pseudospin operators  $\hat{J}_\mu^B$  ( $\mu \in \{x, y, z\}$ ) describe the coupling to the bright state since  $\hat{J}_+^B \equiv \hat{J}_x^B + i\hat{J}_y^B = |B\rangle\langle N|$ . Accordingly,  $\hat{J}_\mu^D$  is related to the dark state as  $\hat{J}_+^D \equiv \hat{J}_x^D + i\hat{J}_y^D = |D\rangle\langle N|$ . We see from the last term of Eq. (2) that  $|D\rangle$  can be coupled to the cavity mode via the time-dependent shaking of the pump, resulting in a periodic coupling between  $|D\rangle$  and  $|N\rangle$ . Note that the necessary nonzero amplitude  $g_1(t)$  can be provided by phase modulation, which breaks the discrete translation symmetry along the pump axis, but not by amplitude modulation. We consider the recoil-resolved regime, i.e., the loss rate of the cavity photons  $\kappa$  is comparable to the recoil frequency  $\omega_{\text{rec}}$ , which for our system is  $\omega_{\text{rec}} = 2\pi \times 3.6$  kHz. We emphasize the importance of this regime [48,49] to

protect the dark state from detrimental resonant excitations to higher energy momentum states.

Next, we discuss the dynamics of the system by solving the semiclassical equations of motion of the three-level model Eq. (2) and those of the atom-cavity Hamiltonian [45] including fluctuations due to photon emission out of the cavity. For the three-level model, the dark state occupation is  $\langle \hat{J}^D \rangle + 1/2$ . For the full atom-cavity model, we apply the following protocol: the pump laser strength is linearly increased within 10 ms, such that we always initially prepare the SR phase. After a holding time of 0.5 ms, the phase of the pump lattice is modulated for 7 driving cycles, starting at  $t = t_0$ . We choose 7 driving cycles since, as is later seen in the experiment, the dark state occupation  $N_D$  is found to equilibrate after 6 driving cycles due to heating [45]. Subsequently, we adiabatically ramp-down the pump strength in 0.5 ms and calculate  $N_D$  as the sum of the occupations in the  $\{\pm 1, \pm 1\} \hbar k$  modes. The ramp-down is necessary to remove all  $\{\pm 1, \pm 1\} \hbar k$  populations, associated with  $|B\rangle$  rather than  $|D\rangle$ , by transferring  $|B\rangle$  into  $|N\rangle$ , which does not affect  $|D\rangle$ . In Fig. 2, we construct the phase diagrams of the three-level and the full models, plotting  $N_D$  for different driving parameters. Our previous work on the emergence of an ITC involved the regime around  $\omega_{\text{dr}} \in [1, 1.2] \times \omega_D$  and  $f_{0,\text{theory}} < 0.4$  [17,19]. We find qualitative agreement between the numerical simulations of the full atom-cavity system and the driven three-level Dicke model as seen in Fig. 2. Significant occupation of the dark state is observed in a large area of the phase diagram for  $\omega_{\text{dr}} > \omega_D$  and also in a small area close to the resonance  $\omega_{\text{dr}} \approx \omega_D$ . We note that the area in the driving parameter space, where the dark state becomes dynamically occupied, is larger in the full atom-cavity model as compared to the three-level Dicke model. This can be attributed to the  $\{0, \pm 2\} \hbar k$  and  $\{\pm 2, 0\} \hbar k$  modes,

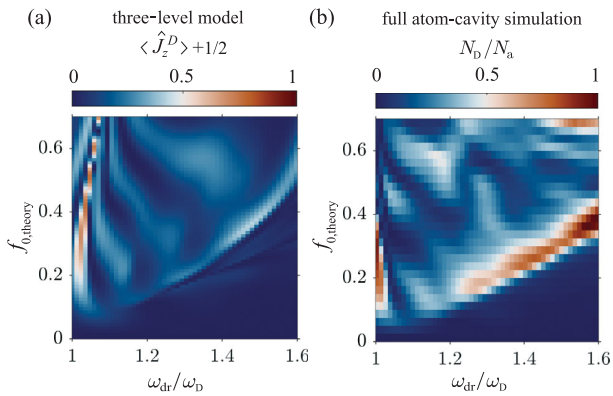


FIG. 2. (a),(b) Population of the dark state for different driving frequencies  $\omega_{\text{dr}}$  and driving strengths  $f_{0,\text{theory}}$ . The driving frequency axis is rescaled by the characteristic frequency of the dark state  $\omega_D$ . (a) The results from the three-level model and (b) the full atom-cavity simulation. The phase diagrams are constructed for 7 driving cycles.

which are neglected in the three-level model [45]. Atoms in these modes may be transferred to the dark state upon scattering photons into the cavity, thus increasing its efficient population. This process competes with a direct resonant transfer of atoms into the second band of the pump wave without scattering photons into the cavity, which impedes efficient population of the dark state as detailed in the Supplemental Material [45]. The respective resonance frequency arises in Fig. 2 for  $\omega_{\text{dr}}/\omega_D \approx 1.7$ , i.e., slightly outside the shown range.

Next, we employ the truncated Wigner approximation (TWA) to capture the leading-order quantum effects [26,50–52]. We include not only the dissipation due to photon emission out of the cavity but also the associated fluctuations. We further demonstrate that the observed dark state is indeed a finite momentum condensate by calculating the eigenvalues of the single-particle correlation function at equal time,  $\langle \Psi(y, z)^\dagger \Psi(y', z') \rangle$ , for our full atom-cavity model. This appears in the Penrose-Onsager criterion for condensates, and its largest eigenvalue corresponds to the condensate fraction [53]. We denote the eigenvalues as  $n_{\text{NO}}$ . We show in Fig. 3(a) the  $n_{\text{NO}}$  obtained from TWA simulations for the same pump protocol used in Fig. 2(b), but without the final ramp-down of the pump wave. When the system enters the SR phase (at about 5.2 ms), the condensate fragments manifested in the

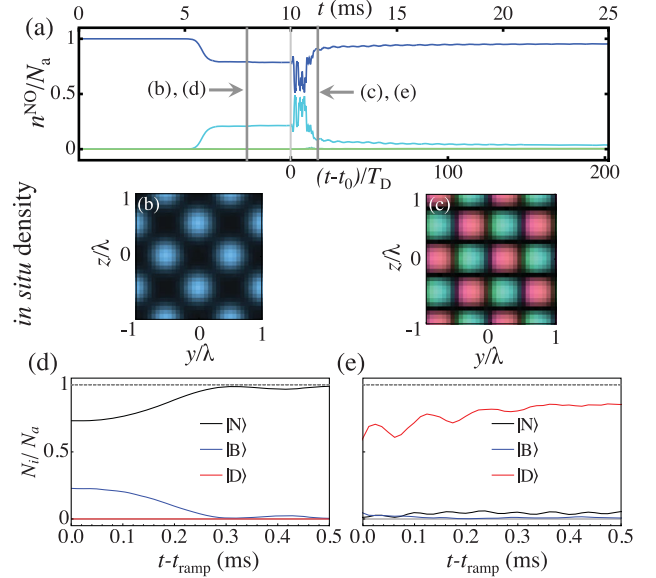


FIG. 3. (a) Simulations of the evolution of the three highest eigenvalues of the single-particle correlation function are shown. Gray dashed and solid vertical lines denote, respectively, the times when the snapshots of the single-particle densities in (b) and (c) are taken. The real-space densities in (b) and (c) are color coded to show the phase of  $\Psi(y, z)$ . (d),(e) Evolution of the occupations of  $|N\rangle$ ,  $|B\rangle$ , and  $|D\rangle$ , while the pump is adiabatically ramped down. Panels (d) and (e), respectively, correspond to initial conditions according to the dashed and solid gray vertical lines in (a).

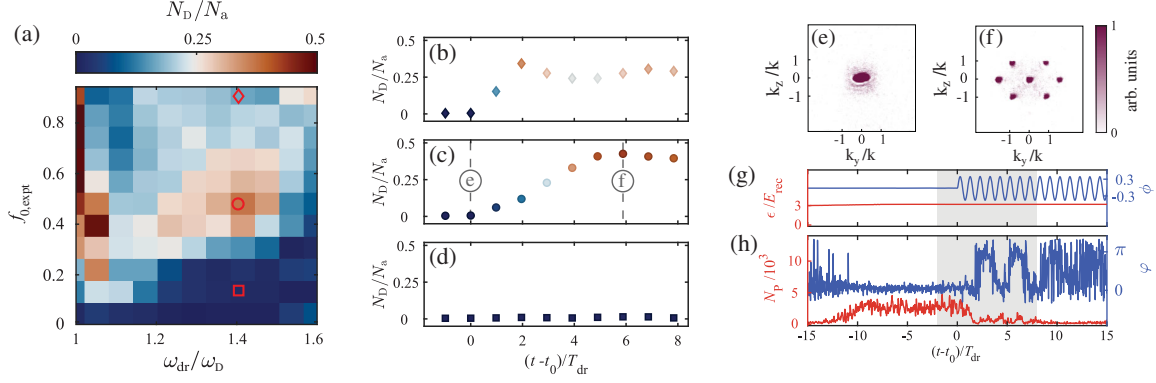


FIG. 4. Experimental phase diagram of the population of the dark state for different driving frequencies  $\omega_{dr}$  and driving strengths  $f_{0,exp}$ . The driving frequency axis is rescaled by the characteristic frequency of the dark state  $\omega_D$ . The phase diagram is constructed for 6 driving cycles. (b)–(d) Population of the dark state as a function of the driving cycles for the parameter sets marked by a diamond, a circle, and a rectangle in (a). The population of the dark state is rescaled by the total particle number  $N_a$  for different driving cycles derived from time-of-flight (TOF) images in (b)–(d). Examples of TOF images are provided before shaking starts at  $t = 0$  (e) and after around 6 driving cycles (f). All TOF images are obtained after an adiabatic ramp-down of the pump wave and ballistic expansion of 25 ms. (g) Time sequence for the pump strength (red) and the phase  $\phi$  of the pump field (blue). (h) Phase difference  $\varphi$  between the pump and intracavity field (blue) and intracavity photon number  $N_P$  (red) for the driving parameters marked by a circle in (a).

reduction of the largest eigenvalue and the corresponding increase of the second largest eigenvalue [54]. The real-space density  $|\Psi(y, z)|^2$  shown in Fig. 3(b) illustrates the prevailing SR phase at the time indicated by the dashed gray line, before driving starts at  $t = t_0$ . In Fig. 3(c), we show  $|\Psi(y, z)|^2$  at the time indicated by the solid gray line, after driving has acted for about 0.6 ms, indicating a substantial population of the dark state. The zeros (black regions) coincide with the intensity maxima of the pump lattice along the  $y$  direction, while there is no significant standing wave potential along the cavity direction. The different colors in Fig. 3(c) denote opposite phases of  $\Psi(y, z)$ . In Figs. 3(d) and 3(e), we show the occupations of the relevant states as the pump lattice is ramped down at the times indicated by the dashed [Fig. 3(d)] and solid [Fig. 3(e)] gray lines. It can be seen in Fig. 3(d) that for the SR phase [prevailing at the time denoted by the dashed vertical line in Fig. 3(a)] practically all atoms are transferred back to the normal state  $|N\rangle$  after the ramp-down. On the other hand, for the driven case in Fig. 3(e), associated with the time indicated by the solid gray line in Fig. 3(a), the dark state  $|D\rangle$  has the largest occupation at  $t = t_{\text{ramp}}$ . After the ramp-down, its occupation increases further, forming a long-lived state, compared to the decay time of the SR state. These results corroborate that the population of the  $\{\pm 1, \pm 1\}\hbar k$  modes after the pump is adiabatically switched off is the appropriate observable to quantify the *in situ* occupation of the dark state.

Finally, we experimentally demonstrate driving-induced condensation into a dark state of the atom-cavity system [45]. We present in Fig. 4(a) the resulting experimental phase diagram of the occupation of  $N_D$  for varying driving parameters. We find qualitative agreement with the theoretical phase diagrams depicted in Fig. 2. For technical

reasons, such as atom losses, a complete population inversion into the dark state, as seen in the numerical simulations, is not observed in the experiment. We note that there is a slight difference between the numerical and the experimental results for the driving strength needed to populate the dark state. This can possibly be attributed to the pump in the experiment having a nonzero width in frequency space, so that the effective pump power is smaller than it would be for monochromatic pump beam. Therefore, the experimental realization might require a nominally larger pump power than in the theoretical model.

Figures 4(b)–4(d) show the occupation of the dark state for varying numbers of driving cycles and fixed driving frequencies. Each panel corresponds to a value of the driving strength  $f_{0,exp}$  indicated by the red markers in Fig. 4(a). Between the red circular and the red rectangular marker, there is a sharp transition from large occupation of  $|D\rangle$  [see also Fig. 4(c)] toward a region where  $|D\rangle$  is practically unoccupied [see also Fig. 4(d)]. In the limit of strong driving around the diamond-shaped marker in Fig. 4(a), the dark state becomes highly occupied after only 2 driving cycles, but the occupation number slightly decreases again for larger numbers of driving cycles as shown in Fig. 4(b). This is explained by the excitation of the  $|\pm 2\hbar k, 0\rangle$  modes, as discussed below. Each data point is obtained via averaging over 10 TOF images. We also present the corresponding TOF images [see Figs. 4(e) and 4(f)] at two instances of time, i.e., at  $t = t_0$  before driving is started and after six driving cycles at  $t = t_0 + 6T_{dr}$  as indicated in Fig. 4(c). These TOF images correspond to the spatial orders calculated in Figs. 3(d) and 3(e). We display the time evolution of the cavity field for a single experimental realization in Fig. 4(h) showcasing the



vanishing intracavity light field as a macroscopic fraction of the atoms occupy the dark state.

For the case depicted in Fig. 4(c), we find that initially  $N_D$  increases and saturates beyond 6 driving cycles. The system approaches a steady state because of atom losses before all atoms can be transferred into the dark state. In contrast to the SR phase in Fig. 4(e), the large occupation of the four momentum components  $\{\pm 1, \pm 1\}\hbar k$  in Fig. 4(f) in combination with the small intracavity photon number in Fig. 4(h) indicates a large occupation of the dark state  $|D\rangle$ . Furthermore, a substantial fraction of atoms populates the  $\{\pm 2, 0\}\hbar k$  momentum modes as the driving frequency is tuned close to the resonance frequency for excitation to the second band of the pump wave. This process inhibits efficient population of the dark state as is discussed in the Supplemental Material [45]. For reasons explained in Ref. [45], in the experiment, the respective resonance is shifted to  $\omega_{\text{dr}}/\omega_D \approx 1.45$ , i.e., within the domain shown in Fig. 4(a), acting to suppress the dark state population on the right side of the red circle.

In conclusion, in an atom-cavity system pumped by a periodically shaken standing wave, we have found that in a specific parameter domain, a stationary excited dark state condensate emerges, in which scattering of pump photons into the cavity mode is suppressed. We show that a three-level Dicke model captures this phenomenon qualitatively. Both theoretically and experimentally, we observe that, upon adiabatic ramp-down of the pump wave, the atomic condensate in the dark state is essentially unaffected, while the bright sector of the system undergoes a dynamical phase transition [3]. Our work points out a general approach to form stationary excited many-body states using the concept of dark states known from single-particle quantum optics.

We thank C. Georges, J. Klinder, and L. Broers for helpful discussions. This work was funded by the UP System Balik PhD Program (OVPAA-BPhD-2021-04), the QuantERA II Programme that has received funding from the European Union's Horizon 2020 research and innovation programme under Grant Agreement No. 101017733, the Deutsche Forschungsgemeinschaft (DFG, German Research Foundation) "SFB-925" Project No. 170620586, and the Cluster of Excellence "Advanced Imaging of Matter" (EXC 2056), Project No. 390715994. J. S. acknowledges support from the German Academic Scholarship Foundation.

\*These authors contributed equally to this work.

- [1] K. Baumann, C. Guerlin, F. Brennecke, and T. Esslinger, Dicke quantum phase transition with a superfluid gas in an optical cavity, *Nature (London)* **464**, 1301 (2010).
- [2] H. Ritsch, P. Domokos, F. Brennecke, and T. Esslinger, Cold atoms in cavity-generated dynamical optical potentials, *Rev. Mod. Phys.* **85**, 553 (2013).
- [3] J. Klinder, H. Keßler, M. Wolke, L. Mathey, and A. Hemmerich, Dynamical phase transition in the open Dicke model, *Proc. Natl. Acad. Sci. U.S.A.* **112**, 3290 (2015).
- [4] V. D. Vaidya, Y. Guo, R. M. Kroeze, K. E. Ballantine, A. J. Kollár, J. Keeling, and B. L. Lev, Tunable-Range, Photon-Mediated Atomic Interactions in Multimode Cavity QED, *Phys. Rev. X* **8**, 011002 (2018).
- [5] R. H. Dicke, Coherence in spontaneous radiation processes, *Phys. Rev.* **93**, 99 (1954).
- [6] P. Kirton, M. M. Roses, J. Keeling, and E. G. Dalla Torre, Introduction to the Dicke model: From equilibrium to nonequilibrium, and vice versa, *Adv. Quantum Technol.* **2**, 1800043 (2019).
- [7] F. Damanet, A. J. Daley, and J. Keeling, Atom-only descriptions of the driven-dissipative Dicke model, *Phys. Rev. A* **99**, 033845 (2019).
- [8] C. C. Sung and C. M. Bowden, Phase transition in the multimode two- and three-level Dicke model (Green's function method), *J. Phys. A* **12**, 2273 (1979).
- [9] M. Hayn, C. Emary, and T. Brandes, Phase transitions and dark-state physics in two-color superradiance, *Phys. Rev. A* **84**, 053856 (2011).
- [10] V. M. Bastidas, C. Emary, B. Regler, and T. Brandes, Nonequilibrium Quantum Phase Transitions in the Dicke Model, *Phys. Rev. Lett.* **108**, 043003 (2012).
- [11] R. Chitra and O. Zeitler, Dynamical many-body phases of the parametrically driven, dissipative Dicke model, *Phys. Rev. A* **92**, 023815 (2015).
- [12] Z. Zhiqiang, C. H. Lee, R. Kumar, K. J. Arnold, S. J. Masson, A. S. Parkins, and M. D. Barrett, Nonequilibrium phase transition in a spin-1 Dicke model, *Optica* **4**, 424 (2017).
- [13] M. Soriente, T. Donner, R. Chitra, and O. Zeitler, Dissipation-Induced Anomalous Multicritical Phenomena, *Phys. Rev. Lett.* **120**, 183603 (2018).
- [14] E. I. Rodríguez Chiacchio and A. Nunnenkamp, Dissipation-Induced Instabilities of a Spinor Bose-Einstein Condensate Inside an Optical Cavity, *Phys. Rev. Lett.* **122**, 193605 (2019).
- [15] B. Buča and D. Jaksch, Dissipation Induced Nonstationarity in a Quantum Gas, *Phys. Rev. Lett.* **123**, 260401 (2019).
- [16] K. C. Stitely, S. J. Masson, A. Giraldo, B. Krauskopf, and S. Parkins, Superradiant switching, quantum hysteresis, and oscillations in a generalized Dicke model, *Phys. Rev. A* **102**, 063702 (2020).
- [17] J. Skulte, P. Kongkhambut, H. Keßler, A. Hemmerich, L. Mathey, and J. G. Cosme, Parametrically driven dissipative three-level Dicke model, *Phys. Rev. A* **104**, 063705 (2021).
- [18] L. Broers and L. Mathey, Floquet engineering of non-equilibrium superradiance, *SciPost Phys.* **14**, 018 (2023).
- [19] P. Kongkhambut, H. Keßler, J. Skulte, L. Mathey, J. G. Cosme, and A. Hemmerich, Realization of a Periodically Driven Open Three-Level Dicke Model, *Phys. Rev. Lett.* **127**, 253601 (2021).
- [20] R. Lin, R. Rosa-Medina, F. Ferri, F. Finger, K. Kroeger, T. Donner, T. Esslinger, and R. Chitra, Dissipation-Engineered Family of Nearly Dark States in Many-Body Cavity-Atom Systems, *Phys. Rev. Lett.* **128**, 153601 (2022).

- [21] H. Habibian, A. Winter, S. Paganelli, H. Rieger, and G. Morigi, Bose-Glass Phases of Ultracold Atoms due to Cavity Backaction, *Phys. Rev. Lett.* **110**, 075304 (2013).
- [22] C. Kollath, A. Sheikhan, S. Wolff, and F. Brennecke, Ultracold Fermions in a Cavity-Induced Artificial Magnetic Field, *Phys. Rev. Lett.* **116**, 060401 (2016).
- [23] F. Mivehvar, F. Piazza, and H. Ritsch, Disorder-Driven Density and Spin Self-Ordering of a Bose-Einstein Condensate in a Cavity, *Phys. Rev. Lett.* **119**, 063602 (2017).
- [24] C. Georges, J. G. Cosme, L. Mathey, and A. Hemmerich, Light-Induced Coherence in an Atom-Cavity System, *Phys. Rev. Lett.* **121**, 220405 (2018).
- [25] M. Landini, N. Dogra, K. Kroeger, L. Hruby, T. Donner, and T. Esslinger, Formation of a Spin Texture in a Quantum Gas Coupled to a Cavity, *Phys. Rev. Lett.* **120**, 223602 (2018).
- [26] J. G. Cosme, J. Skulte, and L. Mathey, Time crystals in a shaken atom-cavity system, *Phys. Rev. A* **100**, 053615 (2019).
- [27] N. Dogra, M. Landini, K. Kroeger, L. Hruby, T. Donner, and T. Esslinger, Dissipation-induced structural instability and chiral dynamics in a quantum gas, *Science* **366**, 1496 (2019).
- [28] G. Bentsen, I.-D. Potirniche, V. B. Bulchandani, T. Scaffidi, X. Cao, X.-L. Qi, M. Schleier-Smith, and E. Altman, Integrable and Chaotic Dynamics of Spins Coupled to an Optical Cavity, *Phys. Rev. X* **9**, 041011 (2019).
- [29] S. B. Jäger, M. J. Holland, and G. Morigi, Superradiant optomechanical phases of cold atomic gases in optical resonators, *Phys. Rev. A* **101**, 023616 (2020).
- [30] H. Keßler, P. Kongkhambut, C. Georges, L. Mathey, J. G. Cosme, and A. Hemmerich, Observation of a Dissipative Time Crystal, *Phys. Rev. Lett.* **127**, 043602 (2021).
- [31] C. Georges, J. G. Cosme, H. Keßler, L. Mathey, and A. Hemmerich, Dynamical density wave order in an atom-cavity system, *New J. Phys.* **23**, 023003 (2021).
- [32] R. Rosa-Medina, F. Ferri, F. Finger, N. Dogra, K. Kroeger, R. Lin, R. Chitra, T. Donner, and T. Esslinger, Observing Dynamical Currents in a Non-Hermitian Momentum Lattice, *Phys. Rev. Lett.* **128**, 143602 (2022).
- [33] P. Kongkhambut, J. Skulte, L. Mathey, J. G. Cosme, A. Hemmerich, and H. Keßler, Observation of a continuous time crystal, *Science* **377**, 670 (2022).
- [34] D. Dreon, A. Baumgärtner, X. Li, S. Hertlein, T. Esslinger, and T. Donner, Self-oscillating pump in a topological dissipative atom-cavity system, *Nature (London)* **608**, 494 (2022).
- [35] Z. Zhang, D. Dreon, T. Esslinger, D. Jaksch, B. Buca, and T. Donner, Tunable non-equilibrium phase transitions between spatial and temporal order through dissipation, *arXiv*: 2205.01461.
- [36] M. O. Scully and M. S. Zubairy, *Quantum Optics* (Cambridge University Press, Cambridge, England, 1997).
- [37] U. Gaubatz, P. Rudecki, S. Schieman, and K. Bergmann, Population transfer between molecular vibrational levels by stimulated Raman scattering with partially overlapping laser fields. A new concept and experimental results, *J. Chem. Phys.* **92**, 5363 (1990).
- [38] N. V. Vitanov, A. Rangelov, B. W. Shore, and K. Bergmann, Stimulated Raman adiabatic passage in physics, chemistry, and beyond, *Rev. Mod. Phys.* **89**, 015006 (2017).
- [39] M. Fleischhauer, A. Imamoglu, and J. P. Marangos, Electromagnetically induced transparency: Optics in coherent media, *Rev. Mod. Phys.* **77**, 633 (2005).
- [40] K.-J. Boller, A. Imamoglu, and S. E. Harris, Observation of Electromagnetically Induced Transparency, *Phys. Rev. Lett.* **66**, 2593 (1991).
- [41] M. O. Scully, S.-Y. Zhu, and A. Gavrielides, Degenerate Quantum-Beat Laser: Lasing without Inversion and Inversion without Lasing, *Phys. Rev. Lett.* **62**, 2813 (1989).
- [42] J. Mompert and R. Corbalán, Lasing without inversion, *J. Opt. B* **2**, R7 (2000).
- [43] E. G. Dalla Torre, J. Otterbach, E. Demler, V. Vuletic, and M. D. Lukin, Dissipative Preparation of Spin Squeezed Atomic Ensembles in a Steady State, *Phys. Rev. Lett.* **110**, 120402 (2013).
- [44] A. Piñeiro Orioli, J. K. Thompson, and A. M. Rey, Emergent Dark States from Superradiant Dynamics in Multilevel Atoms in a Cavity, *Phys. Rev. X* **12**, 011054 (2022).
- [45] See Supplemental Material at <http://link.aps.org/supplemental/10.1103/PhysRevLett.130.163603> for more details, which includes Refs. [46,47].
- [46] M. Abramowitz and I. A. Stegun, *Handbook of Mathematical Functions with Formulas, Graphs, and Mathematical Tables* (Dover, New York, 1964).
- [47] J. Keeling, M. J. Bhaseen, and B. D. Simons, Collective Dynamics of Bose-Einstein Condensates in Optical Cavities, *Phys. Rev. Lett.* **105**, 043001 (2010).
- [48] H. Keßler, J. Klinder, M. Wolke, and A. Hemmerich, Optomechanical atom-cavity interaction in the sub-recoil regime, *New J. Phys.* **16**, 053008 (2014).
- [49] J. Klinder, H. Keßler, C. Georges, J. Vargas, and A. Hemmerich, Bose-Einstein condensates in an optical cavity with sub-recoil bandwidth, *Appl. Phys. B* **122**, 299 (2016).
- [50] A. Polkovnikov, Phase space representation of quantum dynamics, *Ann. Phys. (Amsterdam)* **325**, 1790 (2010).
- [51] H. Keßler, J. G. Cosme, M. Hemmerling, L. Mathey, and A. Hemmerich, Emergent limit cycles and time crystal dynamics in an atom-cavity system, *Phys. Rev. A* **99**, 053605 (2019).
- [52] Richelle Jade L. Tuquero, J. Skulte, L. Mathey, and J. G. Cosme, Dissipative time crystal in an atom-cavity system: Influence of trap and competing interactions, *Phys. Rev. A* **105**, 043311 (2022).
- [53] O. Penrose and L. Onsager, Bose-Einstein condensation and liquid helium, *Phys. Rev.* **104**, 576 (1956).
- [54] A. U. J. Lode and C. Bruder, Fragmented Superradiance of a Bose-Einstein Condensate in an Optical Cavity, *Phys. Rev. Lett.* **118**, 013603 (2017).

# Chapter 5

## Blue-detuned pump experiments

In publication V we presented, for the first time, the observation of a time crystalline phase that breaks continuous time translation symmetry, hence referred to as a *continuous time crystal* (CTC). This observation realizes a class of time crystals, which is closer to the original proposal by Wilczek in 2012. The no-go theorems are circumvented by preparing the system in a non-equilibrium state and using a well-controlled dissipation channel to prevent the system from approaching an infinite temperature state. For these experiments, we pumped our atom-cavity system with a pump wavelength  $\lambda_p = 792.55$  nm where the pump is blue-detuned with respect to the atomic resonance. Ongoing investigations, which are advertised in section 6.2, also hinted at an observation of a CTC using red-detuned pump light.

### 5.1 Publication V: Observation of a continuous time crystal

It has been proposed that a continuously pumped atom-cavity system with a pump, blue-detuned with respect to the atomic resonance, leads to the emergence of limit cycles, which can be classified as continuous time crystals [106, 107]. In contrast to the red-detuned pump case, atoms localize at the pump field nodes, where scattering of photons from the pump into the cavity, and vice versa, is suppressed. This leads to a dynamical phase, which breaks a continuous time translation symmetry and is robust against temporal perturbations. The key feature of the CTC we observed is a persistent oscillation of the intra-cavity light intensity with frequency  $\omega_{lc} \approx 2\pi \times 10$  kHz, while the atomic density distribution is cycling through recurring patterns. We observed that the time phase difference of the oscillation from two experimental realizations take random values between 0 and  $2\pi$ , as expected for the spontaneously breaking of the continuous time translation symmetry. Simulations show that the recoil resolution of the cavity that causes the retardation between the cavity field dynamics and the atomic field dynamics makes it possible to observe the self-sustained CTC dynamics in our atom-cavity system [107, 108].

#### Status of the publication:

The results were published as a Science First Release online article on June 9th, 2022 and as a printed version in Science [4] on August 5th, 2022. It was featured in the Science perspective article [109]. The corresponding supplemental material can be found in appendix D.

**Note:**

Due to a mismatch between notation used in different publications and this thesis, I would like to improve the readability of the publication by listing the notation in table 5.1.

parameters	this thesis	publication V
pump strength	$\epsilon_p$	$\epsilon$

*Table 5.1:* Notation differences between this thesis and publication V.

## QUANTUM DYNAMICS

## Observation of a continuous time crystal

Phatthamon Kongkhambut<sup>1</sup>, Jim Skulte<sup>1,2</sup>, Ludwig Mathey<sup>1,2</sup>, Jayson G. Cosme<sup>3</sup>, Andreas Hemmerich<sup>1,2\*</sup>, Hans Keßler<sup>1\*</sup>

Time crystals are classified as discrete or continuous depending on whether they spontaneously break discrete or continuous time translation symmetry. Although discrete time crystals have been extensively studied in periodically driven systems, the experimental realization of a continuous time crystal is still pending. We report the observation of a limit cycle phase in a continuously pumped dissipative atom-cavity system that is characterized by emergent oscillations in the intracavity photon number. The phase of the oscillation was found to be random for different realizations, and hence, this dynamical many-body state breaks continuous time translation symmetry spontaneously. Furthermore, the observed limit cycles are robust against temporal perturbations and therefore demonstrate the realization of a continuous time crystal.

Time crystals are dynamical many-body states that break time translation symmetry in a spontaneous and robust manner (1, 2). The original quantum time crystal envisaged by Wilczek involves a closed many-body system with all-to-all coupling that breaks continuous time translation symmetry by exhibiting oscillatory dynamics in its lowest-energy equilibrium state even though the underlying Hamiltonian is time-independent (1). This would constitute a startling state of matter in motion, fundamentally protected from bringing this motion to a standstill through energy removal. However, a series of no-go theorems have shown that nature prohibits the realization of such time crystals in isolated systems (3–5). The search for time crystals was thus extended to include equilibrium scenarios in periodically driven closed systems (6–8). This has led to realizations of discrete time crystals, which break the discrete time translation symmetry imposed by the external drive (9–17). In such discrete time crystals, during a short initial phase, the drive slightly excites the system until the system decouples from the drive, so that further energy or entropy flow is terminated. The system develops a subharmonic response, an intrinsic oscillation at a frequency slower than that of the drive. Initially, it was argued that dissipation, and hence the use of open systems, must be carefully avoided; then, so-called dissipative discrete time crystals were theoretically predicted (18) and experimentally realized (19–21). As shown in a number of theoretical works (22–24), the use of open systems comes with the unexpected consequence that continuous instead of periodic driving suffices to induce time crystal dynamics. These continuous time crystals (CTCs) realize the spirit of

the original proposal more closely than discrete time crystals and circumvent the no-go theorems through their open character.

Here, we report the observation of a CTC in the form of a limit cycle phase in a continuously pumped dissipative atom-cavity system (Fig. 1A). In classical nonlinear dynamics, the term “limit cycle”, coined by Poincaré in a math-

ematical context (25), denotes a closed phase space trajectory, asymptotically approached by at least one neighboring trajectory. Although limit cycles are well-established in classical nonlinear physics (26), there are two essential conditions for limit cycles in open quantum systems to form a CTC. First, the formation of the limit cycle must be associated with spontaneous breaking of continuous time translation symmetry. That is, the relative time phase of the oscillations for repeated realizations takes random values between 0 and  $2\pi$ . Second, the limit cycle phase is robust against temporal perturbations of technical or fundamental character, such as quantum noise and, for open systems, fluctuations associated with dissipation. The characteristic signature of the CTC presented here is a persistent oscillation of the intracavity intensity and atomic density (Fig. 1, B and C), which complies with the robustness and spontaneous symmetry-breaking criteria (Fig. 1D).

Our experimental setup consists of a Bose-Einstein condensate (BEC) of  $N_a \approx 5 \times 10^4$  Rb atoms inside a high-finesse optical cavity. The system is transversely pumped with a standing

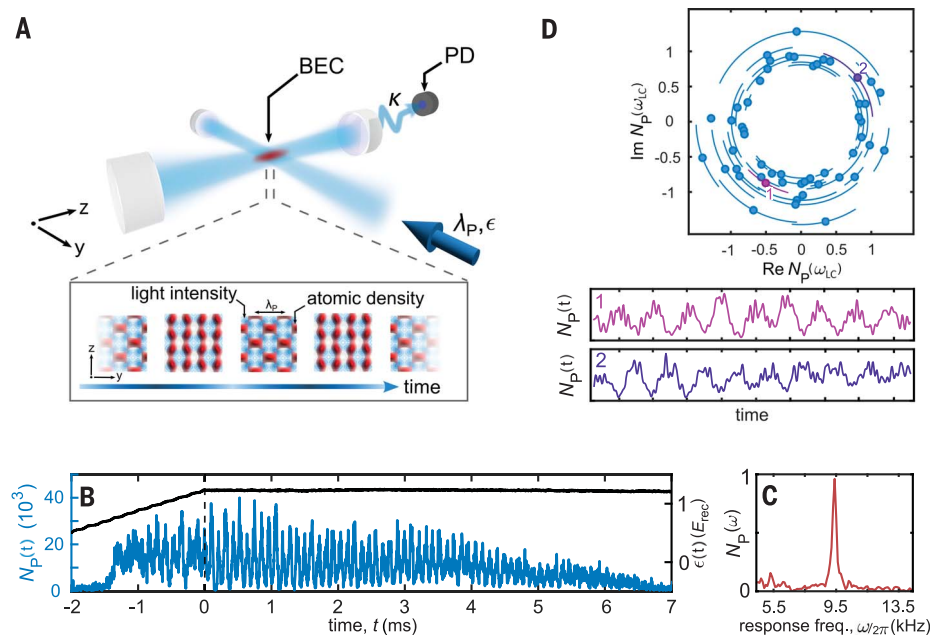


**Fig. 1. CTC in an atom-cavity system.** (A) Schematic drawing of the atom-cavity system pumped transversely with an optical pump lattice, blue detuned with respect to an atomic transition. (Inset) The photon field (blue) and the atomic density (red) of the limit cycle dynamics, based on simulations. The blue color shading of the time axis indicates the intracavity photon number. (B) Single experimental realization of the limit cycle phase for  $\delta_{\text{eff}}/2\pi = -3.8$  kHz and  $\epsilon_f = 1.25 E_{\text{rec}}$ . The vertical dashed black line indicates the start of the 10 ms holding time, during which the pump strength is held constant. The black line indicates the time trace of the pump strength  $\epsilon$ , and the blue line indicates the time evolution of the intracavity photon number  $N_P(t)$ . (C) Normalized and rescaled single-sided amplitude spectrum of  $N_P$  calculated from the data shown in (B). (D) (Top) Distribution of the time phase in the limit cycle phase for  $\delta_{\text{eff}}/2\pi = -5.0$  kHz and  $\epsilon_f = 1.25 E_{\text{rec}}$ . The error bars indicate the phase uncertainty within our discrete Fourier transform resolution of 100 Hz. However, the uncertainty with regard to the radial dimension—the amplitude uncertainty—is negligibly small. For clarity, we removed the errors bars, around 30%, which are overlapping. (Bottom) The evolution of the intracavity photon number for two specific experimental realizations, marked with “1” and “2” at top, which have a time phase difference of almost  $\pi$ .

<sup>1</sup>Zentrum für Optische Quantentechnologien and Institut für Laser-Physik, Universität Hamburg, 22761 Hamburg, Germany. <sup>2</sup>The Hamburg Center for Ultrafast Imaging, 22761 Hamburg, Germany. <sup>3</sup>National Institute of Physics, University of the Philippines, Diliman, Quezon City 1101, Philippines. \*Corresponding author. Email: hemmerich@physnet.uni-hamburg.de (A.H.); hkeßler@physnet.uni-hamburg.de (H.K.)



wave field with a wavelength  $\lambda_p = 792.55$  nm (Fig. 1A). This wavelength is blue detuned with respect to relevant atomic  $D_1$  transition of  $^{87}\text{Rb}$  at a wavelength of 794.98 nm. The cavity operates in the recoil resolved regime (27)—its field decay rate  $\kappa = 2\pi \times 3.4$  kHz is smaller than the recoil frequency  $\omega_{\text{rec}} = 2\pi \times 3.7$  kHz. The cavity resonance frequency  $\omega_c$  is shifted because of the refractive index of the BEC by an amount of  $\delta_- = N_a U_0/2$ , where  $U_0 = 2\pi \times 1.3$  Hz is the maximal light shift per intracavity photon. We define the effective detuning as  $\delta_{\text{eff}} = \delta_c - \delta_-$ , where  $\delta_c \equiv \omega_p - \omega_c$  is the detuning between the pump field frequency  $\omega_p$  and the resonance frequency of the empty cavity  $\omega_c$ .

To determine the regime of the CTC, we measured the time dependence of the intracavity photon number  $N_p(t)$  that emerges in the protocol given below. We show  $N_p(t)$  in Fig. 2A and two derived quantities, the crystalline fraction  $\Xi$  and the limit-cycle frequency  $\omega_{\text{LC}}$  in Fig. 2, B and C, respectively. In our protocol, the intracavity photon number  $N_p(t)$  was recorded as we linearly ramped the pump strength  $\epsilon$  from 0 to  $3.5 E_{\text{rec}}$  within 10 ms, while keeping  $\delta_{\text{eff}}$  fixed. Initially, for weak pump intensities, the BEC phase was stable, and  $N_p$  was zero. Above a critical value of  $\epsilon$ , the BEC became unstable toward the formation of a self-organized superradiant phase

heralded by a nonzero  $N_p$ . This represents a many-body state as the cavity photons mediate a retarded infinite-range interaction between the atoms. Although this superradiant phase transition has been intensively studied for a red-detuned pump (28–31), it has only been realized recently for a blue-detuned pump after its theoretical prediction (32, 33). For blue detuning, the atoms are low-field seeking and localize at the intensity minima of the light field. Nevertheless, the atoms can still self-organize into the superradiant phase, as evident from the large blue areas shown in Fig. 2A. However, the self-organized superradiant phase may become unstable for higher pump strengths because it costs energy for the atoms to localize away from the nodes of the pump lattice. This behavior leads to the disappearance of the self-organized phase for higher pump strengths (32). A phase diagram in fig. S1 in (34) shows a larger range of  $\epsilon$ , demonstrating the disappearance of the self-organization for strong pumping. In the recoil-resolved regime, because of the retarded character of the cavity-mediated interaction, we additionally observed the emergence of a new dynamical phase or a limit cycle phase characterized by self-sustained oscillations of  $N_p$  as the atoms cycled through different density wave patterns (33, 35). The resolution of the experimental imaging system

is insufficient to observe the real-space density of the cloud; instead, simulations of the evolution of the single-particle density by use of a mean-field model are shown in fig. S3 (34). Physically, the limit cycles can be understood as a competition between opposing energy contributions: one coming from the pump lattice potential, and another coming from the cavity-induced all-to-all interaction between the atoms (33). In the superradiant phase, the cavity-induced interaction energy dominates, and the atoms localize at the antinodes. In the limit cycle phase for sufficiently strong pump intensities, localization of low-field-seeking atoms at the antinodes becomes energetically costly, resulting in a decrease in the density modulations and  $N_p$  as the system attempts to go back to the normal homogeneous phase. However, this is unstable toward self-organization because the chosen pump strength already exceeds the critical value, and thus, the cycle starts anew. The regime of recoil-resolution of the cavity, in which the dynamics of the atomic density and the light field evolve with similar time scales, has turned out to be the key ingredient to realize the limit cycle phase. This can be understood by noting that the delayed dynamics of the cavity field, with respect to the atomic density, leads to cavity cooling, which in contrast to broadband cavity

Downloaded from https://www.science.org at Staats und Universitätsbibliothek Hamburg on May 17, 2023

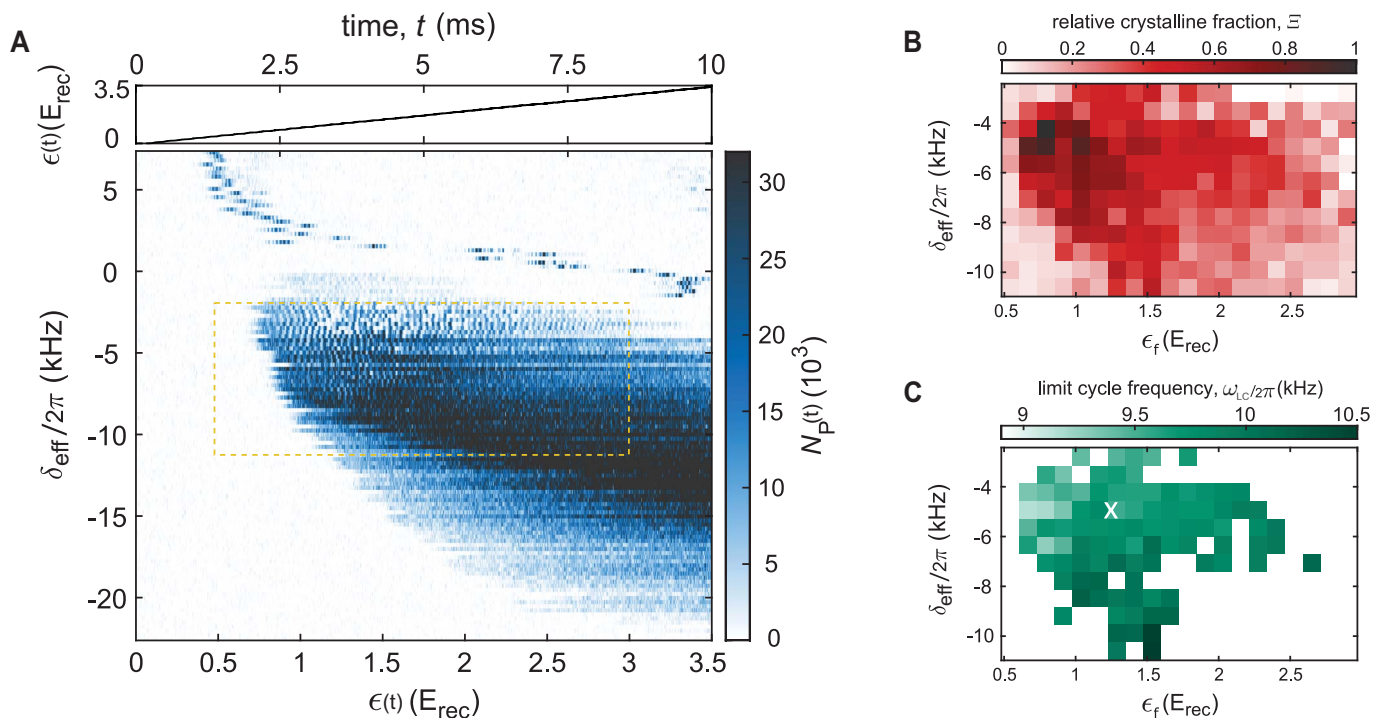


**Fig. 2. Determining the time-crystalline regime.** (A) (Top) Pump strength protocol. (Bottom) The corresponding intracavity photon number  $N_p$  as a function of  $\delta_{\text{eff}}$  and  $\epsilon$ . The area enclosed by the yellow dashed lines indicates the parameter space spanned in (B) and (C). (B) Relative crystalline fraction  $\Xi$  and (C) limit cycle frequency  $\omega_{\text{LC}}$  plotted versus  $\delta_{\text{eff}}$  and  $\epsilon_f$ . To obtain (B) and (C), for fixed  $\delta_{\text{eff}}$ , the pump strength is ramped to its final value  $\epsilon_f$  and

subsequently held constant for 10 ms. The relative crystalline fraction  $\Xi$  and the corresponding value of  $\omega_{\text{LC}}$  identify the time-crystalline state. The parameter space is divided into 20 by 24 plaquettes and averages across 5 to 10 experimental implementations are produced. The white cross indicates the parameter values  $\delta_{\text{eff}}/2\pi = -5.0$  kHz and  $\epsilon_f = 1.25 E_{\text{rec}}$ . The white area in (C) corresponds to data with  $\Xi$  below  $1/e$ .

setups restricts the atoms to occupy only a small number of momentum modes. This prevents the system from heating up and entering chaotic dynamics. We observed the limit cycle phase in the region shown in Fig. 2A enclosed by the yellow dashed lines. To further highlight the dynamical nature of this phase, we show a typical single-shot realization in Fig. 1, B and C.

Next, we quantitatively identified the area in the parameter space, spanned by the pump strength  $\epsilon$  and the effective detuning  $\delta_{\text{eff}}$ , where limit cycles can be observed. For fixed  $\delta_{\text{eff}}$ , we linearly ramped  $\epsilon$  to the desired final value  $\epsilon_f$ , using the same slope as for the measurement shown in Fig. 2A, and held  $\epsilon$  constant for 10 ms. The protocol is depicted by the black curve in Fig. 1B. We show in Fig. 1C an example of the normalized and rescaled single-sided amplitude spectrum  $N_P(\omega) = \bar{N}_P(\omega)/\bar{N}_{P,\text{max}}(\omega_{\text{LC}})$  obtained from  $N_P(t)$  within the holding time window  $[0,10]$  ms in Fig. 1B.  $\bar{N}_P(\omega)$  is the normalized single-sided amplitude spectrum, and  $\bar{N}_{P,\text{max}}(\omega_{\text{LC}})$  is the maximum value of the measured limit cycle amplitude. In the case of pronounced limit cycle dynamics as in Fig. 1C, the single-sided amplitude spectrum shows a distinct peak, with a width associated with the limit cycle lifetime of several milliseconds. The narrowest peaks observed exhibit a  $e^{-2}$  width  $\Delta\omega \approx 2\pi \times 1.4$  kHz: The limit cycle frequency  $\omega_{\text{LC}}$ , plotted in Fig. 2C, is defined as the frequency of the dominant peak in the single-sided amplitude spectrum within the frequency interval  $\Delta_{\text{LC}} = [3.5, 15.5] \times 2\pi$  Hz, chosen much larger than  $\delta_{\text{LC}} \in [\omega_{\text{LC}} - \Delta\omega/2, \omega_{\text{LC}} + \Delta\omega/2]$ . The oscillation frequency of a CTC is not necessarily fixed, and robustness refers to the persistence of the CTC in the thermodynamic limit and for a wide range of system parameters [finite-size effects are discussed in the supplementary materials (34)] (22). We calculated a common measure for time crystallinity, the crystalline fraction  $\Xi'$  (10, 11), as the ratio between the area under the single-sided amplitude spectrum within  $\delta_{\text{LC}}$  and the total area within  $\Delta_{\text{LC}}$ . That is,  $\Xi' \equiv \sum_{\omega \in \delta_{\text{LC}}} N_P(\omega) / \sum_{\omega \in \Delta_{\text{LC}}} N_P(\omega)$ . The relative crystalline fraction  $\Xi$  shown in Fig.

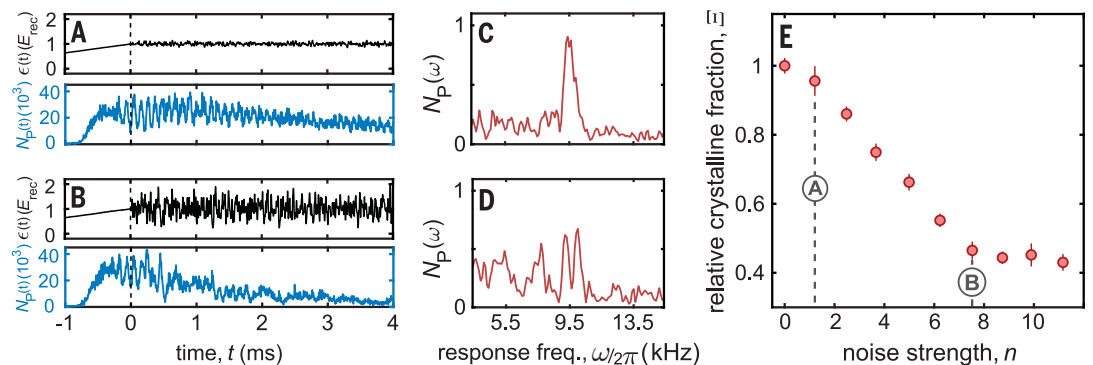
2B is normalized to the maximum crystalline fraction measured in the parameter space explored in this work. Because of the finite lifetime of the BEC, it is difficult to access the long-time behavior of the system, which makes it experimentally challenging to distinguish between the areas of stable limit cycle, chaos, and possible transient phases. Hence, we define a cut-off or threshold value for the relative crystalline fraction,  $\Xi_{\text{cut}} = 1/e$ , to identify regions with observable limit cycle dynamics. In Fig. 2C, the frequency response of the limit cycle phase is only shown if its relative crystalline fraction is higher than the cut-off value:  $\Xi > \Xi_{\text{cut}}$ . The experimental lifetime of our time crystal is limited by atom loss. Furthermore, the short-range contact interaction, due to collisions between the atoms, leads to dephasing of the system and hence melting of the time crystal. Simulations that include contact interactions and phenomenological atom loss can be found in the supplementary materials.

The spontaneous symmetry breaking of a many-body system indicates a phase transition. We demonstrated strong evidence that the limit cycle phase emerges through spontaneous breaking of continuous time translation symmetry, and thus, it is a CTC. We repeated the experimental pump protocol shown as the Fig. 1B black line more than 1500 times with fixed  $\delta_{\text{eff}}/2\pi = -5.0$  kHz and  $\epsilon_f = 1.25 E_{\text{rec}}$ . These parameter values are indicated in Fig. 2C with a white cross. Because of technical instabilities, the number of the atoms in the BEC  $N_a$  fluctuates by 5%. This leads to a fluctuating value of  $\delta_{\text{eff}}$  and hence of  $\omega_{\text{LC}}$ . Pictorially, this can be understood by observing that fluctuations in  $N_a$  effectively shift the CTC regime in Fig. 2C either up or down. For the parameter values indicated by a white cross in Fig. 2C, the median of  $\omega_{\text{LC}}$  is  $\bar{\omega}_{\text{LC}} = 2\pi \times 9.69$  kHz. Our discrete Fourier transform resolution, set by the 10-ms time window, is 100 Hz. Thus, we only considered experimental runs, which yielded response frequencies of  $\omega_{\text{LC}} = \bar{\omega}_{\text{LC}} \pm 2\pi \times (50 \text{ Hz})$ . For each single-shot measurement, we obtained the time phase defined as the principal argument  $\arg[N_P(\omega_{\text{LC}})]$  of the

Fourier transformed intracavity photon number  $N_P(\omega_{\text{LC}})$  evaluated at the limit cycle frequency  $\omega_{\text{LC}}$ . In Fig. 1D, we show the distribution of the observed time phases, which randomly covers the interval  $[0, 2\pi]$ . This corroborates the spontaneous breaking of continuous time translation symmetry in the limit cycle phase. In the bottom of Fig. 1D, we show two specific experimental realizations, which have a time phase difference of almost  $\pi$ . Simulations representing the BEC as a coherent state show a range of the response frequency distribution of 300 Hz. Because we post-selected our data far below this limit, the origin of the spread over  $2\pi$  in the time phase distribution is not due to technical noises but rather to quantum fluctuations. In the supplementary materials, we show a more detailed theoretical analysis to support this argument. The error bars along the angular direction in Fig. 1D indicate the phase uncertainty within 100 Hz of our Fourier limit. The average phase uncertainty is around  $0.25\pi$ . The uncertainty in the radial direction corresponding to the oscillation amplitude is, however, negligible. Moreover, we removed 30% of the error bars for clarity in Fig. 1D.

Last, we demonstrated the robustness of the limit cycle phase against temporal perturbations, which is a defining feature of time crystals. We introduced white noise onto the pump signal with a bandwidth of 50 kHz. The noise strength is quantified by  $n \equiv \sum_{\omega=0}^{2\pi \times 50 \text{ kHz}} |\mathcal{A}_{\text{noisy}}(\omega)| / \sum_{\omega=0}^{2\pi \times 50 \text{ kHz}} |\mathcal{A}_{\text{clean}}(\omega)| - 1$ , where  $\mathcal{A}_{\text{noisy}}$  and  $\mathcal{A}_{\text{clean}}$  are the single-sided amplitude spectrum of the pump in the presence and absence of white noise, respectively. We chose the parameters  $\delta_{\text{eff}}/2\pi = -5.0$  kHz and  $\epsilon_f = 1.25 E_{\text{rec}}$  in the center of the stable limit cycle region, indicated by the white cross in Fig. 2C, and added white noise with varying strengths. In Fig. 3, A and B, top, single-shot realizations of the noisy pump signal are shown for weak and strong noise, respectively. The corresponding dynamics of  $N_P$  is shown in Fig. 3, A and B, bottom. In Fig. 3E, we show how increasing the noise strength can “melt” the CTC as inferred by the decreasing relative crystalline fractions calculated from single-sided amplitude spectra, similar to those shown in Fig. 3, C

**Fig. 3. Robustness against temporal perturbations.** (A and B) Single experimental runs for noise strengths indicated in (E). (Top) Time traces of the pump strength  $\epsilon$ . (Bottom) Corresponding dynamics of  $N_P$ . (C and D) Single-sided amplitude spectra of (A) and (B), respectively. (E) Relative crystalline fraction for varying noise strength  $n$  and fixed  $\delta_{\text{eff}}/2\pi = -5.0$  kHz and  $\epsilon_f = 1.25 E_{\text{rec}}$ .



and D. The system takes time to react to the noise, so that a few oscillations can always be observed before decay sets in. This leads to an offset of 0.4 in the crystalline fraction, even for very strong noise. Nevertheless, we found that the limit cycle phase indeed exhibits robust oscillatory behavior over a wide range of the noise strength. This, together with the observation of spontaneous breaking of a continuous time translation symmetry, suggests that the observed limit cycle phase is a CTC.

We have experimentally demonstrated a CTC and provided a theoretical understanding. This class of dynamical many-body states expands the concepts of long-range order and spontaneous symmetry breaking into the time domain and is therefore of fundamental interest. This result, and the precision and control achieved with our atom-cavity platform, paves the way toward a broad and comprehensive study of dynamical many-body states of bosonic or fermionic quantum matter in the strongly correlated regime. For example, an increased atom-photon coupling could generate a new class of time crystals associated with symmetry-broken periodic entanglement. Furthermore, technological applications, such as toward time metrology, can be envisioned.

#### REFERENCES AND NOTES

1. F. Wilczek, *Phys. Rev. Lett.* **109**, 160401 (2012).
2. A. Shapere, F. Wilczek, *Phys. Rev. Lett.* **109**, 160402 (2012).
3. P. Nozières, *Europhys. Lett.* **103**, 57008 (2013).
4. P. Bruno, *Phys. Rev. Lett.* **111**, 070402 (2013).
5. H. Watanabe, M. Oshikawa, *Phys. Rev. Lett.* **114**, 251603 (2015).
6. D. V. Else, C. Monroe, C. Nayak, N. Y. Yao, *Annu. Rev. Condens. Matter Phys.* **11**, 467–499 (2020).
7. K. Sacha, *Time Crystals* (Springer, 2020).
8. V. Khemani, R. Moessner, S. L. Sondhi, arXiv:1910.10745 [cond-mat.str-el] (2019).
9. J. Zhang *et al.*, *Nature* **543**, 217–220 (2017).
10. S. Choi *et al.*, *Nature* **543**, 221–225 (2017).
11. J. Rovny, R. L. Blum, S. E. Barrett, *Phys. Rev. Lett.* **120**, 180603 (2018).
12. J. Smits, L. Liao, H. T. C. Stoof, P. van der Straten, *Phys. Rev. Lett.* **121**, 185301 (2018).
13. S. Autti, V. B. Eltsov, G. E. Volovik, *Phys. Rev. Lett.* **120**, 215301 (2018).
14. J. O'Sullivan *et al.*, *New J. Phys.* **22**, 085001 (2020).
15. A. Kyprianidis *et al.*, *Science* **372**, 1192–1196 (2021).
16. J. Randall *et al.*, *Science* **374**, 1474–1478 (2021).
17. X. Mi *et al.*, *Nature* **601**, 531–536 (2022).
18. Z. Gong, R. Hamazaki, M. Ueda, *Phys. Rev. Lett.* **120**, 040404 (2018).
19. H. Keßler *et al.*, *Phys. Rev. Lett.* **127**, 043602 (2021).
20. P. Kongkhambut *et al.*, *Phys. Rev. Lett.* **127**, 253601 (2021).
21. H. Taheri, A. B. Matsko, L. Maleki, K. Sacha, *Nat. Commun.* **13**, 848 (2022).
22. F. Iemini *et al.*, *Phys. Rev. Lett.* **121**, 035301 (2018).
23. B. Buča, J. Tindall, D. Jaksch, *Nat. Commun.* **10**, 1730 (2019).
24. H. Keßler, J. G. Cosme, M. Hemmerling, L. Mathey, A. Hemmerich, *Phys. Rev. A* **99**, 053605 (2019).
25. H. Poincaré, *J. Math. Pures Appl.* **7**, 375 (1881).
26. S. H. Strogatz, *Nonlinear Dynamics and Chaos: With Applications to Physics, Biology, Chemistry, and Engineering* (Westview Press, 2015).
27. H. Keßler, J. Klinder, M. Wolke, A. Hemmerich, *New J. Phys.* **16**, 053008 (2014).
28. P. Domokos, H. Ritsch, *Phys. Rev. Lett.* **89**, 253003 (2002).
29. A. T. Black, H. W. Chan, V. Vuletić, *Phys. Rev. Lett.* **91**, 203001 (2003).
30. K. Baumann, C. Guerlin, F. Brennecke, T. Esslinger, *Nature* **464**, 1301–1306 (2010).
31. J. Klinder, H. Keßler, M. Wolke, L. Mathey, A. Hemmerich, *Proc. Natl. Acad. Sci. U.S.A.* **112**, 3290–3295 (2015).
32. P. Zupancic *et al.*, *Phys. Rev. Lett.* **123**, 233601 (2019).
33. F. Piazza, H. Ritsch, *Phys. Rev. Lett.* **115**, 163601 (2015).
34. Supplementary text is available in the supplementary materials.
35. H. Keßler, J. G. Cosme, C. Georges, L. Mathey, A. Hemmerich, *New J. Phys.* **22**, 085002 (2020).
36. P. Kongkhambut *et al.*, Data for “Observation of a continuous time crystal”. Zenodo (2022).

#### ACKNOWLEDGMENTS

H.K. thanks J. Klinder and C. Georges for helpful discussions and their support. J.G.C. thanks R. J. L. Tuqero for valuable insights and discussions. A.H. acknowledges useful discussions with C. Zimmermann and J. Marino. **Funding:** This work is funded by the Deutsche Forschungsgemeinschaft (DFG, German Research Foundation) through grant DFG-KE2481/1–1. P.K., J.S., L.M., and A.H. acknowledge the DFG for funding through SFB-925–project 170620586, and the Cluster of Excellence “Advanced Imaging of Matter” (EXC 2056)–project 390715994. J.S. acknowledges support from the German Academic Scholarship Foundation.

**Author contributions:** P.K. and H.K. performed the experiments and data analysis. The simulations were performed by J.S. and J.G.C., supported by L.M. The project was designed and supervised by H.K. and A.H. All authors contributed to the discussion and interpretation of the results, as well as to writing the manuscript.

**Competing interests:** The authors declare no competing interests. **Data and materials availability:** All data presented in this paper and simulation scripts are deposited at Zenodo (36).

**License information:** Copyright © 2022 the authors, some rights reserved; exclusive licensee American Association for the Advancement of Science. No claim to original US government works. <https://www.science.org/about/science-licenses-journal-article-reuse>

#### SUPPLEMENTARY MATERIALS

[science.org/doi/10.1126/science.abo3382](https://science.org/doi/10.1126/science.abo3382)

Materials and Methods

Supplementary Text

Figs. S1 to S7

References (37, 38)

Submitted 14 February 2022; accepted 25 May 2022

10.1126/science.abo3382





## Observation of a continuous time crystal

Phatthamon Kongkhambut, Jim Skulte, Ludwig Mathey, Jayson G. Cosme, Andreas Hemmerich, and Hans Keler

*Science*, **377** (6606), .

DOI: 10.1126/science.abo3382

### Continuous time crystals

Time crystals are a new dynamical phase of quantum matter resulting from the breaking of time-translation symmetry and the subsequent interplay between interactions forming self-organized phases. To date, discrete time crystals have been observed in periodically driven systems. By contrast, Kongkhambut *et al.* report the observation of spontaneous breaking of a continuous time translation symmetry in an atomic Bose-Einstein condensate inside a high-finesse optical cavity (see the Perspective by LeBlanc). Using a time-independent pump, the authors observed a limit cycle phase that is characterized by emergent periodic oscillations of the intracavity photon number and is accompanied by the atomic density cycling through recurring patterns: a continuous time crystal. —ISO

### View the article online

<https://www.science.org/doi/10.1126/science.abo3382>

### Permissions

<https://www.science.org/help/reprints-and-permissions>

Use of this article is subject to the [Terms of service](#)

---

*Science* (ISSN ) is published by the American Association for the Advancement of Science. 1200 New York Avenue NW, Washington, DC 20005. The title *Science* is a registered trademark of AAAS.  
Copyright © 2022 The Authors, some rights reserved; exclusive licensee American Association for the Advancement of Science. No claim to original U.S. Government Works



# Chapter 6

## Conclusions and Outlook

In this thesis we presented several observations of discrete and continuous dissipative TCs in an atom-cavity system. Our experimental setup is unique in the sense that the optical cavity operates in the recoil-resolved regime, resulting in a retardation between the cavity field and atomic field dynamics. It has been shown recently that the recoil resolution of the cavity is crucial for observing stable TC dynamics [107, 108]. Publication I presented, for the first time, an observation of a DTC in an open system. The main characteristic of the DTC is the period-doubled oscillation between two  $Z_2$ -symmetry broken checkerboard patterns, driven by the intensity modulation of the pump field. Publication II presented a dynamical phase emerging from a periodically shaken pump potential experiment, referred to as a dynamical bond density wave phase. This phase is characterized by an incommensurate switching between the two  $Z_2$ -symmetry broken checkerboard patterns. Since the shaking of the standing wave pump potential enables an additional coupling to the bond density wave state, the standard two-level Dicke model cannot sufficiently explain the dynamics of the atom-cavity system in this shaken scenario. Publication III introduced the parametrically driven three-level Dicke model, which captures the dynamics of the shaken atom-cavity system and predicts the emergence of an ITC, the observation of which is presented in publication II. For sufficiently large shaking amplitudes, a parameter regime emerges in which the ITC exhibits transient behavior, leading to the formation of a condensate in a dark state of the atom-cavity system. The observation of this dark state is presented in IV.

Since 2017, several DTCs have been realized experimentally, but the CTC was yet to be observed. While the no-go theorems prevent CTCs from emerging in the ground state of a closed system [12–14], we circumvented this by employing an open system, and thus could observe a CTC for the first time. This observation is presented in publication V. The observable which exhibit the signature of the CTC dynamics is the persistent oscillation of the intra-cavity field intensity, while its real-space atomic density distribution is cycling through recurring patterns. We also observed the uniform time-phase distribution of the intra-cavity field intensity oscillations, which is expected as a result of the spontaneous breaking of continuous time translation symmetry.

One follow-up experiment is to study a transition between a CTC and a DTC. Like other parametric oscillators, an appropriate external drive leads to an entrainment effect, where the system responds by locking its frequency onto a rational fraction of the driving frequency [110, 111]. After preparing the system in a CTC phase,

we periodically drive the pump intensity at nearly twice of the intrinsic oscillation frequency of the CTC and observe a sub-harmonic response of the intra-cavity field intensity dynamics. We will advertise this ongoing project in section 6.1. Moreover, we are also currently exploring the emergence of limit cycles by using pump light, which is red-detuned with respect to the atomic transition, see section 6.2. This work will further clarify the underlying mechanism that leads to the observation of limit cycles and their intrinsic frequencies.

## 6.1 From a continuous to a discrete time crystal

Inspired by the proposal in 2020 [112], we prepared our system in the CTC phase and modulated the intensity of the pump field close to twice the intrinsic frequency of the CTC. As a consequence, we observed a period-doubled oscillation of the intra-cavity field intensity  $N_p(t)$ , which is the central signature of a DTC.

The periodically driven pump strength is written as  $\epsilon_p(t) = \epsilon_f(1 + f_0 \sin(\omega_{\text{dr}}t))$ , where  $\omega_{\text{dr}} \approx 2 \times \omega_{\text{lc}}$  is the driving frequency and  $f_0$  is the modulation strength. The data presented in fig. 6.1 (a-b) show an example of a single experimental realization with an optimal modulation strength  $f_0 = 0.45$  and driving frequency  $\omega_{\text{dr}} = 2\pi \times 22.5$  kHz. We start to apply the periodic drive when the system is in the CTC phase, at  $t = 0$ . After applying the periodic drive,  $N_p$  oscillates with the sub-harmonic frequency  $\omega_{\text{lc}} \approx \omega_{\text{dr}}/2$ <sup>1</sup>. In fig. 6.1 (c), we repeated the protocol for multiple realizations and plotted the response frequency distribution with ( $f_0 = 0.45$ ) and without ( $f_0 = 0$ ) the drive. The histogram of the driven case (pink) shows a narrowed frequency distribution centered at  $0.5 \omega_{\text{dr}}$ . On the other hand, the histogram of the non-driven case (purple) exhibits fluctuations of  $\omega_{\text{lc}}$  in a broader frequency range, due to unavoidable technical noise. Furthermore, we can show that the drive fixes the time phase of the  $N_p$  oscillation to only two time phases, differing by  $\pi$  for various experimental realizations, see fig. 6.1 (d). Note that this is expected from the commensurate DTCs, characterized by a sub-harmonic frequency response. The related discrete time phase distributions of the DTC in publication I can be found in appendix A.

---

<sup>1</sup>We obtain  $\omega_{\text{lc}}$  from fitting a dominant frequency peak in the Fourier spectrum of  $N_p$  which is calculated from  $t = 0$  to  $t = 10$  ms.

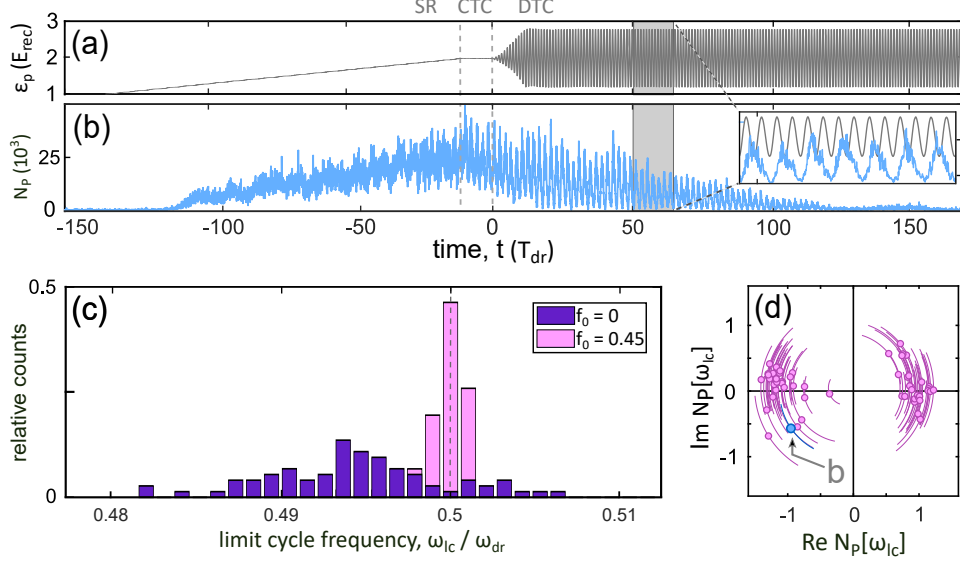


*Figure 6.1:* From a continuous to a discrete time crystals. (a) shows the pump protocol. The pump intensity is periodically modulated at  $t = 0$ . The modulation frequency used in this experimental realization is  $\omega_{\text{dr}} = 2\pi \times 22.5$  kHz with the modulation strength  $f_0 = 0.45$ . (b) shows a time evolution of the intra-cavity field intensity  $N_p$ . The inset in (b) shows the magnified view of  $\epsilon_p$  and  $N_p$  within the time interval marked by the gray rectangles. (c) shows histograms of the response frequency distribution without modulation  $f_0 = 0$  (purple) and with modulation  $f_0 = 0.45$  (pink). (d) shows a time phase distribution of the data from the modulated case with  $f_0 = 0.45$ . The error bars represent the time phase uncertainty according to the Fourier limit. A single realization shown in (b) is highlighted with light blue color.

## 6.2 Observation of limit cycles for red-detuned pump light

We recently observed limit cycles (LCs) when pumping the atom-cavity system with a standing wave pump which is red-detuned with respect to the atomic transition. To identify the LCs, we first recorded a phase diagram, similar to fig. 2.4, with the pump wavelength  $\lambda_p = 803.63$  nm, see fig. 6.2 (a). For the area marked with the blue box, we observed an oscillatory behavior of the intra-cavity field intensity  $N_p$  as we increase the pump strength. This hints at an observation of limit cycles. We then investigated this behavior in more detail by preparing the system at a fixed pump detuning of  $\delta_{\text{eff}} = -1.6$  kHz and a fixed pump strength  $\epsilon_p$  of  $2.6 E_{\text{rec}}$ , see fig. 6.2 (b). At this set of parameters, we observed a persistent oscillation of  $N_p$ , where its dominant frequency is at 5 kHz, see a Fourier spectrum of the observed  $N_p$  in fig. 6.2 (c). This suggests an observation of LCs for a red-detuned pump light. Consequently, one must extend the explanation of the origin of LCs emerging in a blue-detuned pump light, presented in publication V [4], to cover the red-detuned pump light scenario as well.

Although the recent proposal by P. Gao et al. [113] numerically predicted the emergence of LCs in a red-detuned pump regime, a generic paradigm, explaining emergence of LCs in both pump detunings, still remains inconclusive. Our investi-

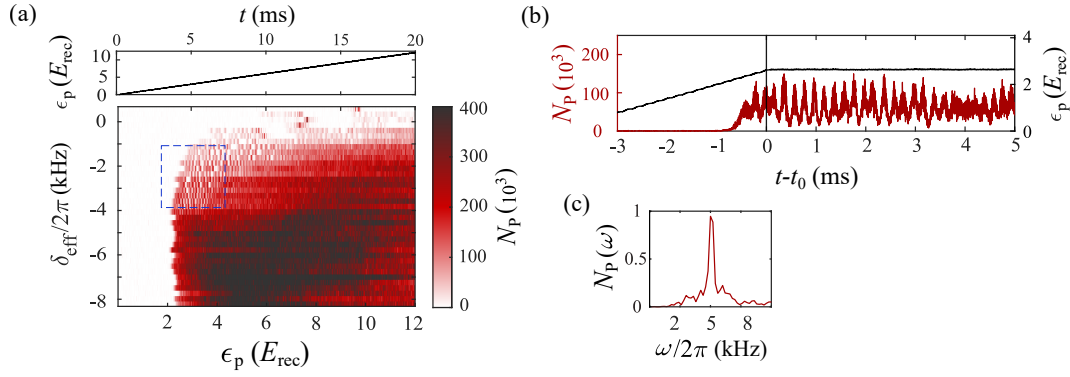


**Figure 6.2:** Observation of limit cycle using red-detuned pump light. (a) top: pump strength protocol. bottom: phase diagram spanned by the quantities pump detuning  $\delta_{\text{eff}}$  and pump strength  $\epsilon_p$ . The color code represents the detected photon number  $N_p$ . The blue box represents the area where LCs can be observed in the phase diagram. (b) shows an exemplary single realization of a limit cycle, leading to an oscillatory behavior of  $N_p$ . The data is taken at fixed  $\delta_{\text{eff}} = -1.6$  kHz and  $\epsilon_p$  is kept constant at  $2.6 E_{\text{rec}}$  for times  $t$  larger than  $t_0$ , marked with a vertical line. (c) shows a Fourier spectrum of  $N_p$  observed in (b).

gations aim to uncover the general explanation of how LCs emerge in the atom-cavity system, regardless of the pump detuning. We are developing a model that allows for understanding the phenomena beyond the existing numerical simulations. Preliminary results are suggesting that the emergence of LCs in our system arises as a first step of *a route to chaos*. A route to chaos is the process where a stable dynamical system transitions into exhibiting chaotic behavior. Often, this route includes a series of bifurcation processes [114]. Bifurcations in a route to chaos are well-known in non-linear physical systems, for example, circular Couette flow systems<sup>2</sup> [115], Rayleigh-Bénard convection systems<sup>3</sup> [115, 116], acoustical turbulence systems<sup>4</sup> [117], Q-switched CO<sub>2</sub> lasers [118], driven nonlinear semiconductors [119], and many more.

<sup>2</sup>A system of viscous fluid confining in a gap between two rotating cylinders.

<sup>3</sup>A system comprising a layer of fluid between two horizontal plates, where the lower plate is warmer.

<sup>4</sup>A system of liquid irradiated with high-intensity sound.

# **Appendix A**

## **Supplement material of publication I**



# Supplemental Material for Observation of a dissipative time crystal

Hans Keßler,<sup>1</sup> Phatthamon Kongkhambut,<sup>1</sup> Christoph Georges,<sup>1</sup>  
Ludwig Mathey,<sup>1,2</sup> Jayson G. Cosme,<sup>3</sup> and Andreas Hemmerich<sup>1,2</sup>

<sup>1</sup>Zentrum für Optische Quantentechnologien and Institut für Laser-Physik, Universität Hamburg, 22761 Hamburg, Germany

<sup>2</sup>The Hamburg Center for Ultrafast Imaging, Luruper Chaussee 149, 22761 Hamburg, Germany

<sup>3</sup>National Institute of Physics, University of the Philippines, Diliman, Quezon City 1101, Philippines

## I. EXPERIMENTAL DETAILS

The experimental set-up, as sketched in Fig. 1a in the main text, is comprised of a magnetically trapped BEC of  $N_a = 65 \times 10^3$   $^{87}\text{Rb}$  atoms, dispersively coupled to a narrow-band high-finesse optical cavity. The cavity field has a decay rate of  $\kappa = 2\pi \times 4.55$  kHz, which is the same order of magnitude as the recoil frequency  $\omega_{\text{rec}} = E_{\text{rec}}/\hbar = 2\pi \times 3.55$  kHz. The wavelength of the pump laser is  $\lambda_P = 803$  nm, which is red detuned with respect to the relevant atomic transition of  $^{87}\text{Rb}$  at 795 nm. The maximum light shift per atom is  $U_0 = -2\pi \times 0.36$  Hz. We fix the effective detuning to  $\delta_{\text{eff}} \equiv \delta_C - (1/2)N_a U_0 = -2\pi \times 18.5$  kHz, where  $\delta_C = \omega_P - \omega_C$  is the pump-cavity detuning. An experimental sequence starts by preparing the system in the self-organized density wave (DW) phase. This is achieved by linearly increasing the pump strength  $\epsilon$  from zero to its final value  $\epsilon_0 = 3.3 E_{\text{rec}}$  in 10 ms at a fixed pump-cavity detuning  $\delta_{\text{eff}} = -2\pi \times 18.5$  kHz.

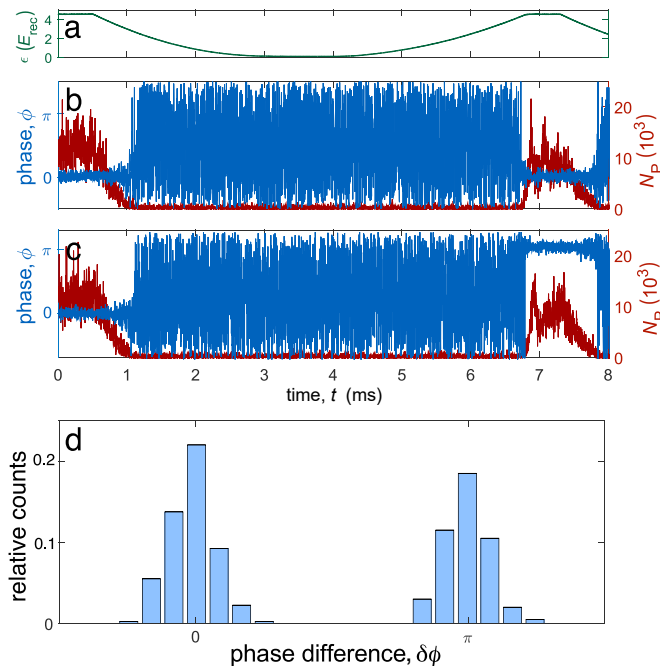


FIG. 1:  $\mathbb{Z}_2$  symmetry breaking in space. (a) Pump protocol starting in the DW phase, tuning into the BEC phase and back to the DW phase. (b),(c) Relative phases  $\phi$  (blue) and intracavity photon numbers  $N_P$  (red), measured by the heterodyne detector for single experimental runs, showing the two typical outcomes (b)  $\delta\phi \approx 0$  and (c)  $\delta\phi \approx \pi$ . (d) Histogram of the phase difference  $\delta\phi$  for 397 experimental runs.

## II. $\mathbb{Z}_2$ SYMMETRY BREAKING IN SPACE

Due to optical path length drifts, we cannot compare the phase  $\phi$  for DW realisations of different experimental runs. The stability of our balanced heterodyne detection is however sufficient to compare the phase for two subsequent DW realisations within the same experimental sequence applying the pump protocol in Fig. 1(a). In a perfect system, the

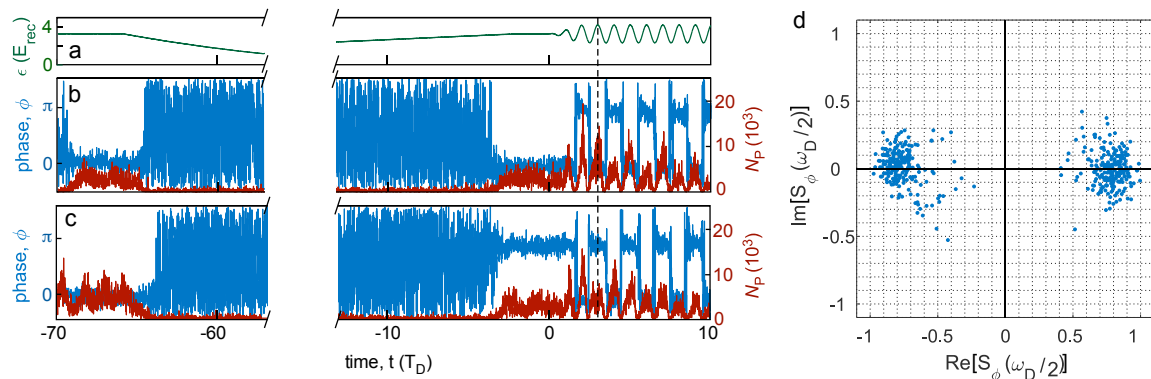


FIG. 2: Spontaneous breaking of the  $\mathbb{Z}_2$  time translation symmetry. (a) Pump protocol starting in the DW phase, tuning into the BEC phase and back to the DW phase. After a waiting time of 0.5 ms the modulation strength  $f_0$  is linearly increased to  $f_0 = 0.3$ . (b),(c) Relative phases  $\phi$  (blue) and intracavity photon numbers  $N_P$  (red), measured by the heterodyne detector for single experimental runs showing the two typical outcomes  $\delta\phi = 0$  (b) or  $\delta\phi = \pi$  (c). As a consequence, also the time-phase difference between the subharmonic response and the modulated pump strength is constrained to the values zero and  $\pi$ . This is seen by observing the relative phase  $\delta\phi$  at the time  $t_{\max}$ , where the modulated pump strength acquires a maximum, indicated by the vertical black dashed line at  $t \approx 3T_D$ . (d) Normalised Fourier component  $S_\phi(\omega_D/2)$  of the relative phase  $\delta\phi(t)$  rescaled by its maximum for 423 experimental runs.

phase difference  $\delta\phi$  between two subsequent realizations of the DW phase can take two values  $\delta\phi = 0$  or  $\delta\phi = \pi$  and does not depend on any system parameters. Since the underlying discrete symmetry breaks spontaneously, we expect equiprobable realisation of the two possible outcomes shown in Figs. 1(b) and 1(c). The relative occurrence of  $\delta\phi$  for 397 realisations is plotted in Fig. 1(d) using a binning of  $0.08\pi$ . The two maxima, corresponding to  $\delta\phi = 0$  and  $\delta\phi = \pi$ , are clearly distinguishable and the ratio of all realisations where  $\delta\phi \in [-\frac{\pi}{2}, \frac{\pi}{2}]$  over  $\delta\phi \in [\frac{\pi}{2}, \frac{3}{2}\pi]$  is 1.15. This number is close to unity, which shows that the underlying spatial  $\mathbb{Z}_2$  symmetry in our system is well established.

### III. $\mathbb{Z}_2$ SYMMETRY BREAKING IN TIME

In this section we show how the  $\mathbb{Z}_2$  symmetry breaking associated with the DW phase leads to a spontaneous breaking of the discrete  $\mathbb{Z}_2$  time translation symmetry associated with the modulated pump strength. Again, the stability of the phase reference of our heterodyne detection system is not sufficient to compare the phases  $\phi$  for different experimental runs. Therefore we follow a similar procedure as in Fig. 1, entering the DW phase twice within the same experimental run. After entering the DW phase for the second time, we start to modulate the pump strength in the same way as in Fig. 1 of the main text. The applied pump protocol is presented in Fig. 2(a). As discussed in Fig. 1(d), the phase difference  $\delta\phi$  between two subsequent realizations of the DW phase can take two values  $\delta\phi = 0$  or  $\delta\phi = \pi$  and does not depend on any system parameters. As a consequence, the time-phase difference between the observed subharmonic time-crystal oscillation and the oscillation of the pump strength becomes constrained to the possible values zero and  $\pi$ . This is seen by evaluating the relative phase  $\delta\phi$  at the time  $t_{\max}$ , where the modulated pump strength acquires a maximum, indicated by the vertical black line in Fig. 2(a) at  $t = 3T_D$ . Since the underlying discrete symmetry breaks spontaneously, we expect equiprobable realisation of the two possible outcomes shown in Figs. 2(b) and 2(c). The normalised complex value of the Fourier spectrum at the subharmonic frequency,  $S_\phi(\omega_D/2)$  of the relative phase  $\delta\phi(t)$ , rescaled by its maximum for 423 experimental runs, is shown in 2(d). The ratio between the occurrences with  $Re[S_\phi(\omega_D/2)] < 0$  over the events with  $Re[S_\phi(\omega_D/2)] > 0$  is 1.05, which shows that the discrete time translation symmetry associated with the modulation is well established.

### IV. THEORETICAL MODEL

In the frame rotating at the pump frequency  $\omega_P = 2\pi/\lambda_P$ , the Hamiltonian for the system reads[1, 2]

$$\hat{H} = \hat{H}_C + \hat{H}_A + \hat{H}_{AA} + \hat{H}_{AC}. \quad (1)$$

In Eq. (1), the Hamiltonian for the cavity with a single mode function  $\cos(kz)$  is

$$\hat{H}_C = -\hbar\delta_C\hat{a}^\dagger\hat{a}, \quad (2)$$

where  $\hat{a}$  ( $\hat{a}^\dagger$ ) is the cavity mode annihilation (creation) operator. The single-particle Hamiltonian for the atoms is given by

$$\hat{H}_A = \int dydz\hat{\Psi}^\dagger(y,z)\left[-\frac{\hbar^2}{2m}\nabla^2 + \epsilon\cos^2(ky)\right]\hat{\Psi}(y,z), \quad (3)$$

where  $m$  is the mass of an atom and  $\hat{\Psi}(y,z)$  is the atomic field operator. The short-range collisional interaction between the atoms is captured by the Hamiltonian

$$\hat{H}_{AA} = U_a \int dydz\hat{\Psi}^\dagger(y,z)\hat{\Psi}^\dagger(y,z)\hat{\Psi}(y,z)\hat{\Psi}(y,z). \quad (4)$$

The effective 2D interaction strength is  $U_a = \sqrt{2\pi}a_s\hbar^2/m\ell_x$ , where  $a_s$  is the  $s$ -wave scattering length and  $\ell_x$  is the harmonic oscillator length in the  $x$  direction. The Hamiltonian for the light-matter interaction reads

$$\begin{aligned} \hat{H}_{AC} = \hbar U_0 \int dydz\hat{\Psi}^\dagger(y,z)\left[\cos^2(kz)a^\dagger a \right. \\ \left. + \alpha_P(a + a^\dagger)\cos(ky)\cos(kz)\right]\hat{\Psi}(y,z), \end{aligned} \quad (5)$$

where  $\alpha_P \equiv \sqrt{\epsilon/\hbar|U_0|}$  is the unitless amplitude of the pump field. The dynamics of the system follows from the Heisenberg-Langevin equations,

$$\frac{\partial}{\partial t}\hat{\Psi} = \frac{i}{\hbar}[\hat{H}, \hat{\Psi}] \quad (6)$$

$$\frac{\partial}{\partial t}\hat{a} = \frac{i}{\hbar}[\hat{H}, \hat{a}] - \kappa\hat{a} + \xi, \quad (7)$$

where the stochastic noise term  $\xi$  satisfies  $\langle \xi^*(t)\xi(t') \rangle = \kappa\delta(t-t')$ . We simulate the dynamics in the semiclassical limit by transforming  $\hat{\Psi}$  and  $\hat{a}$  into classical fields according to the truncated Wigner approximation (TWA) method [3–5].

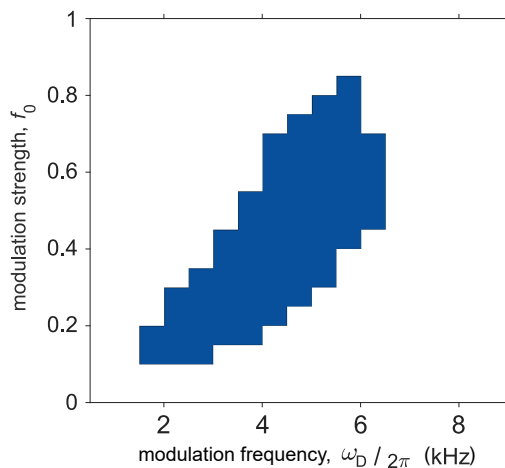


FIG. 3: Mean-field stability region of the DTC. Blue area denotes the region in the  $(f_0, \omega_D)$ -plane where a stable period-doubling response exists within the mean-field model in the absence of short-range interaction.

The TWA is a semiclassical phase space method that goes beyond mean-field theory and can be utilised to test the robustness of time crystals against quantum and stochastic noise due to the dissipative cavity [6, 7]. We numerically integrate the resulting equations of motion for an ensemble of  $10^3$  initial conditions, which sample the initial quantum

noise in the fields and the stochastic noise due to the dissipative cavity. In our simulations, apart from  $\epsilon_0$  chosen as  $\epsilon_0 = 1.03 \epsilon_{\text{cr}}$ , where  $\epsilon_{\text{cr}}$  is the critical pump strength for the BEC-DW phase transition, we use the same parameters and protocol for the pump strength as in the experiment. In the comparison of calculations of  $N_{\text{P}}(t)$  and  $C(t)$  for variable collisional interaction strengths  $E_a$  in Fig. 4 in the main text, we adjust the pump strengths such that the number of intracavity photons in the DW phase is fixed to the same value.

## V. MEAN-FIELD PHASE DIAGRAM

In order to obtain a rough orientation with regard to the system parameters suitable for the appearance of a dissipative time crystal (DTC) phase, we construct a dynamical phase diagram in the clean mean-field limit, wherein the mean-field breaking short-range interaction is neglected. In particular, we seek period-doubling solutions, which are stable for at least 40 modulation cycles. As depicted in Fig. 3, modulation frequencies in the range  $\omega_{\text{D}} \in 2\pi \times [2, 8]$  kHz provide an island with a stable DTC phase. This is consistent with the experimental results in Fig. 2(g) in the main text. Fig. 4(a) and 4(b) show single shot measurements of the evolution of the intracavity photon number  $N_{\text{P}}$  (red) and the relative phase  $\phi$  between the pump and the cavity light field (blue). In Fig. 4(c) and 4(d), the corresponding mean-field simulations including phenomenological atom loss are presented.

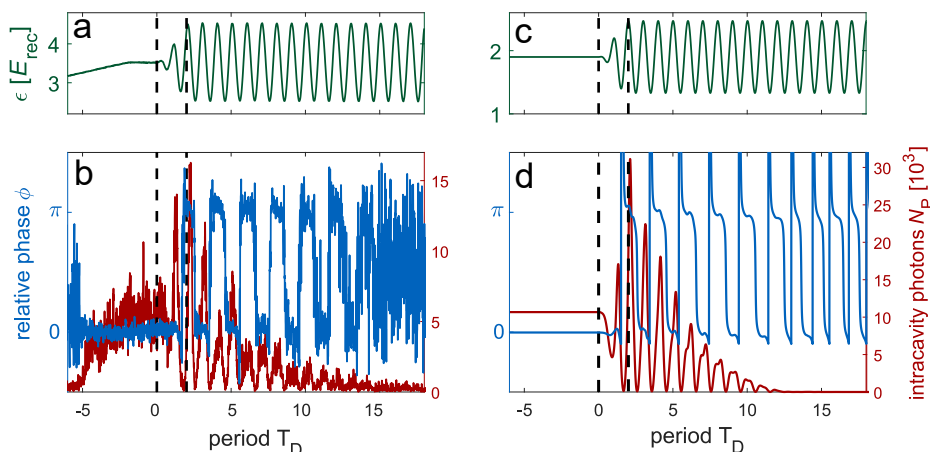


FIG. 4: Comparison of experimental data to mean-field simulations including phenomenological atom loss. (a) Time sequence for the pump with modulation strength  $f_0 = 0.3$  and modulation period  $T_{\text{D}} = 0.25$  ms. In the time interval delimited by dashed lines,  $f_0$  is linearly ramped from zero to its desired value. (b) The corresponding response of the intracavity photon number  $N_{\text{P}}$  (red) and the relative phase  $\phi$  between the pump and the cavity light field (blue). (c),(d) Corresponding mean-field simulations including atom loss.

## VI. THEORETICAL RESULTS WITH TEMPORAL DISORDER

In Fig. 5, we present the results of our TWA simulations for a noisy drive. Specifically, we add a Gaussian white noise onto the pump strength signal. An exemplary trace of the noisy drive is shown in Figs 5(a) and 5(b). Note, however, that the noise in our numerical results shown here is band-limited to 0.025 GHz, which is set by the integration step of our stochastic differential equation solver. In contrast, the noise in the experiment is band-limited to 50 kHz. This explains the appearance of a more intermittent noise in the pump signal when Fig. 5 is compared to Fig. 3 in the main text. Similar to the experiment, we quantify the noise strength by  $n \equiv \sum_{\omega} |\mathcal{E}_{\text{noisy}}(\omega)| / \sum_{\omega} |\mathcal{E}_{\text{clean}}(\omega)|$ , where  $\mathcal{E}_{\text{noisy}}$  ( $\mathcal{E}_{\text{clean}}$ ) is the Fourier spectrum of the pump in the presence (absence) of white noise. The noise strength used in Fig. 5 is  $n = 2.0$ . For this relatively weak temporal disorder, which breaks the discrete time translation symmetry imposed by the drive, our TWA results suggest that the system still exhibits long-lived period-doubling without any sign of decay after  $\sim 350$  driving cycles. This corroborates the robustness of the DTC against temporal perturbations as explored experimentally in the main text.

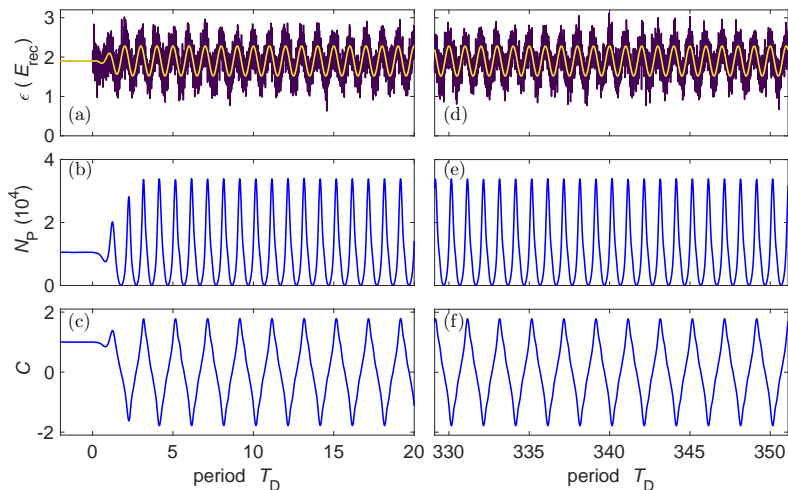


FIG. 5: Numerical results from TWA for noisy drive. (a)-(c) Short-time and (d)-(f) long-time dynamics. (a),(d) Single realization of the disordered drive [dark] and the clean periodic drive [light]. TWA results for the (b),(e) intracavity photon number and (c),(f) non-equal time correlation. The modulation strength is  $f_0 = 0.3$  and modulation period is  $T_D = 0.25$  ms.

## VII. MAPPING TO THE DICKE MODEL

The period-doubling instability of the DTC can be understood using a simple albeit incomplete description according to the mapping of the full atom-cavity Hamiltonian onto the Dicke model via the Schwinger-boson representation. Using the Holstein-Primakoff representation in the thermodynamic limit of  $N \rightarrow \infty$ , the collective spin in the Dicke model can be transformed back into bosons, leading to a coupled oscillator system, where the coupling strength is periodically driven. This coupled oscillator Hamiltonian can then be diagonalised to obtain a Hamiltonian for the lower and upper polaritonic states, where their respective frequencies are parametrically driven. Thus, driving at twice the lower polariton frequency leads to an exponential instability, which translates to a period-doubling response in the full atom-cavity model due to the presence of dissipation and the nonlinearity of the cavity-mediated interaction between the atoms.

- 
- [1] H. Ritsch, P. Domokos, F. Brennecke, and T. Esslinger, *Rev. Mod. Phys.* **85**, 553 (2013).
  - [2] D. Nagy, G. Szirmai, and P. Domokos, *Eur. Phys. J. D* **48**, 127 (2008).
  - [3] A. Polkovnikov, *Ann. Phys.* **325**, 1790 (2010), ISSN 0003-4916.
  - [4] P. B. Blakie, A. S. Bradley, M. J. Davis, R. J. Ballagh, and C. W. Gardiner, *Adv. Phys.* **57**, 363 (2008).
  - [5] I. Carusotto and C. Ciuti, *Rev. Mod. Phys.* **85**, 299 (2013).
  - [6] J. G. Cosme, J. Skulte, and L. Mathey, *Phys. Rev. A* **100**, 053615 (2019).
  - [7] H. Keßler, J. G. Cosme, C. Georges, L. Mathey, and A. Hemmerich, *New J. Phys.* **22**, 085002 (2020).

# **Appendix B**

## **Supplement material of publication II**

**Supplemental Material for  
Realization of a periodically driven open three-level Dicke model**

Phatthamon Kongkhambut,<sup>1</sup> Hans Keßler,<sup>1</sup> Jim Skulte,<sup>1,2</sup> Ludwig  
Mathey,<sup>1,2</sup> Jayson G. Cosme,<sup>3</sup> and Andreas Hemmerich<sup>1,2</sup>

<sup>1</sup>*Zentrum für Optische Quantentechnologien and Institut für Laser-Physik, Universität Hamburg, 22761 Hamburg, Germany*

<sup>2</sup>*The Hamburg Center for Ultrafast Imaging, Luruper Chaussee 149, 22761 Hamburg, Germany*

<sup>3</sup>*National Institute of Physics, University of the Philippines, Diliman, Quezon City 1101, Philippines*

(Dated: November 1, 2021)



## I. EXPERIMENTAL DETAILS

The experimental set-up, as sketched in Fig. 1(a) in the main text, is comprised of a magnetically trapped BEC of  $N_a = 65 \times 10^3$   $^{87}\text{Rb}$  atoms, dispersively coupled to a narrow-band high-finesse optical cavity. The cavity field has a decay rate of  $\kappa = 2\pi \times 3.6$  kHz, which almost equals the recoil frequency  $\omega_{\text{rec}} = E_{\text{rec}}/\hbar = 2\pi \times 3.55$  kHz. The wavelength of the pump laser is  $\lambda_P = 803$  nm, which is red detuned with respect to the relevant atomic transition of  $^{87}\text{Rb}$  at 795 nm. The maximum light shift per atom is  $U_0 = -2\pi \times 0.36$  Hz. We fix the effective detuning to  $\delta_{\text{eff}} \equiv \delta_C - (1/2)N_a U_0 = -2\pi \times 18.5$  kHz, where  $\delta_C = \omega_P - \omega_C$  is the pump-cavity detuning. A typical experimental sequence starts by preparing the system in the superradiant phase. This is achieved by linearly increasing the pump strength  $\epsilon$  from zero to its final value  $\epsilon_0 = 3.3 E_{\text{rec}}$  in 10 ms at a fixed effective pump-cavity detuning  $\delta_{\text{eff}} = -2\pi \times 18.5$  kHz.

## II. THREE-LEVEL SYSTEM

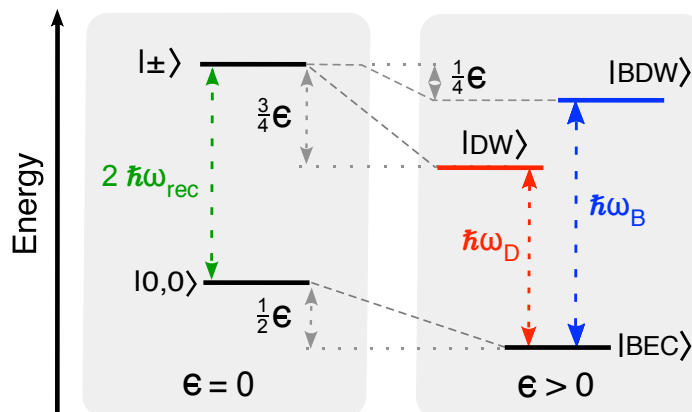


FIG. 1. V-shaped three-level system. On the left, the case of zero pump field strength  $\epsilon = 0$  is shown with the zero momentum ground state  $|0,0\rangle$  and two degenerate excited states  $|+\rangle \equiv \sum_{\nu,\mu \in \{-1,1\}} |\nu\hbar k, \mu\hbar k\rangle$  and  $|-\rangle \equiv \sum_{\nu,\mu \in \{-1,1\}} \nu |\nu\hbar k, \mu\hbar k\rangle$  associated with an energy  $2\hbar\omega_{\text{rec}}$  above that of  $|0,0\rangle$  ( $\hbar\omega_{\text{rec}} = \text{recoil energy}$ ). For  $\epsilon > 0$ , these bare states acquire different light-shifts giving rise to the modified states  $|BEC\rangle$ ,  $|DW\rangle$ , and  $|BDW\rangle$ . They span a three-level system with the resonance frequencies  $\omega_D$  and  $\omega_B$  for the left and right leg of the V-shaped coupling scheme, respectively.

Consider atoms in their electronic ground state. For each atom, a V-shaped three-level system arises as sketched in Fig. 1. For a vanishing pump field  $\epsilon = 0$ , the ground state is the bare zero momentum state  $|0,0\rangle$  and we consider two degenerate excited momentum states given by the even and odd superpositions  $|+\rangle \equiv \sum_{\nu,\mu \in \{-1,1\}} |\nu\hbar k, \mu\hbar k\rangle$  and  $|-\rangle \equiv \sum_{\nu,\mu \in \{-1,1\}} \nu |\nu\hbar k, \mu\hbar k\rangle$ , respectively. Here,  $|\pm\hbar k, \pm\hbar k\rangle$  denotes the momentum eigenstates with  $\pm\hbar k$  momentum along the pump axis ( $y$ -axis) and  $\pm\hbar k$  momentum along the cavity axis ( $z$ -axis). As shown in Fig. 1, in the presence of a pump field, these states acquire light-shifts of different sizes, giving rise to the three modified states  $|BEC\rangle$ ,  $|DW\rangle$  and  $|BDW\rangle$ . The  $|BEC\rangle$  state is associated with the zero momentum state  $|0,0\rangle$ , and hence a homogeneous density distribution. The light-shift for this state is  $-\epsilon/2$  with  $\epsilon$  denoting the potential depth of the pump standing wave [1].  $|DW\rangle$  is associated with the bare momentum state  $|+\rangle$  and therefore a density distribution proportional to  $|\cos(ky)\cos(ky)|^2$ . This distribution is localized in the antinodes of the pump wave and thus possesses a larger light-shift  $-3\epsilon/4$  [1]. Finally,  $|BDW\rangle$  is associated with  $|-\rangle$  and therefore a density distribution proportional to  $|\sin(ky)\cos(ky)|^2$ , which matches with the nodes of the pump wave and hence possesses the smallest light-shift  $-\epsilon/4$  [1].

The preceding discussion strictly applies, if  $\epsilon$  remains below a critical value  $\epsilon_{\text{crt}}$ , beyond which the  $|BEC\rangle$  state undergoes a phase transition to the superradiant state of the regular two-level Dicke model. In particular, above  $\epsilon_{\text{crt}}$  a coherent intra-cavity field arises, which mixes  $|BEC\rangle$  and  $|DW\rangle$  and adds additional light-shifts to these states. In the present work, we operate either below or slightly above  $\epsilon_{\text{crt}}$ , where this additional mixing and the associated

light-shifts are assumed sufficiently small to be neglected.

### III. ATOM-CAVITY MODEL

Considering only the pump and cavity directions and neglecting contact interactions between the atoms, the shaken atom-cavity system can be modeled by the many-body Hamiltonian

$$\hat{H}/\hbar = -\delta_C \hat{a}^\dagger \hat{a} + \int dy dz \hat{\Psi}^\dagger(y, z) \left[ -\frac{\hbar}{2m} \nabla^2 - \omega_{\text{rec}} \epsilon \cos^2(ky + \phi(t)) + U_0 \hat{a}^\dagger \hat{a} \cos^2(kz) \right. \\ \left. - \sqrt{\omega_{\text{rec}} |U_0| \epsilon_p} \cos(ky + \phi(t)) \cos(kz) (a^\dagger + a) \right] \hat{\Psi}(y, z), \quad (1)$$

where  $\delta_C$  is the pump-cavity detuning,  $U_0 < 0$  is the maximum light shift per atom, and  $\epsilon$  is the pump intensity in units of the recoil energy  $E_{\text{rec}}$ . This Hamiltonian can be mapped onto the driven open three-level Dicke model (cf. main text) by considering only the five lowest momentum modes of the atoms,  $|0, 0\rangle$  and  $|\pm \hbar k, \pm \hbar k\rangle$ , where  $k = 2\pi/\lambda_P$  is the wavenumber of the pump (see [1] for details). This assumption is valid when the occupations of higher momentum modes are kept negligible, by initializing the system close to the phase boundary between the homogeneous  $|\text{BEC}\rangle$  state and the superradiant phase. The matter sector of the superradiant phase, then mainly consists of the  $|\text{BEC}\rangle$  state with a small admixture of the  $|\text{DW}\rangle$  state, which exhibits a density modulation  $\propto |\sin(ky) \cos(kz)|^2$  and hence, the bosonic atomic field operator can be expanded as  $\hat{\Psi}(y, z) \sim \hat{c}_1 + \hat{c}_2 2 \cos(ky) \cos(kz)$  [2]. The Schwinger boson representation can be used to map the transversely pumped atom-cavity Hamiltonian onto the standard two-level Dicke model [2, 3]. The order parameter for the  $|\text{DW}\rangle$  state is  $\Theta_{\text{DW}} = \langle \cos(ky) \cos(kz) \rangle$  in bosonic operator representation, while it is  $\Theta_{\text{DW}} = \langle \hat{J}_x^{\text{D}} \rangle$  in pseudospin representation. In our experiment, periodic shaking allows for occupation of the  $|\text{BDW}\rangle$  state, which displays a density modulation  $\propto |\sin(ky) \cos(kz)|^2$ . The order parameter for  $|\text{BDW}\rangle$  is either  $\Theta_{\text{BDW}} = \langle \sin(ky) \cos(kz) \rangle$  or  $\Theta_{\text{BDW}} = \langle \hat{J}_x^{\text{B}} \rangle$ . Taking this into account, the atomic field operator should be extended as  $\hat{\Psi}(y, z) \sim \hat{c}_1 + \hat{c}_2 2 \cos(ky) \cos(kz) + \hat{c}_3 2 \sin(ky) \cos(kz)$ . The driven three-level Dicke model in the main text can then be obtained using an extended Schwinger boson representation that includes this new mode [1]. The mapping leads to an effective cavity field frequency of  $\omega = (3U_0 N)/4 - \delta_C$ . The strength of the light-matter interaction is  $\lambda/\sqrt{N} = -\sqrt{\omega_{\text{rec}} \epsilon_p |U_0|}/2$ . Moreover, we obtain  $\omega_{\text{D}} = 2\omega_{\text{rec}}(1 - \epsilon_p/8)$  and  $\omega_{\text{B}} = 2\omega_{\text{rec}}(1 + \epsilon_p/8)$  (see Eq. (2) of the main text). These frequency shifts are depicted in Fig. 1.

### IV. DEPENDENCE OF THE DENSITY WAVE FREQUENCY ON THE MODULATION STRENGTH

As shown in Fig. 2, the density wave frequency  $\omega_{\text{DW}}$  depends weakly on the modulation strength  $f_0$  but the slope is much smaller as for the dependence on the modulation frequency  $\omega_{\text{dr}}$  and we neglect this effect in the construction of the phase diagram in Fig. 3(b) of the main text. It can be explained as follows. Due to the modulation the atoms are sitting on the slope of the light-induced potential and they effectively feel a slightly weaker pump lattice depth  $\epsilon$ . This effect increases with increasing  $f_0$ . Since the position of the bond density wave resonance  $\omega_{\text{BDW}}$  shifts to lower values for smaller  $\epsilon$  and  $\omega_{\text{DW}} = \omega_{\text{BDW}} - \omega_{\text{dr}}$ , the density wave frequency response  $\omega_{\text{DW}}$  increases with increasing modulation strength  $f_0$ .

### V. MEASURING THE POSITION OF THE PARAMETRIC RESONANCE BY THE DEPLETION OF THE INTRACAVITY FIELD.

As mentioned in the main text, there are three possibilities to measure the position of the bond density wave resonance  $\omega_{\text{BDW}}$ . Firstly, as shown in Fig. 3(a) of the main text, via a linear fit of the density wave frequency response  $\omega_{\text{DW}}$ , and, secondly, from the oscillation of the asymmetry of the momentum modes with negative and positive momentum with respect to the pump direction  $F_{+1, \pm 1} - F_{-1, \pm 1}$ . The third method is demonstrated in this paragraph by looking at the depletion of the cavity field in the parameter space spanned by the modulation frequency  $\omega_{\text{dr}}$  and modulation strength  $f_0$ . On resonance the intracavity photon number  $N_P$  depletes fastest for a fixed  $f_0$ . To quantify this effect, we divide the parameter space into  $20 \times 16$  plaquettes. Then, we average  $\sum N_P$  in the interval from 2 to 3 ms after starting the modulation, and over multiple experimental runs.

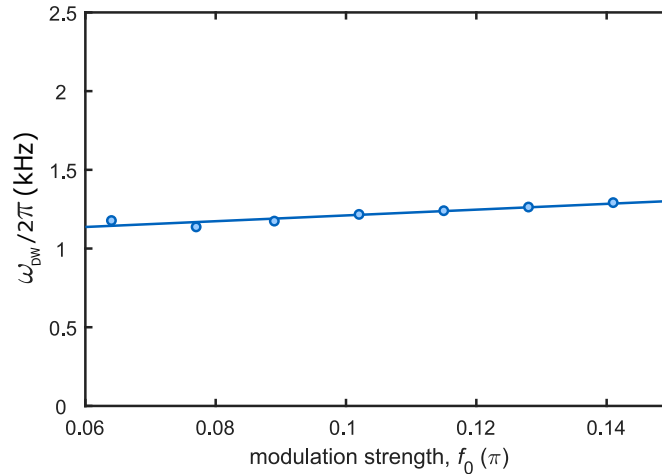


FIG. 2. Response frequency  $\omega_{\text{DW}}$  versus modulation strength.  $\omega_{\text{DW}}$  is plotted against  $f_0$  for fixed  $\omega_{\text{dr}} = 2\pi \times 11.5$  kHz, using the protocol described in Fig. 3(a) of the main text.

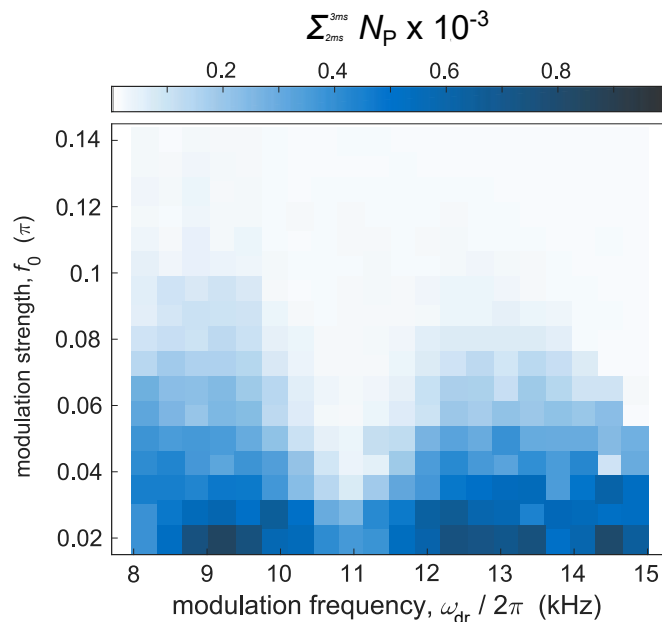


FIG. 3. Sum of  $N_P$  in the interval from 2 to 3 ms. We follow the protocol described in Fig. 3 of the main text for variable modulation frequencies  $\omega_{\text{dr}}$  and strengths  $f_0$ . The color scale parametrizes the sum over the intracavity photon number  $N_P$  in the interval [2,3] ms after reaching the final modulation strength  $f_0$ .

## VI. RELATION BETWEEN THE MOMENTUM IMBALANCE AND THE DENSITY WAVE/BOND DENSITY WAVE ORDER PARAMETERS

The density wave and bond density wave order parameters are defined as

$$\Theta_{\text{DW}} = \int \cos(ky) \cos(kz) |\psi(y, z)|^2 dx dy \quad (2)$$

$$\Theta_{\text{BDW}} = \int \sin(ky) \cos(kz) |\psi(y, z)|^2 dx dy, \quad (3)$$

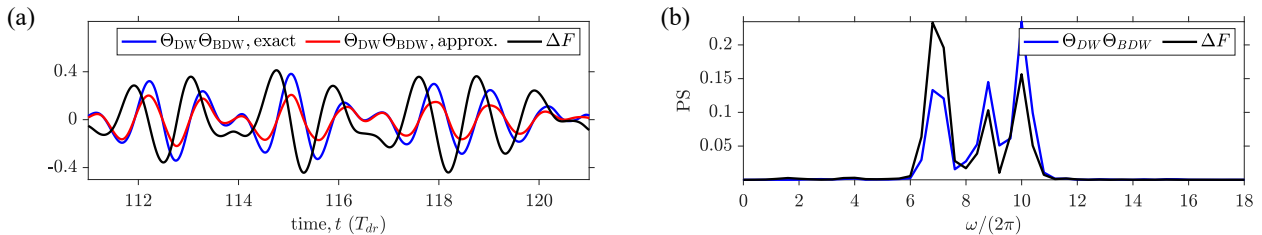


FIG. 4. Comparison between the product of the two order parameters  $\Theta_{\text{DW}} \times \Theta_{\text{BDW}}$  and the momentum imbalance  $\Delta F$ . The modulation strength is  $f_0 = 0.1$ . (cf. text)

respectively. Using the spatial translation symmetry in the system we expand the atomic field in terms of plane waves as

$$\psi(y, z) = \sum_{n,m} \phi_{n,m} e^{iny} e^{imz}. \quad (4)$$

With this the order parameter can be written in the momentum basis as

$$\Theta_{\text{DW}} = \frac{1}{4} \sum_{n,m} (\phi_{n+1,m+1}^* + \phi_{n+1,m-1}^* + \phi_{n-1,m+1}^* + \phi_{n-1,m-1}^*) \phi_{n,m} \quad (5)$$

$$\Theta_{\text{BDW}} = \frac{1}{4i} \sum_{n,m} (\phi_{n+1,m+1}^* + \phi_{n+1,m-1}^* - \phi_{n-1,m+1}^* - \phi_{n-1,m-1}^*) \phi_{n,m}. \quad (6)$$

In the following we will only retain the lowest five momentum modes  $\{\phi_{0,0}, \phi_{\pm,\pm}\}$ . We approximate the order parameters as

$$\Theta_{\text{DW}} = \frac{1}{4} (\phi_{+,+}^* + \phi_{+,-}^* + \phi_{-,+}^* + \phi_{-,-}^*) \phi_{0,0} + \text{h.c.} \quad (7)$$

$$\Theta_{\text{BDW}} = \frac{1}{4i} (\phi_{+,+}^* + \phi_{+,-}^* - \phi_{-,+}^* - \phi_{-,-}^*) \phi_{0,0} + \text{h.c.} \quad (8)$$

As the momentum modes along the  $z$ -direction will stay degenerate, we denote  $\phi_{+,\pm} = \phi_+$  and  $\phi_{-,\pm} = \phi_-$  and introduce the shorthand notation  $\phi_{0,0} = \phi_0$ . Then, the order parameter can be written as

$$\Theta_{\text{DW}} = \frac{1}{2} (\phi_+^* + \phi_-^*) \phi_0 + \text{h.c.} \quad (9)$$

$$\Theta_{\text{BDW}} = \frac{1}{2i} (\phi_+^* - \phi_-^*) \phi_0 + \text{h.c.} \quad (10)$$

The product of these two order parameters leads to

$$\Theta_{\text{DW}} \times \Theta_{\text{BDW}} = \frac{1}{4i} \{ (\phi_0^*)^2 ((\phi_+)^2 - \phi_-^2) - (\phi_0)^2 ((\phi_+^*)^2 - \phi_-^{*2}) + 2|\phi_0|^2 (\phi_-^* \phi_+ - \phi_+^* \phi_-) \} \quad (11)$$

$$= \frac{|\phi_0|^2}{2} (|\phi_+|^2 \sin(2(\theta_+ - \theta_0)) - |\phi_-|^2 \sin(2(\theta_- - \theta_0)) + 2|\phi_+||\phi_-| \sin(\theta_+ - \theta_-)), \quad (12)$$

where we used in the last line  $\psi_i = |\psi_i| \exp(i\theta_i)$ . From our numerics, we find that this observable, as measured in the experiment, can be approximated by

$$\Theta_{\text{DW}} \times \Theta_{\text{BDW}} \approx \frac{|\phi_0|^2}{2} (|\phi_+|^2 - |\phi_-|^2) \equiv \Delta F. \quad (13)$$

Fig. 4 (a) shows a comparison between the product  $\Theta_{\text{DW}} \times \Theta_{\text{BDW}}$  of the two order parameters and the momentum imbalance  $\Delta F$ . The blue trace shows the exact numerical result. The red trace shows an approximation, if only the five lowest momentum modes are accounted for. To further validate our findings, we compute in Fig. 4 (b) the power spectra of  $\Theta_{\text{DW}} \times \Theta_{\text{BDW}}$  and  $\Delta F$ . Fig. 5 shows that for a small ( $f_0 = 0.001$ ) driving strength  $\Theta_{\text{DW}} \times \Theta_{\text{BDW}}$  and  $\Delta F$  approach zero. Hence, the driven three-level Dicke model regime can only be realized for sufficiently strong driving.

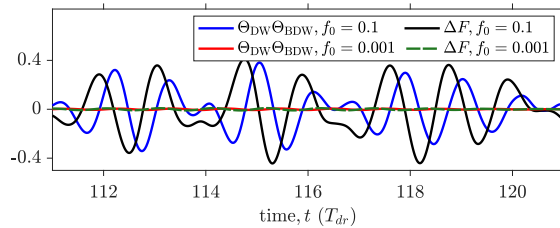


FIG. 5. Comparison of  $\Theta_{\text{DW}} \times \Theta_{\text{BDW}}$  and  $\Delta F$  for driving strengths  $f_0 = 0.1$  and  $f_0 = 0.001$ , respectively.

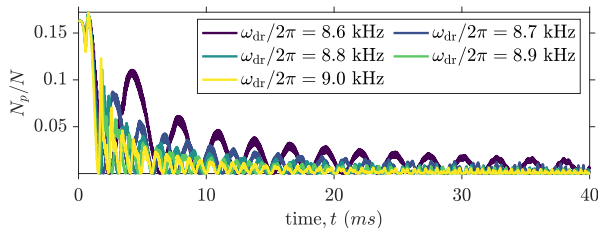


FIG. 6. Decay of the time crystal response for different detunings. We choose a modulation strength of  $f_0 = 0.05$ . The resonance frequency is located at  $\approx 8.45$  kHz. For larger detunings the time crystal melts more quickly.

## VII. LIFETIME OF THE TIME CRYSTALLINE RESPONSE

As was pointed out in [4], the time crystalline response becomes unstable/pre-thermal as one scans further away from the resonance. Using mean-field theory without contact interactions, Fig. 6 shows the decay of the oscillations for different detunings of the driving frequency with respect to the resonance frequency. We note that this effect contributes to the decay observed in the experiment.

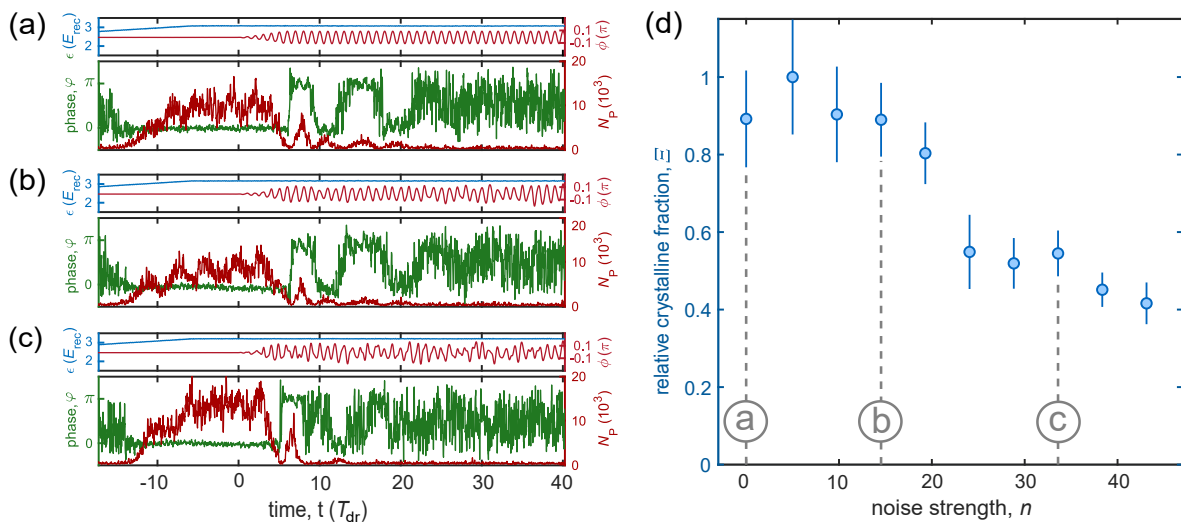


FIG. 7. Robustness of the incommensurate time crystal. (a)-(c) Single-shot experimental runs for the noise strengths marked in subplot (d) with the gray dashed lines. Top panels: single-shot protocols for the pump strength. Bottom panel: corresponding time evolution of the relative phase  $\varphi$  (green trace) and intracavity photon number  $N_P$  (red trace). (d) Dependence of the relative crystalline fraction  $\Xi$  on the noise strength averaged over 10 experimental runs with  $f_0 = 0.1 \pi$  and  $\omega_{\text{dr}} = 2\pi \times 11.5$  kHz.

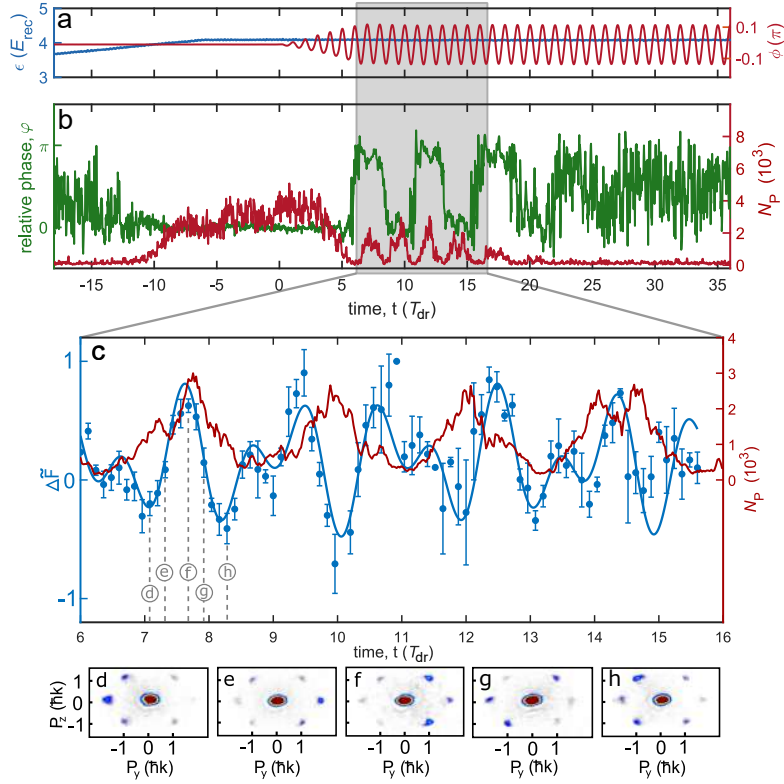


FIG. 8. Single-shot realization of DBDW order. (a) Time sequence for the pump lattice depth (blue) and the phase  $\phi$  of the pump field (red) with modulation strength  $f_0 = 0.13\pi$  and a modulation frequency  $\omega_{\text{dr}} = 12.0$  kHz. (b) Phase difference  $\varphi$  between the pump and intracavity field (green trace) and photon number  $N_P$  in the cavity (red trace). The dashed vertical lines mark the time interval during which the modulation strength is increased. The gray shaded area shows the time window for the zoom presented in (c). (c) The red trace repeats the intracavity photon number  $N_P$  from (b). The blue data points plot the product  $\Theta_{\text{DW}} \times \Theta_{\text{BDW}}$ , approximately given by the difference between the number of atoms populating the momentum modes with positive and negative momentum with respect to the pump direction  $\Delta\bar{F} = (F_{+1, \pm 1} - F_{-1, \pm 1}) / (F_{+1, \pm 1} + F_{-1, \pm 1})_{\text{max}}$  (see also Fig. 1(c) and Fig. 2(c) of the main text). Each data point is averaged over 5 realizations. The solid line shows a fit with a product of two harmonic oscillations. (d)-(h) Single-shot momentum distributions recorded at the times marked in (c).

### VIII. ROBUSTNESS AGAINST TEMPORAL PERTURBATIONS.

The robustness against temporal perturbations is one of the main characteristics of time crystalline dynamics. We have tested the stability of the observed bond density wave phase against artificial white noise on the modulation signal with a bandwidth of 20 kHz. The applied noise strength is measured by  $n \equiv \sum_{\omega=0}^{2\pi \times 20 \text{ kHz}} |\mathcal{E}_{\text{noisy}}(\omega)| / \sum_{\omega=0}^{2\pi \times 20 \text{ kHz}} |\mathcal{E}_{\text{clean}}(\omega)|$ , where  $\mathcal{E}_{\text{noisy}}$  ( $\mathcal{E}_{\text{clean}}$ ) is the Fourier spectrum of the pump in the presence (absence) of white noise. Figures 7(d) show how the relative crystalline fraction  $\Xi$  changes with increasing noise strength for fixed modulation parameters  $f_0 = 0.1$  and  $\omega_{\text{dr}} = 11.5$  kHz. Note that even for a strongly distorted pump signal, as in Fig. 7(b) the system still switches multiple times between the two sublattices before the intracavity field disappears.

### IX. SINGLE-SHOT REALIZATION OF DBDW ORDER FOR $\omega_{\text{dr}} = 12$ KHZ

We measured the momentum mode asymmetry for a second parameter set and present the results in Fig. 8. In Fig. 8(c) we used  $f(t) = \exp(-\tau t) A \sin(\omega_{\text{BDW}} t + \alpha) \sin(\omega_{\text{DW}} t)$  as a fit function. Here,  $\tau$  is the decay rate of  $N_P$  and  $A$  is an overall amplitude parameter. The fast BDW oscillation frequency is independent of  $\omega_{\text{dr}}$  and we measure  $\omega_{\text{BDW}} = 2\pi \times 9.8 \pm 0.1$  kHz. We find a slow oscillation frequency of  $\omega_{\text{DW}} = 2\pi \times 2.6 \pm 0.1$  kHz (see also Fig. 1(c) and Fig. 2(c) of the main text) for a driving frequency of  $\omega_{\text{dr}} = 12.0$  kHz, which agrees well with the theoretical prediction of  $\omega_{\text{DW}} = \omega_{\text{dr}} - \omega_{\text{BDW}} = 2\pi \times (12.0 - 9.8)$  kHz =  $2\pi \times 2.2$  kHz.



- 
- [1] J. Skulte, P. Kongkhambut, H. Keßler, A. Hemmerich, L. Mathey, and J. G. Cosme, [arXiv:2108.10877](#) (2021).
  - [2] F. Mivehvar, F. Piazza, T. Donner, and H. Ritsch, (2021), [arXiv:2102.04473](#).
  - [3] K. Baumann, C. Guerlin, F. Brennecke, and T. Esslinger, *Nature (London)* **464**, 1301 (2010).
  - [4] J. G. Cosme, J. Skulte, and L. Mathey, *Phys. Rev. A* **100**, 053615 (2019).



# **Appendix C**

## **Supplement material of publication IV**

# Supplemental Material for Condensate formation in a dark state of a driven atom-cavity system

Jim Skulte,<sup>1,2,\*</sup> Phatthamon Kongkhambut,<sup>1,\*</sup> Sahana Rao,<sup>1</sup> Ludwig  
Mathey,<sup>1,2</sup> Hans Keßler,<sup>1</sup> Andreas Hemmerich,<sup>1,2</sup> and Jayson G. Cosme<sup>3</sup>

<sup>1</sup>Zentrum für Optische Quantentechnologien and Institut für Laser-Physik, Universität Hamburg, 22761 Hamburg, Germany

<sup>2</sup>The Hamburg Center for Ultrafast Imaging, Luruper Chaussee 149, 22761 Hamburg, Germany

<sup>3</sup>National Institute of Physics, University of the Philippines, Diliman, Quezon City 1101, Philippines

(Dated: April 24, 2023)

## I. BEC, CAVITY, AND PUMP BEAM PROPERTIES

The experimental setup, as sketched in Fig. 1(a) in the main text, is comprised of a magnetically trapped BEC of  $N_a = 4 \times 10^4$   $^{87}\text{Rb}$  atoms, dispersively coupled to a fundamental mode of a narrowband high-finesse optical cavity. The trap creates a harmonic potential with trap frequencies  $(\omega_x, \omega_y, \omega_z) = 2\pi \times (119.0, 102.7, 24.7)$  Hz. The corresponding Thomas-Fermi radii of the ensemble are  $(r_x, r_y, r_z) = (3.7, 4.3, 18.1)$   $\mu\text{m}$ . These radii are significantly smaller than the size of the Gaussian shaped pump beam, which has a waist of  $w_{\text{pump}} \approx 125$   $\mu\text{m}$ . The pump beam is oriented transversally, with respect to the cavity axis, and retro-reflected to form a standing wave. It passes through an electro-optic modulator (EOM) twice. An AC voltage is applied to the EOM to modulate the phase of the pump field, which leads to an effective shaking of the pump lattice potential.

The pump laser is stabilized to the cavity resonance using high bandwidth servo electronics. As a drawback, the pump light is not strictly monochromatic and besides the narrow carrier, the spectrum contains two servo bumps with a frequency shift of roughly  $\pm 2$  MHz. We estimate the light power with in these side peaks being about 30% of the total light power. Since this light is far detuned, with respect to the cavity resonance, it cannot contribute to scatter photons into the cavity. In contrast, light of all frequencies contribute to the depth of the standing wave potential, and hence, contributes to the shift of the resonance frequency of the dark state  $\omega_D = (2 + \epsilon_p/4)\omega_{\text{rec}}$ . Therefore the dark state resonance frequency in the experiment is larger than the one used in our theoretical models.

The cavity field has a decay rate of  $\kappa \approx 2\pi \times 3.6$  kHz, which equals the recoil frequency  $\omega_{\text{rec}} = E_{\text{rec}}/\hbar = 2\pi \times 3.6$  kHz for  $^{87}\text{Rb}$  atoms at the pump wavelength of  $\lambda_P = 803.00$  nm. The pump laser is red detuned with respect to the relevant atomic transition of  $^{87}\text{Rb}$  at 794.98 nm. The maximum light shift per atom is  $U_0 = 2\pi \times 0.4$  Hz.

## II. CAVITY FIELD DETECTION

Our experimental system is equipped with two detection setups for the light leaking out of the cavity. On one side of the cavity, we use a single photon counting module (SPCM), which gives access to the intensity of the intracavity field and the associated photon statistics. On the other side of the cavity, a balanced heterodyne detection setup is installed, which uses the pump beam as a local reference. The beating signal of the local oscillator with the light leaking out of the cavity allows for the observation of the time evolution of the intracavity photon number  $N_P$  and the phase difference between the pump and the cavity field  $\varphi$ .

## III. EXPERIMENTAL PROTOCOL TO OBTAIN THE POPULATION OF THE DARK STATE $N_D$

To obtain the population of the dark state  $N_D$  experimentally, we ramp down the pump laser strength adiabatically within 0.5 ms, similar to the theoretical protocol described in the context of Fig.2(b) in the main text. Subsequently, a ballistic expansion of 25 ms is applied and an absorption image of the resulting density distribution is recorded, time-of-flight (TOF). Finally,  $N_D$  is obtained by summing up the occupations around the momentum modes  $\{\pm 1, \pm 1\}\hbar k$ , in accordance with the findings in Figs.3(d) and Fig.3(e) in the main text.

---

\* These authors have contributed equally to this work.

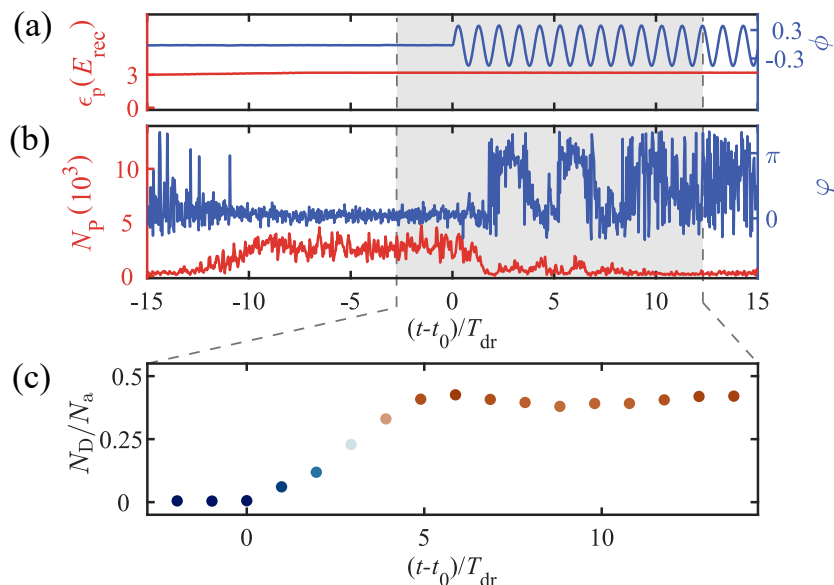


FIG. 1. Typical experimental run. (a) Experimental protocol for the intensity (red) and the phase (dashed blue) of the pump field. (b) In situ number of photons (red) in the cavity  $N_P$  and the corresponding phase difference  $\varphi$  (blue) between the pump and cavity fields. (c) Population of the dark state rescaled by the total particle number  $N_a$  (coherent fraction) for different number of driving cycles derived from TOF images.

#### IV. DYNAMICS DURING A TYPICAL EXPERIMENTAL RUN

Our experimental sequence starts by preparing a BEC and overlap it with the  $\text{TEM}_{00}$  mode of our cavity. We linearly increase the pump strength  $\epsilon$  to its desired value to initialise the system into the self-organized superradiant phase. This is indicated by a finite photon number  $N_P$  (red trace in Fig. 1(b)) and by the fixed phase difference  $\varphi$  between the pump and cavity fields. At time  $t - t_0 = 0$  we switch on the phase modulation of the pump lattice, which leads to a periodic shaking of the optical potential. The system starts to oscillate between the two possible self-organized density patterns, which can be seen by the phase difference  $\varphi$  switching between 0 and  $\pi$ . This is accompanied by an increase in the population of the dark state  $N_D/N_a$  until it reaches its maximum value at time  $t - t_0 = 5 T_{\text{dr}}$ , where  $T_{\text{dr}}$  is the driving period. Due to the increasing population of the dark state the atoms step by step decouple from the cavity field and slowly stop scattering photons from the pump into the cavity and vice versa. The photon number  $N_P$  approaches zero and the light field phase  $\varphi$  shows random values between 0 and  $2\pi$ . The system is now in a steady state and the population of the dark state, normalized to the total number of coherent atoms  $N_D/N_a$ , stays constant. Fig. 2(a) shows the dynamics of the relative population of all relevant momentum modes. Fig. 2(b) depicts the corresponding time evolution of  $N_a$ . As soon as the shaking starts ( $t - t_0 = 0$ ), the total particle number  $N_a$  drops rapidly due to cavity-field-induced heating. After the atoms are decoupled from the cavity field, the heating rate decreases.

#### V. COMPARISON OF THE RELATIVE POPULATION OF THE DARK STATE FOR PUMP LIGHT CLOSE AND FAR DETUNED WITH RESPECT TO THE CAVITY RESONANCE

We present in Fig. 3(a),(c) the experimentally obtained phase diagrams showing the population of the dark state with respect to the driving frequency  $\omega_{\text{dr}}/\omega_D$  and driving strength  $f_0$ . In Figs. 3(b),(d), we show the population of the  $\{p_y, p_z\} = \{\pm 2, 0\}\hbar k$  momentum modes for the pump light, close and far detuned with respect to the cavity resonance. For the far detuned case, the cavity is basically inactive and we do not observe population of the dark state, which demonstrates the importance of cavity photons for the excitation of the dark state. Moreover, the parameter range, wherein we observe population of the  $\{p_y, p_z\} = \{\pm 2, 0\}\hbar k$  momentum modes, is very similar for both cases, only its amplitude increases for the far detuned case since there are no atoms pumped into the dark state.

As explained in the second paragraph of Sec.I, the dark state frequency is larger in the experiment than in our theoretical models. In our experimental observations, the resonance frequency for excitation of the  $\{p_y, p_z\} = \{\pm 2, 0\}\hbar k$  momentum modes lies at  $\approx 1.45 \omega_{\text{dr}}/\omega_D$ . In SFig. 3(a), we see that in fact the transfer of atoms into the dark state is suppressed if the  $\{\pm 2, 0\}\hbar k$  resonance is approached. Rather, the atoms are transferred into the second band, as shown in SFig. 3(b), without photon scattering into the cavity. The plots in (c) and (d) for large pump-cavity detuning  $\delta_C$  show that no dark state population

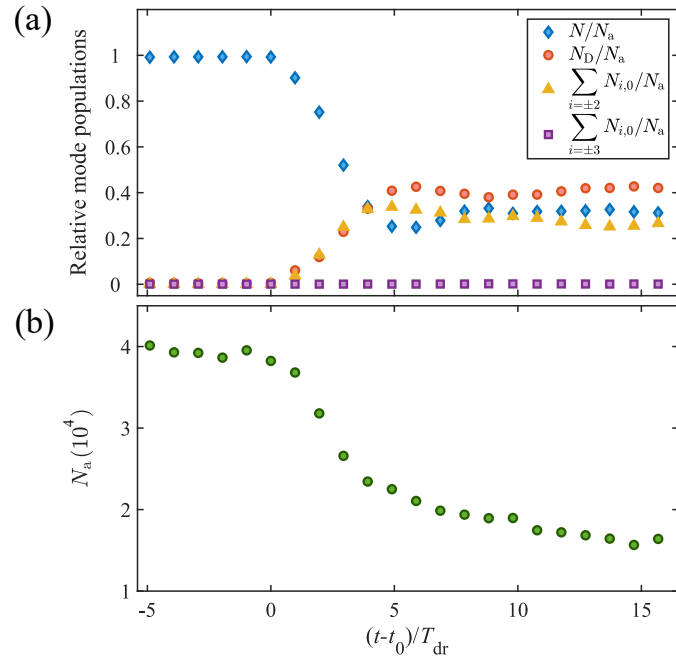


FIG. 2. (a) Time evolution of the population of the relevant momentum modes normalized to the total number of atoms (coherent fraction). (b) Time evolution of the total number of coherent atoms  $N_a$ .

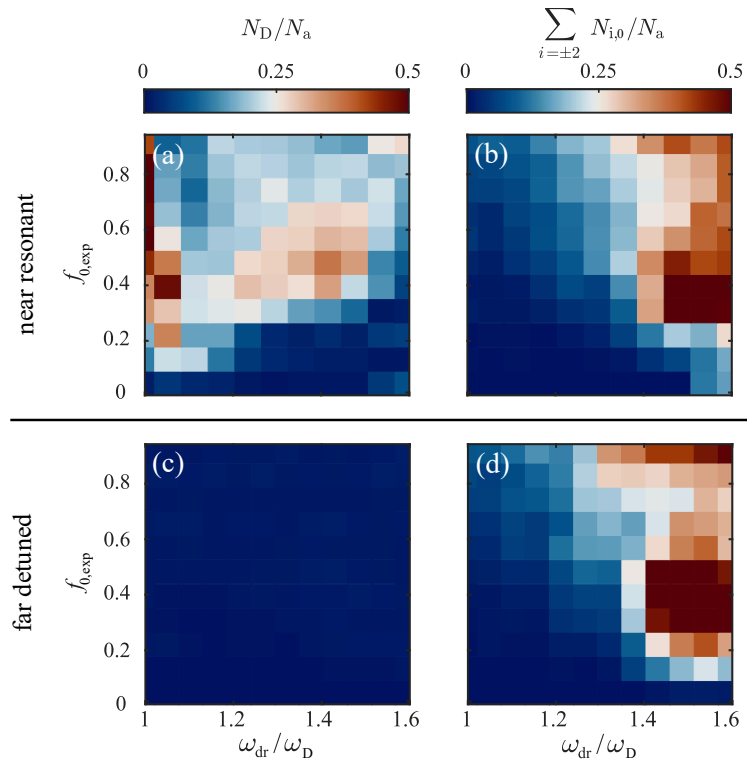


FIG. 3. Relative population of the dark state for different driving frequencies  $\omega_{\text{dr}}/\omega_D$  and driving strengths  $f_0$  for (a) the pump light close to resonance ( $\delta_C = -2\pi \times 30$  kHz) and (c) far detuned from cavity resonance after six driving cycles. The driving frequency axis is rescaled by the resonance frequency of the dark state  $\omega_D$ . (b) and (d) show the relative population of the  $\{p_y, p_z\} = \{\pm 2, 0\}$   $\hbar k$  momentum modes, which indicates the atoms populating the third band.

arises, while the direct excitation of the  $\{\pm 2, 0\}\hbar k$  momentum modes prevails. Finally, in our numerical models, the  $\{\pm 2, 0\}\hbar k$  resonance arises at  $\approx 1.7\omega_{\text{dr}}/\omega_{\text{D}}$ , which lies outside of the range of our simulations.

## VI. ATOM-CAVITY SYSTEM

Our system is well described by the Hamiltonian [1–4]

$$\begin{aligned} \hat{H}/\hbar = & -\delta_{\text{C}}\hat{a}^\dagger\hat{a} + \int dydz\hat{\Psi}^\dagger(y, z) \left[ -\frac{\hbar}{2m}\nabla^2 - \omega_{\text{rec}}\epsilon_{\text{p}}\cos^2(ky + \phi(t)) + U_0\hat{a}^\dagger\hat{a}\cos^2(kz) \right. \\ & \left. - \sqrt{\omega_{\text{rec}}|U_0|\epsilon_{\text{p}}}\cos(ky + \phi(t))\cos(kz)(\hat{a}^\dagger + \hat{a}) \right] \hat{\Psi}(y, z), \end{aligned} \quad (1)$$

where  $\delta_{\text{C}}$  is the pump-cavity detuning, and  $U_0 < 0$  is the frequency shift of the cavity resonance due to a single atom ( $|U_0| = 2\pi \times 0.4$  kHz). The phase of the pump field is periodically driven according to  $\phi(t) = f_0 \sin(\omega_{\text{dr}}t)$  with the modulation index  $f_0$  and the modulation frequency  $\omega_{\text{dr}}$ . Furthermore,  $\hat{a}$  ( $\hat{a}^\dagger$ ) is the annihilation (creation) operator for a photon in the single-mode cavity, while  $\hat{\Psi}$  ( $\hat{\Psi}^\dagger$ ) is the bosonic annihilation (creation) field operator for the atoms. Here,  $k$  denotes the wave number of the pump light,  $\epsilon_{\text{p}}$  is the pump strength, quantified in terms of the maximal energy depth of the pump lattice in units of the recoil energy  $E_{\text{rec}} = \hbar\omega_{\text{rec}}$  with the recoil frequency  $\omega_{\text{rec}} = \hbar k^2/2m$ , where  $m$  is the atomic mass. The experiment operates in the recoil-resolved regime, i.e., the loss rate of the cavity photons  $\kappa$  is smaller than the recoil frequency  $\omega_{\text{rec}}$ . For our system  $\omega_{\text{rec}} = 2\pi \times 3.6$  kHz. We emphasize the importance of the recoil-resolved regime [5, 6] to excite the atoms into the dark state, as the underlying mechanism relies on a coherent coupling of a limited number of momentum modes.

## VII. PROCESSES FOR POPULATING THE DARK STATE

We briefly discuss the different scattering channels for populating the dark state in our theoretical models, i.e., the three-mode Dicke model and full-atom cavity simulations, and in the experimental setup.

First, we discuss the difference between the full atom-cavity model and the three-level Dicke model. In the full atom-cavity system, we achieve a higher dark state population as compared to the results of the three-mode Dicke model after 7 driving cycles. In the three-mode model, we only consider momentum modes up to  $\{p_y, p_z\} = \{\pm 1, \pm 1\}\hbar k$  and neglect the  $\{p_y, p_z\} = \{\pm 2, 0\}\hbar k$  modes. However, as can be seen from the last line in the Hamiltonian in Eq. 4, atoms in the  $\{p_y, p_z\} = \{\pm 2, 0\}\hbar k$  modes can be transferred into the dark state  $|D\rangle \equiv \sum_{\nu, \mu \in \{-1, 1\}} \nu | \nu \hbar k, \mu \hbar k \rangle$ . This enhances the dark state population in the full atom-cavity system as compared to the three-mode Dicke model.

Next, we discuss the population of the dark state in the experiment. While the experiment includes the channel for scattering from  $\{p_y, p_z\} = \{\pm 2, 0\}\hbar k$  into the dark state, there are additional factors that decrease the efficiency of populating the dark state, i.e., heating and atom loss introduced by phase modulation of the pump wave. The atom loss effectively shifts the critical pump strength required to enter the superradiant phase, as the number of scatterers of photons decreases. Since cavity-photon-mediated interactions are necessary for the transfer of atoms into the dark state, atom loss, which decreases the occupation of the cavity mode, attenuates the process of populating the dark state. Furthermore, in the experiment, as discussed in Sec.I, the additional side lobes of the pump beam frequency spectrum push the dark state resonance towards higher frequencies. This effectively reduces the regime where the dark state can be populated, which is restricted to driving frequencies smaller than the resonance for excitation of the  $\{p_y, p_z\} = \{\pm 2, 0\}\hbar k$  momentum modes. The latter resonance gives rise to an efficient transfer of the atoms into the maximum of the second band of the pump wave potential. The relevant driving term in Eq. 1 is  $2\phi(t)\sin(2ky)$ , which arises by approximating  $\cos(ky + \phi(t))^2$  for the case of small driving strengths. We note that the corresponding resonance frequency is light-shifted by the pump beam, however, this effect can be neglected for the relatively shallow pump lattice used in this work.

## VIII. THREE-LEVEL SYSTEM

As first shown in [3], the Hamiltonian in Eq. 1 can be mapped onto a parametrically driven dissipative three level model. Here, to capture the effects for strong driving, where  $f_0 \ll 1$  is not fulfilled, we use trigonometric identities and the following



Jacobi-Anger expansions [7]

$$\cos(z \sin(\theta)) = J_0(z) + 2 \sum_{n=1}^{\infty} J_{2n}(z) \cos(2n\theta) \quad (2)$$

$$\sin(z \sin(\theta)) = 2 \sum_{n=1}^{\infty} J_{2n-1}(z) \cos((2n-1)\theta). \quad (3)$$

The Hamiltonian in Eq. 1 acquires the form

$$\begin{aligned} \hat{H}/\hbar = & -\delta_C \hat{a}^\dagger \hat{a} + U_0 \hat{a}^\dagger \hat{a} \int dy dz \hat{\Psi}^\dagger(y, z) \cos^2(kz) \hat{\Psi}(y, z) \\ & - \omega_{\text{rec}} \epsilon_p \int dy dz \hat{\Psi}^\dagger(y, z) \frac{1 + \cos(2ky) [J_0(2f_0) + 2h_2(t)] - 2 \sin(2ky) g_2(t)}{2} \hat{\Psi}(y, z) \\ & - \sqrt{\omega_{\text{rec}} |U_0| \epsilon_p} (a^\dagger + a) \int dy dz \hat{\Psi}^\dagger(y, z) \cos(ky) \cos(kz) (J_0(f_0) + 2h_1(t)) \hat{\Psi}(y, z) \\ & + \sqrt{\omega_{\text{rec}} |U_0| \epsilon_p} (a^\dagger + a) \int dy dz \hat{\Psi}^\dagger(y, z) \sin(ky) \cos(kz) 2g_1(t) \hat{\Psi}(y, z), \end{aligned} \quad (4)$$

where we defined  $h_2(t) = \sum_{n=1}^{\infty} J_{2n}(2f_0) \cos(2n\omega_{\text{dr}}t)$  and  $g_2(t) = \sum_{n=1}^{\infty} J_{2n-1}(2f_0) \sin((2n-1)\omega_{\text{dr}}t)$  and  $h_1(t) = \sum_{n=1}^{\infty} J_{2n}(f_0) \cos(2n\omega_{\text{dr}}t)$  and  $g_1(t) = \sum_{n=1}^{\infty} J_{2n-1}(f_0) \sin((2n-1)\omega_{\text{dr}}t)$ . Next, the atomic field operator is approximated as

$$\hat{\Psi}(y, z) = \hat{c}_0 \psi_0(y, z) + \hat{c}_1 \psi_1(y, z) + \hat{c}_2 \psi_2(y, z) \quad (5)$$

where  $\hat{c}_i$  are bosonic annihilation operator, and  $\psi_0(y, z) = 1$ ,  $\psi_1(y, z) = 2 \cos(ky) \cos(kz)$  and  $\psi_2(y, z) = 2 \sin(ky) \cos(kz)$ . We note that in applying this approximation we neglect higher momentum mode contributions, e.g.  $\cos(2ky)$ , which contribute heavily for higher driving frequencies around  $\sim 14.5$  kHz as can be seen in Fig. 3.

Under parity change  $y \rightarrow -y$  these wave functions transform as

$$\mathcal{P}_y \psi_0(y, z) = \psi_0(-y, z) = +\psi_0(y, z) \quad (6)$$

$$\mathcal{P}_y \psi_1(y, z) = \psi_1(-y, z) = +\psi_1(y, z) \quad (7)$$

$$\mathcal{P}_y \psi_2(y, z) = \psi_2(-y, z) = -\psi_2(y, z). \quad (8)$$

Hence, only  $\psi_2$  gets a minus sign upon application of  $\mathcal{P}_y$ . Using a Schwinger boson representation, the bosonic operators can be mapped onto pseudo-spin operators to obtain a driven three-level Dicke Hamiltonian

$$\begin{aligned} H/\hbar = & \omega \hat{a}^\dagger \hat{a} + (\omega_B - \Delta_{f_0}) \hat{J}_z^B + (\omega_D + \Delta_{f_0}) \hat{J}_z^D + f_2(t) (\omega_B - \omega_D) \left( \hat{J}_z^D - \hat{J}_z^B \right) + 2g_2(t) (\omega_B - \omega_D) \hat{J}_x^{\text{BD}} \\ & + \frac{2(\lambda_{f_0} + \eta(t))}{\sqrt{N}} (\hat{a}^\dagger + \hat{a}) \hat{J}_x^B - \frac{2\zeta(t)}{\sqrt{N}} (\hat{a}^\dagger + \hat{a}) \hat{J}_x^D, \end{aligned} \quad (9)$$

where  $\omega_D = 2\omega_{\text{rec}}(1 - \frac{\epsilon_p}{8})$ ,  $\omega_B = 2\omega_{\text{rec}}(1 + \frac{\epsilon_p}{8})$ ,  $\Delta_{f_0} = \frac{\epsilon_p \omega_{\text{rec}}}{4}(1 - J_0(2f_0))$ ,  $2\lambda \equiv \sqrt{N_a \epsilon_p \omega_{\text{rec}} |U_0|}$ ,  $\lambda_{f_0} = J_0(f_0)\lambda$ ,  $\eta(t) = 2h_1(t)\lambda$  and  $\zeta(t) = 2g_1(t)\lambda$ . Expanding this Hamiltonian up to linear order in the driving strength  $f_0$  leads to the parametrically driven dissipative three-level Dicke model presented in [3, 4].

### A. Large $\kappa$ limit

Within our three-level Dicke model we can adiabatically eliminate the light field, if  $\kappa \gg \omega_{\text{rec}}$ . That is, we assume  $\frac{da}{dt} \approx 0$  and solve for  $a$  to obtain an atom-only or spin-only like three-level model

$$\begin{aligned} \hat{H}_{\text{eff}}/\hbar = & (\omega_B - \Delta_{f_0}) \hat{J}_z^B + (\omega_D + \Delta_{f_0}) \hat{J}_z^D + f_2(t) (\omega_B - \omega_D) \left( \hat{J}_z^D - \hat{J}_z^B \right) + 2g_2(t) (\omega_B - \omega_D) \hat{J}_x^{\text{BD}} \\ & - \Lambda \left( (J_0(f_0) + 2h_1(t))^2 \hat{J}_x^D \hat{J}_x^D - (J_0(f_0) + 2h_1(t)) 2g_1(t) \left[ \hat{J}_x^D \hat{J}_x^B + \hat{J}_x^B \hat{J}_x^D \right] + 4g_1(t)^2 \hat{J}_x^B \hat{J}_x^B \right), \end{aligned} \quad (10)$$

with  $\Lambda = 8\lambda^2\omega/(N(\kappa^2 + \omega^2))$ . This is the three-level generalisation of the prescription for mapping the standard two-level Dicke model onto the Lipkin-Meshkov-Glick model by adiabatically eliminating the photon dynamics [8]. In Fig. 4, the corresponding phase diagram for varying driving strength and driving frequency is shown for  $\lambda = 1.05 \lambda_{\text{crit}}$ . Note, that in a full description of the atom-cavity setup in terms of Eq. 1, a large value of  $\kappa$  would enable the excitation of higher modes, not included here, with the consequence of decoherence and heating.

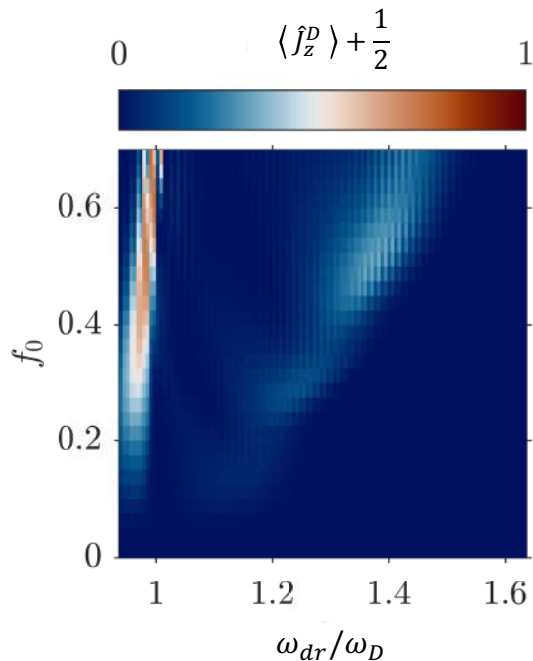


FIG. 4. Population of the dark state for different driving frequencies  $\omega_{dr}$  and driving strengths  $f_0$  calculated for the Hamiltonian Eq. 10. The driving frequency axis is rescaled by the characteristic frequency of the dark state  $\omega_D$ . The phase diagram is constructed for 7 driving cycles.

### IX. DARK STATE CONDENSATION BELOW THE CRITICAL PUMP STRENGTH

Here, we briefly show the dark state condensation starting below the critical pump strength. We ramp up the pump strength to  $\epsilon \approx 0.96 \epsilon_{crit}$  and start the modulation after 10 ms. In Fig. 5, it can be seen that after the modulation is switched on, the light field builds up before it vanishes again after a large fraction of atoms occupies the dark state as can be seen from the long-time behaviour in Fig. 6. This again highlights the importance of the intra-cavity field for transferring the atoms into the dark state. We note that the transition into the dark state is slower compared to the case starting from the superradiant phase discussed in the main text.

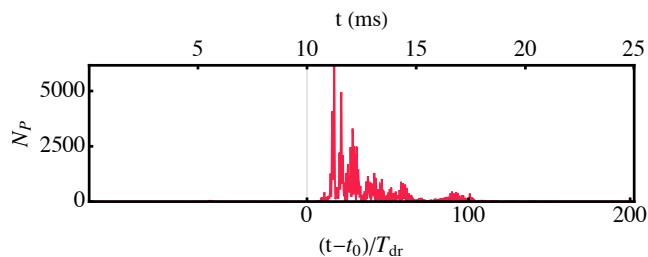


FIG. 5. Number of photons inside the cavity. The periodic drive is switched on at  $t_0$ . The parameters are the same as those used in Fig. 4 except for  $\epsilon \approx 0.96 \epsilon_{crit}$ .

### X. MODE POPULATION DURING THE RAMP-DOWN PROCESS

Fig. 7 presents the occupation of the sum of the  $\{\pm 1, \pm 1\} \hbar k$  momentum modes, the  $|D\rangle$  as well as the  $|N\rangle$ , before, during and after the ramp-down of the pump laser for varying driving strength and driving frequencies rescaled by the characteristic dark state frequency  $\omega_D$ . Before the ramp-down process the population of the  $|D\rangle$  and  $|B\rangle$  cannot be distinguished by summing up the  $\{\pm 1, \pm 1\} \hbar k$  momentum modes in a TOF image. However during the ramp-down the populations of  $|B\rangle$  is transferred back

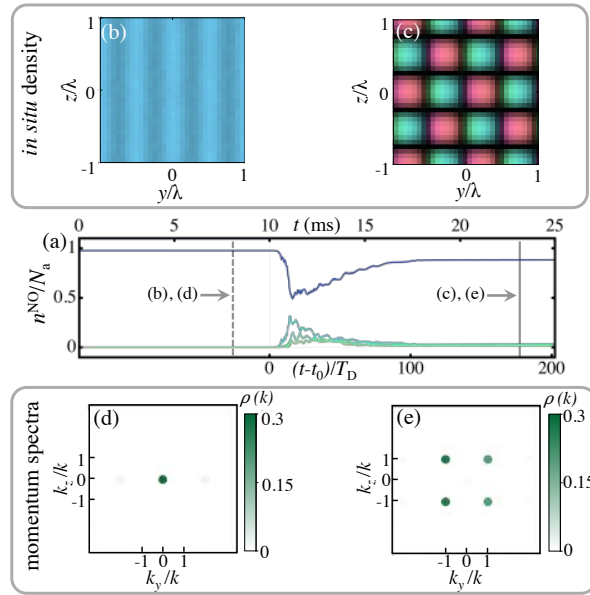


FIG. 6. (a) TWA results for the evolution of the five highest eigenvalues of the single-particle correlation function at equal time (SPCF). Gray vertical lines denote the times when the snapshots of the single-particle density in (b) and (c) are taken. (b), (c) The real space densities are color coded to show the phase within the  $(y, z)$ -plane. (d), (e) Momentum spectra at times indicated in (a).

into the  $|N\rangle$  and the phase diagram of the population of the  $\{\pm 1, \pm 1\} \hbar k$  momentum modes and the population of the dark state  $|D\rangle$  are approximately the same. This motivates us to measure the population of  $|D\rangle$  using this scheme.

- 
- [1] H. Ritsch, P. Domokos, F. Brennecke, and T. Esslinger, Cold atoms in cavity-generated dynamical optical potentials, *Rev. Mod. Phys.* **85**, 553 (2013).
  - [2] J. G. Cosme, J. Skulte, and L. Mathey, Time crystals in a shaken atom-cavity system, *Phys. Rev. A* **100**, 053615 (2019).
  - [3] J. Skulte, P. Kongkhambut, H. Keßler, A. Hemmerich, L. Mathey, and J. G. Cosme, Parametrically driven dissipative three-level Dicke model, *Phys. Rev. A* **104**, 063705 (2021).
  - [4] P. Kongkhambut, H. Keßler, J. Skulte, L. Mathey, J. G. Cosme, and A. Hemmerich, Realization of a periodically driven open three-level Dicke model, *Phys. Rev. Lett.* **127**, 253601 (2021).
  - [5] H. Keßler, J. Klinder, M. Wolke, and A. Hemmerich, Optomechanical atom-cavity interaction in the sub-recoil regime, *New Journal of Physics* **16**, 053008 (2014).
  - [6] J. Klinder, H. Keßler, C. Georges, J. Vargas, and A. Hemmerich, Bose–Einstein condensates in an optical cavity with sub-recoil bandwidth, *Applied Physics B* **122**, 299 (2016).
  - [7] M. Abramowitz and I. A. Stegun, *Handbook of Mathematical Functions with Formulas, Graphs, and Mathematical Tables* (Dover, New York, 1964).
  - [8] J. Keeling, M. J. Bhaseen, and B. D. Simons, Collective dynamics of Bose-Einstein condensates in optical cavities, *Phys. Rev. Lett.* **105**, 043001 (2010).

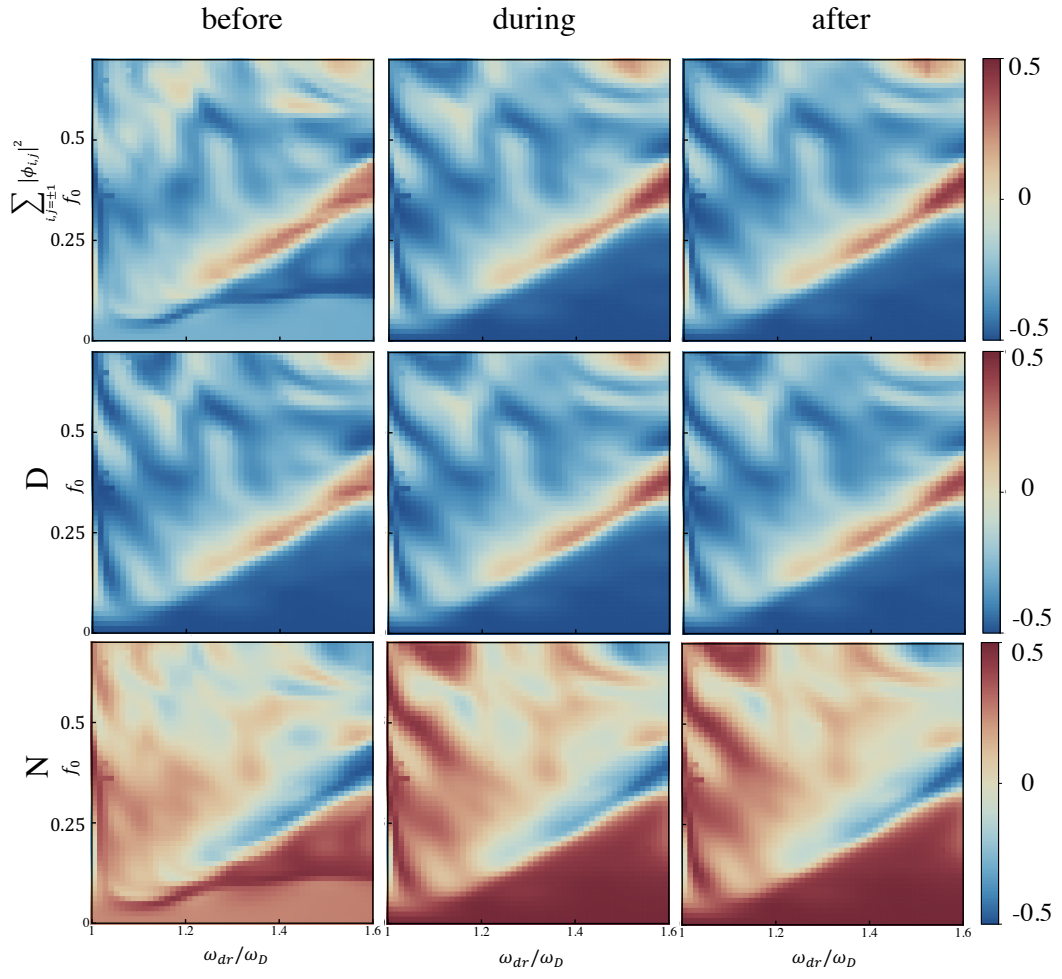


FIG. 7. Population of the  $\{\pm 1, \pm 1\}\hbar k$  momentum modes, the dark state and the ground state for different driving frequencies  $\omega_{dr}$  and driving strengths  $f_0$ . The driving frequency axis is rescaled by the characteristic frequency of the dark state,  $\omega_D$ .



# **Appendix D**

## **Supplement material of publication V**



Supplementary Materials for  
**Observation of a continuous time crystal**

Phatthamon Kongkhambut *et al.*

Andreas Hemmerich, [hemmerich@physnet.uni-hamburg.de](mailto:hemmerich@physnet.uni-hamburg.de); Hans Keßler, [hkessler@physnet.uni-hamburg.de](mailto:hkessler@physnet.uni-hamburg.de)

DOI: [10.1126/science.abo3382](https://doi.org/10.1126/science.abo3382)

**The PDF file includes:**

Materials and Methods  
Supplementary Text  
Figs. S1 to S7  
References



## Experimental details

The experimental setup, as sketched in Fig. 1(A) in the main text, is comprised of a magnetically trapped BEC of  $N_a = 5 \times 10^4$   $^{87}\text{Rb}$  atoms, dispersively coupled to a narrowband high-finesse optical cavity. The trap creates a harmonic potential with trap frequencies  $\omega = 2\pi \times (119.0, 102.7, 24.7)$  Hz. The cavity field has a decay rate of  $\kappa = 2\pi \times 3.4$  kHz, which almost equals the recoil frequency  $\omega_{\text{rec}} = E_{\text{rec}}/\hbar = 2\pi \times 3.7$  kHz for pump wavelength of  $\lambda_P = 792.55$  nm. The pump laser is blue detuned with respect to the relevant atomic transition of  $^{87}\text{Rb}$  at 794.98 nm. The maximum light shift per atom is  $U_0 = 2\pi \times 1.3$  Hz. A typical experimental sequence starts by preparing the BEC and linearly increasing the pump strength  $\epsilon$  to its desired value  $\epsilon_f$  and subsequently holding it constant for 10 ms.

## Phase diagram for large pump strength range

In Fig. S1A we present a phase diagram, similar to the one shown in Fig. 2A in the main text, but for larger pump strength range. The experimental protocol is the same as for Fig. 2A but the ramp time is increased to 20 ms. For strong pumping the system does not favor anymore the self-organization, since the cost of localizing the atoms at the nodes of the potential exceeds the decrease of energy due to the cavity-mediated coupling. In Fig. S1B the phase difference between the pump and cavity field  $\phi$  is plotted against  $\delta_{\text{eff}}$  and  $\epsilon$ . In the self-organized phase,  $N_P$  is finite and  $\phi$  locks to either 0 or  $\pi$  and stay constant. In Fig. S1C, we present the amplitude of the Fourier spectrum calculated from the photon number data. The limit cycle region can be identified by a peak in the frequency response around 10 kHz.

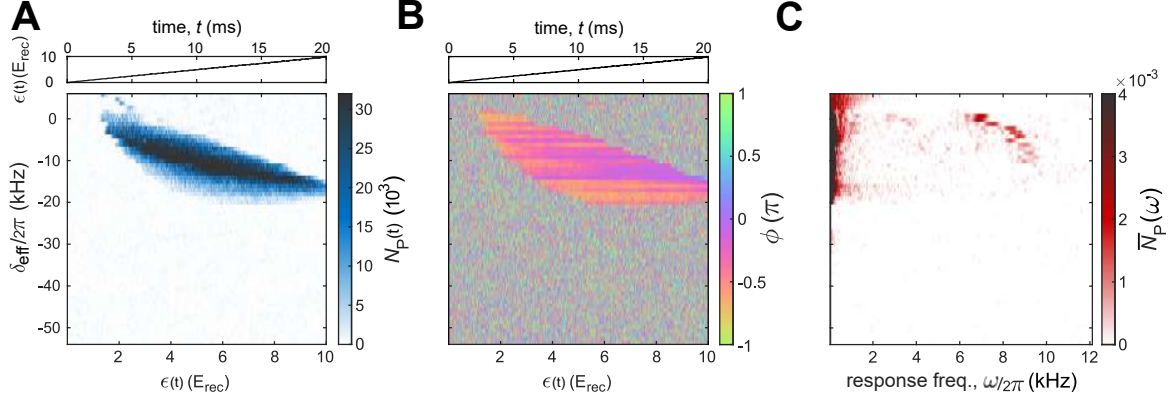


**Fig. S1. Phase diagrams for large pump strength range.** (A) Top panel: Pump strength protocol. Bottom panel: The corresponding intracavity photon number  $N_P$ , as a function of the effective detuning  $\delta_{\text{eff}}$  and pump strength  $\epsilon$  at a pump wavelength of  $\lambda_P = 792.55$  nm. The corresponding light shift per photon is  $U_0 = 2\pi \times 1.3$  Hz. (B) Top panel: Pump strength protocol. Bottom panel: The phase difference between the pump and intracavity field  $\phi$ , as a function of the effective detuning  $\delta_{\text{eff}}$  and pump strength  $\epsilon$ . Note, due to technical instabilities of the phase reference, we observe a drift of the phase signal of the cavity field of about  $0.02\pi$  per ms. (C) The single-sided amplitude of the Fourier spectrum calculated using the data of A, as a function of the effective detuning  $\delta_{\text{eff}}$ .

## Atom-Cavity Model

We only consider the pump and cavity directions. The full atom-cavity system can be modeled using the many-body Hamiltonian with four terms describing the cavity, the atoms, and the atom-cavity interactions, given by

$$\hat{H} = \hat{H}_c + \hat{H}_a + \hat{H}_{\text{aa}} + \hat{H}_{\text{ac}}, \quad (1)$$

where the cavity contribution is  $\hat{H}_c = -\hbar\delta_c \hat{a}^\dagger \hat{a}$  and the detuning between the pump and cavity frequencies is  $\delta_c < 0$ . The cavity mode annihilation and creation operator are denoted by  $\hat{a}$  and  $\hat{a}^\dagger$ . The atomic part is described by

$$\hat{H}_a = \int dydz \hat{\Psi}^\dagger(y, z) \left( -\frac{\hbar^2}{2m} \nabla^2 + V_{\text{ext}}(y, z) \right) \hat{\Psi}(y, z) \quad (2)$$

where the external potential due to the standing wave created by the pump beam is  $V_{\text{ext}}(y, z) = \epsilon_f \cos^2(ky)$  with the potential strength parameter  $\epsilon_f$  and  $m$  the mass of an atom. The short-range collisional interaction between the atoms can be captured via

$$\hat{H}_{\text{aa}} = U_a \int dydz \hat{\Psi}^\dagger(y, z) \hat{\Psi}^\dagger(y, z) \hat{\Psi}(y, z) \hat{\Psi}(y, z), \quad (3)$$

where  $U_a = \sqrt{2\pi} a_s \hbar / m l_x$  is the effective 2D interaction strength with  $a_s$  the s-wave scattering length and  $l_x$  the harmonic oscillator length in the x direction. The atom-cavity interaction part is described by

$$\hat{H}_{\text{ac}} = \int dydz \hat{\Psi}^\dagger(y, z) \left( \hbar U_0 \cos^2(kz) \hat{a}^\dagger \hat{a} + \hbar \sqrt{\hbar \epsilon_f U_0} \cos(ky) \cos(kz) [\hat{a}^\dagger + \hat{a}] \right) \hat{\Psi}(y, z). \quad (4)$$

The light shift per intracavity photon is denoted by  $U_0 > 0$ . For our numerical simulations of the dynamics, we use the semiclassical method based on the truncated Wigner approximation (TWA) (37,38). TWA approximates the quantum dynamics by solving the equations of motions over an ensemble of initial states, which are sampled from the initial Wigner distribution. This methods allows us to incorporate the leading order quantum corrections to the meanfield solution. The c number equation for the light field is

$$i \frac{\partial \alpha}{\partial t} = \frac{1}{\hbar} \frac{\partial H}{\partial \alpha^*} - i\kappa \alpha + i\xi = (-\delta_c + U_0 \mathcal{B} - i\kappa + i\xi) + \sqrt{\hbar \epsilon_f U_0} \Phi, \quad (5)$$

where we have defined the bunching parameter  $\mathcal{B} = \int dydz \cos^2(kz) |\psi(y, z)|^2$  and the density wave order parameter that corresponds to a checkerboard ordering  $\Phi = \int dydz \cos(ky) \cos(kz) |\psi(y, z)|^2$ .

We further included a decay term proportional to  $\kappa$  in the cavity mode dynamics and the resulting stochastic noise term  $\xi(t)$ , which is defined via  $\langle \xi^*(t)\xi(t') \rangle = \kappa\delta(t-t')$ . We obtain the atom-field equations via

$$i\frac{\partial\psi(y,z)}{\partial t} = \frac{1}{\hbar}\frac{\partial H}{\partial\psi^*(y,z)} = \left(-\frac{\hbar}{2m}\nabla^2 + V_{\text{dip}}(y,z) + 2U_a|\psi(y,z)|^2\right)\psi(y,z) \quad (6)$$

with

$$V_{\text{dip}}(y,z) = \hbar\left(U_0|\alpha|^2\cos^2(kz) + \epsilon_f\omega_{\text{rec}}\cos^2(ky) + \sqrt{\hbar\epsilon_fU_0}[\alpha + \alpha^*]\cos(ky)\cos(kz)\right). \quad (7)$$

For the simulations we use the same set of parameters as in the experiment.

## Breaking of continuous time translation symmetry

To gain further insights into the continuous time translation symmetry breaking, we consider three different possibilities for including quantum noise in our theory. First, we sample over the full initial Wigner distribution and also include the corresponding stochastic noise  $\xi$  corresponding to the cavity-field decay rate  $\kappa$ . Secondly, we include only the sampling of the Wigner distribution of the initial state and ignore the stochastic noise in time due to the fluctuation-dissipation term in the cavity field. Third, we fix the initial state and include stochastic noise in the cavity mode. For each case, we consider  $10^3$  trajectories but for clearer presentation we only show the first 500 trajectories in Fig. S2(A-C). To obtain Fig. S2(A-C), we use  $\delta_{\text{eff}} = -2\pi \times 10.4$  kHz and linearly ramp up the pump strength to its final value  $\epsilon_f/\omega_{\text{rec}} = 0.85$  within 10 ms. We compute the fast Fourier transformation between  $t_{\text{start}} = 15$  ms and  $t_{\text{final}} = 65$  ms. We record every 0.00125 ms and thus, our frequency resolution is limited by  $\Delta_{\text{FFT}} = 20$  Hz. In Fig. S2A and S2B the limit cycle frequency varies  $\pm 150$  Hz. For the data set in Fig. S2C, the frequency is fixed. To minimize the fluctuations in the FFT signal due to the offset at  $\omega = 0$  we normalize each trajectory by the maximum of the FFT. For better accessibility, after obtaining

the data from all trajectories we average over the mean value of all points. The TWA results in Fig. S2A nicely show that all phases between  $0$  and  $2\pi$  are realized. The same holds true in Fig. S2B and Fig. S2C. This suggests that the initial quantum noise and stochastic noise from the leaky cavity are sufficient to exhibit the breaking of continuous time translation symmetry.

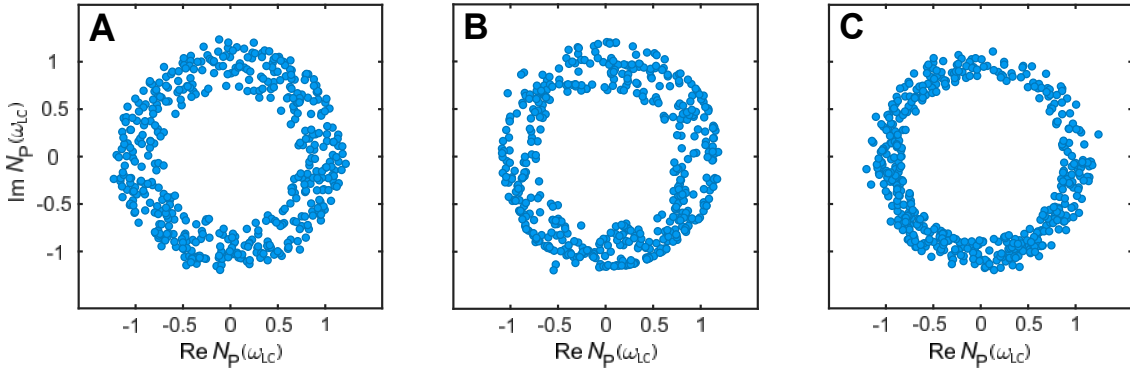


**Fig. S2. Distribution of the time phase in the limit cycle phase.** TWA simulations including (A) both initial quantum noise and stochastic noise, (B) only initial quantum noise, and (C) only stochastic noise. We use  $\delta_{\text{eff}} = -2\pi \times 10.4$  kHz and  $\epsilon_f/\omega_{\text{rec}} = 0.85$ .

## Atom dynamics during one limit cycle

We present the dynamics of the light field and the relevant density wave order parameters for a single exemplary trajectory in the limit cycle phase. We use  $\delta_{\text{eff}} = -2\pi \times 10.4$  kHz and a final pump strength of  $\epsilon_f/\omega_{\text{rec}} = 0.85$ . We ramp up the pump intensity within 10 ms and present in Fig. S3C the limit cycle dynamics after 20 ms. We find that the only non-zero order parameters are those associated to the checkerboard density wave,  $\Phi = \langle \cos(ky) \cos(kz) \rangle$ , and to the density waves related to the cavity and pump bunching parameters,  $\mathcal{B} = \langle \cos(kz)^2 \rangle$  and  $\mathcal{P} = \langle \cos(ky)^2 \rangle$ , respectively. Fig. S3C shows the dynamics of the light field and the three order parameters. The oscillations in the dynamics of the atomic field density wave order parameter

lags behind those in the cavity field occupation. In Fig. S3(A-B) and Fig. S3(C-D), the density of the atomic-field is presented. The atoms slosh back and forth from a checkerboard pattern to the minima of the light field intensity.

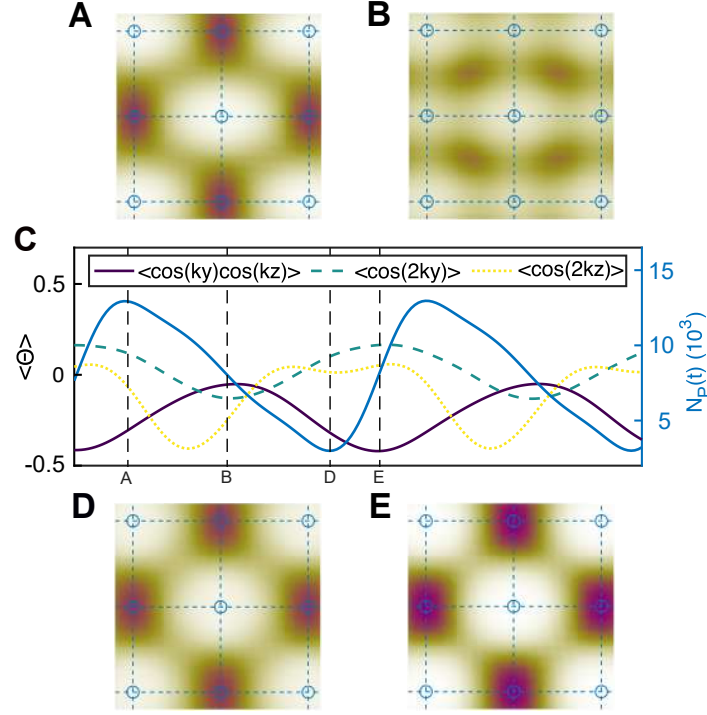


**Fig. S3. Numerical results for the limit cycle dynamics.** (A-B) and (D-E) Atomic density distributions for different times during the limit cycle. The gray dashed lines in C indicate the times for which the density distributions are calculated. Horizontal and vertical dashed blue lines mark the extrema of  $\cos(ky)$  and  $\cos(kz)$ , respectively and solid blue circles denote the extrema of the product  $\cos(ky)\cos(kz)$ , which determines the checkerboard density wave order parameter  $\Phi$ . C Dynamics of the three relevant order parameters and the cavity mode occupation. The vertical dashed lines denote the times when (A-B) and (D-E) are taken. We use  $\delta_{\text{eff}} = -2\pi \times 10.4$  kHz and  $\epsilon_f/\omega_{\text{rec}} = 0.85$ .

## Stability against short-range interactions and atom losses

We present the stability of the limit cycles against short-range interactions and phenomenological atom losses. We measure the interaction strengths via the mean-field collisional interaction energy (19)

$$E_a = \frac{U_a}{N_a} \int dydz |\psi_0(y, z)|^4 \quad (8)$$

with the wavefunction of the homogeneous BEC  $\psi_0$ . We further add a phenomenological atom loss term to our equations of motion of the form of

$$\frac{dN_a}{dt} = -2\gamma N_a \quad (9)$$

to capture the atom losses in the experiment. To quantify the temporal long-range order we compute the two-point temporal correlation function

$$C(t) = \text{Re} \left( \frac{\langle \hat{a}^\dagger(t) a(t_0) \rangle}{\langle \hat{a}^\dagger(t_0) a(t_0) \rangle} \right). \quad (10)$$

The time  $t_0$  is defined as the time of the first maximum of the limit cycle oscillations after the transition into the superradiant phase.

We present the dynamics of the photon number  $N_P$  and the nonequal time correlation  $C$  in Fig. S4 for different collisional interaction strengths  $E_a$  and atom loss rates  $\gamma$ . We observe that short-range interactions do not destroy the temporal long range order for weaker collisional interaction energies  $E_a = 0.1 E_{\text{rec}}$  to strong interactions of  $E_a = 0.2 E_{\text{rec}}$ . However, the combination of strong short-range interactions  $E_a = 0.2 E_{\text{rec}}$  and atom losses of  $\gamma = 40 \text{ s}^{-1}$  lead to a decay of the temporal order similar as observed in the experiment. The loss rate is chosen such that it models the observed atom decay rate in the experiment. We conclude that the main limitation of the limit cycle lifetime stems from atom losses in the experimental set up.

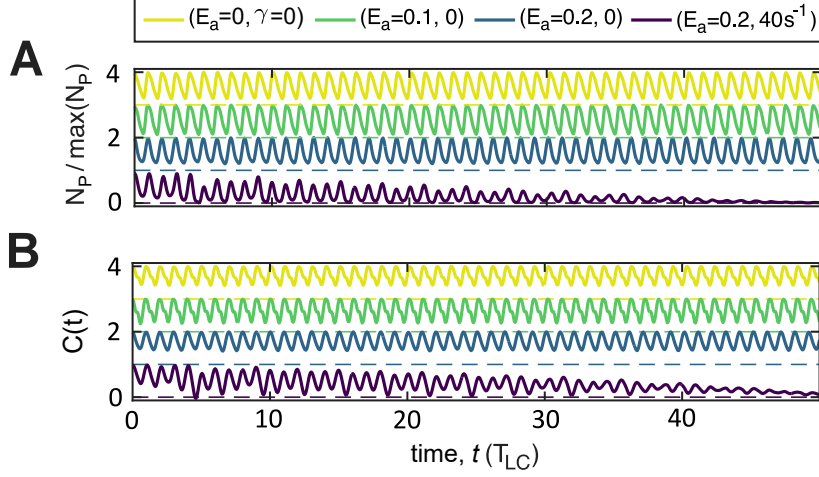


**Fig. S4. Numerical results on short-range interactions and atom losses.** (A) Numerical results on the intracavity photon number  $N_P$  and (B) the corresponding nonequal time correlation  $C$  for different contact interaction energies  $E_a$  and atom losses  $\gamma$ . For better readability, we include an offset of 1, 2, 3 for the blue, green and yellow trace indicated by the dashed lines. We fix  $\delta_{\text{eff}} = -2\pi \times 10.4$  kHz.

## Stability with respect to pump-atom detuning

The pump-atom detuning is in our system parametrized by the single photon light shift  $U_0$ . For all the measurements presented in the main text  $U_0 = 2\pi \times 1.3$  Hz is kept constant. To demonstrate robustness with respect to the pump-atom detuning, and hence with respect to  $U_0$ , we present in Fig. S5 measurements of self-organization phase diagram for  $U_0 = 2\pi \times 1.9$  Hz. The limit cycles are indicated by a peak in the Fourier spectrum of the intracavity photon number (Fig. S5C), which can be found for small negative effective pump-cavity detuning  $\delta_{\text{eff}}/2\pi$ , between  $-10$  and  $-20$  kHz. This measurement is only an example and we experimentally observe stable limit cycles for different values of  $U_0$ .



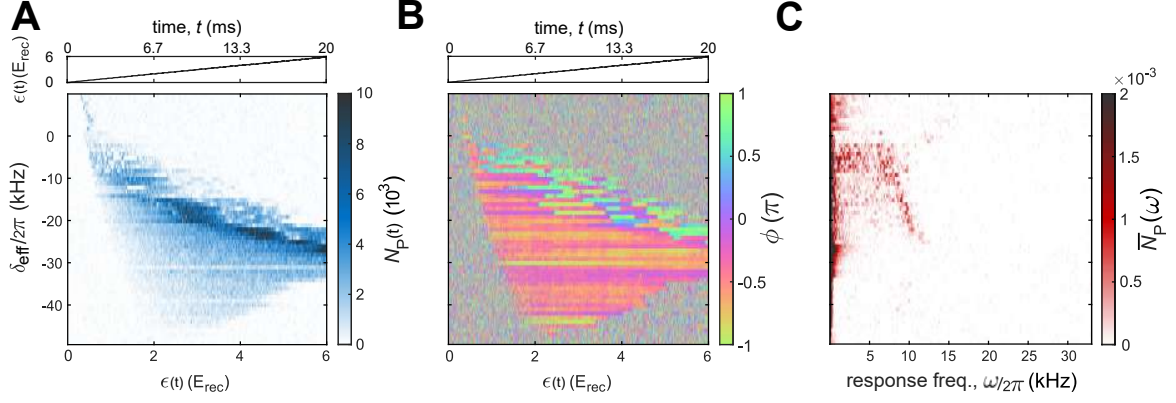


**Fig. S5. Phase diagrams for another pump-atom detuning.** (A) Top panel: Pump strength protocol. Bottom panel: The corresponding intracavity photon number  $N_P$ , as a function of the effective detuning  $\delta_{\text{eff}}$  and pump strength  $\epsilon$  at a pump wavelength of  $\lambda_P = 793.76$  nm. The corresponding light shift per photon is  $U_0 = 2\pi \times 1.9$  Hz. (B) Top panel: Pump strength protocol. Bottom panel: The phase difference between the pump and intracavity field  $\phi$ , as a function of the effective detuning  $\delta_{\text{eff}}$  and pump strength  $\epsilon$ . (C) The single-sided amplitude of the Fourier spectrum calculated using the data of A, as a function of the effective detuning  $\delta_{\text{eff}}$ . Red region around 8 – 10kHz at small negative  $\delta_{\text{eff}}$  indicate a region where limit cycle can be found.

## Finite-size effects

We investigate the effects of a finite particle number on the stability of the time crystal. To this end, we compare the mean-field results, which simulate the thermodynamic limit, and the results of single TWA trajectories, which include stochastic noise associated to cavity loss, for different particle numbers. Owing to the cavity-induced all-to-all coupling between the atoms, the thermodynamic limit is expected to be captured by our mean-field theory. We vary the particle number while keeping  $NU_0$  fixed. We obtain the peaks in the dynamics of the intracavity photon number,  $\tilde{N}_P$ , to highlight the change in the oscillation amplitude of the limit cycle phase for varying particle number. In Fig. S6A, we show the time evolution of  $\tilde{N}_P/N_a$  for some exemplary particle numbers using TWA and the MF result corresponding to the thermodynamic limit. It can be seen that as the particle number is increased, the results approach the MF prediction. This means that the temporal dynamics becomes more regular as we increase the particle number  $N_a$  towards the thermodynamic limit. To further illustrate this point, we calculate the relative crystalline fraction  $\Xi' \equiv \sum_{\omega \in \delta_{LC}} N_P(\omega) / \sum_{\omega \in \Delta_{LC}} N_P(\omega)$ . We rescaled the relative crystalline fraction for varying  $N_a$  by the value in the thermodynamic limit, i.e., the  $\Xi'$  in our mean-field prediction is set to 1 as indicated by the gray dashed line in Fig. S6B. The blue cross marks the typical particle number in our experiment. We find that as  $N_a$  is increased, the crystalline fraction approaches the mean-field prediction. This can be understood from the fact that the initial quantum noise and stochastic noise scales with  $1/N$  in TWA, meaning that as expected for  $N_a \rightarrow \infty$ , we recover the thermodynamic limit.

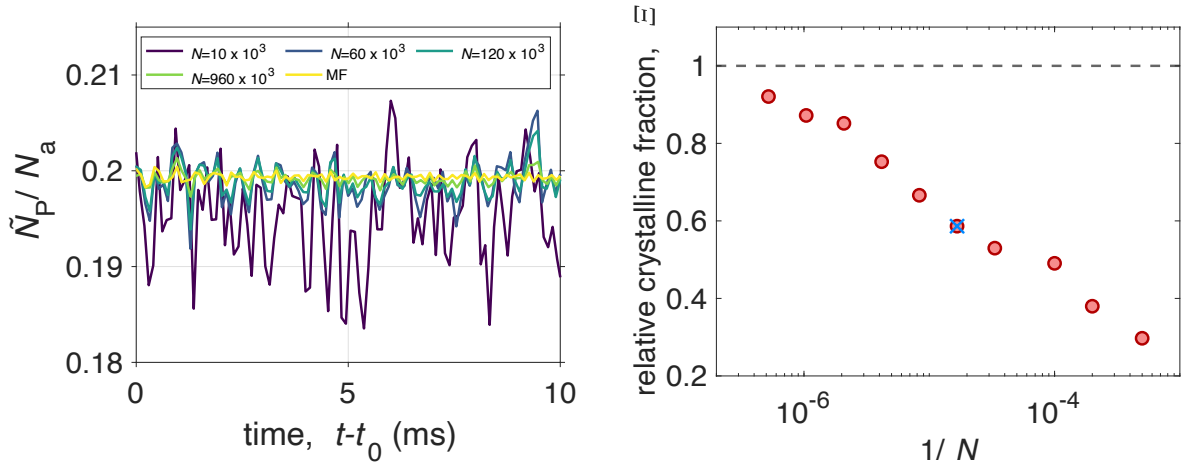


**Fig. S6. Numerical results on the stability for different particle numbers** (A) Results of a single TWA trajectory for the peak height of the intracavity photon number in the limit cycle phase for different particle numbers. (B) The relative crystalline fraction for varying particle numbers obtained from single TWA trajectories, which include stochastic noise from the cavity losses. The gray horizontal dashed line represents the mean-field crystalline fraction, which we set to 1 as a benchmark for finite  $N$ . The blue cross indicates the particle number, in which the experiment operates. We fix  $\delta_{\text{eff}} = -2\pi \times 10.4$  kHz and  $NU_0 = 2\pi \times 60$  kHz = const.

## Stability against temporal perturbations

The stability of the limit cycle phase against temporal noise can be also explored using our theoretical model. We focus on the mean-field regime to show that the limit cycle phases in the thermodynamic limit exhibit the robustness expected of a continuous time crystal. We add a Gaussian white noise onto the pump signal, which is band-limited to 0.025 GHz. This is set by the integration step size of our stochastic differential equation solver. Note that the noise in the experiment is band-limited to 50 kHz. Examples of the noisy pump signal are shown in Fig. S7A. The noise strength is quantified by a parameter similar to the one in the

experiment,  $n \equiv \sum_{\omega} |\mathcal{A}_{\text{noisy}}(\omega)| / \sum_{\omega} |\mathcal{A}_{\text{clean}}(\omega)| - 1$ , where  $\mathcal{A}$  is the Fourier spectrum of the pump signal. In Fig. S7B, we show the peaks in the dynamics of the intracavity photon number,  $\tilde{N}_p(t)$ , for various noise strengths. We find that increasing the temporal noise strength leads to more irregular oscillations in the limit cycle phase. To further quantify this behaviour, we again obtain the relative crystalline fraction as defined in the previous section. The dependence of the relative crystalline on temporal noise strength  $n$  is shown in Fig. S7C. We observe that for small noise strength, the crystalline fraction appears unchanged. The time crystal starts to melt for stronger noise strengths as expected. These numerical results qualitatively agree with the experimental results shown in Fig. 3E and they suggest the robustness of the limit cycle phase in the thermodynamic limit against temporal perturbation.

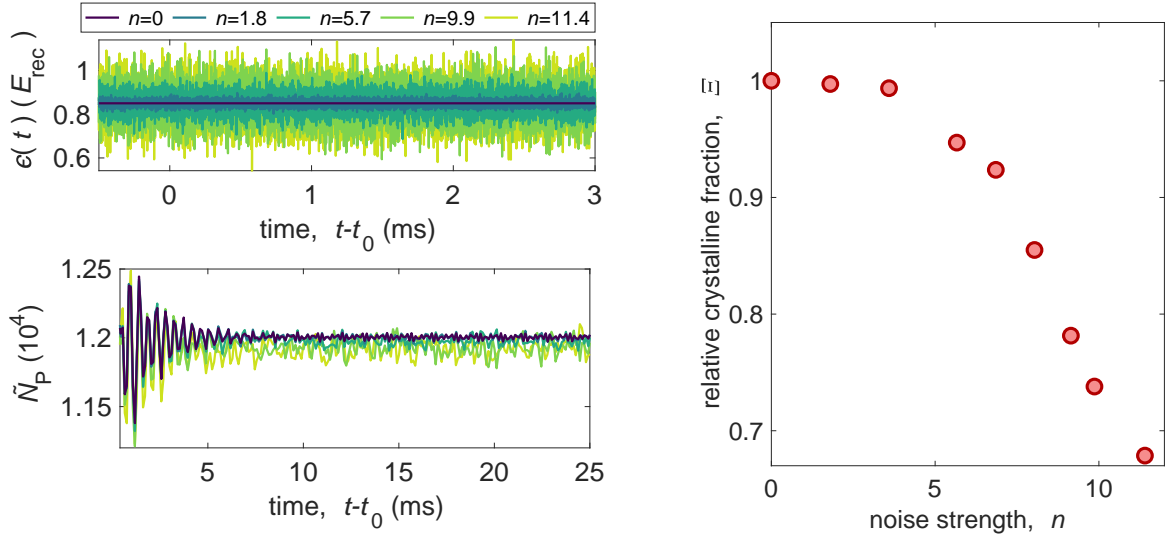


**Fig. S7. Numerical results on the stability against temporal noise** (A) Time dependence of the pump strength  $\epsilon$  for different noise strengths and (B) the corresponding mean-field results for the dynamics of peak height of the intracavity photon number in the limit cycle phase. (C) The relative crystalline fraction for different noise strength.

## **Route to chaos**

Our system exhibits a route to chaos, which we have investigated theoretically in a previous study. The full dynamical phase diagram including the chaotic regime can be found in Ref. (24). We find that the limit cycle phase becomes unstable towards chaotic dynamics for large pump strengths. Due to the limited lifetime of the BEC in our experimental setup, it is difficult to experimentally identify such a chaotic phase, which manifests in its characteristic long-time dynamics.

## References and Notes

1. F. Wilczek, Quantum time crystals. *Phys. Rev. Lett.* **109**, 160401 (2012).  
[doi:10.1103/PhysRevLett.109.160401](https://doi.org/10.1103/PhysRevLett.109.160401) [Medline](#)
2. A. Shapere, F. Wilczek, Classical time crystals. *Phys. Rev. Lett.* **109**, 160402 (2012).  
[doi:10.1103/PhysRevLett.109.160402](https://doi.org/10.1103/PhysRevLett.109.160402) [Medline](#)
3. P. Nozières, EPL. *Europhys. Lett.* **103**, 57008 (2013).
4. P. Bruno, Impossibility of spontaneously rotating time crystals: A no-go theorem. *Phys. Rev. Lett.* **111**, 070402 (2013). [doi:10.1103/PhysRevLett.111.070402](https://doi.org/10.1103/PhysRevLett.111.070402) [Medline](#)
5. H. Watanabe, M. Oshikawa, Absence of Quantum Time Crystals. *Phys. Rev. Lett.* **114**, 251603 (2015). [doi:10.1103/PhysRevLett.114.251603](https://doi.org/10.1103/PhysRevLett.114.251603) [Medline](#)
6. D. V. Else, C. Monroe, C. Nayak, N. Y. Yao, Discrete Time Crystals. *Annu. Rev. Condens. Matter Phys.* **11**, 467–499 (2020). [doi:10.1146/annurev-conmatphys-031119-050658](https://doi.org/10.1146/annurev-conmatphys-031119-050658)
7. K. Sacha, *Time Crystals* (Springer, Cham, 2020).
8. V. Khemani, R. Moessner, S. L. Sondhi, A brief history of time crystals. [arXiv:1910.10745](https://arxiv.org/abs/1910.10745) [cond-mat.str-el] (2019).
9. J. Zhang, P. W. Hess, A. Kyprianidis, P. Becker, A. Lee, J. Smith, G. Pagano, I.-D. Potirniche, A. C. Potter, A. Vishwanath, N. Y. Yao, C. Monroe, Observation of a discrete time crystal. *Nature* **543**, 217–220 (2017). [doi:10.1038/nature21413](https://doi.org/10.1038/nature21413) [Medline](#)
10. S. Choi, J. Choi, R. Landig, G. Kucsko, H. Zhou, J. Isoya, F. Jelezko, S. Onoda, H. Sumiya, V. Khemani, C. von Keyserlingk, N. Y. Yao, E. Demler, M. D. Lukin, Observation of discrete time-crystalline order in a disordered dipolar many-body system. *Nature* **543**, 221–225 (2017). [doi:10.1038/nature21426](https://doi.org/10.1038/nature21426) [Medline](#)
11. J. Rovny, R. L. Blum, S. E. Barrett, Observation of Discrete-Time-Crystal Signatures in an Ordered Dipolar Many-Body System. *Phys. Rev. Lett.* **120**, 180603 (2018).  
[doi:10.1103/PhysRevLett.120.180603](https://doi.org/10.1103/PhysRevLett.120.180603) [Medline](#)
12. J. Smits, L. Liao, H. T. C. Stoof, P. van der Straten, Observation of a Space-Time Crystal in a Superfluid Quantum Gas. *Phys. Rev. Lett.* **121**, 185301 (2018).  
[doi:10.1103/PhysRevLett.121.185301](https://doi.org/10.1103/PhysRevLett.121.185301) [Medline](#)
13. S. Autti, V. B. Eltsov, G. E. Volovik, Observation of a Time Quasicrystal and Its Transition to a Superfluid Time Crystal. *Phys. Rev. Lett.* **120**, 215301 (2018).  
[doi:10.1103/PhysRevLett.120.215301](https://doi.org/10.1103/PhysRevLett.120.215301) [Medline](#)
14. J. O’Sullivan *et al.*, *New J. Phys.* **22**, 085001 (2020).
15. A. Kyprianidis, F. Machado, W. Morong, P. Becker, K. S. Collins, D. V. Else, L. Feng, P. W. Hess, C. Nayak, G. Pagano, N. Y. Yao, C. Monroe, Observation of a prethermal discrete time crystal. *Science* **372**, 1192–1196 (2021). [doi:10.1126/science.abg8102](https://doi.org/10.1126/science.abg8102) [Medline](#)
16. J. Randall, C. E. Bradley, F. V. van der Gronden, A. Galicia, M. H. Abobeih, M. Markham, D. J. Twitchen, F. Machado, N. Y. Yao, T. H. Taminiau, Many-body-localized discrete time crystal with a programmable spin-based quantum simulator. *Science* **374**, 1474–1478 (2021). [doi:10.1126/science.abk0603](https://doi.org/10.1126/science.abk0603) [Medline](#)

17. X. Mi, M. Ippoliti, C. Quintana, A. Greene, Z. Chen, J. Gross, F. Arute, K. Arya, J. Atalaya, R. Babbush, J. C. Bardin, J. Basso, A. Bengtsson, A. Bilmes, A. Bourassa, L. Brill, M. Broughton, B. B. Buckley, D. A. Buell, B. Burkett, N. Bushnell, B. Chiaro, R. Collins, W. Courtney, D. Debroy, S. Demura, A. R. Derk, A. Dunsworth, D. Eppens, C. Erickson, E. Farhi, A. G. Fowler, B. Foxen, C. Gidney, M. Giustina, M. P. Harrigan, S. D. Harrington, J. Hilton, A. Ho, S. Hong, T. Huang, A. Huff, W. J. Huggins, L. B. Ioffe, S. V. Isakov, J. Iveland, E. Jeffrey, Z. Jiang, C. Jones, D. Kafri, T. Khattar, S. Kim, A. Kitaev, P. V. Klimov, A. N. Korotkov, F. Kostritsa, D. Landhuis, P. Laptev, J. Lee, K. Lee, A. Locharla, E. Lucero, O. Martin, J. R. McClean, T. McCourt, M. McEwen, K. C. Miao, M. Mohseni, S. Montazeri, W. Mruczkiewicz, O. Naaman, M. Neeley, C. Neill, M. Newman, M. Y. Niu, T. E. O'Brien, A. Opremcak, E. Ostby, B. Pato, A. Petukhov, N. C. Rubin, D. Sank, K. J. Satzinger, V. Shvarts, Y. Su, D. Strain, M. Szalay, M. D. Trevithick, B. Villalonga, T. White, Z. J. Yao, P. Yeh, J. Yoo, A. Zalcman, H. Neven, S. Boixo, V. Smelyanskiy, A. Megrant, J. Kelly, Y. Chen, S. L. Sondhi, R. Moessner, K. Kechedzhi, V. Khemani, P. Roushan, Time-crystalline eigenstate order on a quantum processor. *Nature* **601**, 531–536 (2022). [doi:10.1038/s41586-021-04257-w](https://doi.org/10.1038/s41586-021-04257-w) [Medline](#)
18. Z. Gong, R. Hamazaki, M. Ueda, Discrete Time-Crystalline Order in Cavity and Circuit QED Systems. *Phys. Rev. Lett.* **120**, 040404 (2018). [doi:10.1103/PhysRevLett.120.040404](https://doi.org/10.1103/PhysRevLett.120.040404) [Medline](#)
19. H. Keßler, P. Kongkhambut, C. Georges, L. Mathey, J. G. Cosme, A. Hemmerich, Observation of a Dissipative Time Crystal. *Phys. Rev. Lett.* **127**, 043602 (2021). [doi:10.1103/PhysRevLett.127.043602](https://doi.org/10.1103/PhysRevLett.127.043602) [Medline](#)
20. P. Kongkhambut, H. Keßler, J. Skulte, L. Mathey, J. G. Cosme, A. Hemmerich, Realization of a Periodically Driven Open Three-Level Dicke Model. *Phys. Rev. Lett.* **127**, 253601 (2021). [doi:10.1103/PhysRevLett.127.253601](https://doi.org/10.1103/PhysRevLett.127.253601) [Medline](#)
21. H. Taheri, A. B. Matsko, L. Maleki, K. Sacha, All-optical dissipative discrete time crystals. *Nat. Commun.* **13**, 848 (2022). [doi:10.1038/s41467-022-28462-x](https://doi.org/10.1038/s41467-022-28462-x) [Medline](#)
22. F. Iemini, A. Russomanno, J. Keeling, M. Schirò, M. Dalmonte, R. Fazio, Boundary Time Crystals. *Phys. Rev. Lett.* **121**, 035301 (2018). [doi:10.1103/PhysRevLett.121.035301](https://doi.org/10.1103/PhysRevLett.121.035301) [Medline](#)
23. B. Buča, J. Tindall, D. Jaksch, Non-stationary coherent quantum many-body dynamics through dissipation. *Nat. Commun.* **10**, 1730 (2019). [doi:10.1038/s41467-019-09757-y](https://doi.org/10.1038/s41467-019-09757-y) [Medline](#)
24. H. Keßler, J. G. Cosme, M. Hemmerling, L. Mathey, A. Hemmerich, Emergent limit cycles and time crystal dynamics in an atom-cavity system. *Phys. Rev. A* **99**, 053605 (2019). [doi:10.1103/PhysRevA.99.053605](https://doi.org/10.1103/PhysRevA.99.053605)
25. H. Poincaré, *J. Math. Pures Appl.* **7**, 375 (1881).
26. S. H. Strogatz, *Nonlinear Dynamics and Chaos: With Applications to Physics, Biology, Chemistry, and Engineering* Westview press (2015).
27. H. Keßler, J. Klinder, M. Wolke, A. Hemmerich, Optomechanical atom-cavity interaction in the sub-recoil regime. *New J. Phys.* **16**, 053008 (2014). [doi:10.1088/1367-2630/16/5/053008](https://doi.org/10.1088/1367-2630/16/5/053008)

28. P. Domokos, H. Ritsch, Collective cooling and self-organization of atoms in a cavity. *Phys. Rev. Lett.* **89**, 253003 (2002). [doi:10.1103/PhysRevLett.89.253003](https://doi.org/10.1103/PhysRevLett.89.253003) [Medline](#)
29. A. T. Black, H. W. Chan, V. Vuletić, Observation of collective friction forces due to spatial self-organization of atoms: From Rayleigh to Bragg scattering. *Phys. Rev. Lett.* **91**, 203001 (2003). [doi:10.1103/PhysRevLett.91.203001](https://doi.org/10.1103/PhysRevLett.91.203001) [Medline](#)
30. K. Baumann, C. Guerlin, F. Brennecke, T. Esslinger, Dicke quantum phase transition with a superfluid gas in an optical cavity. *Nature* **464**, 1301–1306 (2010). [doi:10.1038/nature09009](https://doi.org/10.1038/nature09009) [Medline](#)
31. J. Klinder, H. Keßler, M. Wolke, L. Mathey, A. Hemmerich, Dynamical phase transition in the open Dicke model. *Proc. Natl. Acad. Sci. U.S.A.* **112**, 3290–3295 (2015). [doi:10.1073/pnas.1417132112](https://doi.org/10.1073/pnas.1417132112) [Medline](#)
32. P. Zupancic, D. Dreon, X. Li, A. Baumgärtner, A. Morales, W. Zheng, N. R. Cooper, T. Esslinger, T. Donner, P-Band Induced Self-Organization and Dynamics with Repulsively Driven Ultracold Atoms in an Optical Cavity. *Phys. Rev. Lett.* **123**, 233601 (2019). [doi:10.1103/PhysRevLett.123.233601](https://doi.org/10.1103/PhysRevLett.123.233601) [Medline](#)
33. F. Piazza, H. Ritsch, Self-Ordered Limit Cycles, Chaos, and Phase Slippage with a Superfluid inside an Optical Resonator. *Phys. Rev. Lett.* **115**, 163601 (2015). [doi:10.1103/PhysRevLett.115.163601](https://doi.org/10.1103/PhysRevLett.115.163601) [Medline](#)
34. Supplementary text is available in the supplementary materials.
35. H. Keßler, J. G. Cosme, C. Georges, L. Mathey, A. Hemmerich, From a continuous to a discrete time crystal in a dissipative atom-cavity system. *New J. Phys.* **22**, 085002 (2020). [doi:10.1088/1367-2630/ab9fc0](https://doi.org/10.1088/1367-2630/ab9fc0)
36. P. Kongkhambut *et al.*, Data for ““Observation of a continuous time crystal””. Zenodo (2022); [doi:10.5281/zenodo.6576125](https://doi.org/10.5281/zenodo.6576125).
37. A. Polkovnikov, Phase space representation of quantum dynamics. *Ann. Phys.* **325**, 1790–1852 (2010). [doi:10.1016/j.aop.2010.02.006](https://doi.org/10.1016/j.aop.2010.02.006)
38. J. G. Cosme, J. Skulte, L. Mathey, Time crystals in a shaken atom-cavity system. *Phys. Rev. A* **100**, 053615 (2019). [doi:10.1103/PhysRevA.100.053615](https://doi.org/10.1103/PhysRevA.100.053615)



# Bibliography

- [1] H. Keßler, P. Kongkhambut, C. Georges, L. Mathey, J. G. Cosme and A. Hemmerich, *Observation of a Dissipative Time Crystal*, *Physical Review Letters* **127** (2021) .
- [2] P. Kongkhambut, H. Keßler, J. Skulte, L. Mathey, J. G. Cosme and A. Hemmerich, *Realization of a Periodically Driven Open Three-Level Dicke Model*, *Physical Review Letters* **127** (dec, 2021) , [2108.11113].
- [3] J. Skulte, P. Kongkhambut, H. Keßler, A. Hemmerich, L. Mathey and J. G. Cosme, *Parametrically driven-dissipative three-level Dicke model*, *Physical Review A* **104** (dec, 2021) 063705.
- [4] P. Kongkhambut, J. Skulte, L. Mathey, J. G. Cosme, A. Hemmerich and H. Keßler, *Observation of a continuous time crystal*, *Science* (2022) .
- [5] J. Skulte, P. Kongkhambut, S. Rao, L. Mathey, H. Keßler, A. Hemmerich et al., *Condensate formation in a dark state of a driven atom-cavity system*, *Physical Review Letters* **130** (2022) 163603.
- [6] C. S. Pittendrigh, *Circadian rhythms and the circadian organization of living systems.*, *Cold Spring Harbor symposia on quantitative biology* **25** (1960) 159–184.
- [7] Victor G. Bruce and C. S. Pittendrigh, *Endogenous Rhythms in Insects and Microorganisms*, *The American Naturalist* **91** (1957) 179–195.
- [8] A. T. Winfree, *Biological rhythms and the behavior of populations of coupled oscillators*, *Journal of Theoretical Biology* **16** (1967) 15–42.
- [9] A. T. Winfree, *When Time Breaks Down: The Three-dimensional Dynamics of Electrochemical Waves and Cardiac Arrhythmias*. Princeton University Press, illustrate ed., 1987.
- [10] F. Wilczek, *Quantum time crystals*, *Physical Review Letters* **109** (2012) 1–5, [1202.2539].
- [11] A. Shapere and F. Wilczek, *Classical time crystals*, *Physical Review Letters* **109** (2012) 1–4, [1202.2537].
- [12] P. Bruno, *Comment on "quantum Time Crystals"*, *Physical Review Letters* **110** (2013) 118901.
- [13] P. Bruno, *Impossibility of spontaneously rotating time crystals: A no-go theorem*, *Physical Review Letters* **111** (2013) 1–5, [1306.6275].
- [14] H. Watanabe and M. Oshikawa, *Absence of quantum time crystals*, *Physical Review Letters* **114** (2015) 1–5.
- [15] K. Sacha, *Modeling spontaneous breaking of time-translation symmetry*, *Physical Review A - Atomic, Molecular, and Optical Physics* **91** (2015) 1–5, [1410.3638].
- [16] D. V. Else, B. Bauer and C. Nayak, *Floquet Time Crystals*, *Physical Review Letters* **117** (2016) 1–5.

- [17] D. V. Else, C. Monroe, C. Nayak and N. Y. Yao, *Discrete time crystals*, *Annual Review of Condensed Matter Physics* **11** (2020) 467–499.
- [18] N. Y. Yao and C. Nayak, *Time crystals in periodically driven systems*, *Physics Today* **71** (2018) 40–47.
- [19] J. Zhang, P. W. Hess, A. Kyprianidis, P. Becker, A. Lee, J. Smith et al., *Observation of a discrete time crystal*, *Nature* **543** (2017) 217–220.
- [20] S. Choi, J. Choi, R. Landig, G. Kucsko, H. Zhou, J. Isoya et al., *Observation of discrete time-crystalline order in a disordered dipolar many-body system*, *Nature* **543** (2017) 221–225, [1610.08057].
- [21] J. Rovny, R. L. Blum and S. E. Barrett, *Observation of Discrete-Time-Crystal Signatures in an Ordered Dipolar Many-Body System*, *Physical Review Letters* **120** (2018) 180603.
- [22] J. Smits, L. Liao, H. T. Stoof and P. Van Der Straten, *Observation of a Space-Time Crystal in a Superfluid Quantum Gas*, *Physical Review Letters* **121** (2018) 185301, [1807.05904].
- [23] D. A. Abanin, E. Altman, I. Bloch and M. Serbyn, *Colloquium: Many-body localization, thermalization, and entanglement*, *Reviews of Modern Physics* **91** (2019) 21001.
- [24] R. Chitra and O. Zeitler, *Dynamical many-body phases of the parametrically driven, dissipative Dicke model*, *Physical Review A - Atomic, Molecular, and Optical Physics* **92** (2015) 1–7, [1501.07098].
- [25] Z. Gong, R. Hamazaki and M. Ueda, *Discrete Time-Crystalline Order in Cavity and Circuit QED Systems*, *Physical Review Letters* **120** (2018) 40404.
- [26] B. Zhu, J. Marino, N. Y. Yao, M. D. Lukin and E. A. Demler, *Dicke time crystals in driven-dissipative quantum many-body systems*, *New Journal of Physics* **21** (2019) 0–13, [1904.01026].
- [27] B. Buča, J. Tindall and D. Jaksch, *Non-stationary coherent quantum many-body dynamics through dissipation*, *Nature Communications* **10** (2019) 1–6, [1804.06744].
- [28] N. Y. Yao, C. Nayak, L. Balents and M. P. Zaletel, *Classical discrete time crystals*, *Nature Physics* **16** (2020) 438–447, [1801.02628].
- [29] R. P. Feynman, *Simulating physics with computers*, *Int J Theor Phys* **21** (1982) 467–488.
- [30] J. I. Jané, E. and Vidal, G. and Dürr, W. and Zoller, P. and Cirac, *Simulation of quantum dynamics with quantum optical systems*, *Quantum Information and Computation* **3** (2003) 15–37.
- [31] M. Saffman, T. G. Walker and K. Mølmer, *Quantum information with Rydberg atoms*, *Reviews of Modern Physics* **82** (2010) 2313–2363, [arXiv:0909.4777v2].
- [32] I. Bloch, J. Dalibard and S. Nascimbène, *Quantum simulations with ultracold quantum gases*, *Nature Physics* **8** (apr, 2012) 267 EP –.
- [33] R. Löw, H. Weimer, J. Nipper, J. B. Balewski, B. Butscher, H. P. Büchler et al., *An experimental and theoretical guide to strongly interacting Rydberg gases*, *Journal of Physics B: Atomic, Molecular and Optical Physics* **45** (2012) , [1202.2871].
- [34] L. Henriot, L. Beguin, A. Signoles, T. Lahaye, A. Browaeys, G. O. Reymond et al., *Quantum computing with neutral atoms*, *Quantum* **4** (2020) 1–34, [2006.12326].
- [35] P. Cirac, J. I. and Zoller, *Quantum computation with trapped ions*, *Physical Review Letters* **74** (1995) 4019–4094.

- [36] F. Schmidt-Kaler, H. Häffner, M. Riebe, S. Gulde, G. P. Lancaster, T. Deuschle et al., *Realization of the Cirac-Zoller controlled-NOT quantum gate*, *Nature* **422** (2003) 408–411.
- [37] R. Blatt and C. F. Roos, *Quantum simulations with trapped ions*, *Nature Physics* **8** (2012) 277–284.
- [38] C. Monroe and J. Kim, *Scaling the ion trap quantum processor*, *Science* **339** (2013) 1164–1169.
- [39] J. E. Mooij, T. P. Orlando, L. Levitov, L. Tian, C. H. van der Wal and S. Lloyd, *Josephson Persistent-Current Qubit*, *Science* **285** (1999) 1036–1040.
- [40] L. Dicarlo, J. M. Chow, J. M. Gambetta, L. S. Bishop, B. R. Johnson, D. I. Schuster et al., *Demonstration of two-qubit algorithms with a superconducting quantum processor*, *Nature* **460** (2009) 240–244, [0903.2030].
- [41] F. Arute, K. Arya, R. Babbush, D. Bacon, J. C. Bardin, R. Barends et al., *Quantum supremacy using a programmable superconducting processor*, *Nature* **574** (2019) 505–510.
- [42] W. L. Yang, Z. Q. Yin, Y. Hu, M. Feng and J. F. Du, *High-fidelity quantum memory using nitrogen-vacancy center ensemble for hybrid quantum computation*, *Physical Review A - Atomic, Molecular, and Optical Physics* **84** (2011) 1–4, [1106.2909].
- [43] V. Acosta and P. Hemmer, *Nitrogen-vacancy centers: Physics and applications*, *MRS Bulletin* **38** (2013) 127–130.
- [44] L. Gordon, J. R. Weber, J. B. Varley, A. Janotti, D. D. Awschalom and C. G. Van De Walle, *Quantum computing with defects*, *MRS Bulletin* **38** (2013) 802–808.
- [45] J. L. O’Brien, *Optical quantum computing*, *Science* **318** (2007) 1567–1570.
- [46] X. S. Ma, B. Dakic, W. Naylor, A. Zeilinger and P. Walther, *Quantum simulation of the wavefunction to probe frustrated Heisenberg spin systems*, *Nature Physics* **7** (2011) 399–405, [1008.4116].
- [47] A. Aspuru-Guzik and P. Walther, *Photonic quantum simulators*, *Nature Physics* **8** (2012) 285–291.
- [48] T. W. Hänsch and A. L. Schawlow, *Cooling of gases by laser radiation*, *Optics Communications* **13** (1975) 68–69.
- [49] S. Chu, L. Hollberg, J. E. Bjorkholm, A. Cable and A. Ashkin, *Three-dimensional viscous confinement and cooling of atoms by resonance radiation pressure*, *Phys. Rev. Lett.* **55** (jul, 1985) 48–51.
- [50] *The Nobel Prize in Physics 1997*, 1997.
- [51] P. D. Lett, R. N. Watts, C. I. Westbrook, W. D. Phillips, P. L. Gould and H. J. Metcalf, *Observation of Atoms Laser Cooled below the Doppler Limit*, *Phys. Rev. Lett.* **61** (jul, 1988) 169–172.
- [52] J. Dalibard and C. Cohen-Tannoudji, *Laser cooling below the Doppler limit by polarization gradients: simple theoretical models*, *J. Opt. Soc. Am. B* **6** (nov, 1989) 2023–2045.
- [53] E. L. Raab, M. Prentiss, A. Cable, S. Chu and D. E. Pritchard, *Trapping of Neutral Sodium Atoms with Radiation Pressure*, *Phys. Rev. Lett.* **59** (dec, 1987) 2631–2634.
- [54] M. H. Anderson, J. R. Ensher, M. R. Matthews, C. E. Wieman and E. A. Cornell, *Observation of Bose-Einstein Condensation in a Dilute Atomic Vapor*, *Science* **269** (1995) 198–201.

- [55] K. B. Davis, M. O. Mewes, M. R. Andrews, N. J. van Druten, D. S. Durfee, D. M. Kurn et al., *Bose-Einstein Condensation in a Gas of Sodium Atoms*, *Phys. Rev. Lett.* **75** (nov, 1995) 3969–3973.
- [56] A. Einstein, *Quantentheorie des einatomigen idealen Gases*, *Albert Einstein: Akademie-Vorträge* (2005) 237–244.
- [57] M. Greiner, O. Mandel, T. Esslinger<sup>2</sup>, T. W. Ha, I. Bloch, T. Esslinger et al., *Quantum phase transition from a superfluid to a Mott insulator in a gas of ultracold atoms*, *Nature* **415** (2002) 39–44.
- [58] J. Klinder, H. Keßler, M. R. Bakhtiari, M. Thorwart and A. Hemmerich, *Observation of a Superradiant Mott Insulator in the Dicke-Hubbard Model*, *Physical Review Letters* **115** (2015) 1–5.
- [59] J. Struck, C. Öschlager, R. L. Targat, P. Soltan-Panahi, A. Eckardt, M. Lewenstein et al., *Quantum Simulation of Frustrated Classical Magnetism in Triangular Optical Lattices*, *Science* **333** (2011) 996–1000.
- [60] L. J. Garay, J. R. Anglin, J. I. Cirac and P. Zoller, *Sonic Analog of Gravitational Black Holes in Bose-Einstein Condensates*, *Phys. Rev. Lett.* **85** (nov, 2000) 4643–4647.
- [61] W. Hu, R. Barkana and A. Gruzinov, *Fuzzy Cold Dark Matter: The Wave Properties of Ultralight Particles*, *Phys. Rev. Lett.* **85** (aug, 2000) 1158–1161.
- [62] T. J. Kippenberg and K. J. Vahala, *Cavity optomechanics: Back-action at the mesoscale*, *Science* **321** (2008) 1172–1176.
- [63] M. Aspelmeyer, T. J. Kippenberg and F. Marquardt, *Cavity optomechanics*, *Reviews of Modern Physics* **86** (2014) 1391–1452, [1303.0733].
- [64] P. Lodahl, S. Mahmoodian and S. Stobbe, *Interfacing single photons and single quantum dots with photonic nanostructures*, *Reviews of Modern Physics* **87** (2015) 347–400, [1312.1079].
- [65] H. Ritsch, P. Domokos, F. Brennecke and T. Esslinger, *Cold atoms in cavity-generated dynamical optical potentials*, *Reviews of Modern Physics* **85** (2013) 553–601.
- [66] F. Breuer, Heinz-Peter and Petruccione, *The Theory of Open Quantum Systems*. Oxford University Press, 2007, 10.1093/acprof:oso/9780199213900.001.0001.
- [67] K. G. Baumann, *Experimental Realization of the Dicke Quantum Phase Transition*. PhD thesis, ETH Zurich, 2011.
- [68] R. Mottl, F. Brennecke, K. Baumann, R. Landig, T. Donner and T. Esslinger, *Roton-Type Mode Softening in a Long-Range Interactions*, *Science* **336** (2012) 1570–1573.
- [69] F. Brennecke, R. Mottl, K. Baumann, R. Landig, T. Donner and T. Esslinger, *Real-time observation of fluctuations at the drivendissipative dicke phase transition*, *Proceedings of the National Academy of Sciences of the United States of America* **110** (2013) 11763–11767.
- [70] H. Keßler, J. Klinder, B. P. Venkatesh, C. Georges and A. Hemmerich, *In situ observation of optomechanical Bloch oscillations in an optical cavity*, *New Journal of Physics* **18** (2016) .
- [71] K. W. Murch, K. L. Moore, S. Gupta and D. M. Stamper-Kurn, *Observation of quantum-measurement backaction with an ultracold atomic gas*, *Nature Physics* **4** (2008) 561–564, [0706.1005].
- [72] I. B. Mekhov and H. Ritsch, *Quantum nondemolition measurements and state preparation in quantum gases by light detection*, *Physical Review Letters* **102** (2009) 1–4.
- [73] J. Keeling, M. J. Bhaseen and B. D. Simons, *Collective dynamics of Bose-Einstein condensates in optical cavities*, *Physical Review Letters* **105** (2010) 2–5, [1002.3108].

- [74] G. Mazzucchi, W. Kozłowski, S. F. Caballero-Benitez, T. J. Elliott and I. B. Mekhov, *Quantum measurement-induced dynamics of many-body ultracold bosonic and fermionic systems in optical lattices*, *Physical Review A* **93** (2016) 1–12, [1503.08710].
- [75] F. Mivehvar, F. Piazza, T. Donner and H. Ritsch, *Cavity QED with quantum gases: new paradigms in many-body physics*, *Advances in Physics* **70** (2021) 1–153.
- [76] P. Domokos and H. Ritsch, *Collective Cooling and Self-Organization of Atoms in a Cavity*, *Physical Review Letters* **89** (2002) 1–4.
- [77] K. Hepp and E. H. Lieb, *On the superradiant phase transition for molecules in a quantized radiation field: the Dicke maser model*, *Annals of Physics* **76** (1973) 360–404.
- [78] A. Morro and C. Giorgi, *Phase Transitions in the Dicke Model of Superradiance*, *Modeling and Simulation in Science, Engineering and Technology* **7** (1973) 909–949, [9708021].
- [79] A. T. Black, H. W. Chan and V. Vuletić, *Observation of collective friction forces due to spatial self-organization of atoms: From Rayleigh to Bragg scattering*, *Physical Review Letters* **91** (2003) 203001/1–203001/4.
- [80] K. Baumann, C. Guerlin, F. Brennecke and T. Esslinger, *Dicke quantum phase transition with a superfluid gas in an optical cavity*, *Nature* **464** (2010) 1301–1306, [0912.3261].
- [81] J. Klinder, H. Keßler, M. Wolke, L. Mathey and A. Hemmerich, *Dynamical phase transition in the open Dicke model*, *Proceedings of the National Academy of Sciences of the United States of America* **112** (2015) 3290–3295.
- [82] A. Lambrecht, E. Giacobino and J. M. Courty, *Optical nonlinear dynamics with cold atoms in a cavity*, *Optics Communications* **115** (1995) 199–206.
- [83] S. Ritter, F. Brennecke, K. Baumann, T. Donner, C. Guerlin and T. Esslinger, *Dynamical coupling between a Bose-Einstein condensate and a cavity optical lattice*, *Applied Physics B: Lasers and Optics* **95** (2009) 213–218, [0811.3967].
- [84] H. Keßler, J. Klinder, M. Wolke and A. Hemmerich, *Optomechanical atom-cavity interaction in the sub-recoil regime*, *New Journal of Physics* **16** (2014) .
- [85] M. Wolke, J. Klinner, H. Keßler and A. Hemmerich, *Cavity cooling below the recoil limit*, *Science* **336** (2012) 75–78.
- [86] D. Dreon, A. Baumgärtner, X. Li, S. Hertlein, T. Esslinger and T. Donner, *Self-oscillating pump in a topological dissipative atom-cavity system*, *Nature* **608** (2022) 494–498, [2112.11502].
- [87] J. G. Cosme, J. Skulte and L. Mathey, *Time crystals in a shaken atom-cavity system*, *Physical Review A* **100** (2019) .
- [88] C. Foot, *Atomic Physics*. Oxford University Press, 2005, illustrate ed., 2005.
- [89] J. Nellesen, J. Werner and W. Ertmer, *Magneto-optical compression of a monoenergetic sodium atomic beam*, *Optics Communications* **78** (1990) 300–308.
- [90] M. Wolke, *Laserkühlung in Optischen Resonatoren unter Der Ruchstossgrenze*. PhD thesis, Universität Hamburg, 2012.
- [91] J. Klinner, *Experiments with Ultra-Cold Atomic Ensembles in Optical Resonators with Ultra-High Finesse and Narrow Linewidth Dissertation*. PhD thesis, Universität Hamburg, 2009.
- [92] C. I. W. P. D. Lett, W. D. Phillips, S. L. Rolston, C. E. Tanner, R. N. Watts, *Optical molasses*, *J. Opt. Soc. Am. B* **6** (1989) 2084—2107.



- [93] W. C. Georges, *The dynamical driven atom-cavity system : A realization beyond the open Dicke model*. PhD thesis, Universität Hamburg, 2021.
- [94] T. Esslinger, I. Bloch and T. W. Hänsch, *Bose-Einstein condensation in a quadrupole-Ioffe-configuration trap*, *Phys. Rev. A* **58** (1998) R2664—R2667.
- [95] J. Klinner, M. Wolke and A. Hemmerich, *Increased efficiency of rf-induced evaporative cooling by utilizing gravity*, *Physical Review A - Atomic, Molecular, and Optical Physics* **81** (2010) 1–5.
- [96] J. Klinder, *Vom dynamischen Phasenübergang im offenen Dicke-Modell zum Dicke-Hubbard Modell*. PhD thesis, Universität Hamburg, 2015.
- [97] H. Kessler, *Resonator-kontrollierte Materiewellen-Superradianz*. PhD thesis, Universität Hamburg, 2015.
- [98] W. Ketterle, D. S. Durfee and D. M. Stamper-Kurn, *Making, probing and understanding Bose-Einstein condensates*, *arXiv* (1999) , [9904034].
- [99] S. Rao, *A Balanced Heterodyne Detection Scheme for Sensitive Light Detection on a Strongly Coupled Atom-Cavity System*. PhD thesis, Karlsruhe Institute of Technology, 2022.
- [100] R. Landig, *Quantum phases emerging from competing short- and long- range interactions in an optical lattice*. Phd thesis, ETH Zuerich, 2016. 10.3929/ethz-a-010782581.
- [101] A. Polkovnikov, *Phase space representation of quantum dynamics*, *Annals of Physics* **325** (2010) 1790–1852.
- [102] N. Dogra, M. Landini, K. Kroeger, L. Hruby, T. Donner and T. Esslinger, *Dissipation-induced structural instability and chiral dynamics in a quantum gas*, *Science* **366** (2019) 1496–1499, [1901.05974].
- [103] B. Buča and D. Jaksch, *Dissipation Induced Nonstationarity in a Quantum Gas*, *Physical Review Letters* **123** (2019) 1–5, [1905.12880].
- [104] E. I. Chiacchio and A. Nunnenkamp, *Dissipation-induced instabilities of a spinor bose-einstein condensate inside an optical cavity*, *Physical Review Letters* **122** (2019) 193605, [1901.06996].
- [105] Z. Gong and M. Ueda, *Time Crystals in Open Systems*, *Physics* **14** (2021) 19–21.
- [106] F. Piazza and H. Ritsch, *Self-Ordered Limit Cycles, Chaos, and Phase Slippage with a Superfluid inside an Optical Resonator*, *Physical Review Letters* **115** (2015) 1–5, [1507.08644].
- [107] H. Keßler, J. G. Cosme, M. Hemmerling, L. Mathey and A. Hemmerich, *Emergent limit cycles and time crystal dynamics in an atom-cavity system*, *Physical Review A* **99** (2019) .
- [108] J. G. Cosme, J. Skulte and L. Mathey, *Bridging closed and dissipative discrete time crystals in spin systems with infinite-range interactions*, *Phys. Rev. B* **108** (Jul, 2023) 024302.
- [109] L. J. LeBlanc, *Unleashing spontaneity in a time crystal*, *Science perspective* **377** (2022) 576–577.
- [110] M. H. Jensen, P. Bak and T. Bohr, *Complete devil’s staircase, fractal dimension, and universality of mode- locking structure in the circle map*, *Physical Review Letters* **50** (1983) 1637–1639.
- [111] N. Mitarai, U. Alon and M. H. Jensen, *Entrainment of noise-induced and limit cycle oscillators under weak noise*, *Chaos* **23** (2013) , [1301.2440].

- [112] H. Keßler, J. G. Cosme, C. Georges, L. Mathey and A. Hemmerich, *From a continuous to a discrete time crystal in a dissipative atom-cavity system*, *New Journal of Physics* **22** (2020) .
- [113] P. Gao, Z. W. Zhou, G. C. Guo and X. W. Luo, *Self-organized limit cycles in red-detuned atom-cavity systems*, *Physical Review A* **107** (2023) 23311, [2212.04142].
- [114] J.-P. Eckmann, *Roads to turbulence in dissipative dynamical systems*, *Reviews of Modern Physics*, **53** (1981) 643–654.
- [115] J. P. Gollub and H. L. Swinney, *The Transition to Turbulence*, *Physics Today* **31** (1978) 41–49.
- [116] M. Giglio, S. Musazzi and U. Perini, *Transition to chaotic behavior via a reproducible sequence of period-doubling bifurcations*, *Physical Review Letters* **47** (1981) 243–246.
- [117] W. Lauterborn and E. Cramer, *Subharmonic route to chaos observed in acoustics*, *Physical Review Letters* **47** (1981) 1445–1448.
- [118] F. T. Arecchi, R. Meucci, G. Puccioni and J. Tredicce, *Experimental evidence of subharmonic bifurcations, multistability, and turbulence in a Q-switched gas laser*, *Physical Review Letters* **49** (1982) 1217–1220.
- [119] J. Testa, J. Pérez and C. Jeffries, *Evidence for universal chaotic behavior of a driven nonlinear oscillator*, *Physical Review Letters* **48** (1982) 714–717.